SOLUTION PROCESSED GROUP VI TRANSITION METAL DICHALCOGENIDES: A STUDY ON CONDUCTIVE HYBRIDS AND PHOTOCONDUCTIVITY FOR FUTURE APPLICATIONS IN PRINTED ELECTRONICS

GRAEME CUNNINGHAM

A thesis submitted for the degree of
Doctor of Philosophy

Supervised by Prof. Jonathan Coleman
Chemical Physics of Low Dimensional Nanostructures Group
School of Physics
Trinity College Dublin

2014

To my Mam & Dad

and my family & friends..

DECLARATION

I declare that this thesis has not been submitted as an exercise for a degree at this or any other university and it is entirely my own work.

I agree to deposit this thesis in the University's open access institutional repository or allow the library to do so on my behalf, subject to Irish Copyright Legislation and Trinity College Library conditions of use and acknowledgement.

Elements of this work that have been carried out jointly with others or by collaborators have been duly acknowledged in the text wherever included.

ABSTRACT

Transition metal dichalcogenides (TMDs) constitute a class of inorganic layered compound with generalised MX_2 stoichiometry, where M denotes a transition metal atom and X a chalcogen atom of sulfur, selenium or tellurium (S, Se or Te). As such over forty different varieties may be realised, covering the full array of electronic properties from insulators and semiconductors through to metals and superconductors, depending on the combination of M and X.[1] TMD monolayers are ~0.7 nm thick and consist of a hexagonal plane of transition metal atoms sandwiched between two displaced hexagonal planes of chalcogen atoms as X-M-X. Like graphene, these materials exhibit interesting physical phenomena when manifested in the monolayer limit.

Applications of layered materials will require large quantities, indicating that a solution processing approach will be useful.[2] Liquid phase exfoliation is one such method and has been used previously to successfully disperse carbon nanotubes[3] and graphene[4] in organic solvents. This work begins by extending this approach to exfoliate a set of inorganic layered materials into two-dimensional nanosheets by sonication in a suitably chosen organic solvent. Over 21 solvents have been tested and the effect of varying both transition metal atom and chalcogen atom on solubility has been investigated within the framework of solution thermodynamics. In all cases, good dispersion is shown by solvents with surface tensions close to 40 mJ/m^2 and Hansen parameters close to 18 $MPa^{1/2}$, 8.5 $MPa^{1/2}$ and 7 $MPa^{1/2}$ for the dispersive, polar and H-bonding components of bonding respectively. This allows an estimation of the Flory-Huggins parameter, χ. For each combination of nanosheet and solvent it is shown that the dispersed concentration falls off exponentially with χ, indicating that solution thermodynamics can indeed be used as a model to understand the dispersion of these layered materials.

In many areas, applications of films of exfoliated layered compounds will be limited by their relatively low electrical conductivity. Among such applications are battery

and supercapacitor electrodes as well as thermoelectrics. To address this, composites of a nano-conductor (nanotubes or graphene) embedded in a matrix of exfoliated MoS_2 nanosheets have been prepared and characterised. Solvent exfoliation of MoS_2 nanosheets, followed by blending with dispersions of graphene or nanotubes allowed the formation of such composite films by vacuum filtration onto porous membranes which may then be transferred to any desired substrate by subsequently dissolving the membrane. This gave spatially uniform mixtures with fully tunable nano-conductor content. By addition of the nano-conducting phase, it was possible to vary the electrical conductivity of the composite over nine orders of magnitude. For both filler types the conductivity followed percolation scaling laws both above and below the percolation threshold. In the case of SWNT-filled composites, conductivities as high as 40 Sm^{-1} were achieved at volume fractions as low as 4%.

Group VI TMDs (e.g. MoS_2) are nominally semiconducting due to their fully filled lowest lying d-band. As such they exhibit photoconductivity on illumination. Solution-exfoliated MoS_2 nano-platelets have been formed into thin films by deposition onto a water surface followed by transfer to indium tin oxide coated glass to test the photo-conductivity. A gold electrode evaporated on top completes the sandwich structure with Ohmic-like contacts. Illumination of this device with broadband light of 1 kW m^2 intensity results in a fourfold increase in conductivity. The photocurrent increases sub-linearly with intensity and exponentially with time indicating the presence of traps.

Being naturally abundant, $MoS_2$and iso-electronic WS_2 are prototypical TMDs and have been widely studied over the past few years. However, much less work exists on the analogous selenides and tellurides of these materials. This is unfortunate as these varieties have smaller bandgaps than the sulfides, reflecting the increased covalency of their bonding and so extend the spectral range for optoelectronic device applications. Thin-film networks of nanosheets of five different TMDs comprising MoS_2, $MoSe_2$, $MoTe_2$, WS_2 and WSe_2 have been fabricated on Si/SiO_2 substrates. Both the dark and photoconductivity have been measured under broad band illumination in the intensity range from 0-1000 Wm^{-2}. The dark conductivity varies from ~10^{-6} S/m for

MoS_2 to ~10^{-3} S/m for WSe_2, with an apparent exponential dependence on bandgap. All materials studied show photocurrents which rise exponentially with time and depend sub-linearly on light intensity, again, both hallmarks of trap limited processes. Because the photoresponse depends relatively weakly on bandgap, the ratio of photo- to dark conductivity is largest for the sulfides because of their larger band gap and resulting lower dark conductivity.

It is hoped that the work in this thesis will be useful as liquid phase exfoliated nanomaterials are developed towards low-cost device applications such as photodetectors, network transistors, solar cells, battery electrodes and thermoelectrics for printed electronics on flexible substrates.

PUBLICATIONS

1. Large variations in both dark- and photoconductivity in nanosheet networks as material is varied from MoS_2 to WTe_2 Cunningham, G.; Hanlon, D.; McEvoy, N.; Duesberg, G.S.; Coleman, J.N.; *Nanoscale* 2015, 7, 198-208

2. Photoconductivity of solution-processed MoS_2 films Cunningham, G.; Khan, U.; Backes, C.; Hanlon, D.; McCloskey, D.; Donegan, J. F.; Coleman, J. N., *Journal of Materials Chemistry C* 2013, 1, 6899-6904

3. Percolation scaling in composites of exfoliated MoS_2 filled with nanotubes and graphene Cunningham, G.; Lotya, M.; McEvoy, N.; Duesberg, G. S.; van der Schoot, P.; Coleman, J. N., *Nanoscale* 2012, 4, 6260-6264.

4. Solvent Exfoliation of Transition Metal Dichalcogenides: Dispersability of Exfoliated Nanosheets Varies Only Weakly between Compounds Cunningham, G.; Lotya, M.; Cucinotta, C. S.; Sanvito, S.; Bergin, S. D.; Menzel, R.; Shaffer, M. S. P.; Coleman, J. N., *ACS Nano* 2012, 6 (4), 3468-3480.

5. Inkjet deposition of liquid-exfoliated graphene and MoS_2 nanosheets for printed device applications

Finn, D.J.; Lotya, M.; Cunningham, G.; Smith, R.J.; McCloskey, D.; Donegan, J.F.; Coleman, J.N., *Journal of Materials Chemistry C* 2014, 2, 925-932

Pollution is nothing but the resources we are not harvesting

(Richard Buckminster Fuller)

'Reality' is what you can get away with

(Robert Anton Wilson)

ACKNOWLEDGMENTS

Firstly i'd like to thank Professor Jonathan Coleman for giving me the opportunity to expand my education and pursue this PhD in his group. Specifically for all the funding, sound advice, guidance and influential discussions over the past four years. I'd also like to thank the School of Physics staff for all their help along the way: Marie, Jeanette, Ciara, Sam, Robbie, Pa, Joe, Ken, Nigel & Alan, without whom none of us students would be able to do our research.

My time here has been an extremely positive experience and i've met a lot of good-hearted people along the way whom I am now happy to count among my friends. Over in 22 Westland Row, 'the office' has come to be a home in the very heart of the city. I've had the pleasure of sharing this building with a number of interesting characters in this time.

I want to say thank you to those who helped me settle in: Darren, Niall, Mustafa, Marguerite, Karen, Phil, Paul, Arlene, Sophie, Pete May and Ronan. It's great so many of you are still around Trinity in some capacity and that we'll get to catch up from time to time. I'm indebted to Mustafa Lotya for showing me the ropes, Niall McEvoy for all things Raman and your good-natured sense of humour and lastly but certainly not least Paul King: selfless in your serving of others whilst maintaining steadfast focus upon your own goals, you've been an inspiration and I'm very thankful for all the advice along the way both in the lab and all things gym & fitness as well as your honest encouragement of my work. To the current crop of giants; Conor, Seb and Pete Lynch, it has been a lot of fun to share the office with you over the past couple of years.

To Auren & Ivan next door and Ro, Tom & Damo downstairs, I sincerely enjoyed your company and a few (un)memorable beers along the way. To the newbies Andrew, Dave & Adam I wish you the very best of luck, the time will accelerate quickly so enjoy it now and while it lasts. Also a big thanks to the post-docs for keeping us right and getting us through difficult patches of research. Distinct thanks must go the wise old hand in the group, Umar Khan: your unconventional approach to problem solving evokes admiration for its chaotic-creativity and it seems to me that there really is no distinction for you between work & play in the lab or in life. As the length of this list shows, whilst one name goes on the cover of a thesis it cannot be done all alone. Before I forget, I must also thank Rob & Ronan for keeping us fit with all the fun & lively games of football in Botany Bay and Sportsco during this period.

Outside of college I want to thank my close circle of three true friends throughout this time; Bert, Faj & Johny. Bertie I owe you a lot, you've been my patron with your mates-rates rents in a very expensive city to live, and without your sincere kindness & friendship I would never have been able to do this work. I'd like to dedicate this thesis to my parents for providing me with a beautiful childhood and an upbringing where I never wanted for anything: you always put my education first and instilled in me the values of learning, hard-work and perseverance and there is no way I would have completed this work without your continued love and support. To my special girl Deirdre, thank you from the bottom of my heart for all your love and dedication, for putting up with me and for cheering me up if ever I am down; we make a great team.

CONTENTS

LIST OF FIGURES

LIST OF TABLES

1

INTRODUCTION

Historically, advances in technology have consistently allowed humans to access untapped energy resources. Previously, the stone and the bronze ages gave way to the iron age and as we now near the end of what is often termed the silicon age. Silicon CMOS technology has driven dimensional scaling down toward nanometre (nm) length scales and is now ushering in what may be viewed as a new technological era: the age of dimensionality. Dimensionality is one of the most defining material properties and the same compound behaves very differently depending on whether it is obtained in its zero, one, two or three dimensional form.

Nanoscience refers to the physics, chemistry and biology of materials endowed with at least one dimension with length scale on the order of nanometres. Such length scales are well below the wavelengths of our visible spectrum, on the order of the de Broglie wavelength for electrons. New fundamental physical properties, superior to those found in bulk, may manifest here due to the effects of quantum confinement. Manipulation of materials down at these length scales could become increasingly important for society if technological progress and economic growth are to continue in a clean environment of relative political stability.

Worldwide energy demands currently stand at 13 TW and are increasing exponentially.[8] Predicted to double by 2050 and treble by the end of the century, meeting such demands may be the defining challenge of our era. A revolutionary jump is required in clean energy production. Nanotechnology offers hope in the form of a new molecular toolkit of fundamental building blocks which may be harnessed to increase energy conversion efficiency. Understanding the fundamental principles of these energy conversion processes is required in addition to developing new materials to exploit them.

Thesis Outline

This work uses liquid phase exfoliation in organic solvents to process a set of inorganic layered nanomaterials from the family of transition metal dichalcogenides (TMDs). The factors affecting dispersion solubility are investigated within the framework of solution thermodynamics. Having been understood, these dispersions are used to make thin films of networks of individual nanosheets. Such films have potential in a large number of applications, specifically in low-cost energy conversion and storage. However for many of these, the inherent low conductivity of such disordered networks presents a significant problem. Fortunately, as is shown in this work, this low conductivity problem may be mitigated with the addition of small quantities of nanoconductors such as carbon nanotubes or graphene nanosheets. These carbon based nanomaterials may be exfoliated in the same set of solvents and so hybrid films may be produced by simple blending of the dispersions. This is an extremely powerful technique as it allows a tunable conductivity over at least nine orders of magnitude.

The group VI TMDs studied throughout this work are semiconducting. In bulk form they have indirect gaps which are shifted up into the visible region of the spectrum and become direct when thinned to a monolayer. This gives these materials huge potential in optoelectronic applications such as sensors, LEDs and solar cells. However as the bandgap is a strong function of layer number, and liquid phase dispersions tend to have a degree of polydispersity this would render such films energetically inhomogeneous. As such, photoconductive studies of films bulk group VI TMDs have been performed to remove this variability in the bandgaps of the entities making up the networks. Such studies are an important starting point to develop these networks for photovoltaic energy conversion: Cost is currently the main barrier to solar energy proliferation and solution processed networks can be fabricated using high throughput, low temperature solution procesing techniques in atmospheric conditions offering ample opportunity for industrial scale up which should result in drastic cost reductions. It is hoped the work in this thesis may serve as a starting point for the study and development of solution processed nanosheet networks in optoelectronic device applications.

2

TRANSITION METAL DICHALCOGENIDES - BACKGROUND AND OVERVIEW

Two dimensional (2D) materials are those with one dimension small enough (thickness < nm) for their electrons to experience restricted motion by quantum confinement in this direction. They are free to move as normal within the ~infinite 2D plane (usually ~μm). This leads to interesting and novel physical phenomena not seen in bulk, which could open up a new wave of technology and devices that could transform and innovate how we live and communicate. This 2D nature fundamentally stems from an anisotropy in the bonding, whereby in-plane bonding is strong and covalent yet out-of-plane bonding is weak van der Waals. As such individual 2D layers are only weakly stacked to form 3D crystals and may be exfoliated down to individual true 2D objects.

The best known 2D material is graphene; a monolayer of graphite. This hexagonal plane of sp^2 hybridised carbon atoms was first studied theoretically in the in the 1940s. Until its isolation in 2004,[9] it was believed such materials were not stable and could not exist. Its inception has sparked interest in other 2D layered materials, of which there are many.[10] Transition metal dichalcogenides (TMDs) are one such class of layered material. This class of 2D materials shall now be introduced in more detail.

2.1 TRANSITION METAL DICHALCOGENIDES

First studied in the 1960s,[1] TMDs have recently experienced an academic renaissance and become a highly popular research topic. This follows on from the experimental isolation of 2D graphene in 2004,[9, 11] and the resulting research demonstrating the material's superlative electronic,[12] optical,[13] thermal[14] and mechanical[15]

properties. Similarly TMDs also exhibit fascinating and highly beneficial changes to their properties once thinned to a monolayer.

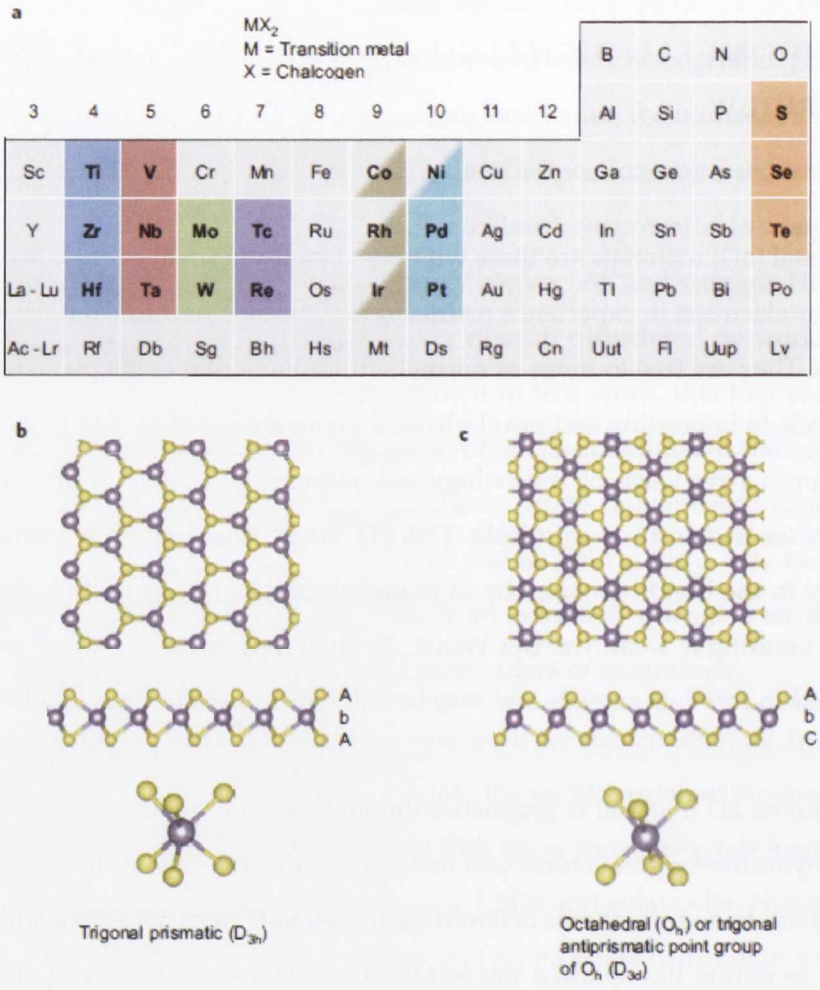

Figure 2.1: TMD crystal structure. (a) Part of the periodic table with group IV-X transition metal atoms and chalcogen atoms highlighted. Top and side views of generic monolayer TMD with (b) trigonal prismatic and (c) octahedral co-ordinations.[16]

TMDs constitute a class of inorganic layered compound with generalised MX_2 stoichiometry, where M denotes a transition metal atom and X a chalcogen atom of sulfur, selenium or tellurium (S, Se or Te). As such over forty different varieties may be realised depending on the combination of M and X. Whereas graphene and its insulating analogue hexagonal boron nitride (h-BN) are ~0.35 nm thick and composed of a single monolayer of atoms, TMD monolayers are ~0.7 nm thick and consist

of a hexagonal plane of transition metal atoms sandwiched between two displaced hexagonal planes of chalcogen atoms as X-M-X (figure 2.1). Such layers are stacked to form 3D crystals. Different stacking polymorphs exist; 1T - trigonal, 2H - hexagonal and 3R- rhombohedral. The integer refers to the number of layers in the unit cell. Different polymorphs are favoured depending on the combination of M and X. In the 2H (3R) polytype with ABA (ABA CAC BCB) stacking, the transition metal is co-ordinated in a trigonal prismatic arrangement, where each metal atom is bound to six chalcogens. This is in contrast to the 1T polytype with ABC stacking and octahedral co-ordination of the metal atom.[16] Bonding is strong and ionic/covalent within each layer but only weak van der Waals between each layer, similar to the anisotropy in graphene. This allows exfoliation or delamination of bulk crystals to mono and few layer 'nanosheets' which can be μm in length with just nm thickness, rendering them two dimensional nanomaterials.

2.2 TMD BAND STRUCTURE

Solid-state theory predicts whether a compound will behave as a metal, semiconductor or insulator based upon its periodic array of atomic potentials and the subsequent derivation of Bloch wavefunctions. From these, classes of delocalised energy states available to electrons and holes are manifested, giving rise to the bandstructure and electronic properties of crystalline solids.[17] The bandstructure is a representation of the distinctive energy levels of the constituent atoms (E) comprising the crystal's unit cell and their wave vectors (k) according to how they crystallize. The term bandstructure is often used interchangeably with the term $E - k$ relation. It can be probed directly via photoelectron emission spectroscopy. Using this technique, electrons are emitted from the sample surface following absorption of energetic photons and their energy distributions are measured.[18, 19]

Transition metals are characterised by their progressively filled d-orbitals on scanning from left to right in the periodic table. Partial filling of these outermost orbitals allows them to readily form covalent bonds with other atoms. The electronic structure of TMDs

is a function of the co-ordination of the transition metal atom and its d-electron count meaning they can manifest the properties of insulator, semiconductor or metal.[1, 16] These combinations are summarized in table 2.1.

Electronic character of different layered TMDs

Group	M	X	Properties
4	Ti, Hf, Zr	S, Se, Te	Semiconducting (E_g = 0.2-2 eV). Diamagnetic.
5	V, Nb, Ta	S, Se, Te	Narrow band metals (ρ ~10^{-4} Ω.cm) or semimetals. Superconducting. Charge density wave (CDW). Paramagnetic, antiferromagnetic, or diamagnetic.
6	Mo, W	S, Se, Te	Sulfides and selenides are semiconducting (E_g ~1 eV). Tellurides are semimetallic (ρ ~10^{-3} Ω cm). Diamagnetic.
7	Tc, Re	S, Se, Te	Small-gap semiconductors. Diamagnetic.
10	Pd, Pt	S, Se, Te	Sulfides and selenides are semiconducting (E_g = 0.4 eV) and diamagnetic. Tellurides are metallic and paramagnetic. $PdTe_2$ is superconducting.

Table 2.1: Summary of electronic properties of TMDs as a function of the combination of M and X atoms[1]

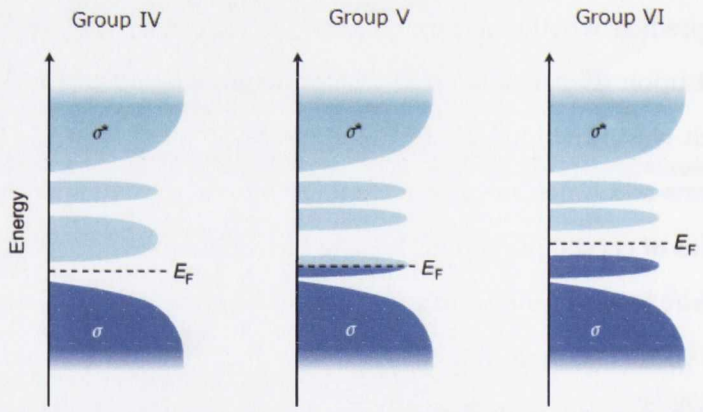

Figure 2.2: Progressive d-orbital filling within bonding (σ) and anti-bonding (σ*) states gives rise to the electronic character of group IV, V and VI TMDs. Filled and unfilled states are shaded in dark and light blue respectively.[16]

Strong covalent mixing between chalcogen and metal core s and p orbitals results in bonding (σ) and anti-bonding bands (σ*) well below and above the Fermi level respectively. This energy gap is known as the σ-σ* gap. Within this gap reside states

which are primarily derived from transition metal atom d-orbitals. It is these orbitals and their degree of filling which is responsible for the diverse array of electronic properties observed in TMDs. Group IV TMDs form two non-bonding d-orbitals $d_{yz, xz, xy}$ (lower) and d_{z^2, x^2-y^2} (upper) whilst those from group V and VI form three d-orbitals whose character is predominantly d_{z^2}, $d_{x^2-y^2, xy}$ and $d_{xz, yz}$ (from top-bottom) as in figure 2.1.[16] As such, the group IV TMDs (e.g. HfS_2) are insulators or wide-gap semiconductors.[20] Group V TMDs (e.g. $NbSe_2$) are metallic having an additional electron which renders the lowest d-band half full. This intersects the Fermi level at several points throughout the Brillouin zone. Group VI TMDs (e.g. MoS_2) are nominally semiconducting due to the presence of one further electron now completely filling this lowest lying d-band.[21]

2.2.1 *Group VI TMD Band Structure*

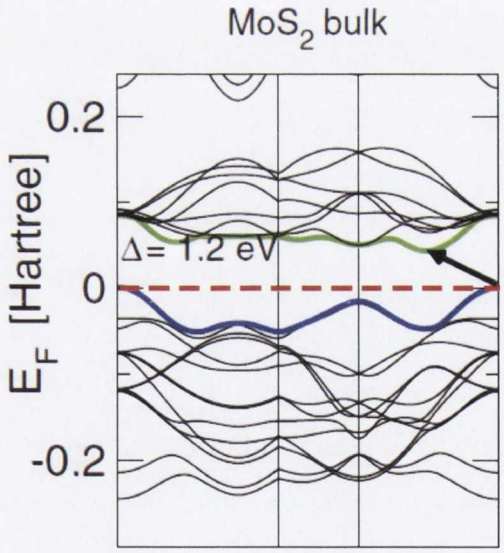

Figure 2.3: Band-structure of bulk MoS_2 within the σ-σ^* gap calculated using DFT where the dashed red line indicates the Fermi levelKuc et al. [22]

The band-structure for MoS_2 is plotted along high symmetry directions throughout the Brillouin zone in figure 2.3. MoS_2 is the most common TMD and often referred to as

a model system for group VI TMDs; all the other 5 TMDs in this group have similarly shaped band-structures. A progressive narrowing of the bandgap and shifting up in energy of the conduction band minimum (CBM) and valence band maximum (VBM) occurs as the chalcogen atomic number increases (S- Se- Te).[23, 24] This reflects the increased covalency[25] of the bonding and is accompanied by a broadening of the d-band.[16] Whilst isoelectronic, W-based common X systems have bandstructures higher in energy than Mo-based due to the higher energy of the 5d compared with the 4d orbital.[23] This group commonly crystallise as the 2H polytype at room temperature, with two X-M-X layers making up the unit cell. As such, the band-structure within the σ-σ^* gap is comprised of ten metal atom d-bands and twelve chalcogen atom p-bands.

The occupied part of the d-band is dominated by M d_{z^2} orbitals, however, the electronic states of different wave-vectors have electron orbitals with different spatial distributions and it also contains considerable M $d_{x^2-y^2,\,xy}$ character interspersed with varying degrees of X p_z character as a function of the bandwidth.[26, 27] There are two important transitions along the Γ-K high symmetry line within the Brillouin zone which bear large influence on the materials' electronic and optical properties. The indirect (fundamental) gap originates at Γ and terminates halfway between Γ and K at Λ. The band structure at Γ contains considerable contribution from chalcogen p_z orbitals covalently mixed with M d_{z^2} orbitals.[28] The out-of-plane orientation of these orbitals results in strong interlayer coupling which has the effect of depressing the VB and raising the CB as the layer number is reduced.[22] The optical (direct) gap at K is spin-orbit split and is responsible for the two prominent resonance features (the A & B excitons) in the absorption spectra of these TMDs.[29] As this gap is determined by orbitals contributing only weakly to the bonding, generation of electron-hole pairs by light does not break any bonds, resulting in remarkable stability against photocorrosion.[30] The states contributing to the band-structure here are almost solely derived from transition metal atom $d_{x^2-y^2,\,xy}$ and chalcogen $p_{x,\,y}$ orbitals.[28] These show very weak dispersion with the metal atom located at the centre of the unit cell and so the direct gap is not a strong function of layer number.[27, 31] This dictates that in the monolayer limit it becomes energetically favourable for these materials to transition from indirect to direct gap semiconductors.

2.2.2 *Group VI Monolayer TMD Band Structure*

Whereas in bulk form this group of TMDs are indirect gap semiconductors, it is in monolayer form that these materials truly display their fascinating and most-useful properties. Their direct bandgaps are well matched to the visible region of the spectrum, favouring optoelectronic applications.[32]

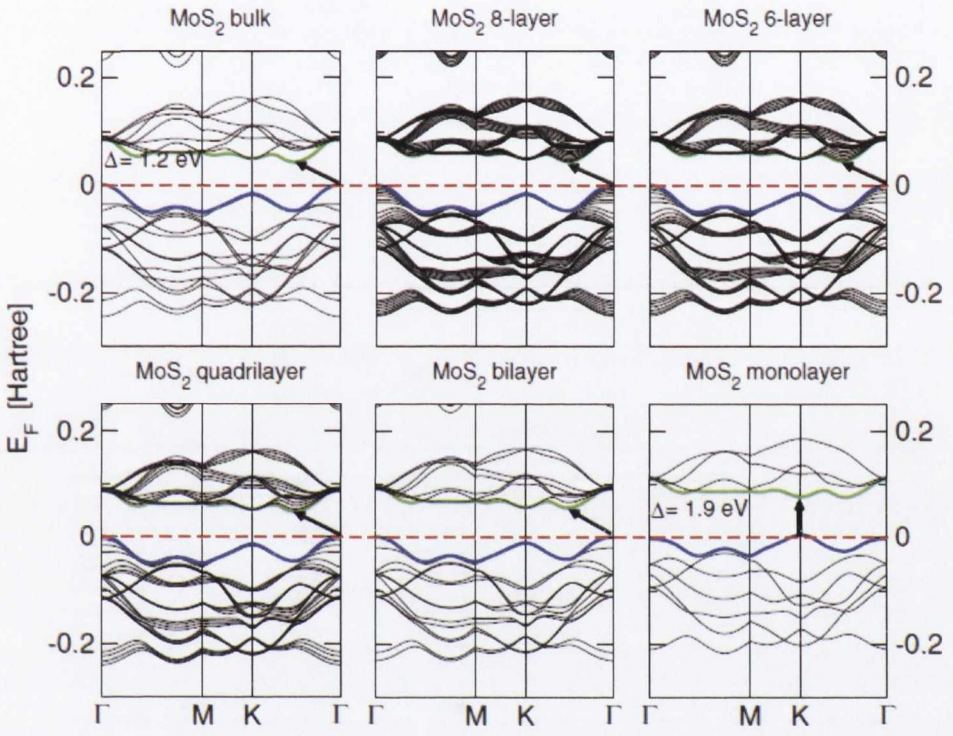

Figure 2.4: Energy dispersion evolution from bulk through to monolayer MoS_2 calculated using DFT where the Fermi level is indicated by the dashed red line. The VB-edge is coloured in blue whereas the CB-edge is marked green[22]

Generally speaking, as the number of layers is reduced the (indirect) VBM shifts down as the CBM shifts up in energy due to quantum confinement. Whilst the bulk band-structures of each of the TMDs in this group are similar, any differences that exist are accentuated in the monolayer limit and can enhance the already useful properties of these materials. For example, $MoSe_2$ has smaller differences between the direct and indirect bandgaps compared with MoS_2, especially as the layer number is reduced.[33]

In few layer form this TMD shows appreciable photoluminescence (PL) intensity as the temperature is raised to 500 K. This is un-intuitive but stems from a slight expansion of the inter-layer distance on temperature increase. This decouples neighbouring layers, increasing the degeneracy of the direct and indirect gaps and the PL intensity. Contrast this with MoS_2, whose larger difference between direct and indirect gaps ensures that the thermally induced degeneracy cannot result in an increase in PL.

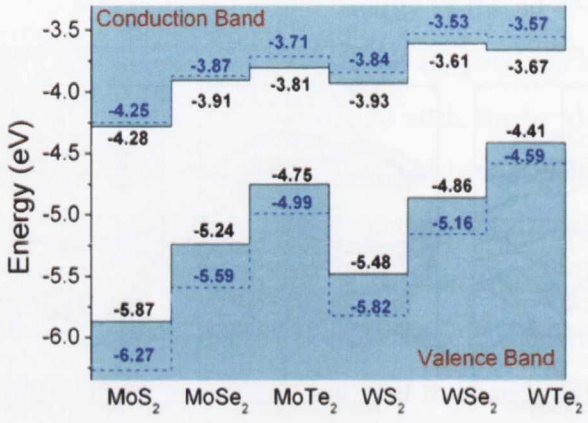

Figure 2.5: Calculated band alignment for MX_2 monolayers. Solid and dashed lines obtained by PBE and HSE respectively. Vacuum level is taken as zero reference[23]

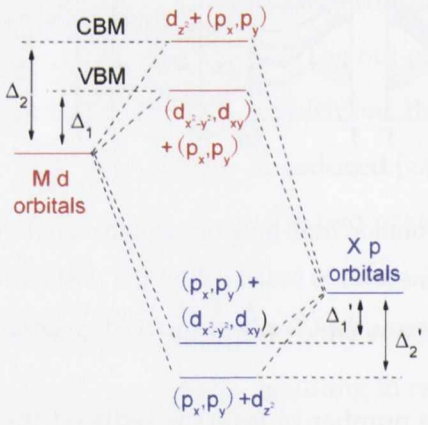

Figure 2.6: Schematic of the origin of the VBM and CBM of MX_2 monolayers at the K-point.[23]

Comparing the direct gaps across this family of monolayers, the magnitude of the CB offsets are much smaller than the VB offsets as the atomic number of the chalcogen increases. This trend is illustrated in figure 2.5 and deserves further consideration as to its origin.[23] At the K-point, the VBM originates mainly from the repulsion

between metal $d_{x^2-y^2, xy}$ orbitals and chalcogen $p_{x, y}$ orbitals. So the metal d-orbitals are pushed up by Δ_1 to form the VBM whilst the chalcogen p orbital is pushed down by Δ'_1 as shown in figure 2.6. The CBM originates from the repulsion between metal d_{z^2} orbitals and chalcogen $p_{x, y}$ orbitals. As such, the d orbitals here are pushed up by Δ_2 , forming the CBM whereas the p orbital is pushed down by Δ'_2 . So for common M systems the VBM & CBM are determined by the magnitude of the repulsions Δ_1 and Δ_2 , which are larger in heavier X systems due to the shallower p orbitals repelling the M d-orbitals more due to increased wavefunction overlap. Also, Δ_2 is stronger than Δ_1 reflecting the more dominant σ-character of the bonding in the former as opposed to π-character in the latter. This means the decrease in overlap on moving from S-Se-Te for common M systems affects the CBM more than the VBM, resulting in the smaller observed offset for the CB than the VB. The repulsions depend on the overlap between the M d and X p orbitals and their difference in energy. So a larger overlap (smaller difference in energy) leads to larger repulsions and explains the larger bandgaps in sulfide, over selenide, over telluride species. One small anomaly to note is the increase in bond length of the tellurides leading to decreased overlap of the orbitals. This partly counteracts the increase in repulsion and can be seen clearly in figure 2.6 for WTe_2. This TMD has the largest bond length in the group VI variety, actually resulting in a lower lying CBM than for WSe_2.[23]

2.3 RAMAN SPECTROSCOPY

2.3.1 *Raman Scattering*

Raman scattering is a non-destructive inelastic light scattering technique in which light from a monochromatic source is used to probe lattice vibrations (phonons). The atoms in a crystal lattice can be modelled as harmonic oscillators; masses held together by springs with an equilibrium length about which they can vibrate according to the ratio of spring force constant to atom mass. Such lattice vibrations are quantized and known as phonons. These are a signature of the bond strengths in a material.

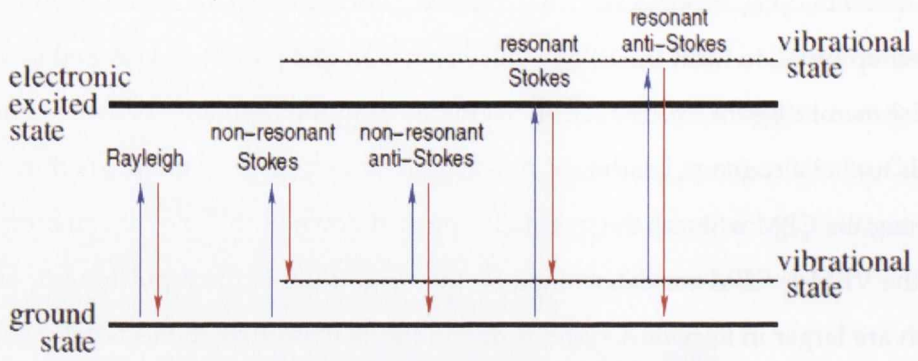

Figure 2.7: Typical processes observed in Raman spectroscopy.[34]

An incoming photon and its associated electric field interact with a material's electron cloud inducing a dipole moment. The strength of this interaction is proportional to the material polarizability. In the event that a photon absorbs (anti-Stokes) or emits (Stokes) an optical phonon on interaction with the lattice, it is subsequently re-emitted with a slight shift in energy due to the energy of the vibration which is measured as[34]

$$v = \frac{1}{\lambda_i} - \frac{1}{\lambda_s} \tag{2.1}$$

Here λ_i is the wavelength of the incident light and λ_s the wavelength of the scattered light. Unless the excitation is resonant corresponding to an electronic level (will have increased scattering amplitude), the excited state does not correspond to a stationary state and is referred to as a short lived virtual level as shown in figure 2.7.

A Raman spectrum then is a plot of the relationship between scattered light intensity as a function of energy (Raman shift in units of cm^{-1}), representing the phonon density of states. As photons interact strongly with electrons, a Compton background will be present in the spectra which may be subtracted. Obtaining spectra allows comparison with theoretical values to verify TMD sample purity. Important spectral features are peak positions, widths and intensities. These can give information on effects such as doping, disorder, stress, functionalisation and interlayer coupling.[34] Disorder, defects and impurities as well as the substrate interaction may in some cases allow phonon modes forbidden by selection rules to be weakly observed.

The first Brillouin zone (BZ) is the set of points that can be reached from the origin without crossing any Bragg planes. A first order Raman process involves a scattering event with one phonon and must obey the conservation law known as the fundamental selection rule, whereby the photoexcited electron has to go back to its original k-state to recombine with a hole.[35] This forbids phonons not of wave vector $q \approx 0$ in the neighbourhood of the zone centre, corresponding to the high symmetry Γ point. First order discrete peaks are broadened into a Lorentzian band of frequencies due to intercellular interactions. Second and higher order Raman processes display broader peaks not being restricted to near the zone centre. Overtones (two phonons of equal frequency) as well as combination bands (two phonons with different frequencies) due to acoustic-optical and optical-optical combinations can be observed. Generally these are two phonon scattering events, although a second order, one phonon elastic-scattering event is possible in the presence of defects.[36]

2.3.2 *TMD Raman Spectra*

The symmetry of the 2H polytype belongs to the D^4_{6h} space group. The lattice vibrations at the Brillouin zone centre, Γ, may be decomposed into twelve modes represented in table 2.2.[37, 38] Three acoustic (A^1_{2u} & E^1_{1u}) and two IR (A^2_{2u} & E^2_{1u}) active modes exist. These are anti-symmetric under inversion. There are also four Raman active modes (A_{1g}, E_{1g}, E^1_{2g} & E^2_{2g}) shown in figure 2.8 which are symmetric under inversion. This is why despite being degenerate in energy with the Raman active E^1_{2g} mode, the conjugate IR-active E^2_{1u} mode is not Raman active, due to the interlayer phase shift of 180^o. The E^2_{2g} mode is a rigid layer mode in which the phase of motion of one layer to the next is opposite. The only restoring force present in such a vibration is the weak interlayer interaction so it is very low frequency and often masked by the Rayleigh scattered light whereas the E_{1g} cannot be viewed in the backscattering arrangement. These Raman active modes shall now be elaborated for group VI TMDs.

Irreducible Representation	Transformation Properties	Activity	Polarization of Vibration	Atoms Involved	υ (cm^{-1})
A_{2u}	T_z	Acoustic	c-axis	Mo+S	
E_{1u}	(T_x, T_y)	Acoustic	basal plane	Mo+S	
A_{2u}	T_z	IR (E$\|\|$c)	c-axis	Mo+S	466
B^1_{2g}		Inactive	c-axis	Mo+S	466
E_{1u}	(T_x, T_y)	IR (E$\perp$c)	basal plane	Mo+S	384
E^1_{2g}	$(\alpha_{xx}- \alpha_{yy}, \alpha_{xy})$	Raman	basal plane	Mo+S	384
A_{1g}	$(\alpha_{xx}+ \alpha_{yy}, \alpha_{zz})$	Raman	c-axis	S	409
B_{1u}		Inactive	c-axis	S	409
E_{1g}	$(\alpha_{yz}, \alpha_{zx})$	Raman	basal plane	S	519
E_{2u}		Inactive	basal plane	S	519
B^2_{2g}		Inactive	c-axis	Mo+S	low
E^2_{2g}	$(\alpha_{xx}- \alpha_{yy}, \alpha_{xy})$	Raman	basal plane	Mo+S	low

Table 2.2: Long wavelength lattice modes of MoS_2.[37]

2.3.2.1 *MoS_2 & WS_2*

Raman spectra of exfoliated MoS_2[39, 41, 42] & WS_2[40, 42, 43] are similar and have been characterised widely throughout the literature. For bulk MoS_2 (WS_2) the expected Raman active modes are the E^1_{2g} in-plane peak at ~384 cm^{-1} (~357 cm^{-1}) and the A_{1g}

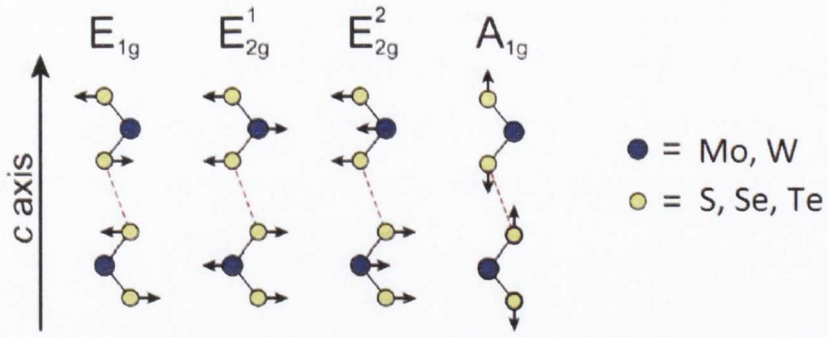

Figure 2.8: Raman active modes of TMDs, adapted from [5]

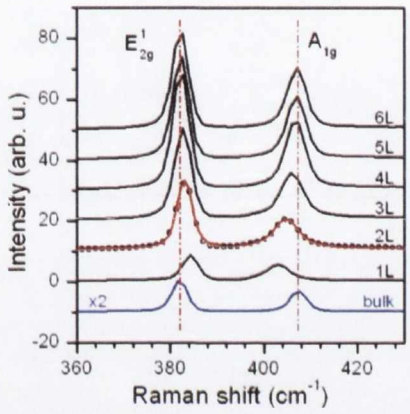

Figure 2.9: MoS_2 Raman spectra excited with 514 nm laser.[39]

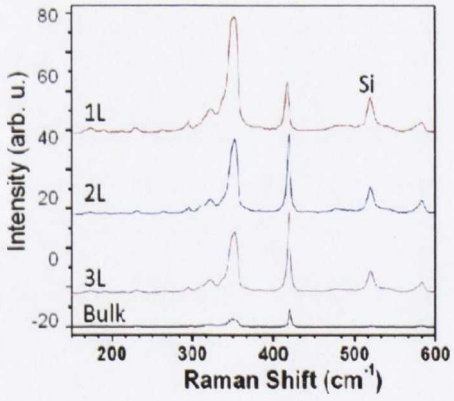

Figure 2.10: WS_2 Raman spectra excited with 514 nm laser.[40]

out-of-plane peak at ~407 cm^{-1} (~423 cm^{-1}). As layer number increases the separation between these two modes does also: specifically the A_{1g} mode stiffens as the $E^1{}_{2g}$ mode softens. This blue shift of the A_{1g} peak is as expected; the van der Waals interlayer

interaction of S atoms in neighbouring planes increasing the effective restoring forces on the atoms and suppressing the vibrations. The red shift of the E^1_{2g} peak is less intuitive. It may be down to the stronger dielectric screening of long range Coulomb interactions in thicker samples,[39, 43] or else stacking induced strucutral changes can be at play.[41]

2.3.2.2 *$MoSe_2$*

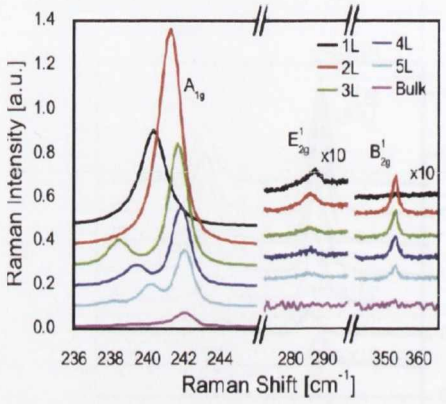

Figure 2.11: $MoSe_2$ Raman spectra excited with 514 nm laser.[5]

The A_{1g} mode appears at a lower wave number (~242 cm^{-1}) than the E^1_{2g} mode in $MoSe_2$. This discrepancy in $MoSe_2$ as opposed to the MS_2 variety, reflects the difference in chalcogen atomic mass.[43] Again the position of this mode is a function of layer number. Davydov splitting is seen in the A_{1g} mode depending on the number of layers in the sample, caused by adjacent TMD layers vibrating with a phase shift due to the Se atoms moving towards or away from the Mo atom. The weak peak at ~286 cm^{-1} corresponds to the in-plane E^1_{2g} mode for bulk $MoSe_2$. The appearance of a small hump around 353 cm^{-1} is attributed to the B^1_{2g} mode. This mode is not Raman active in bulk but becomes so in the few layer limit due to the breakdown of translational symmetry along the c-axis direction.[5]

2.3.2.3 *$MoTe_2$*

Expected Raman active modes for $MoTe_2$ are the small out of plane A_{1g} peak at ~174 cm^{-1} and the prominent in-plane E^1_{2g} peak at ~235 cm^{-1}. The higher weight of the

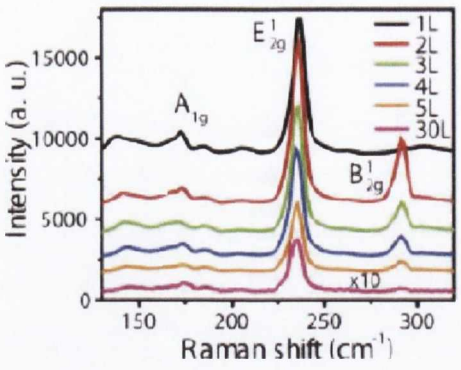

Figure 2.12: Raman spectra for $MoTe_2$ taken with 532nm laser.[44]

Te atoms ensures the frequency of this mode in $MoTe_2$ is smaller than for MoS_2 and $MoSe_2$. Few layer samples also exhibit the small Raman active B^1_{2g} peak at ~291 cm^{-1}, similar in origin as for $MoSe_2$.[44]

2.3.2.4 *WSe_2*

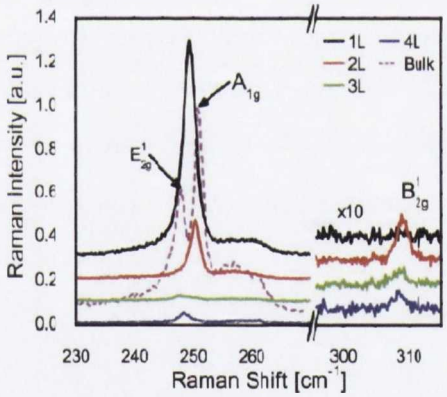

Figure 2.13: Raman spectra for WSe_2 taken with 514nm laser.[5]

The WSe_2 Raman spectrum has caused confusion in the literature. This is mainly due to its E^1_{2g} and A_{1g} phonon modes being nearly degenerate. In bulk WSe_2 these peak positions should occur around 248 cm^{-1} and 250.8 cm^{-1} respectively.[5] These peaks are too close to be resolved using standard 1200 and 1800 line/mm gratings and require a grating with resolution above 2400 lines/mm to be sufficiently resolved.[43] Both the modes show slight shifts with layer number (E^1_{2g} softens as A_{1g} stiffens with

layer number increase) as for MoS_2 & WS_2 but the effect is much less marked in WSe_2 due to the heavier constituent atoms.[45]

For mono and few layer samples, only one single maximum is found as the modes essentially become degenerate with the spectral peaks then overlapping. To further complicate things, the 2LA(M) mode is situated at ~260 cm^{-1}. This mode is a second order Raman mode due to LA phonons at the M point in the Brillouin zone.[41, 43] Its appearance is somewhat broad for a typical first order phonon process; this peak has been erroneously assigned as the A_{1g} mode in the past.[46] An additional small Raman active B^1_{2g} peak exists at ~310 cm^{-1} in few layer samples, like for $MoSe_2$ and $MoTe_2$.

2.4 EXFOLIATION AND MATERIAL SYNTHESIS

The synthesis of layered materials is an underlying subject that continues to evolve and enable research and development of useful devices and applications. However the ability to control compositions, shapes, morphology and quantities of these nanomaterials is still inadequate for commercialisation. A key challenge is to merge these building blocks into functional systems. No one way has all the answers and it is likely that a successful approach will draw on salient features of a combination of different methods, requiring novel integration to transform them into final products. For example, in certain applications such as large area displays where quality and resolution requirements are relaxed, minimizing cost is the most important consideration and a production method compatible with solution processing can be useful. However for circuitry or logic applications required for processing information, material quality is paramount and only precise growth techniques such as epitaxy or CVD are viable options.

2.4.1 *Mechanical Exfoliation*

Mechanical exfoliation is a simple method based on peeling apart successive layers of layered material with scotch tape, until thinned down to just a single layer. The adhesive force of the tape is strong enough to overcome the weak van der Waals forces. This layer can then be transferred onto a substrate such as SiO_2. Such a process is ideal for producing high quality samples to probe fundamental physics and intrinsic material properties and was pioneered by Geim and Novoselov, later Nobel Laureates, who first used this method to isolate graphene monolayers.[9] They applied the same method to isolate monolayer MoS_2 and $NbSe_2$ in 2005.[11] These layers are then successively pulled apart, eventually thinning down to mono and few layer samples which can be deposited onto a substrate. The main drawback associated with mechanical exfoliation is that it is a slow and tedious method whose low yield does not lend itself to scale up for industrial purposes.

2.4.2 *Chemical Exfoliation*

Reactive alkali metals like lithium can be adsorbed under inert conditions between the TMD's van der Waals gap in a process known as intercalation.[47–49] Alkali metals have a low electron affinity[50] and so can readily donate an electron to the host lattice. On reaction of the intercalated TMD with water, hydrogen gas is produced, expanding the interlayer distance. This decreases the van der Waals bond strength, facilitating delamination when sonicated. The Li atoms pass into the solution as hydrated Li^+ ions. Whilst this method results in appreciable monolayer yield the main drawbacks are non-atmospheric processing requiring a glovebox and undesirable changes in the TMD's electronic properties whereby a transition from the trigonal prismatic (2H) semiconducting phase to the octahedral (1T) metallic phase occurs, requiring a thermal anneal at around 300 °C to restore the semiconducting phase.

2.4.3 *Liquid Phase Exfoliation*

This is the method used throughout this work to process TMDs. A more rigorous treatment of the exfoliation mechanism is given in chapter 4. Mild sonication of the material in powdered crystallite form in an organic solvent results in mono and few layer nanosheets. It is a quick and easy method, capable of producing large quantities and was first used to produce graphene in organic solvents in 2008.[4] Echoing the well known chemistry rule of like dissolves like, the chosen solvent must have similar surface energy to the layered material, resulting in a low enthalpy of mixing and therefore energetic cost of exfoliation. This method is compatible with solution processing roll-to-roll print manufacturing techniques which are high throughput and low cost. Also, for applications where toxicity of the solvents presents a problem, the dispersions can be produced in aqueous surfactant solutions.[51] The main drawbacks associated with this method are low monolayer yield and (for optoelectronic applications) the numerous interflake junctions charge carriers must traverse which severely degrades the mobility. However recent work has shown a significant degree of control over the polydispersity of the dispersions can be obtained by size selection methods involving different centrifugation rates and/or establishment of a density gradient.[52] This should allow production of monolayer rich dispersions. In addition, hybrid dispersions and films containing a percentage of nanoconductive filler particles may be easily produced to tune the conductivity over several orders of magnitude as in chapter 5, depending on the application.[53–55]

2.4.4 *Chemical Vapour Deposition*

All the above methods are top-down approaches. However high-end applications require electronic grade material that can be synthesized reproducibly and uniformly over relatively large areas. Chemical vapour deposition (CVD) is a bottom-up growth process compatible with existing semiconductor manufacturing techniques which will facilitate future integration of these materials. It shows much promise and has recently

been used in the case of graphene to synthesize wafer scale single crystal monolayer graphene films on germanium wafers.[56] For the case of MoS_2, samples are generally grown by sulfurization of evaporated metal films[57] or the corresponding TMO powders[58] in a furnace at high temperatures (> 500 °C). This results in polycrystalline mono to few layer films with domains up to ~100 μm.[59] The grain boundaries in $MoS_2$are more complicated than homo-elemental graphene and tend to be strongly faceted. Such boundaries house line defects such as simple tilt-boundaries as well as more complicated mirror twins in which the positions of Mo and S atoms are swapped at the boundary. These affect the photoluminescence (PL) and conductivity in non-trivial ways (PL can increase, quench and/or shift peaks) depending on the defect identity and concentration. Importantly for electronic applications the explicit effects of the boundaries on the conduction are only little more than the sample to sample variation in pristine samples.[60]

2.5 TMDS FOR DIGITAL ELECTRONICS

Silicon is ubiquitous in semiconductor technology due to the success of the CMOS logic process based on its natural abundance, suitable native oxide and reasonable mobility for both electrons and holes. Moore's Law dictates that microprocessor performance doubles every eighteen months by scaling down transistor size, increasing speed and making it possible to integrate more transistors on a single chip. This means transistor supply and threshold voltages must also be scaled down along with channel length to limit power consumption.[61] This is due to short channel effects such as drain-induced barrier lowering, whereby the potential barrier in the channel is a function of both gate-source and drain-source voltages, effectively reducing the threshold voltage. Also, the gate oxide must be thinned commensurately with the channel length, resulting in increased leakage currents tunnelling via the gate oxide. These effects result in high leakage current and increased power dissipation. This poses a significant problem, especially for low power applications.

As a general rule of thumb the thickness of the semiconducting channel in an FET must kept to roughly $\leq 1/3$ the channel length to maintain effective gate control.[62] This poses problems for traditional tetrahedrally bound 3D semiconductors such as Si as the channel length continues to be reduced. FETs based on group VI TMDs have ultrathin bodies which confine the charge carriers resulting in enhanced gate coupling and thus excellent electrostatic control. In addition, their sizeable bandgaps and low dielectric constants endow them with a resistance to short channel effects. This is quantified by short characteristic lengths, the length-scale at which short channel effects begin to transpire:

$$\lambda = \sqrt{\left(\frac{\varepsilon_s}{\varepsilon_{ox}} t_s t_{ox}\right)} \tag{2.2}$$

Even with a 300 nm SiO_2 thick gate oxide (poorer gate control) no short channel effects are encountered in MoS_2 even as the channel length approaches 100 nm.[63] Contrast this with Ge and InGaAs FETs which begin to show short channel effects at 150 nm. A thinner gate oxide and/or higher k dielectric would allow scaling below 10 nm (the characteristic length for conventional semiconductors) with MoS_2. Moreover, the smooth inert surfaces of TMDs eschew dangling bonds providing a degree of immunity against interface states and surface roughness scattering.

2.5.0.1 *p- and n-type Conduction*

Manifestation of both n and p-type TMDs is important as a number of working devices and circuits require both to function optimally. For example, CMOS logic devices consume less power than their unipolar counterparts, pn hetero-junctions are fundamental building blocks of a wide range of optoelectronic devices such as junction-diodes[64, 65], solar cells,[66, 67] and LEDs.[66–68] Also, thermoelectric modules are more efficient when configured with one p-type leg electrically in series with one n-type leg (see section 2.6.2).

Mono and few layer MoS_2 transistors have been well characterised electrically by a number of groups and a clearer picture is now beginning to emerge as to why it normally exhibits n-type operation. WSe_2 offers an avenue for p-type operation when

contacted with high work function metals.[69] Both these TMDs shall now be reviewed as model n & p-type TMD systems for nanoelectronic device applications.

2.5.1 MoS_2

2.5.1.1 *Mobility*

Reference	Material	μ_n (cm^2/Vs)	Dielectric	Contact	Gate
Das[7]	Few layer MoS_2	700	Al_2O_3	Sc	Top
Gu[70]	Few layer MoS_2	370	SiO_2	Ni	Back
Pradhan[71]	Few layer MoS_2	300	SiO_2	Au	Back
Radisavljevic[72]	Single layer MoS_2	200	HfO_2	Au	Top
Kim[73]	Few layer MoS_2	100	Al_2O_3	Au	Back
Ayari[74]	Few layer MoS_2	50	SiO_2	Au	Back
Liu [63]	Few layer MoS_2	30	SiO_2	Ni	Back
Ghatak[75]	Few layer MoS_2	10	SiO_2	Au	Back

Table 2.3: Table comparing transistor operation for mono and few layer MoS_2.

Graphene has a superlative charge carrier mobility in excess of 100,000 cm^2/Vs.[76] Unfortunately the absence of an inherent bandgap in graphene severely limits its use as a field effect transistor (FET). Electrically MoS_2 has sparked interest due to the presence of a sizeable bandgap. Nominally an n-type semiconductor, it has a bulk in-plane mobility of 260 cm^2/V s.[77] Field effect mobilities of ~0.5-3 cm^2/V s are typical in the mono and few layer regime.[11, 72, 74] This may be boosted in high-k dielectric environments which screen the effect of trapped charge at the interface.[78] Mobilities up to 700 cm^2/V s for few layer[7] and 200 cm^2/V s for monolayer[72] MoS_2 have been realised. Whilst the large bandgap (1.3 eV bulk, 1.9 eV monolayer) makes for impressive on: off ratios of at least 10^8, it also limits the ability to screen random potential fluctuations due to trapped charge at substrate or dielectric interfaces.

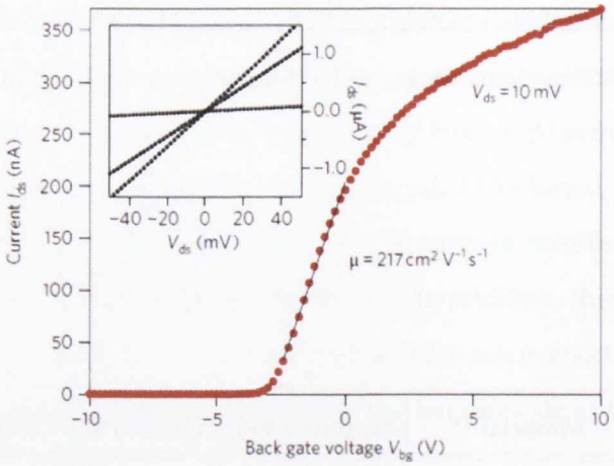

Figure 2.14: Typical n-type transfer curve for an MoS_2 monolayer FET with gold contacts on an SiO_2 substrate (270 nm oxide thickness) at room temperature. Inset: Linear I_{ds}-V_{ds} curves acquired for back gate voltages of 0, 1 and 5 V.[72] Initially the linearity of such curves lead to the belief that Au forms ohmic contacts for this system. However, the linearity is now known to occur due to Fermi level pinning close to the MoS_2 CB; the thermionic tunnelling component of current being appreciable at room temperature.

Hence high-k dielectrics such as HfO_2[72] and Al_2O_3[73] (ε_r= 25 and 9 respectively)[79] may be used to suppress the resultant Coulomb scattering, enhancing the measured mobility.[72] The absence of dangling bonds and trapped charge at the smooth van der Waals interface allow a near ideal sub-threshold swing (see section 2.5.2.1) of 74 mV/dec resulting in abrupt switching.[72] These encouraging features mean MoS_2 has a great deal of potential for use as an FET in low power electronic applications.

When the work-function metal is not suitably aligned with the appropriate band for conduction, TMD based FETs operate as Schottky Barrier (SB) transistors. SB transistors comprise metal-semiconductor (MS) junctions rather than the usual highly doped pn junctions. The rationale behind fabricating SB transistors in the case of TMDs is the current absence of viable stable doping strategies and inherent difficulty in implanting an ultrathin body (see section 2.5.2.2). As MS junctions are majority carrier only devices SB transistors operate in enhancement mode with the on state due to accumulation (rather than inversion) of majority (minority) carriers.[80, 81] As the channel length is

scaled down the MS contact resistance represents a more appreciable contribution to the overall device resistance, which may mitigate any intended scaling benefits. This necessitates the contact work-function be well matched to the semiconductor CB. If not, extracted mobility values are not intrinsic to the material due to the large parasitic voltage drops incurred at the MS interface.

2.5.1.2 *TMD-Metal Contacts*

Low work-function metals such as scandium ($\phi_{Sc} = 3.5$ eV)[7] and titanium ($\phi_{Ti} = 4.3$ eV)[82] are a sound choice for making electron injecting contacts to MoS_2. Indeed, in the case of Sc, the barrier height has been measured to be only 30 meV, comparable to the thermal broadening of the Fermi function at room temperature.[7] However due to Fermi level pinning (see next section 2.5.1.3) close to the CB of MoS_2 and its high electron affinity (>4 eV),[23, 24] even higher work-function metals such as gold ($\phi_{Au} = 5.1$ eV) result in n-type contacts which appear Ohmic, at least at room temperature.[6, 72, 83–88]

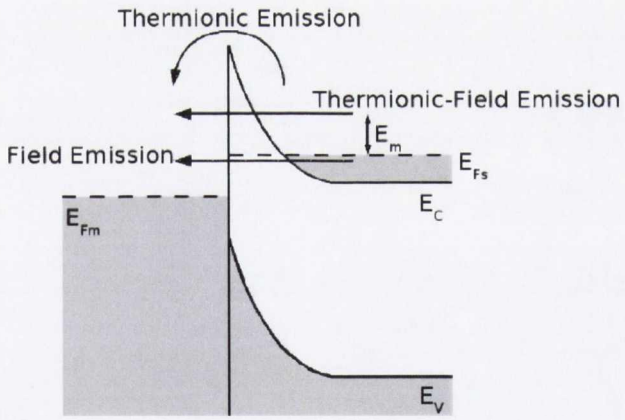

Figure 2.15: Illustrations for carrier transport mechanisms for a Schottky Barrier on an n-type semiconductor under forward bias.[81][89]

Shown in figure 2.15 are the three mechanisms for current flow at a MS SB junction: (1) field emission or tunnelling through the lower portion of the barrier, (2) thermionic emission over the barrier and (3) thermionic-field emission through the upper narrower portion of the barrier. (1) dominates at low temperatures, as the temperature is increased contributions from (2) and then (3) become more dominant.[90] Stan-

dard thermal emission theory[91] was first developed for traditional semiconductors with high doping densities at the contacts and correspondingly narrow barriers. This increases the tunnelling probability rendering field emission the dominant current component. However as mentioned, TMD FETs are of the SB variety; the thermally assisted tunnelling of high energy carriers through the upper portion of the barrier is significant. This current component is not accounted for in standard thermal emission theory:[7]

$$I_{ds} = A^{**}T^2 \exp\left(\frac{-q\phi_B}{kT}\right)\left[1 - \exp\left(\frac{qV_{ds}}{kT}\right)\right] \tag{2.3}$$

In this equation I_{ds} is the current through the device, A^{**} is Richardson's constant and ϕ_B the barrier height. All other symbols have their usual meanings. The thermionic-field emission current component is strongly temperature dependent and can be appreciable at room temperature. This obscures the presence of the SB resulting in linear I-V's leading to perceived ohmic contacts at room temperature.[7] A transfer characteristic showing the regions of gate bias where each current component dominates is shown in figure 2.16.

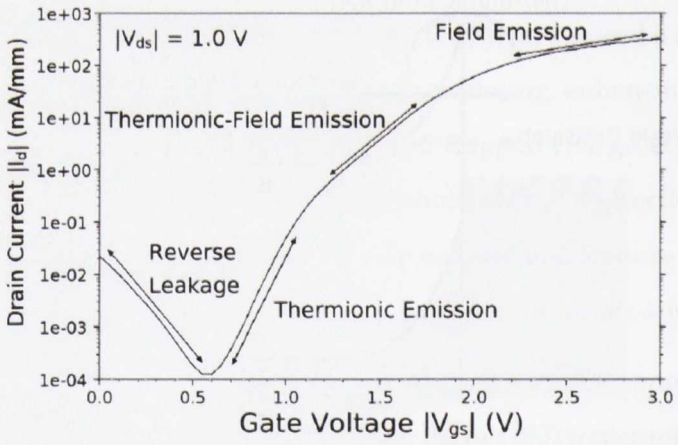

Figure 2.16: Typical transfer characteristic of an n-type Schottky Barrier transistor. Regions of gate bias where particular carrier transport mechanisms dominate are labelled.[81]

2.5.1.3 *Fermi-Level Pinning*

Fermi level pinning is generally an undesirable effect whereby the Fermi level locks onto the charge neutrality level (level at which interface is neutral), effectively fixing

the achievable built in potential.[92] Any change in electron or hole concentration impacts the Fermi level position and so it is affected by localised states due to defects which are present in the bandgap. When such states are present at high enough density at a given energy their localised levels broaden out into a defect band due to their proximity and wave function overlap. Once the density of states of this defect band becomes large enough, the Fermi level will move towards the charge neutrality level, effectively pinning it there independent of contact metal workfunction.

This effect has been studied in MoS_2 via a detailed temperature dependent study on few layer transistors (bulk regime).[7] Different metals have been used as contacts, from low work-function scandium through to high work function platinum ($\phi_{Pt} = 5.9$ eV) with titanium ($\phi_{Ti} = 4.3$ eV) and nickel ($\phi_{Ni} = 5.0$ eV) in between. All transistors exhibit n-type conduction with an increasing barrier height (30 meV - 230 meV) as the metal of the work-function increases. So whilst the barrier height is not independent of contact metal choice the metal-MoS_2 interface is strongly pinned (the pinning parameter, $\frac{d\phi_B}{d\phi_M} = 0.1$ as opposed to 0.27 for Si). Interestingly the most common MoS_2 contact, gold, was not investigated in this study. Whilst it has not yet been fully discerned, the source of such Fermi level pinning may be sulfur vacancies. These defects have a low formation energy in MoS_2 meaning they are common and contribute a localised level in the bandgap close to the CB.[93–97] A prominent defect level here would pin the Fermi level and manifest n-type conduction, largely independent of the metal work-function. In consequence, this makes p-type operation very hard to realise in MoS_2 SB transistors.

2.5.1.4 *Effect of Interlayer Coupling*

The theoretical maximum room temperature mobility for monolayer MoS_2 shows a $\mu \propto T^{-1.69}$ temperature dependence limited by optical phonon scattering and has been calculated to be 410 cm^2/V s.[78] When the channel is sandwiched between a substrate and dielectric the homo-polar out of plane phonon mode is quenched for a top gate geometry. This only weakly affects the in-plane mobility, lending weight to the hypothesis that the mobility boost in high-k environments is due to improved screening of trapped charges.

However, the situation is more complicated when the FET is fabricated with a global back gate geometry using the SiO_2 substrate as a dielectric, often resulting in mobilities below the theoretical value. A resistor network model for this has been proposed based on the interlayer coupling and Thomas-Fermi (TF) charge screening.[98, 99] The interplay between the back gate voltage and the interlayer access resistances changes the centroid of the current distribution, affecting the contact resistance in a non-monotonic fashion.

In the development of this model it is assumed the top contacts inject only into the topmost layer of the few layer devices. In layered materials layer-layer transport is more resistive than in-plane transport as charge carriers must tunnel from layer to layer. Access to lower layers involves an internal resistance, R_{int} (where $R_{int} = R_C - R_{SB}$, the difference between the contact resistance and the resistance due to the barrier at the metal contact). When this is large current flow is restricted to flow through the top layers. However in back-gate configuration the largest number of charges are induced in the lowest layers due to the TF-screening, whereby the carrier concentration decays exponentially away from the gate according to

$$\frac{Q_i}{Q_{i-1}} = \exp\left(\frac{-d_{ML}}{\lambda}\right) = C \tag{2.4}$$

and

$$\sum_{i=1}^{N} Q_i = Q_{Gate} \tag{2.5}$$

where Q_i is the charge in the i^{th} layer, λ is the screening length and d_{ML} is the monolayer thickness. From fitting R_{int} as a function of $(V_G - V_{th})$ the screening length for MoS_2 has been calculated as ~7 nm (as opposed to ~0.5 nm for graphene). The appreciable value obtained for MoS_2 reflects its relatively low carrier density (λ would be infinite for the case no screening). The layers close to the substrate have the most pronounced charged impurity scattering due to the trapped charge that resides there. The TF screening decreases the scattering far away from the gate oxide interface. Despite the bottom layers having more charge induced in them, they have a lower mobility than the top layers and are more resistive. As the gate voltage is increased the intrinsic resistance of each layer decreases and the current is ultimately limited by

R_{int}. All this manifests as an optimum number of layers (6-12 nm) existing in terms of performance (figure 2.17), and explains the reduced values recorded for monolayer MoS_2 fabricated with a back gate geometry with no high-k encapsulation.

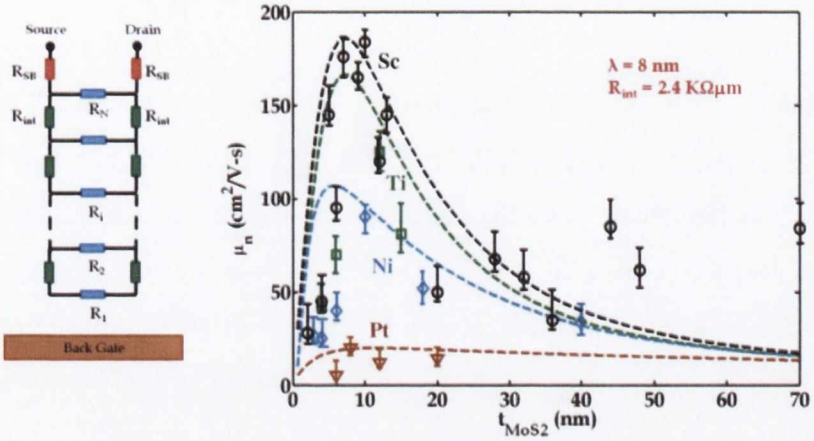

Figure 2.17: Resistor network model incorporating Thomas Fermi charge screening (left). Extracted field effect mobilityas a function of MoS_2 layer thicknessfor Sc, Ti, Ni and Pt contactsDotted lines are fit to the data using the model with λ=8 nm and R_{int}=2.4 kΩ μm.[99]

Many layer devices also suffer due to R_{int} and λ resulting in low charge carrier densities in the top layers. This is in contrast to an identical system composed of graphene with much lower values for R_{int} and λ due to its superior conductivity and screening. The centroid in such a system resides very close to the gate oxide. The layers close to the source-drain contacts are largely depleted of charge carriers and access to the bottom layers is not compromised, making the topmost layers much more resistive.[100]

2.5.2 WSe_2

Bulk WSe_2 has a field effect hole mobility of ~500 cm^2/Vs.[101] This TMD is generally p-type in polarity due to its high valence band edge (~3.5 eV).[23, 24] However, n-type operation is possible using low work-function metals,[102] chemical[50] or electrostatic doping.[67, 68, 103] When exfoliated, electron and hole mobilities are similar in

magnitude,[69] generally ranging from 100-250 cm^2/Vs.[50, 102, 104] This is important not only from the point of efficient LEDs[68] and photodiodes/photovoltaics,[67, 105] but also as p and n-type complementary digital circuits offer significant performance advantages over the uni-polar variety.[62] However due to having the highest lying CB edge of any group VI TMDs, developing low resistance n-type contacts to this material is challenging. Low work-function aluminium results in non-linear I-V curves and an electron mobility less than 0.1 cm^2/Vs indicating the presence of a significant barrier.[102] DFT simulations indicate that despite its low work-function, Al has a low density of states near the Fermi level of WSe_2. The low electron density at the interface, attributed to Al's absence of d-orbitals, results in small overlap with those in WSe_2. As shown in figure 2.18, whilst titanium results in a midgap ambipolar contact to

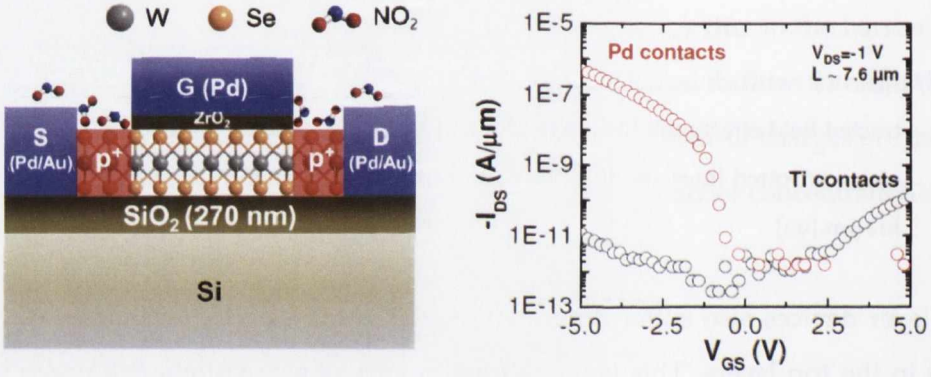

Figure 2.18: WSe_2 p-type transistor with surface charge degenerate doping at contact regions (left). Transfer characteristics using Pd contacts (p-type) and Ti (ambipolar).[104]

WSe_2 with large contact resistance the VB can be contacted resulting in hole transport with high work-function palladium.[104] Indeed ambipolar conduction is commonly observed in WSe_2 samples,[67, 69] suggesting the Fermi level pinning to be much weaker in WSe_2 than MoS_2. Whilst a reason for this is not yet fully clear it has been noted that WSe_2 is more resistive to oxidation than MoS_2 in humid environments.[102]

2.5.2.1 *Sub-threshold Swing*

One major advantage of these TMDs for transistor operation is that the low density of interface traps associated with their smooth basal plane surface renders the sub-threshold swing (SS) very close to that of an ideal MOSFET. The SS is a measure of the

inverse of the slope of the linear region in a semi-log plot of log (I_{ds}) versus V_{gs} and indicates how effectively a transistor may be switched on or off. For an ideal MOSFET the SS is limited to 60 mV/dec at room temperature by thermionic emission from the source.[104] Low values therefore are desirable and it can be calculated by[61, 106]

$$SS = \left(\frac{d\left(\log_{10} I_{ds}\right)}{dV_{gs}} \right)^{-1} = 2.3\frac{kT}{q}\eta \tag{2.6}$$

where η is related to the body-factor as

$$\eta = 1 + \frac{C_{it}}{C_{ox}} \tag{2.7}$$

Here the interface capacitance is related to the density of interface states by $C_{it} = D_{it}q^2$ and the oxide capacitance $C_{ox} = \frac{\varepsilon_{ox}\varepsilon_0}{t_{ox}}$ is a function of the gate-oxide thickness and permittivity. WSe_2 monolayer p-type transistors with degenerately doped WSe_2 at the Pd contacts and a 17.5 nm thick ZrO_2 gate dielectric has been demonstrated with a SS very close to this ideal limit of 60 mV/dec.[104] Equation 2.7 suggests $C_{it} \ll C_{ox}$ due to the low density of interface states at the oxide, for reasons already mentioned.

2.5.2.2 *Doping TMDs*

Ability to controllably dope a sample is important for being able to realise truly ohmic contacts as well as modulating a semiconductor's polarity. However a viable strategy to controllably dope TMDs does not currently exist as it does for Si technology. This is due to the inherent difficulty from an engineering perspective in implanting into an atomically thin body. In addition, TMD doping presents a challenge statistically, as there are so few atoms in a monolayer device, subsequently any potential variations due to the presence of dopant atoms will be much stronger. Also, as exfoliated low-dimensional TMDs are a new research topic, not much is yet known about other solid solubilities within them to assist in sensible choices for doping agents. A number of routes have been explored to this end, though much development is needed.

Doping can be performed electrostatically in TMDs[67] or reversibly at the surface with reactive gas molecules.[50, 104] The little that is known about TMD doping generally comes from computational studies on MoS_2.[107, 108] Halogens have an extra electron so can substitutionally n-dope at the sulfur site.[109] Similarly, rhenium

(Re) has an extra unpaired electron, when substituted for Mo this is known to contribute a level just below the MoS_2 CB. P-doping can be achieved by substituting a group V (N, P or As) element at the sulfur site or substituting Nb for Mo. Alkali metals can be intercalated into the van der Waals gap of layered materials, with the effect of n-doping due to donating their extra electron. In addition, defects also impact the degree of TMD doping.[93–96] Defect production under electron irradiation has been compared computationally across MoS_2, $MoSe_2$ and $MoTe_2$.[97] The formation energy for chalcogen vacancies is found to decrease as the chalcogen weight increases. This would suggest such defects to be more common in the heavier anion analogues of MoS_2 and WS_2, though experimental work is needed to clarify this.

2.5.3 *TMD Thin Films*

So far this section has outlined the state of the art in single and few-layer mechanically cleaved single crystal TMD samples to illustrate the intrinsic electronic properties of group VI semiconducting TMDs in 2D form. However, as indicated in section 2.4, applications of these layered materials will likely require the materials be in thin film form in large quantities. Whether exfoliated by a solution processing route or grown by CVD, such thin films will contain numerous inter-sheet junctions or grain boundaries which degrade the mobility compared to single crystal exfoliated samples.

Crystalline media possess translational symmetry whereas amorphous solids, like liquids, have only very short range order on the scale of nearest neighbours. Polycrystalline films may be viewed as somewhere in between; being made up of single-crystalline regions with different grain sizes and orientations. Concepts from both crystalline and amorphous solids then may be useful for understanding conduction in polycrystalline media. Disorder has a first order effect on the mobility due to the increased scattering and reduced mean free path associated with it meaning $\mu_{amorph} < \mu_{poly} < \mu_{xtal}$.[110]

The term polycrystalline technically refers to the presence of crystalline domains between well stitched grain boundaries, for example as grown by CVD.[59, 60, 111] Films

produced by liquid phase exfoliation are different in that they consist of disordered porous nanosheet networks which can be easily deposited over large areas.[53, 55, 112] Due to significantly reduced production expenses (at the expense of quality or efficiency) they may become practical for applications where cost is the main bottleneck, e.g. solar cells. Whilst not amorphous but still not technically polycrystalline, liquid phase formed networks are certainly not crystalline. As such, it may be pragmatic to consider affects native to polycrystalline and amorphous solids to see how the role of disorder impacts their bandstructures and the nature of their conduction.

2.5.3.1 *Amorphous Solids*

Amorphous solids tend to suffer from very low mobilities ($\ll 1$ cm^2/V s) due to the large degree of disorder and scattering present.[113] Implicit in the calculation of a material's bandstructure is that lattice periodicity is a pre-requisite for formation of a bandgap. However, only the primitive cell and thus the nearest neighbours need be considered.[114] No solids with covalent bonding exist in a totally disordered fashion due to the directionality of the bonding and amorphous solids are characterised by a degree of short range order due to these covalent forces that exist between nearest neighbours. Their arrangement in amorphous solids is similar to the crystalline case, with only slight distortions in bond lengths and angles. This is affirmed by X-ray absorption spectroscopy of amorphous Si and Ge, showing the same nearest neighbour environments as for the crystalline phases, albeit with much broader peaks.[113, 115]

As the mean-free path in amorphous media is so low (of the order of the interatomic spacing) the wavefunction fluctuates so randomly that k is no longer a good quantum number for describing the energy eigenstates. This renders the concept of a well-defined Fermi surface invalid and rules out plotting the $E - k$ relation.[113] However photoemission studies show that the density of states (DoS) of non-crystalline media is not overly dissimilar to the crystalline case apart from some band-broadening. This means amorphous materials may serve as semiconductors, having energetic bands where conduction is allowed and forbidden.[114]

The striking difference in the band-like structures of disordered solids and the $E - k$ relations of crystalline semiconductors is the existence of exponentially decaying

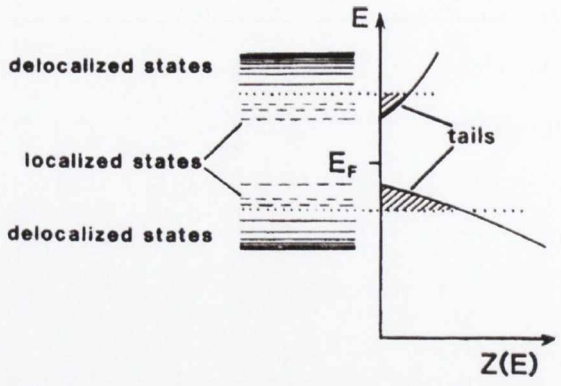

Figure 2.19: Localised and de-localised states and the DoS for amorphous semiconductors. Note the band tails which are caused by the localised states due to disorder.[116]

band-tails beyond the CB and VB edges (figure 2.19). These are a direct result of the disorder and separate extended states (which arise from covalent bonding) where charge carriers are considered mobile, from localised states where charge carriers are immobile if there is not sufficient spatial wavefunction overlap with other similar states.[113] This gives rise to what are termed mobility edges in amorphous media. These mobility edges for electrons and holes result in formation of a mobility gap or pseudo-gap which functions as a bandgap for conduction; defining the energy ranges where conduction is permitted and where it is forbidden. Beyond the mobility edges, a quasi-continuum of extended states permit delocalised-like transport, the large degree of wavefunction overlap allowing ease of transition from one state to another. Between mobility edges some conduction may proceed by phonon assisted hopping between localised states depending on the defect density and Fermi level position.

2.5.3.2 *Polycrystalline Solids*

In addition to the localised states associated with structural disorder, semiconductor surfaces and interfaces (i.e. nanosheet edge sites or CVD grain boundaries) are infamous for their high density of defect states, stemming from the abrupt termination of the lattice. This can result in exposed dangling bonds with different nearest neighbour configurations and hence energies from the bulk phase. This departure from crystalline periodicity results in electrically active localised states, often within the forbidden

bandgap. These interface states can trap mobile carriers, effectively removing them from the conduction process until freed. This reduces the charge carrier density and can also be detrimental to the mobility via increased scattering. Moreover, the discontinuity at the grain boundaries increases the likelihood of charge carrier scattering, further decreasing the mobility.

The resulting region of space charge in the vicinity of the grain boundaries gives rise to a potential (ϕ_B in figure 2.20) which results in band-bending and a barrier to transport. This barrier height is a function of both the doping level and dielectric

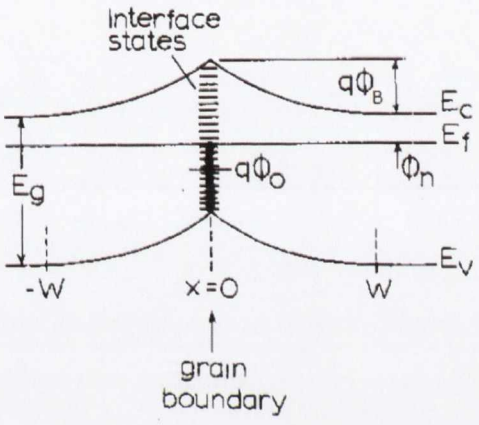

Figure 2.20: Energy band diagram for an n-type semiconductor in the region of a grain boundary (x=0) showing an energy distribution of localised interface states.[117]

constant of the bulk material.[118] These barriers dominate the transport which now has two channels for conduction: the conductivity within the boundaries which is bulk-like and an additional resistance from the barriers at the boundaries

$$\rho = \rho_{grain} + \rho_{GB} \tag{2.8}$$

where $\rho_{GB} >> \rho_{grain}$.[118, 119] To take part in conduction the charge carriers must tunnel through or be emitted over these grain boundary barriers giving I-V's of the form[118]

$$J \propto \exp\left(\frac{-q\phi_B}{kT}\right)\left[\exp\left(\frac{-qV}{kT}\right) - 1\right] \tag{2.9}$$

The presence of grain boundaries complicates the conduction process as they have significant structural and electronic inhomogeneity.[120] This makes modelling of

transport problematic in polycrystalline films. Different size, orientation, shape, quality and surface terminations associated with individual grains also makes for poorer reproducibility in device performance, decreasing yield.[8]

2.6 TMDS FOR ENERGY CONVERSION

Typical TMD mobilities are too low (~10^2 cm^2/V s) for high performance digital electronics (~10^3 cm^2/V s) and will ultimately prove much more suited to low power applications. However TMDs demonstrate enormous potential for applications in energy conversion and storage. For example, MoS_2 & WS_2have been demonstrated as hydrogen evolution catalysts,[121, 122] electrodes in lithium ion batteries[123, 124] and dye sensitized solar cells.[125] Also, Bi_2Te_3 shows potential as an exceptional thermoelectric material at room temperature.[126, 127] The potential of TMDs in two of these areas, photovoltaics and thermoelectrics shall now be evaluated in more detail. Both these technologies currently suffer from being prohibitively expensive. As a solution processing technique, liquid phase exfoliation may find low-cost niches within these spaces.

2.6.1 *Photovoltaics*

The earth's original and most abundant power source is the sun. This giant fusion reactor donates a massive 120,000 TW of power to the earth's surface at any instant. However, with less than 1% of the world's electricity generation due to photovoltaics (PV), [128] there is clearly a massive gulf between solar power's capacity and our utilisation. Just 0.16% coverage of the earth's land with 10% efficient solar cells would generate 20 TW [129]. Once it can be harnessed the sun's energy is a clean and abundant source, free from the price volatility of fossil fuels. It's also useful for generating power in remote areas or areas with poor electrical infrastructure.

Despite these advantages it cannot currently compete with fossil fuels for convenience. Important criteria for a power source are reliability, performance and cost.

These elements must be improved if PVs are to displace fossil fuels as the world leader in energy supply. Power derived non-renewably from gas, coal and oil totals about 85% as of 2013.[130] However, as PV technology evolves, costs continue to decrease at an increasing rate. These aggressive cost reductions are driven by strong market growth, production scale up and process improvement.[131]

2.6.1.1 *Basic Operation*

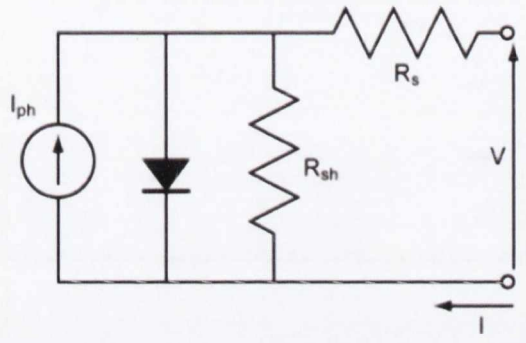

Figure 2.21: Solar Cell equivalent circuit, represented as a photodiode with associated parasitic series and shunt (parallel) resistances. A high series resistance ($R_S = R_{bulk} + R_C$) reduces the fill-factor whereas low values for the shunt resistance (often due to defects) provide alternate paths for the light generated current, circumventing the diode and decreasing the deliverable power output from the cell.[132]

The first practical solar cell (6% efficient) was developed by Bell Labs in 1954 from a single crystal silicon (c-Si) pn junction.[133] A solar cell is a device that can: (1) Absorb incoming photons to generate electron-hole pairs, (2) transport charge carriers from the absorption site to the contacts and (3) convert this excited energy into electricity. This amounts to selecting a material with an absorption spectrum well matched to the visible range and producing absorbing layer films with minimal defects and grain boundaries. Electron-hole pairs are spatially separated from their mutual Coulomb potential by the electric field from either a pn junction (usually) or an MS junction. The active element in the cell then is modelled as a diode as in figure 2.21. The junction's potential and depletion width serves to sweep out the generated charge carriers for collection by the external circuit.[132] This results in a short circuit current, J_{SC} which

by convention is negative for a device under illumination (i.e. opposite the direction of the forward bias current in the diode). At open circuit conditions these generated charge carriers pile up resulting in an open circuit voltage, V_{OC}. The device is not operated at either of these points as at J_{SC}, $V = 0$ and at V_{OC}, $J = 0$ resulting in no power. The max power (MP) is defined by the fill-factor (FF - a measure of the 'squareness' of the IV-curve) and the solar cell is operated at the max power point by matching the load to the internal resistance, biased by light. These parameters are shown in figure 2.22.[134]

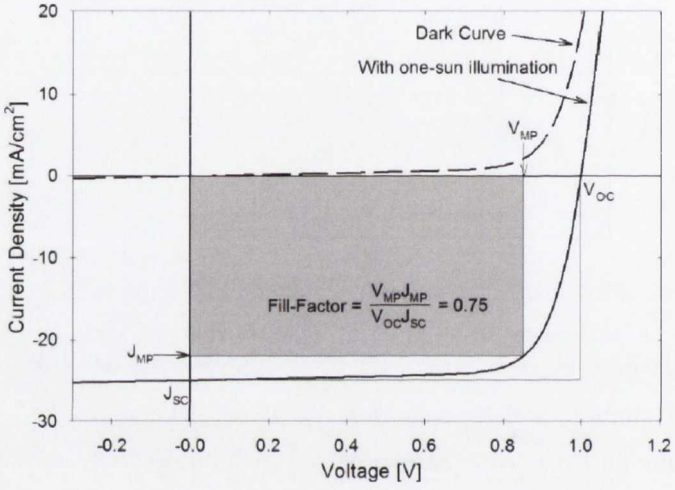

Figure 2.22: Typical I-V curve for a solar cell in dark (dashed line) and under one-sun illumination (solid). The parameters J_{SC} and V_{OC} are shown along with the resulting fill-factor.[134]

Generally the I-V curve of a solar cell is the superposition of the diode in the dark and the light generated current. The light shifts the I-V down into the fourth quadrant and power can be extracted from the diode,[135]

$$J = J_0 \left[\exp\left(\frac{qV}{nkT}\right) - 1 \right] - J_L \tag{2.10}$$

where J_L is the light generated current. If the cell series resistance is not too high (<10 Ω cm^2) J_L and J_{SC} can be used interchangeably. The ideality factor n is equal to 1 for an ideal diode, with higher values indicating non-ideal recombinations present in the cell at the junction and/or contacts. As the V_{OC} occurs at zero current

$$V_{OC} = \frac{nkT}{q} \ln\left(\frac{J_L}{J_0} + 1\right) \tag{2.11}$$

The FF is a measure of the squareness of the I-V curve and in conjunction with J_{SC} and V_{OC}, determines the maximum power that the cell can deliver

$$FF = \frac{V_{MP}J_{MP}}{V_{OC}J_{SC}} \tag{2.12}$$

This FF directly feeds into the device efficiency, the ratio of electrical output to incident energy which is defined as

$$\eta = \frac{P_{out}}{P_{in}} = \frac{V_{OC}J_{SC}FF}{P_{in}} = \frac{P_{max}FF}{P_{in}} \tag{2.13}$$

Generally efficiencies of 10% must be reached for a solar technology to become economically attractive.[136] Best single junction cell efficiencies currently obtainable are around 25%.[137]

2.6.1.2 *Thermodynamic Limits*

Realistically solar cells are unable to operate reversibly and so cannot reach the Carnot efficiency of 93% at 1 Sun illumination (1 kW/m^2).[138] When illuminated, a solar cell increases in temperature and emits more energy as blackbody radiation. This component cannot be used for useful work. Spectral losses account for roughly half of the wasted energy: light below the bandgap cannot be absorbed and light far above the bandgap promotes carriers which quickly thermalise to the band edge, with excess energy lost as heat. Also, despite being minimised by antireflection coatings, some reflection always occurs at the light transmitting electrode. [139]

The Shockley-Quiesser limit is a theoretical thermodynamic limit to the efficiency with which a solar cell can convert light into electricity.[140] It is calculated on the principle of detailed balance (at equilibrium a process should be balanced by its reverse, i.e. electron-hole generation and radiative recombination here) and ideally assumes an infinite mobility and only radiative recombination losses. The optimal bandgap for power generation is between 1.1-1.5 eV, giving an efficiency of ~33%. As the bandgap of the absorbing material increases the V_{OC} attainable increases. However, as only energy above the bandgap can be absorbed, this simultaneously decreases J_{SC}. This trade off ensures there exists an optimal bandgap for the best efficiency.[141]

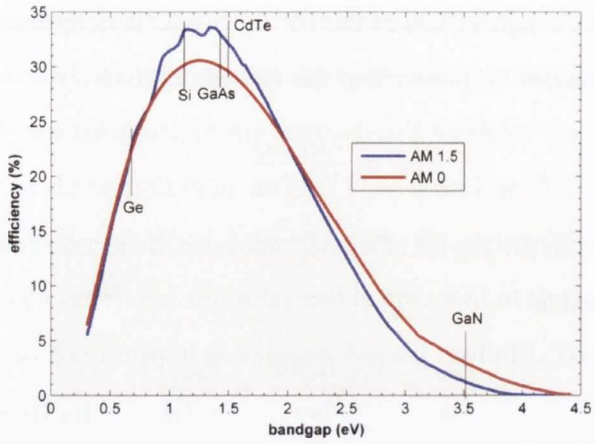

Figure 2.23: Limiting solar cell efficiency as a function of E_g for one-sun illumination assuming only radiative recombination and infinite mobility. This lowers the obtainable efficiencies in real cells as non-radiative recombination and parasitic resistances are present.[132]

2.6.1.3 *TMD Solar Cell Absorbing Layers*

One strategy to reduce the costs of PV is to use materials with a high absorption coefficient. Direct bandgap semiconductors are highly desirable for this purpose as absorption of light does not require absorption or emission of a phonon to occur. The main drawback of c-Si technology is it requires ~100 μm to absorb all the light that shines on it. Thin film technologies on the other hand require only 1 μm (e.g. CdTe $E_g = 1.5$ eV). This is beneficial as in addition to being less susceptible to material price changes it allows deposition on flexible substrates for conformal coating of curved surfaces.

As they are abundant, cheap, non-toxic, flexible[101, 143–145] and photo-stable[30] with extremely high absorption coefficients (>10^5)[142] and the absence of dangling bonds,[146] MoS_2 and WS_2 make ideal candidates for high quality solar cell absorbing layers. As mentioned previously in section 2.2.2, it becomes energetically favourable for group VI TMDs to undergo a transition to direct-gap semiconductors when thinned to a monolayer.[22, 23]

Monolayer group VI TMDs are only 0.65 nm in thickness. Yet they have been calculated to absorb 5-10% of the sun's light (figure 2.24).[142] This is a huge amount;

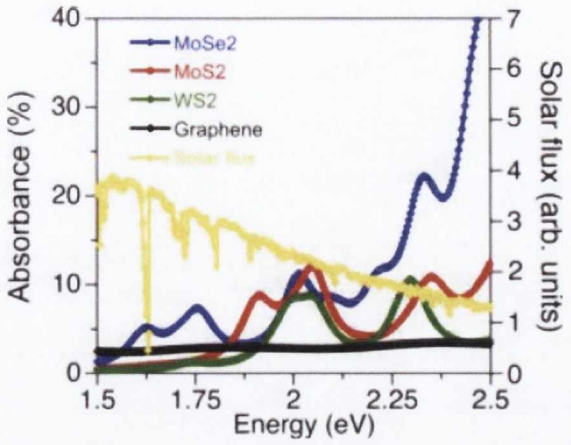

Figure 2.24: Absorbance of three monolayer TMDs and graphene overlaid with AM 1.5 solar spectrum.[142]

graphene is highly absorbing across the whole spectrum and absorbs just 2.3% of the available light. Comparing this to the most ubiquitous PV absorbing material currently employed, 50 nm of indirect gap c-Si would be required to absorb similar quantities of light. As such, solar cells fabricated using TMD monolayers would require significantly less material allowing reductions in cost as well as a degree of freedom from the supply & demand concerns of the raw materials. In addition, the increase in magnitude of the monolayer bandgap shifts it into the visible spectrum, close to the peak for the value for the Shockley-Quiesser limit as in figure 2.23. Both of the above factors mean TMDs in their idealised monolayer form have compelling advantages over current state of the art materials for solar energy conversion.

2.6.1.4 *Vertically Stacked TMD Hetero-junctions*

Whilst Schottky Barrier solar cells based on asymmetric work-function metal electrodes (one ohmic or neutral and one rectifying) are possible to fabricate and have been done so in the lab with TMDs,[87, 147] nearly all commercial solar cells are made with at least one pn junction in the interests of efficiency. The basal planes of TMDs are smooth and inert, allowing formation of atomically thin pn junctions from a monolayer of both p and n-type material. Vanishingly small interface dipoles have even been demonstrated between 3D semiconductors such as CdTe grown on bulk single crystal

TMD substrates.[146] This allows integration of mature 3D semiconductor materials with 2D TMDs; the van der Waals gap and inert basal plane surface circumventing the usual constriction of crystallographic lattice matching so important at heterojunction interfaces.[148, 149] Lattice mismatch at the interface where absorption takes place would form a high density of recombination centres in this region. This ability to stack 2D building blocks opens up the possibility of creating different combinations of TMD[67, 150] and TMD-graphene[142, 151–155] hetero-junctions with favourable bandgaps not inherently found in nature.

2.6.1.5 *Type-II Band Alignment*

WX_2 TMDs have bands higher in energy than MoX_2 species due to the higher energy of the 5d W orbitals over the 4d orbitals. This results in type-II band alignments at their interface, whereby both the CB-edge and VB-edge of one material are lower than those of the other constituent material as in figure 2.25 (top-left). Such alignment is

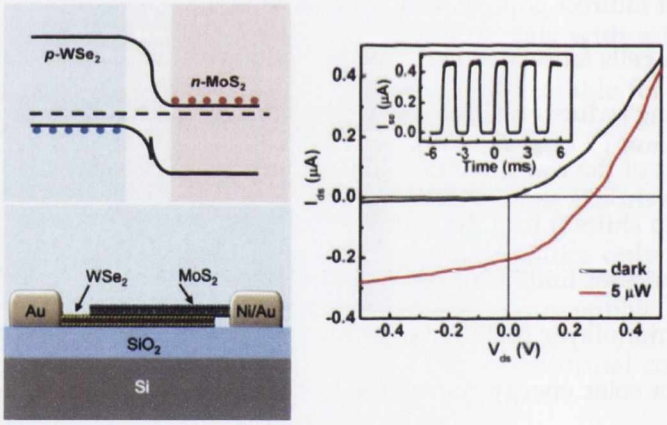

Figure 2.25: Ideal band diagram of WSe_2-MoS_2 hetero-junction pn diode under zero-bias (top left). Schematic illustration of cross-section of WSe_2-MoS_2 vertical heterojunction device (bottom left). Output characteristic of device in dark and under 514 nm illumination (right). Inset - temporal photocurrent response of photocurrent generation at 10 μW.[66]

highly beneficial for dissociation of light generated electron-hole pairs and required for photovoltaic energy generation. The fact that it is easy to establish p-type conduction in monolayer WSe_2 and n-type in monolayer MoS_2 makes them ideal candidates to

combine in ultrathin junction solar cells. In addition, the junction in this case is atomically sharp resulting in stronger electric fields than 3D semiconductor hetero-junctions, where the transition region is typically established over a couple of monolayers.[156] This has been illustrated recently in such a device exhibiting well defined current rectification (ideality factor, $n = 1.2$) with photocurrent external quantum efficiency (EQE) of 12% (at 0.5 μW).[66] Respectable values for V_{OC} and I_{SC} of 0.27 V and 0.22 μA are obtained respectively (note that the authors of this publication unfortunately have not measured the active area of overlap between the two materials and so do not quote the short circuit current normalised to the film area.) This is in contrast to electrostatically doped homo-junctions in monolayer WSe_2which showed EQEs of 0.1-3%, attributed to the spatially graded doping profile in such devices.[67, 105]

2.6.1.6 *Bulk Nano Heterojunction Solar Cells*

The large number of inter-flake junctions in liquid phase exfoliated films poses a problem for solar cells. As is outlined in section 6.1.2, associated localised states within the bandgap at these sites promote charge carrier trapping and recombination. However a novel approach may mitigate recombination by mixing optimised quantities of suitably matched n- and p-type semiconductors in the liquid phase. The mixture can be used to form films with a graded junction area between two pure layers of the n- and p-type material (figure 2.26).[157, 158]

This is a potentially powerful technique for liquid phase exfoliation to exploit and mixing materials to make nanocomposites with well-tailored electronic properties has already been demonstrated.[53–55] With this in mind one can envision bulk nano hetero-junctions (BNHs)[157–159] made from TMDs by liquid phase exfoliation. Such BNHs have been demonstrated for complementary n- and p-type semiconducting nanoparticles. Significant improvements in device performance compared to the bilayer analogue can be realised once the mixed phase composition is optimised. Suppressed recombination results due to more efficient charge separation and transport. This leads to increased linearity in the intensity dependence of the short circuit current as in figure 2.27.[157]

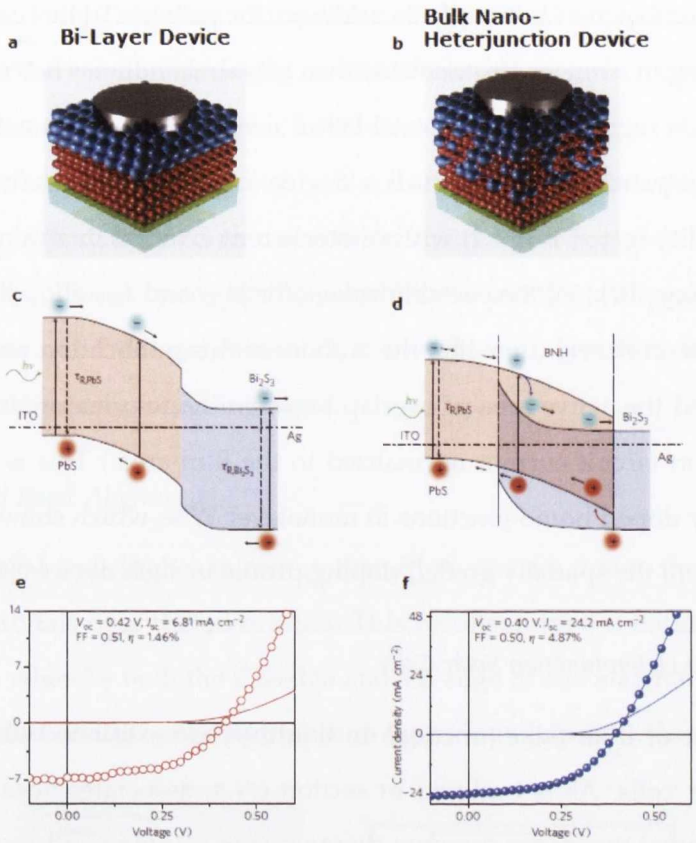

Figure 2.26: (a) Schematic of bilayer device consisting of ITO-PbS quantum dots (red)-Bi_2S_3(blue)-Ag layers. (b) Schematic of BNH device with nanocomposite transition layer between bilayers. Band diagram of (c) bilayer and (d) BNH device. Dark (solid) and one-sun (dashed) I-V characteristics of (e) bilayer and (f) BNH devices.[157]

2.6.2 *Thermoelectrics*

Good thermoelectric materials demonstrate a high Seebeck effect, whereby charge carriers diffuse from hot-cold in the presence of a temperature gradient. Thus an open circuit voltage is generated across the ends of such a material ($V = S\triangle T$) as in figure 2.28 (top). Thermoelectric modules are comprised of individual thermoelectric devices or elements, each consisting of two legs (one p-type & one n-type) connected electrically in series but thermally in parallel. Under a temperature gradient charge carriers at the hot ends have more kinetic energy and so diffuse to the cold ends where

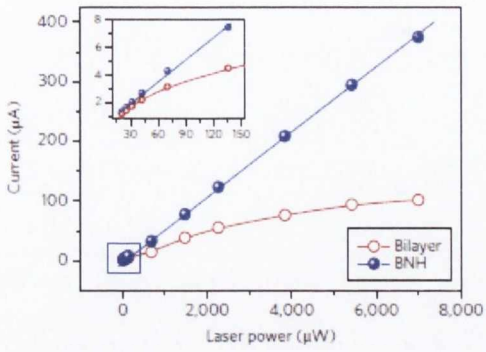

Figure 2.27: Short-circuit current dependence on illumination intensity. Bilayer device shows strong saturation due to accelerated recombination at high intensity.[157]

they accumulate. Connecting a load across the cold end, this functions as a voltage source with an internal resistance due to the two legs, which can drive current and generate power as in figure 2.28 (left). Also, as free charges carry heat as well as charge, they can provide solid-state active cooling/heating when driven by an external power supply via the Peltier Effect ($Q = STI$) as in figure 2.28 (right).[160]

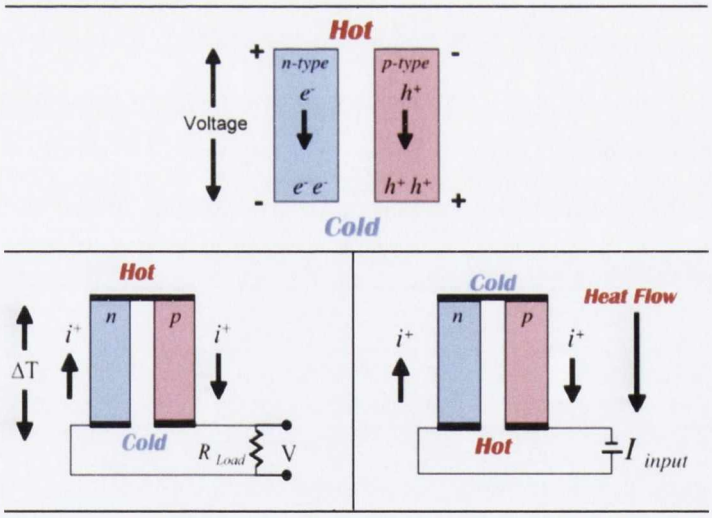

Figure 2.28: Illustrations of the Seebeck Effect (top) upon which thermoelectric generators (left) and the associated Peltier Effect on which thermoelectric coolers (right) are based. Taken from Thermoelectrics Group at Caltech website.[161]

This technology provides a means to harvest electrical energy from heat-sources such as dissipated microprocessor heat for on-chip power generation, waste heat from

car engines to improve fuel efficiency or even body heat for wearable technology. Among the notable advantages this technology offers are; increased reliability (and no noise) due to no moving mechanical parts, requiring no refrigerant or compressor due to their compact size, which allows them to be used in places where traditional cooling solutions simply will not fit. Additionally, they allow one to heat or cool by simply reversing the current. The principle drawback with this technology is its poor efficiency (5-8% typical) making it expensive. This has largely limited their use so far to niche applications where no cheaper alternatives exist. For example, they have been in use since the 1950's as power generators for spacecraft where a radioactive element provides the heat-source.[162]

2.6.2.1 *Thermoelectric Figure of Merit, ZT*

Recently the need for non-carbon-based energy generation has led to a new interest in thermoelectric materials that could scavenge electricity from waste heat produced by factories and engines; more than 60% of the energy produced in the UK is lost as waste heat.[163] The key challenge is to impair heat conduction whilst promoting the electrical transfer of charge & energy. A material such as this is often aptly referred to as an 'electronic crystal-phonon glass', obtained by engineering low thermal conductivity materials whilst retaining their attractive electrical, mechanical and optical properties. The relationship between all these concepts is encapsulated in the dimensionless thermoelectric figure of merit (FoM)

$$ZT = \left(\frac{S^2\sigma_{DC}}{\kappa}\right) T \tag{2.14}$$

The FoM is directly related to the efficiency with which a thermoelectric material can operate. In this equation T represents the temperature, σ_{DC} the electrical conductivity and κ the thermal conductivity where $\kappa = \kappa_{lattice} + \kappa_{electron}$. The Seebeck coefficient, S has units of V K^{-1}. In terms of the power-factor ($S^2\sigma_{DC}$), highly doped semiconductors ($n = 10^{19} - 10^{21}$ cm^{-3}) make for ideal thermoelectric materials as opposed to insulators whose σ_{DC} is too low, or metals with their low S (~-5 μVK^{-1}) and negative temperature co-efficients of resistance. A higher FoM brings the efficiency closer to the Carnot efficiency. For maximum power generation, the external load resistance should be

matched to the resistance of the generator. Then the efficiency, given by the electrical output W over the heat absorbed at the hot junction Q_H reads

$$\eta_{Max} = \frac{W}{Q_H} = \frac{\triangle T}{T_{hot}} \times \frac{\sqrt{1+ZT_{ave}}-1}{\sqrt{1-ZT_{ave}}+\frac{T_C}{T_H}} \tag{2.15}$$

In practice values of $ZT > 1$ are very hard to realise.[164] However, as ZT scales with the electrical conductivity, there is scope for further improvement if the electrical conductivity could be increased.[2, 51, 165] At the same time, the factors comprising Z are all intimately related competing quantities; enhancing one usually results in degradation of one or both of the others. For example, as $S \propto m^*$ an increased effective mass may seem to offer an opportunity to increase the power factor. In practise this is negated due to the decrease it induces in σ_{DC} by reducing the carrier velocity.[160] Moreover, doping boosts the electrical conductivity via an increase in the charge carrier density. Unfortunately, this simultaneously increases the thermal conductivity κ_{e^-} via its electronic component by the Wiedemann-Franz Law where L denotes the Lorentz number as

$$\kappa_{e^-} = L\sigma T \tag{2.16}$$

More importantly, the Seebeck coefficient is also degraded simultaneously, the higher density of charge carriers serving to decrease the entropy difference associated with the high and low temperature surfaces of the device which drives their diffusion.[166] In contrast with bulk materials, nano-structured composite materials offer an avenue to synergistically reduce the thermal conductivity through increased phonon interface scattering, whilst also providing a decoupled, unimpeded electrical pathway through the material due to different mean free paths for charge carriers and phonons.[164]

2.6.2.2 *Liquid Phase Exfoliated TMD Films for Thermoelectrics*

Thin films of layered materials produced by liquid phase exfoliation may offer several avenues to improve the thermoelectric figure of merit and thus the efficiency. Composite films of single wall carbon nanotubes (SWNT) and MoS_2 (similar to the ones in chapter 5) have been fabricated by our group and tested for the power factor as a function on SWNT volume fraction.[51] The small decrease in the Seebeck co-efficient is more than offset by the increase in σ_{DC} and a well defined peak exists at a certain nanotube

loading level (figure 2.29). However measurement of the thermal conductivity has so far proven challenging due to the inherently low thermal conductivity coupled with the low mechanical strength of such films.

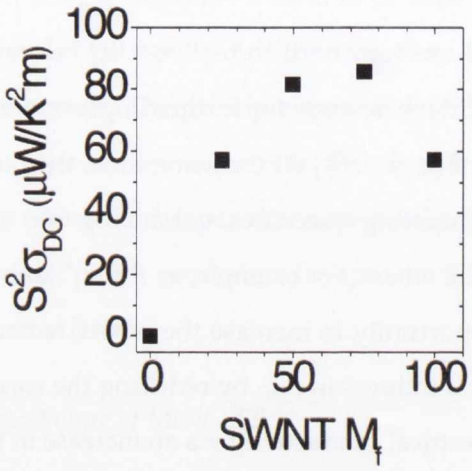

Figure 2.29: Thermoelectric power factor, $S^2\sigma_{DC}$ for MoS_2-SWNT hybrid films as a function of SWNT mass% (film thickness 50 μm).[51] Small decrease Seebeck co-efficient is offset by significant power factor increase where there is a clear peak versus SWNT loading level.

As is shown throughout this thesis, liquid phase exfoliation produced films are composed of disordered nanosheet networks containing a large number of flake edges. Whilst these ultimately prove detrimental for optoelectronic applications by diminishing the mobility and acting as traps and recombination centres within the bandgap, such interfaces may actually prove beneficial in the case of thermoelectrics. Though their impact on κ is complicated, the inherent disorder and accompanying high density of material interfaces in these as-produced films can beneficially attenuate phonons when optimized. Additionally, liquid-phase processed films are typically ~40-50% porous containing large amounts of free-volume between flakes.[167, 168] Porosity can serve to decrease κ and is a signature of good thermal insulators such as Styrofoam. As heat-flow through a heavily-disordered, mesoscopic material is carried by a spectrum of phonons with varying wavelengths (mean free paths <1 nm - 10 μm), phonon scattering at a variety of length scales is important for broadband impedance so that a temperature difference may be maintained across a thermoelectric module

or element.[160] Finally the bonding anisotropy inherent in 2D materials gives rise to corresponding anisotropies in both their electrical and thermal conductivities. In the case of κ this is a symptom of the weaker van der Waals bonding and so lower spring constant in the out-of-plane direction. This fact can be geometrically exploited in module design to further reduce the device thermal conductivity.[169] In fact, Bi_2Te_3 is one such layered chalcogenide (composed of five hexagonal monatomic layers perpendicular to the c-axis, referred to as quintuples)[170] that is already known as an exceptional thermoelectric material, showing a $ZT > 1$ around room temperature.[127] This is fundamentally due to its small bandgap (~0.2 eV) and heavy constituent elements, which lower the sound velocity through the material according to

$$\kappa = \frac{1}{3} C_V v_p l \tag{2.17}$$

In this equation C_V is the specific heat capacity per unit volume and v_p & l are the phonon velocity and mean free path respectively.[171]

3

METHODS

3.1 INTRODUCTION

This chapter outlines the main methods used for materials preparation and characterisation throughout this thesis. Liquid phase exfoliation is a simple method to process layered materials. Sonication of the materials in bulk powdered form, in organic solvents, results in stable dispersions of exfoliated nanosheets. Centrifugation is used to remove any large unexfoliated crystallites and aggregates. UV-visible absorption spectroscopy can characterise the dispersions of these materials via their electronic transitions. An estimate of concentration can be performed using the Beer-Lambert Law. Dispersions may then be dropped onto TEM grids or cast into films for further physical (SEM & Raman spectroscopy) and photoelectrical characterisation.

3.2 DISPERSION PREPARATION

3.2.1 *Sonication*

Ultrasonic refers to high frequency sound waves above an audible level for humans (>16 kHz). Application of ultrasonic energy has several uses across different branches of science and engineering such as navigation, diagnostic imaging and plastic welding. It is also been employed in cleaning, having sufficient power to overcome the adhesive forces of a particle on a surface.[172] Using it in a similar manner then, dispersions of layered materials in organic solvents are produced by ultrasonication, or just sonication as it is commonly referred to.

Being longitudinal, such waves cause the solvent molecules to oscillate about their mean positions due to the rarefaction and compression stages of the cycle. On rarefaction, the cohesive forces in the liquid are overcome. Solvent molecules move apart from each other and eventually rupture, resulting in cavitation, formation of small bubbles within the liquid medium. Such cavities grow before collapsing on the compression wave cycle. Liquid motion generates very large strain gradients caused by rapid streaming of solvent molecules around the cavitation bubble. Also, intense shock waves are produced on bubble collapse.[173] As adjacent layers are only weakly van der Waals bound, shear results in delamination or exfoliation of layers from the bulk material. These thinner layers are then stabilised against re-aggregation by favourable interaction with the surrounding solvent medium.[2]

In plane covalent bonds exist within each 2D layer which are much stronger than the out of plane van der Waals bonds. Sonication induced scission, refers to such covalent bonds being broken, resulting in the cutting of flakes into smaller entities. This process increases down to some terminal length with sonication time ($l \propto t^{-1/2}$, where l is mean flake length) and has been shown to occur in layered materials such as graphene,[174] MoS_2,[175] and more recently, the transition metal oxide (TMO), MoO_3.[55] The same relationship was previously found to hold for 1D carbon nanotubes.[176]

Most modern sonication devices apply a high frequency AC voltage to a piezoelectric crystal causing a change in its dimensions. The transducer then converts electrical energy to ultrasonic (mechanical) energy. Two main types of sonication apparatus are used throughout this work. Both employ what is known as power sonication, using high energy, low frequency waves (20-100 kHz) as opposed to the low power, high frequency ultrasound used in imaging.[177]

3.2.1.1 *Sonic Bath*

Apart from the large scale solvent study in chapter 4, a Branson 1510E-MT sonic bath (20 kHz, 16 W) has been used in this thesis. Sonic baths are typically low power (<25 W). As such they require longer sonication times to achieve a given degree of exfoliation. The steel bath is filled with water and the sample held within a vessel,

typically a vial within a beaker. The sound waves then penetrate the walls of the vial and beaker. Baths tend to suffer from poor reproducibility even when a common model is used due to effects such as water heating.[174] As such they are usually employed only to help homogenize mixtures or re-agitate older samples that may have undergone a degree of sedimentation. A large bath can facilitate a higher throughput and is useful when a solvent study is required across multiple materials. However they house several transducers which means they suffer from less homogenous power output. This can be mitigated by cycling samples throughout different zones within the bath for allocated times.

3.2.1.2 *Sonic Tip*

Figure 3.1: Programmable Sonic Tip offers improved reproducibility over the bath.

The model of tip used frequently in the work of this thesis is the Vibracell, GEX750, 750 W, 20 kHz from Sonics Materials Inc.[178] With this apparatus a probe is placed within the sample held in a vial. The standard procedure is to centre the probe in contact with the bottom of the vial then raising it just above bottom before beginning to sonicate. The energy input can be controlled by the user by varying the amplitude of vibration and allowing for on-off pulsing of the tip, facilitating sample cooling. Much shorter sonication times are required due to the higher power. A horned probe may be used for larger volume sonication. Samples are generally cooled using ice or an external chiller.

3.2.1.3 *Organic Solvents*

solvent	δ_D $(MPa)^{1/2}$	δ_P $(MPa)^{1/2}$	δ_H $(MPa)^{1/2}$
DMF	17.4	13.7	11.3
NMP	18	12.3	7.2
cyclohexanone	17.8	8.4	5.1
IPA	15.8	6.1	16.4
chloroform	17.8	3.1	5.7
acetone	15.5	10.4	7

Table 3.1: Solubility Paramters of typical high (DMF, NMP, cyclohexanone) and low (IPA, chloroform, acetone) boiling point solvents.[179]

A solvent is a liquid that serves as a medium for a reaction. A range of solvents can be used to exfoliate layered materials depending on the application. Solubility parameters (see chapter 4) are based on material properties such as the surface energy or cohesive energy density. Their role in sonication of TMDs is outlined in detail chapter 4. The Hansen solubility parameters (based on cohesive energy density) of the most commonly used of these in liquid phase exfoliation are shown in table 3.1. Of these, the characteristics of a typical high and low boiling point solvent are outlined below.

3.2.1.4 *N-Methyl-2-pyrrolidone (NMP)*

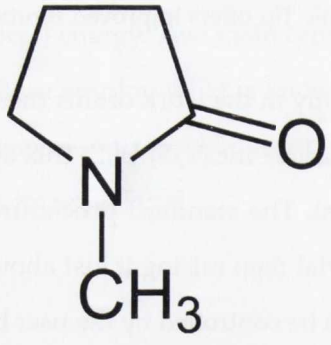

Figure 3.2: NMP molecule. NMP is one of the best performing solvents for liquid phase exfoliation of nanomaterials. However it is notoriously difficult to remove due to its high boiling point.

NMP is a high boiling point (~204 °C), viscous, aprotic polar solvent of chemical formula C_5H_9NO. It has a high dielectric constant (ε_r= 32) and dipole moment (μ_D= 4.1 D). Its uses in industry include as a paint stripper, de-greaser and drug solubilizer. It is colourless, though it can appear slightly yellow with age. As it is hygroscopic it is important to store it carefully or use fresh stock when exfoliating. It is one of the most successful solvents at exfoliating low dimensional nanostructures such as CNTs,[3] graphene,[180] TMDs[181] and TMOs.[55] The main drawbacks with such a solvent are being hard to remove, its toxicity[182] and ability to penetrate common nitrile lab-gloves. In addition, it spoils for long sonication times, polymerizing and turning yellow, leading to fall out of the dispersion.

3.2.1.5 *Isopropanol (IPA)*

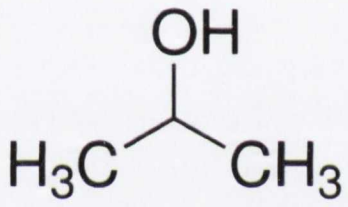

Figure 3.3: IPA molecule. IPA is poorer for exfoliation but is much easier to remove and also promotes film formation from dispersions directly on a water surface as in chapter 6 due to its strong H-bonding.

As NMP can be hard to remove, a lower boiling point (though poorer) alternative solvent is often desirable depending on the application in mind for the exfoliated nanosheets e.g. for AFM analysis. IPA is commonly found in labs for cleaning purposes. For exfoliation work higher grade HPLC IPA is used as it generally results in more stable dispersions.[179] IPA is a colourless compound with a strong odour and chemical formula C_3H_7OH. It is a protic, (somewhat) polar solvent with a dielectric constant of 18 and dipole moment of 1.66 D. Having a boiling point of 82 °C it is highly volatile. It has low toxicity and is readily miscible in water due to its high H-bonding component.

3.2.2 *Centrifugation*

In this work all centrifugation was performed using a standard refrigerated bench-top centrifuge, the Hettich Mikro 22R. Centrifugation rate is programmable from 500-18000 RPM. Six large vials up to 28 ml can be accommodated and spun up to 6000 RPM using the standard rotor of 90 mm radius. Twenty four smaller tubes (2 ml) may be accommodated on the high speed rotor of 87 mm radius, which can be spun up to 18000 RPM.[183]

A centrifuge is driven by an electric motor and rotates an object about a fixed axis, with the centripetal force then being applied perpendicular to this axis. Once sonicated, the dispersions contain a range of flake lengths and thicknesses. Centrifugation works on the sedimentation principle whereby heavier, unexfoliated crystallites and aggregates separate along the radial direction toward the bottom of the tube. Thus the lighter, exfoliated components remain towards the top of the dispersion in the supernatant. This process will occur itself over time under gravity. Centrifuging speeds up this process by increasing the gravitational force.

The supernatant containing the exfoliated nanosheets is decanted for further use. Such a supernatant will still be polydisperse, consisting of a range of nanosheet sizes. However these resultant dispersions may be spun at different rates and decanted to allow size selection and narrow the polydispersity.[52, 55]

It is useful to calculate the relative centrifugal force (RCF) on the particles in the dispersion. This quantity can be compared consistently across centrifuges of different radii, whereas RPM cannot. During the circular motion a centripetal force is applied. The acceleration due to this force is measured in multiples of g, giving a dimensionless quantity. Other symbols are denoted by r - radius and ω - angular velocity.

$$RCF = \frac{\omega^2 r}{g} \tag{3.1}$$

$$RCF = (1.118 \times 10^{-3}) \times r \times RPM^2 \tag{3.2}$$

3.3 FILM FORMATION

3.3.0.1 *Langmuir-Blodgett Method*

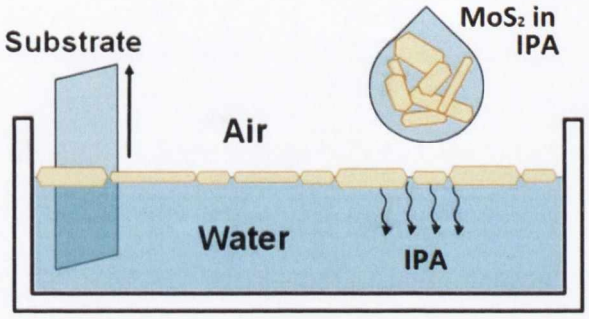

Figure 3.4: Langmuir-Blodgett deposition process. Figure adapted from [184]

Popular film formation techniques employed by our group include vacuum filtration onto porous membranes (which can be transferred to desired substrate and dissolved),[185] spraying[186] and inkjet printing.[187] Such techniques generally require well exfoliated entities to make up the resultant films, for example to prevent the nozzle clogging whilst inkjet printing. However, when using films fabricated in these ways in an out of plane geometry, this leads to shorting of the metal electrodes on the evaporation step. This fact led to the preparation of dispersions of larger particle size, which were either un-centrifuged (chapter 6) or centrifuged only to remove the smallest flakes (chapter 7). Dispersions such as these with larger than usual entities do not lend themselves to being processed in thestandard ways just mentioned. This coupled with TMD's inherent hydrophobicity, led to fabrication of the films on a water surface, using a technique based in principle on the Langmuir-Blodgett method.

Typically the Langmuir-Blodgett method is used to form very thin films of organic molecules. More recently, the method has been used to form thin films made from 2D graphene.[184, 188] A plastic or Teflon coated trough holding water with movable barrier blocks that can compress the film are used. DI water (18 MΩ cm) is used as even small amounts of contaminants will significantly change the surface tension of the water phase. Air contamination could be avoided by performing film formation in a cleanroom environment. Stability can be improved by mounting the trough on a

vibration isolation table. The trough should be thoroughly cleaned with IPA before filling with water. The dispersion is then slowly dropped onto the water surface using a micro-syringe until it uniformly covers the surface. A pump can be used to continuously drop dispersion at a constant rate to keep the film on the water surface uniform.

For transfer to the substrate, depending on the molecular species forming the film can be extracted vertically, at an angle or horizontally. Ideally this is done in an automated manner, at a slow constant speed, by using a motor and pulley. Multilayers are achieved by successive dipping once the layer has dried sufficiently.

3.4 SAMPLE CHARACTERISATION

3.4.1 *UV-Visible Absorption Spectroscopy*

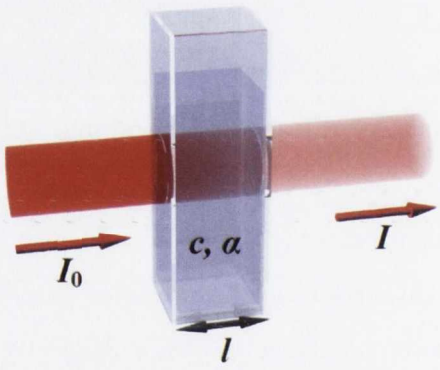

Figure 3.5: Monochromatic light of incident intensity I_0passing through a quartz cuvette of length l. The absorbance over the path length is proportional to the concentration by the Beer-Lambert law at low concentrations.

The equipment used throughout this thesis for characterising the absorption of dispersions of nanomaterials is a Varian Cary 6000i (200 – 1800 nm) dual beam spectrometer. This machine uses a tungsten lamp as a source of visible-IR light and a deuterium arc source for UV.[189] Splitting the incident & reference beams improves accuracy and minimizes reflection, scatter and absorption of light by the solvent. A

chopper allows the detector alternate between sample and reference beams as in figure 3.5. Light from the source is split into its individual wavelengths by a monochromator which consists of a diffraction grating and series of mirrors and slits. Light is detected using an InGaAs photodiode.[190]

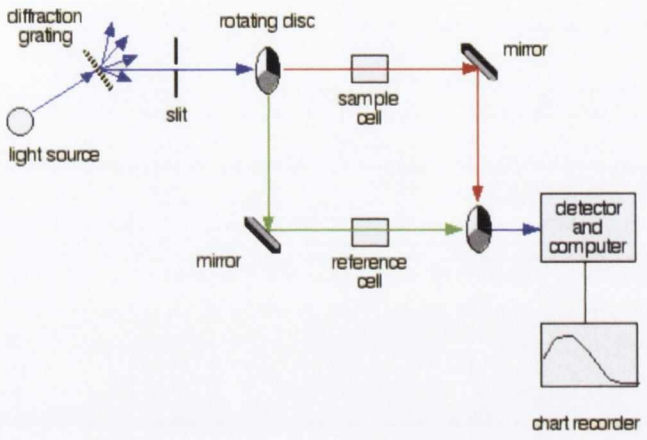

Figure 3.6: Path of light beams within the double-beam spectrometer. Note different colours do not refer to different wavelengths of light, only different light paths.

Ultraviolet-visible (UV-Vis) absorbance spectra are recorded by holding the dispersion in a quartz cuvet and exposing it to light of different wavelengths via a diffraction grating. Photon absorption occurs at particular energies by exciting an electronic transition within the material.[189] This decrease in irradiance reaching the detector is recorded as an increase in absorbance (a measure of how efficient the absorption is). For semiconductors, an appreciable amount of light will only be absorbed once the bandgap has been exceeded. By Fermi's Golden Rule, the absorption spectrum then is a measure of the joint density of states in the conduction band. Whilst this spectroscopy works well for solutions, dispersions have a significant scattering component of light which does not reach the detector. In addition, molecules are close together enough in solution to influence each other's energy levels. This broadens the peaks into absorption bands over a number of wavelengths. UV and visible light are also energetic enough to promote vibrational (IR) and rotational (microwave) transitions in molecules which also contribute to the broadening.[191]

This process can be understood through the Beer-Lambert Law. Let a monochromatic parallel beam of light of intensity I pass through an absorbing material of infitinitesmal thickness dl as in figure 3.5. Light passing through the reference sample is at intensity I_0. If $I < I_0$ the material has absorbed a portion of the incident light

$$A = \log_e \left(\frac{I}{I_0} \right) = -\log_e T \tag{3.3}$$

The amount of light absorbed depends on the number of molecules it interacts with, which is proportional to the concentration C. Also, standard cuvettes are often 1 mm or 1 cm in thickness so the path length l of the light through the sample is known. The extinction co-efficient ε has units of Litres/g/m and is a function of the light's wavelength.

$$A = -\varepsilon C l \tag{3.4}$$

3.4.2 *Electron Microscopy*

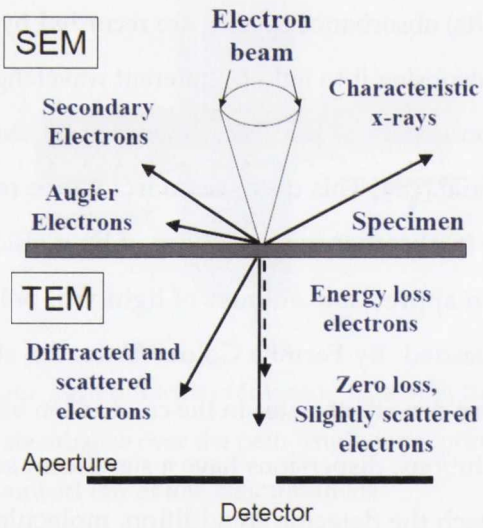

Figure 3.7: Typical processes electrons undergo when interacting with matter.[192]

As nanomaterials exist below the wavelength of visible light, their imaging requires high resolution. Optical microscopy has a theoretical resolution of

$$d = \frac{\lambda}{2n \sin\theta} \approx \frac{\lambda}{2NA} \tag{3.5}$$

limiting its resolution to a couple hundred nm. In the above equation, n is an integer multiple of the wavelength λ, whereas θ is the angle of incidence and reflection and NA is the numerical aperture. As electrons have an associated de Broglie wavelength and interact with matter they may be used for imaging.

$$\lambda = \frac{h}{p} = \frac{h}{mv} \tag{3.6}$$

In an electron microscope, electrons from a source are produced at the top of a column by thermionic or field emission. These are extracted under vacuum and are condensed and focused into a beam using electromagnetic lenses and apertures. The magnetic lenses can be varied in focal length and magnification by simply modifying the amount of current passing through them. The beam then traverses a vertical path through the microscope toward the sample. Being charged the electrons may have their kinetic energy increased by an accelerating voltage.

$$\frac{1}{2}mv^2 = eV \tag{3.7}$$

A relationship can then be established between electron wavelength and accelerating voltage. By increasing the voltage the wavelength of the accelerated electrons is decreased, improving the resolution.

$$\lambda = \frac{h}{\sqrt{2meV}} \tag{3.8}$$

In practice, whilst electron microscopes are not diffraction limited they suffer from aberrations (chromatic and astigmatism) and as such are far away from these resolution limits.

3.4.2.1 *Transmission Electron Microscopy (TEM)*

TEM imaging in this work has been carried out with a Jeol 2100 TEM system operating at a voltage of 200 kV. This equipment uses a LaB_6 source and can operate between 80-200 kV with a maximum high contrast resolution of 0.31 nm.[193]

In TEM high energy electrons (100-400 kV, magnification x50-10^6) are used to image thin, electron transparent samples (<200 nm). The image consists of the spatial variation of slightly scattered electrons reaching the detector, forming a 2D projection of the

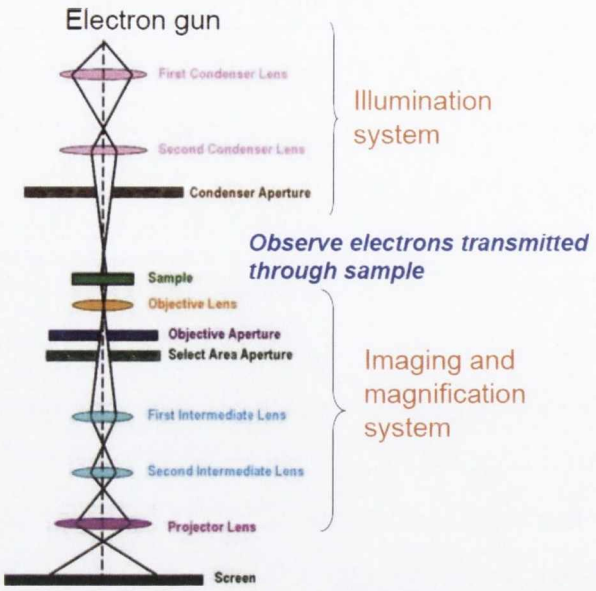

Figure 3.8: Components of a TEM column.[192]

3D object. Typical max resolution for TEM is ~0.2 nm and is limited by aberrations. Aberrations become more prominent as one moves to higher resolution imaging. The three main types are spherical and chromatic aberrations as well as astigmatism. Astigmatism is caused by an asymmetric magnetic field along the pole piece. It can be somewhat corrected for with a weak quadrupole lens, a stigmator.

The microscope consists of 3 main sub-systems under vacuum; the illumination, objective lens and imaging systems. The illumination system at the top consists of an electron source (LaB_6 crystal, or W filament) and two condenser lenses. Alignment is most crucial at this stage to form a well resolved image. Emitted electrons are focused and formed into a beam that is extracted from source down through the sample. Electrons undergo scattering events within the sample and are emitted with a variety of angles and energies to be collected by the objective lens. This lens gathers electrons directly from the object being observed and focuses them to form a real image. It is centrally important and determines the quality of the final image.

Once transmitted the imaging system projects and magnifies the transmitted beam to form an image in the image plane. A projector lens uses the image formed by a preceding lens as an object rather than a physical object. Electrons can then be detected

by a cooled CCD to record images. Also, a diffraction pattern which can be used to determine crystal structure, is created in the back focal plane due the electrons having wavelengths similar in size to typical lattice sizes.[194]

3.4.2.2 *Scanning Electron Microscopy (SEM)*

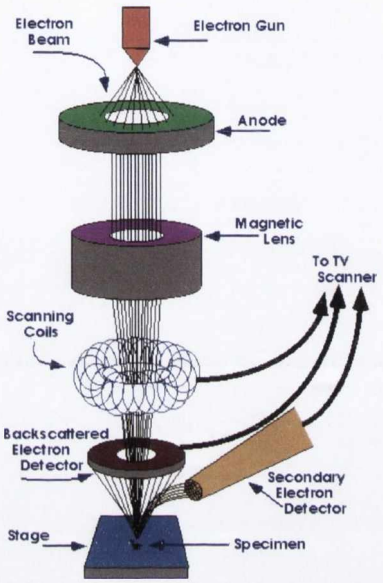

Figure 3.9: SEM and its sub-systems.[192]

In this work a Carl Zeiss Ultra Plus with LaB_6 source has been used. All imaging has been carried out at <5 kV. The SEM operates at typically lower energies (100 eV-50 keV, magnification x10-300,000) than the TEM. It is useful for imaging surface morphology and obtaining information on chemical composition of thicker samples. The electron beam (~1 nm) is extracted by the anode and condensed by the condenser lens. It is then raster scanned by varying current through the scanning coils and interacts with the sample atoms at or near the surface. Electrons as well as characteristic x-rays are emitted back towards the source. The sample must be conductive or coated with a thin metal layer to avoid electrostatic charging, which deflects the beam.

Resolution is typically limited to a few nm by a combination of the size of the electron spot and the interaction volume. The interaction volume is teardrop shaped and large in relation to the beam spot size. The size of the teardrop depends on the atomic number of the sample as well as its density and the electron acceleration energy.

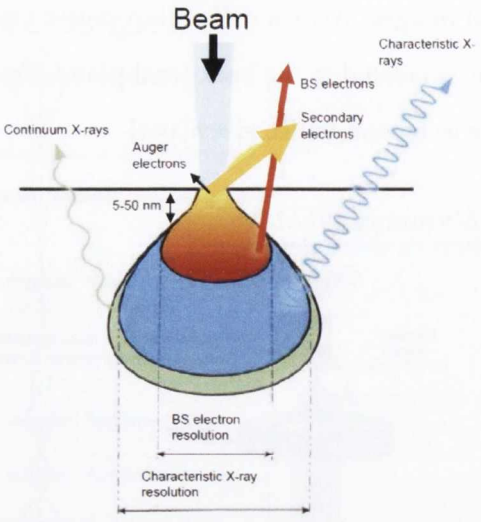

Figure 3.10: Teardrop shaped interaction volume for electrons involved in SEM imaging.[192]

The two primary types of electrons involved in SEM imaging are back (elastically) scattered electrons and secondary (inelastic) electrons. Low energy (<5 eV), inelastically scattered electrons give information within a few nm of the sample surface. Thus they are good for surface imaging. Back scattered electrons are higher in energy and produced from deeper within the interaction volume. Since heavier elements backscatter electrons more strongly this can be used to detect contrast between areas of different chemical composition. Similarly characteristic x-rays are emitted when the electron beam removes core shell electrons from the sample which are filled by an electron from a higher shell.

3.5 PHOTO & ELECTRICAL CHARACTERISATION

3.5.1 *Electrode Fabrication*

3.5.1.1 *UV Lithography*

In this work the photomask has been written using a Heidelberg DWL 2000. UV exposure has been performed with an OAI 800 FSA frontside mask aligner system, which can define feature sizes down to roughly 5 µm.

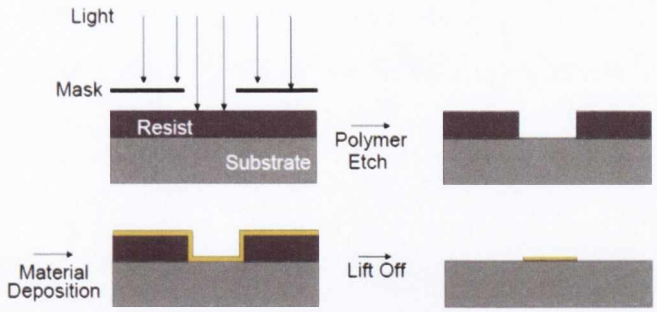

Figure 3.11: UV litho process steps for patterning electrodes in SiO_2 substrates.[192]

UV lithography is a micro-fabrication process to transfer a geometric pattern from a photomask to a light sensitive polymer-solvent solution known as a photoresist. Masks are made from quartz coated with chrome and resist layers. The chrome is opaque to the UV light, blocking it from irradiating the resist where present. Once the mask pattern has been designed using CAD software such as CleWin the blank mask is exposed to a laser to be written and etched. UV light is used as the feature size which can be resolved is proportional to the wavelength of the light divided by the numerical aperture (NA). The process is relatively quick and easy. Substrates must

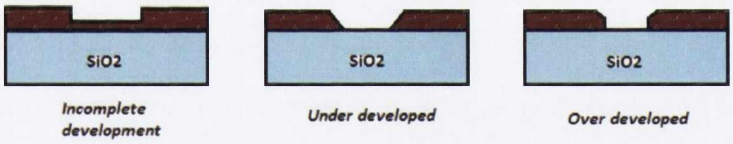

Figure 3.12: Development of exposed (positive) photoresist.

be well cleaned before use to promote resist adhesion. They are then baked at 150 °C for 5 minutes to dehydrate the substrate. Having cooled down, a spin coater is used to deposit the thin layer of resist onto the substrate, usually a silicon wafer. Typical recipes used spin the substrate at 5000 RPM for 1 minute to produce a resist thickness of 1 µm. A thinner resist film will generally improve resolution. S1813 positive photoresist has been chosen. Positive photoresists also improve resolution over negative resists (exposed resist not developed away). The resist covered substrate is then baked for 75 seconds at 115 °C to drive off any remaining solvent before being exposed to intense UV light. This causes a chemical change in the exposed areas which allows removal by

an alkaline corrosive developer solution (MF-319). Care must be taken at this point not to over or under develop the sample which will lead to either patchy electrodes or else short them out. Metal can then be deposited before being removed by lift-off in acetone to leave behind the desired metal pattern.

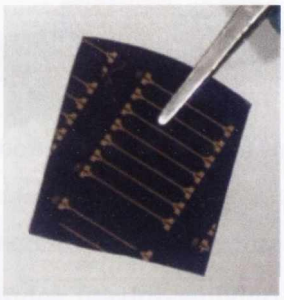

Figure 3.13: UV lithographically patterned 50 nm thick gold electrodes deposited on SiO_2(300 nm oxide thickness) substrate. Channel separations increase in steps of 10 μm from 20-80 μm.

3.5.1.2 *Metal Deposition*

All metal deposition in this work has been carried out using a Temescal FC 2000 e-beam evaporation system. Electrons are generated by a heated filament. These are then extracted and bent as a beam to be applied to the metal under high vacuum. The kinetic energy of the electrons comprising the beam is transformed into heat energy on contact with the metal, resulting in a concentrated heat source for melting. The directed vapour stream of metal particles then condense onto the substrate as a thin film and a crystal monitor measures the deposited film thickness and evaporation rate.[195]

A rise and soak method is used so stable heating of the metal can occur. The e-beam power supply can provide up to 6 kW of continuous power from 0-10 kV. Once it is switched on, the high voltage is raised to an intermediate level and held before being brought up to full power.

The vacuum system in this tool consists of an isolated rough (compression) pump and onboard cryopump which can reach down to a pressure of 10^{-7} Torr. Low pressures are required to enable molecular flow conditions, so that the evaporated film will form

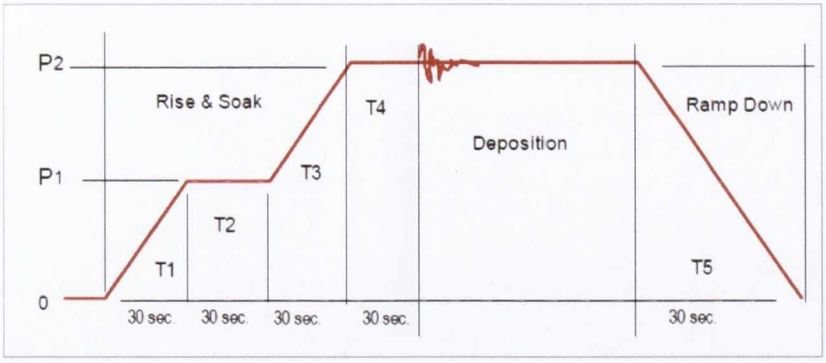

Figure 3.14: Rise and soak cycles used to heat the metal to be evaporated uniformly. Allows higher quality film deposition.[195]

uniformly on the substrate. During the roughing cycle pressure is measured with a Pirani gauge. Such gauges are useful over a pressure range from $1\text{-}10^{-4}$ Torr and are based on thermal conductivity. A heated tungsten filament increasingly loses heat to the gas as molecules collide with it as the pressure is increased. Tungsten is chosen for its high temperature co-efficient of resistance. This decrease in temperature is read as a decrease in resistance of the filament in a Wheatstone bridge circuit.

The cryopump consists of a cold head (connected to a remote compressor) and two condensing arrays and is isolated until the system is roughed down. The outer array is generally for condensing high boiling point liquids like water and oil. The inner stage is used to trap lighter elements and as such requires lower temperatures (~10 K). Ionisation gauges are used to measure pressures from $10^{-3}\text{-}10^{-9}$ Torr, where the particle count is very low. Such gauges work off ionizing a gas before counting and amplifying the signal. Two main types exist; hot cathode and cold cathode. A hot cathode gauge liberates electrons from a thermionic cathode which are accelerated and collide with gas molecules causing impact ionisation. A cold cathode gauge is used in the Temescal. These gauges contain no hot filament. An electron plasma is confined and circulated by crossed electric and magnetic fields to increase its path length, increasing collisions with gas molecules. Positively charged ions are then measured as a current as an indirect measure of gas pressure.

Once placed in a source crucible or pocket the metal must be pre-melted before depositing. Failure to do so results in poor uniformity of the evaporated film and contamination due to outgassing. This tool can accommodate up to 6 pockets for different metals. The source to substrate distance is quite large at 19.5". This combined with the rotating dome substrate holder ensures good film uniformity. However this results in more metal being wasted to evaporate a film of a given thickness. This is especially undesirable in the case of expensive precious metals such as gold and platinum. The process chamber can be isolated by a gate valve to facilitate fast loading and unloading of samples.

3.5.2 *Electrical Measurements*

A Keithley 2400 source meter has been used throughout this work for sourcing voltage and measuring current on TMD films in order to measure the conductivity via their I-V curves. Such a unit allows one to source voltage from 5 μV- 200 V and to measure current from 10 pA- 1 A and also functions as a high impedance digital multimeter. This instrument has been chosen as it offers a flexible low cost solution for facile device characterisation. Compared with a conventional power supply it gives superior resolution (5.5 digits) and a high dynamic range.[196] All I-V measurements and I(t) measurements at constant bias were controlled and recorded using a LabView program.

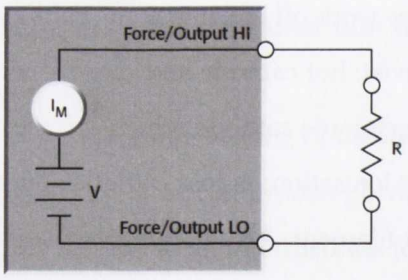

Figure 3.15: Keithley 2400 being used to source voltage and measure current for a (photo)resistor.

Typical film resistances of such films generally ranged from GΩ (MoS_2) to MΩ (WSe_2) depending on the transition metal and chalcogenide composing the TMD. These measurements were performed in a two terminal configuration, postulating that the total resistance of the films should be large compared to the contact resistance and thus the electrical properties being measured are still dominated by the bulk material despite the voltage drop at the contacts.

3.5.2.1 *Metal Contacts*

Contacts used in this work are usually pre-patterned bottom contacts. Access resistance is less of an issue for such contacts as they are in the same plane as the channel.[197] As these films are composed of a disordered array of nanoplatelets they generally exhibit a good deal of surface roughness. This makes it difficult to use cleanroom processing techniques on a film surface leading to poor reproducibility. The fact the electrodes are pre-deposited means selecting a higher workfunction metal so that metal in contact with semiconductor is not oxidised. Gold is a common choice in TMD electrical studies and has been the metal of choice for most of this work. Another consideration with top contacts is evaporation of the metal onto the semiconductor may promote alloying as well as metal diffusion through the network along the many grain boundaries. In out of plane electrode geometries this has led to shorting liquid phase processed films.[112]

3.5.3 *Solar Simulator*

A low cost, low power solar simulator (Newport 960000), fitted with an ozone free high pressure (10 bar) Xe-arc discharge lamp (150 W) with wavelength range 250-2200 nm has been used for the photoconductive studies in this work. This produces a 33 mm diameter collimated beam and was calibrated against a standard Si based reference cell in the presence of an air mass (AM) 1.5 filter. Use of such a simulator is justified where the precise uniformity and spectral match of a much more expensive class AAA solar simulator are not required.

Light intensity at the sample is controlled using a set of neutral density filters (NDFs). The housing holds the lamp, a rear reflector to collect back radiation, fan, and an F/1 quartz condensing lens. A low F number can collect and collimate more light at the cost of aberrations. If image quality or spot size are important a higher F number can be used.[198]

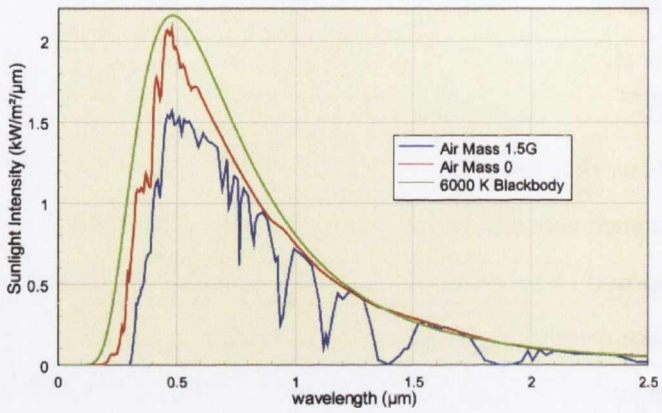

Figure 3.16: Comparative curves of light intensity as a function of wavelength for a 6000 K blackbody (surface of the sun), AM0 or zero atmosphere (for space applications) and AM1.5 representing the atmosphere (at temperate latitiudes)[132]

The Xe spectrum is broadband and mimics that of the surface of the sun. Although roughly featureless, an additional strong line output exists in the 800-1100 nm region. The surface of the sun closely approximates a 5800 K blackbody. This line output must be filtered as most absorption spectra of semiconducting materials are far from flat and this can lead to misleading results if the line output corresponds to a region where the semiconductor's responsivity is high. An air mass filter modifies the spectrum to approximate standard terrestrial solar conditions including direct and diffuse (known as 'global') light. Such a source gives an intense collimated beam due to the small (0.5 x 2.2 mm), high radiance arc source. Other than lasers, arc lamps are the brightest manufactured source of DC radiation. It should be noted the output of arc lamps decreases with time due to bulb blackening which can result in a decrease in output of up to 20%. The spectrum also changes slightly with lamp aging.

Irradiance in units of W/m^2 is the power incident on a surface, also known as the intensity. Spectral irradiance refers to irradiance at a specific wavelength and so is

usually quoted in units of W/m^3 (W/m^2nm). The total power density emitted from a source can be calculated by integrating this spectral irradiance over all wavelengths. It

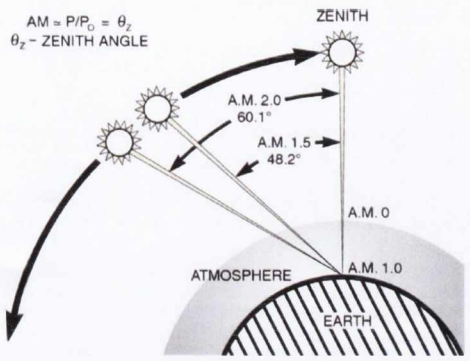

Figure 3.17: Schematic showing relation between the air mass the sun's light must pass through and the zenith angle of the sun[198].

is convenient to describe this irradiance in 'suns'. Thus one sun is equal to an intensity of 1360 W/m^2 at 25 °C and is the standard value of the solar constant just outside the earth's atmosphere. This is known as AM 0 conditions as the sun's light has not yet passed through any atmosphere. At the Earth's surface irradiance is attenuated due to absorption, scattering & reflection by air molecules and aerosols in proportion to the path length through the atmosphere. Variations in atmospheric composition, global location, seasons and time of day are also influencing factors. Atmospheric absorption, for example, ozone absorbs UV, and water vapour absorbs strongly in the IR, also modifies the terrestrial spectrum, creating dips. Standard solar cell testing conditions are known as AM 1.5 conditions, corresponding to a zenith angle of 48.2 °C, where $AM=1/\cos(\vartheta)$. The power density in this case is 1000 W/m^2.[199]

4

SOLVENT EXFOLIATION OF TRANSITION METAL DICHALCOGENIDES

4.1 INTRODUCTION

Whilst mechanical exfoliation can produce high quality samples for research, applications of layered materials will require them to be processed in large amounts. Solution processing based methods can generate such quantities whilst being compatible with current roll to roll printing techniques for thin film formation. Such techniques (e.g. dip coating, spraying, inkjet printing etc.) are high throughput and require low processing temperatures (~70 °C), making them economically attractive.

Liquid phase exfoliation (LPE) is a method based on sonication assisted exfoliation in organic solvents or aqueous surfactant solutions.[2, 51] It results in mono and few layer sheets of layered material stabilised by interaction with the solvent or surfactant. This is a facile method, compatible with atmospheric conditions and amenable to industrial scale up.[200] It is the processing technique used throughout this thesis to enable all subsequent studies.

Predicting which solvents will dissolve a given solute requires a reliable method. Interaction potentials and thus forces between molecules have thermodynamic implications and determine the properties of a system of molecules. Mixing thermodynamics and solubility theory was first developed for solutions of small molecules in solvents and subsequently extended to polymer-solvent mixtures. Such methods have been modified to consider the interaction taking place at a well defined surface in the case of nanomaterials.[201] This methodology has been applied to study the dispersion of CNTs[3] and graphene[180] in organic solvents. In this chapter we look to verify this extension of solution thermodynamics to dispersions of TMDs in organic solvents.

4.2 SOLUTION THERMODYNAMICS

For non-electrolytic liquids the solubility of a given solute is understood via the free energy of mixing

$$\triangle G_{Mix} = \triangle H_{Mix} - T\triangle S_{Mix} \tag{4.1}$$

where $\triangle H_{Mix}$ is the enthalpy of mixing and $\triangle S_{Mix}$ is the entropy of mixing. $\triangle G_{Mix}$ represents the maximum amount of work that can be freed from system to perform useful work,[202] in this case to increase surface area on exfoliation. Solvation is thermodynamically favoured if $\triangle G_{Mix} < 0$.

A solution constitutes a microscopically homogeneous single phase mixture of small solute molecules with solvent. In such a mixture the entropy of mixing is large and drives the mixing process. Being rigid macromolecules, the entropic term for low dimensional nanostructures such as 1D nanotubes or 2D nanosheets in a solvent is much smaller. Such mixtures comprise a two phase colloidal dispersion of a nanomaterial dispersed in a continuous medium, displaying aggregation and sedimentation over time.

The lack of entropy change on mixing in such colloidal dispersion renders the enthalpy term in the reaction crucially important. The enthalpy of mixing is the difference in energy between the mixed state and the two unmixed components. Exfoliation is favoured by minimizing the net energetic cost to do so.

$$\triangle H_{Mix} = H_{A+B} - (H_A + H_B) \tag{4.2}$$

The energy change on mixing can be found by calculating the intermolecular binding energies between adjacent cells in a cubic lattice model.[201] In this model solvent molecules occupy a single site n, whereas 2D platelets or nanosheets occupy a square array of $(n \times n)$ sites. Use of the lattice model works well as van der Waals interactions are short range, falling off as r^{-6}. This means only nearest neighbour interactions, z need be considered for each of the N molecules. The enthalpy of mixing then depends

on the sum of the interactions between adjacent molecules of the form $\varepsilon_{S\text{-}S}$, $\varepsilon_{NS\text{-}NS}$ and $\varepsilon_{S\text{-}NS}$ where S represents solvent and NS the nanosheet. The concept of volume fraction $\phi$is also useful in this model. If the interaction $\varepsilon_{S\text{-}NS}$ is favoured, $\triangle H_{Mix}$ will be low and exfoliation can occur.

$$\frac{\triangle H_{Mix}}{V_{Mix}} = \frac{zN}{2}\phi\left(1-\phi\right)\left(\varepsilon_{S-S}+\varepsilon_{NS-NS}-2\varepsilon_{S-NS}\right) \tag{4.3}$$

In a liquid or solid a molecule is surrounded by other like molecules and so has an inherent cohesive energy due to the sum of these interactions. The cohesive energy density is a more intrinsic material property related to the intermolecular interaction energies. For a liquid, it is related to the vaporization energy required to break all the van der Waals bonds holding its molecules together. Hildebrand proposed the square root of the cohesive energy density could be used as a solubility parameter, which would determine if a solute should dissolve in a given solvent.[203]

$$\frac{E}{V} = \delta_T^2 \tag{4.4}$$

V is the solvent molar volume. The enthalpy of mixing can then be written according to the Hildebrand-Scratchard equation.

$$\frac{\triangle H_{Mix}}{V_{Mix}} = \phi\left(1-\phi\right)\left(\delta_{T,S}-\delta_{T,NS}\right)^2 \tag{4.5}$$

Equivalently, the strength of the solvent-solute interaction is characterised by a dimensionless number, χ, the Flory-Huggins parameter. If $\chi \leq 0$ the solvent-solute interaction is energetically favoured and mixing will proceed. Normally one can assume the material concentration is low enough in the solvent to write $(1-\phi) \approx 1$.

$$\triangle H_{Mix} = \chi\phi\left(1-\phi\right)kT \tag{4.6}$$

The Hildebrand framework was developed for small molecules, primarily interacting via dispersive forces which are proportional to a molecule's polarizability.[201] The symmetry between the solvent & nanosheet for this type of interaction allows approximation using the geometric mean whereby $\varepsilon_{A-B} = \sqrt{(\varepsilon_{A-A}.\varepsilon_{B-B})}$. However, the total cohesive energy density generally consists of three main types of (attractive) interactions present between molecules in the liquid phase. These interactions are also present in solvent-solute systems.

1. Dispersion or London interactions occur for all atoms due to quantum fluctuations in electron density. This manifests as an instantaneous dipole and thus an attraction between molecules. The intersite interaction energy is proportional to the product of the polarizabilities of the lattice sites[192]

$$\varepsilon_{D,S-NS} = k_1 \alpha_S \alpha_{NS} \tag{4.7}$$

2. Polar interactions refer here to both dipole-dipole (Keesom) interactions as well as dipole-induced dipole (Debye) interactions. The intersite interaction energy is proportional to the square of the product of the dipole moments associated with the lattice sites[192]

$$\varepsilon_{P,S-NS} = k_2 \mu_S^2 \mu_{NS}^2 \tag{4.8}$$

$$\varepsilon_{DiD,S-NS} = k_3 \left(\mu_S^2 \alpha_{NS} + \mu_{NS}^2 \alpha_S \right) \tag{4.9}$$

3. Hydrogen bonding (H-bonding) interactions are complicated and cannot be simply expressed in terms of intrinsic material properties due to the asymmetric roles played by donor and acceptor. Whilst hydrogen can form covalent bonds via its one electron, H-bonding is largely ionic, being formed only between the most electronegative atoms (O, N, F).[36] In this case it is attracted to two nearby atoms forming a H-bond between them of the order of 0.1 eV. Its interaction energy is different to 1 and 2 in that it falls off as roughly r^{-2}.[204]

Interactions 1 & 2 are relatively weak ($\leq$0.5 eV) van der Waals interactions ($\propto r^{-6}$). The term 'physisorbtion' is sometimes evoked to describe interactions with such small binding energies. When molecules get too close they experience a Pauli repulsive force ($\propto r^{-12}$).

Hansen proposed dividing the cohesive energy into three separate parts to reflect the dispersive (D), polar (P) and H-bonding (H) contributions to the intermolecular interactions, yielding three new solubility parameters.[205]

$$\delta_T^2 = \delta_D^2 + \delta_P^2 + \delta_H^2 \tag{4.10}$$

Combining the Hildebrand-Scratchard (equation 4.5) and the Flory-Huggins (equation 4.6) equations with the Hansen approach, χ is minimised (mixing favourable) when

all three solubility parameters are simultaneously matched for solvent and nanosheet. Hansen included the factors of 1/4 in this equation empirically as it fit the data more accurately.[205]

$$\chi = \frac{v_0}{kT}\left[(\delta_{D,S} - \delta_{D,NS})^2 + \frac{(\delta_{P,S} - \delta_{P,NS})^2}{4} + \frac{(\delta_{H,S} - \delta_{H,NS})^2}{4}\right] \tag{4.11}$$

The nanomaterial-solvent interaction takes place at a well defined surface. Solubility parameters developed in terms of surface energy then may be more appropriate. Molecules at a surface have fewer nearest neighbours and so have higher energy than those in the bulk of a material. Thus surface is less energetically favourable than bulk and an increase in nanosheet surface area requires work. The surface energy of a layered material is the energy required to overcome van der Waals forces when peeling two layers apart. In a liquid, surface tension acts inwards from the surface and is the force responsible for minimising the surface area. It is related to the surface energy by the universal value for surface entropy of liquids at room temperature of 0.1 mJ K^{-1} m^{-1}.[3]

$$\gamma = E_{sur}^{solvent} - TS_{sur}^{solvent} \tag{4.12}$$

The enthalpy of mixing expressed in terms of the surface energies of solvent and nanomaterial for graphene has been derived as[4]

$$\frac{\triangle H_{Mix}}{V_{Mix}} = \frac{2}{T_{NS}}(\delta_S - \delta_{NS})^2 \phi \tag{4.13}$$

This expression accounted the energy required to separate all the solvent molecules and individual graphene flakes to infinity, minus the energy required to bring them back together as a dispersion with cavities in the solvent medium to hold the flakes of now different thickness. Here δ_i is the square root of surface energy of phase i and T_{NS} is the nanosheet thickness. Whilst surface energy has been used as a solubility parameter for CNTs and graphene, prior to this work it was not clear if surface energy predicted from solubility measurements is viable for TMDs, another set of van der Waals bound solids.

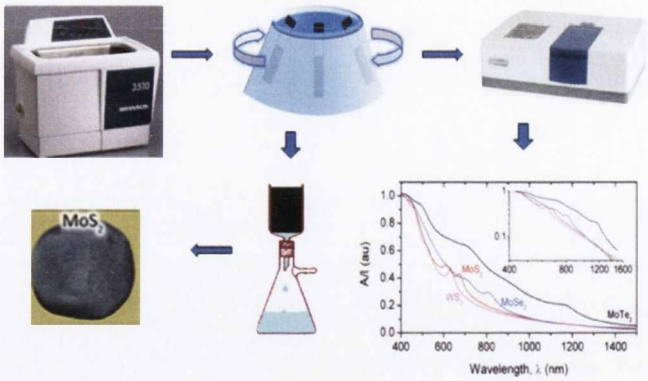

Figure 4.1: Liquid Phase Exfoliation Process

4.3 SAMPLE PREPARATION

All materials were > 99% pure and purchased in powder form. For each material supplier and particle sizes were as follows: MoS_2 (Sigma Aldrich, <2 μm), $MoSe_2$ (Materion, <45 μm), $MoTe_2$ (Materion, <10 μm) and WS_2 (Sigma Aldrich, <2 μm). In all cases, dispersions were prepared by adding 75 mg of TMD powder to 10ml of solvent in glass vials. For each TMD/solvent combination, three dispersions were prepared. Samples were batch sonicated using a Bandelin, Sonorex RK1028H 28 litre sonic bath (35 kHz, 300 W) for a total of 400 minutes. As the power is unlikely to be equally distributed throughout the bath, it was divided into eight equally sized sections and samples were cycled through each of the 8 sections remaining for 50 minutes in each.

Following established procedures,[2] samples were then centrifuged at 1500 RPM (226 g) for 90 minutes. The top 6 ml of each dispersion was then removed by pipette. These supernatants were placed in either 1 mm or 10 mm cuvettes and their absorbance spectra recorded using a Varian Cary 6000i in the wavelength range 300-1200 nm. We report the mean (over three independent dispersions) absorbance per cell length (A/l) at the following fixed wavelengths (corresponding to the first visible peak in each spectrum): MoS_2 - 670 nm, $MoSe_2$ - 808 nm, $MoTe_2$ - 701 nm, WS_2 - 627 nm. The quoted error is half of the difference between minimum and maximum recorded A/l values. We do not convert A/l to concentration as well defined absorption coefficients are not available for each material in a wide group of solvents. The nanosheets in

each dispersion may have different sizes resulting in variations in the exponent of the scattering background, making it difficult to define an absorption coefficient intrinsic to each material.

To test the dispersions of each material for stability CHP was chosen as the solvent. 100 mg of TMD powder was added to 10 ml of CHP. These mixtures were bath sonicated for 3 hours in a smaller Branson 1510E-MT sonic bath (20 kHz, 16 W). They were then sonicated using a point probe (VibraCell CVX, 750 W, 25% amplitude). Following this samples were then centrifuged using a Hettich Mikro 22R at 1500 RPM for 90 minutes and the top 6 ml retained for analysis. To achieve the transparency required for sedimentation analysis these dispersion were diluted by a factor of 20 with CHP (10 for WS_2).

Samples were prepared for TEM analysis by dropping 5 or 6 drops of dispersion onto holey carbon grids. TEM was performed using a Jeol JEM2100 LaB_6 at 200 kV. Thin films were prepared by filtration through porous Millipore membranes with 25 nm pore size. SEM analysis was performed with a Zeiss Ultra Plus.

Raman spectra were recorded using a WiTec Alpha 300R with a 532 nm excitation laser and 1800 lines/mm grating. Average spectra were obtained for each sample from line scans consisting of 50 discrete spectra, each with an integration time of 60 s, taken over a line 200 μm in length. A 20x objective lens was used with a laser power less than 0.5 mW. This lens has a numerical aperture of 0.4, corresponding via the Rayleigh criterion to a max resolution of ~800 nm ($R = 0.61\frac{\lambda}{NA}$).

4.4 RESULTS AND DISCUSSION

In this section, results of the experiment to estimate the dispersability of four different types of nanosheet in a wide range of solvents are presented. By varying the chalcogen atoms we can modify the nature of the surface which is interacting with the solvent. The results are then analysed with solution thermodynamics to test if it indeed provides a valid framework for these TMD-solvent systems.

4.4.1 *Characterisation*

4.4.1.1 *UV-Vis Spectroscopy*

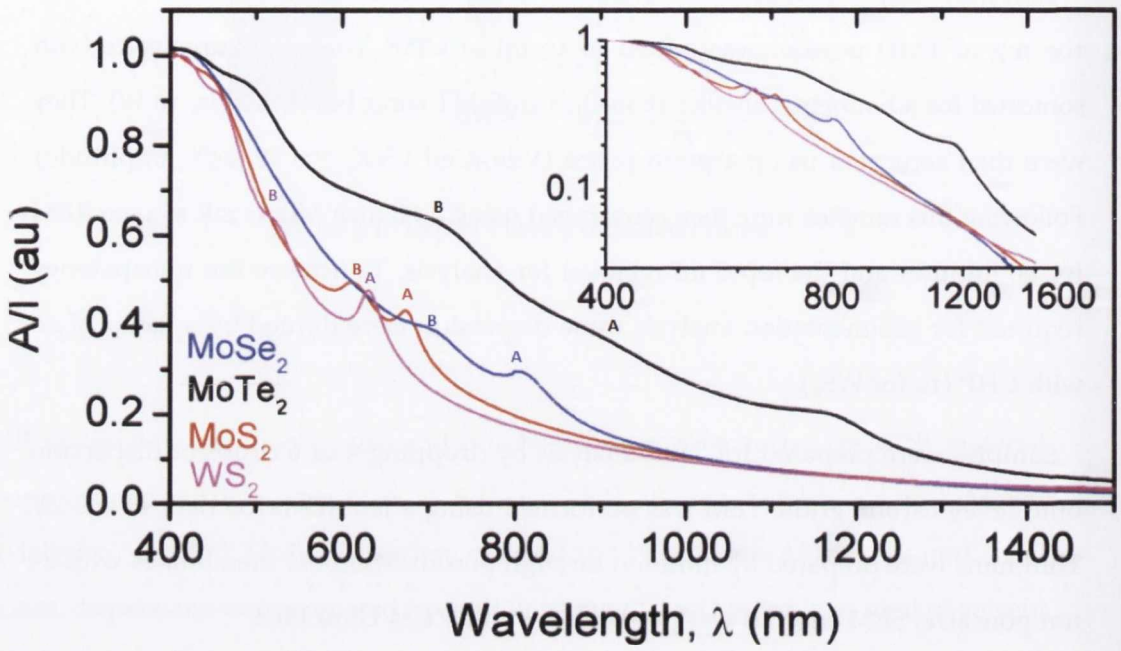

Figure 4.2: Normalised extinction spectra for TMD dispersions in cyclohexylpyrrolidone (CHP). Inset: log-log plot suggests presence of a power law scattering background.

Optical absorbance spectra of dispersions of MoS_2, $MoSe_2$, $MoTe_2$ & WS_2 have been measured in 21 different solvents. Typical spectra are shown in figure 4.2 and appear superimposed on a power law scattering background (inset). The exponent associated with this background is known to vary with centrifugation rate and thus fake size.[2, 51] Otherwise the spectral shapes are as expected, exhibiting peaks at energies corresponding to electronic transitions. For example, the MoS_2 spectrum is dominated by the prominent A & B exciton resonance peaks at 610 & 670 nm and a strong broad hump around 450 nm. The A & B excitons originate from the direct transition at the K point of the Brillouin Zone and are valence band split by spin-orbit coupling.[206]

Absorbance over cell length can be used as a measure of dispersed concentration by the Beer-Lambert Law($A = \alpha Cl$). All measured values are listed in table 4.3 in the

appendix at the end of this chapter. The dispersed concentration varied over three orders of magnitude for the range of solvents used. In all cases the best solvent is either NMP or CHP, which are also known to efficiently disperse nanotubes and graphene.[3, 180]

4.4.1.2 *Transmission Electron Microscopy (TEM)*

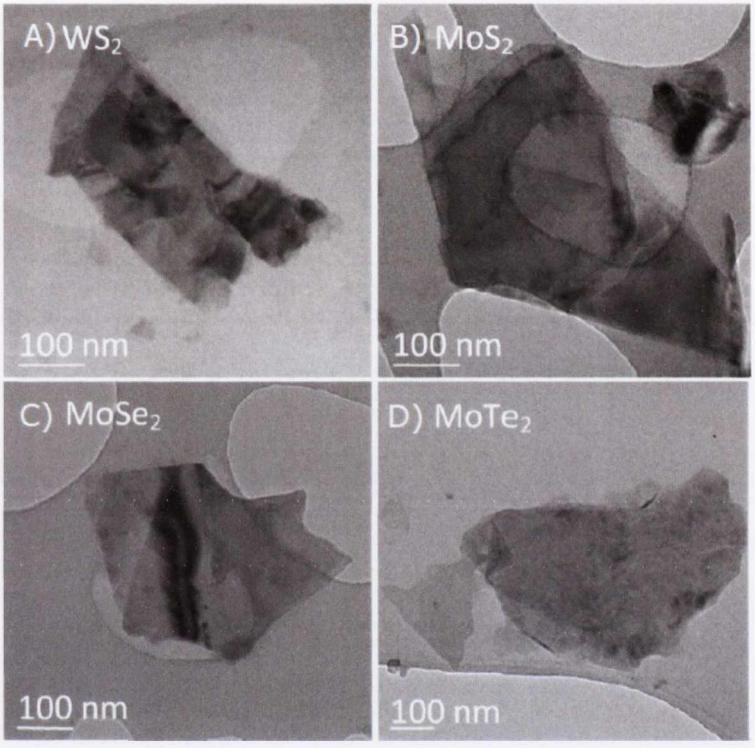

Figure 4.3: Representative TEM images of multilayer nanosheets of each of the four TMDs.

TEM allows us assess the state of the dispersed material. Figure 4.3 shows typical images of TMD flakes from CHP dispersions. In all cases multilayer nanosheets were found with no clear evidence for individual monolayers. In this study roughly 250 dispersions have been produced. In the interest of increasing the throughput in such a large study it was decied to opt for a large volume, low power density bath which results in a lower degree of exfoliation as compared with smaller sonic baths with optimised sonication conditions. The sub-optimal exfoliation regime used here will also be a factor in the experimental scatter found in the results. Typical flake lengths are a few hundred nm, consistent with previous work.[2]

4.4.1.3 *Scanning Electron Microscopy (SEM)*

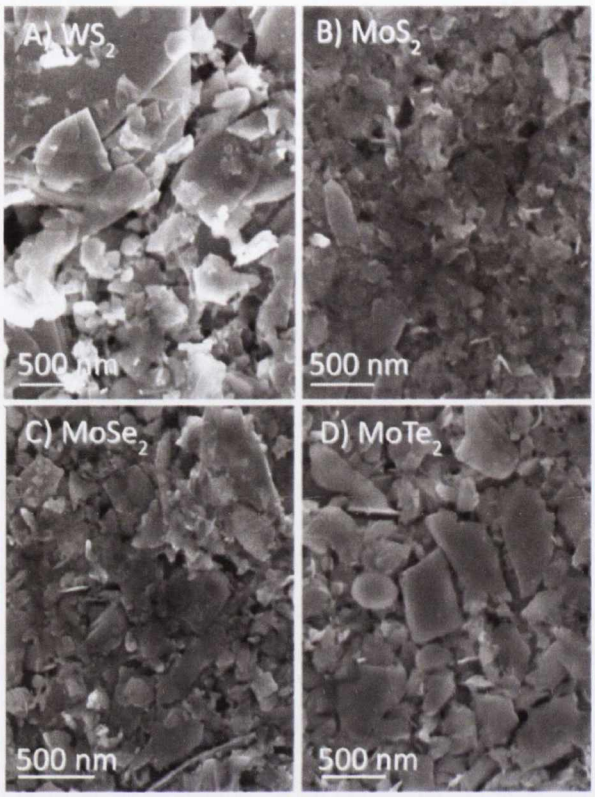

Figure 4.4: SEM images of surface morphologies of vacuum filtered thin films of each of the four TMDs investigated in this study.

Films can be quickly cast from the dispersions by filtering onto a porous membrane. Such films may then be transferred to the desired substrate. SEM images of such films are shown in figure 4.4. As expected the films appear continuous when viewed at low magnification. However, at increased magnification a network comprising a disordered array of 2D objects is seen.

4.4.1.4 *Raman Spectroscopy*

Films of each material have been characterised by Raman spectroscopy using a 532 nm laser to excite the samples. The spectra represent averages taken over 50 spectra scanned across a line of 180 μm. In each case a number of well defined peaks are observed in the region of 150-450 cm^{-1}. Such peaks can be used to identify layered compounds by comparing to values in the literature, and are marked with arrows in

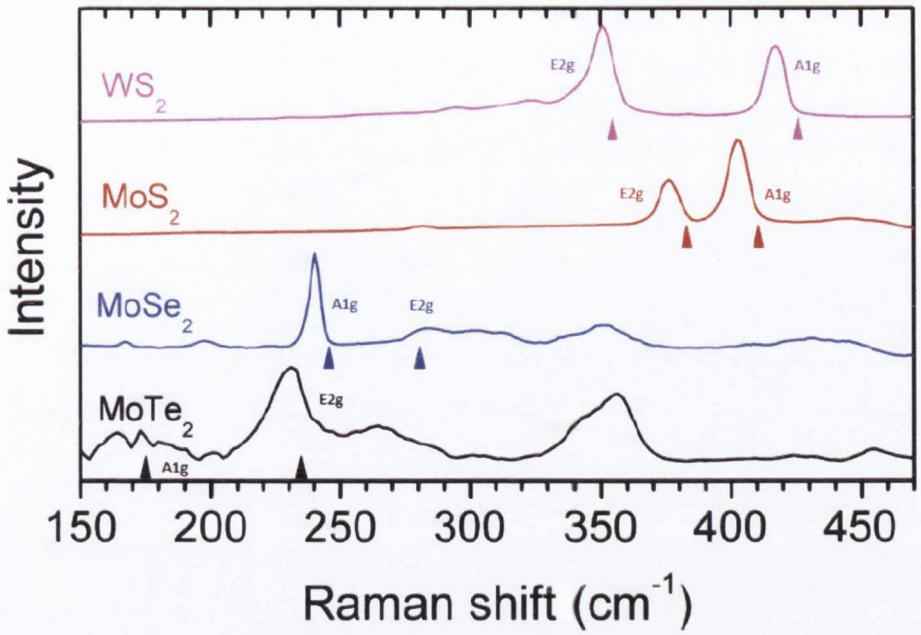

Figure 4.5: Raman spectra (λ_{ex}=532 nm) of films of each TMD. Arrows mark the positions of the main lines for bulk crystals of each material.

figure 4.5. All the spectra obtained here agree well with values obtained elsewhere in the literature.Tonndorf et al. [5], Lee et al. [39], Berkdemir et al. [40], Yamamoto et al. [44] However slight shifts are to be expected, the peak position being a function of layer number in MX_2 compounds, as the dispersions used to make these films contain a large degree of polydispersity.[39] Size selection protocols can be used to narrow the particle size distribution if required.Backes et al. [52]

4.4.2 *Dispersion Stability*

One of the best performing solvents for all materials, CHP, has been chosen to measure the stability of these dispersions. As mentioned in section 4.3 these dispersions were prepared using a small bath and sonic tip to ensure a sufficient degree of exfoliation. Stability was measured using a home built sedimentation apparatus. This apparatus measures the absorbance of a dispersion as a function of time using a succession of laser pulses. For each dispersion the subsequent plots are shown in figure 4.6. Some sedimentation exists in all cases, however after the first 100 hours, over 90% of the

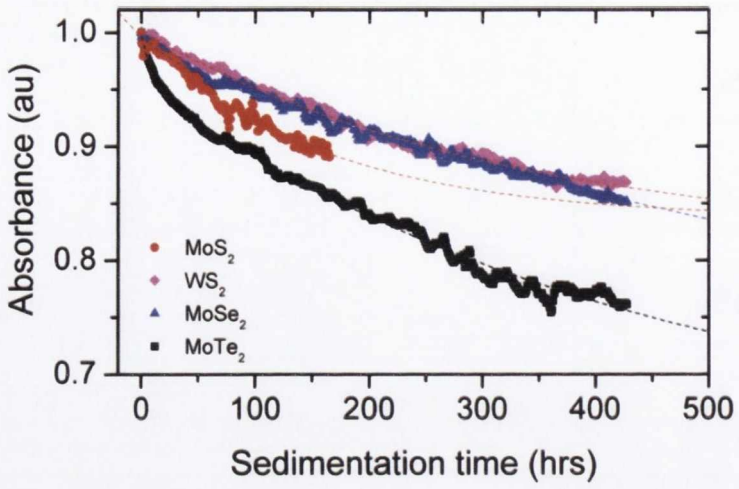

Figure 4.6: Sedimentation data for each of the four layered compounds dispersed in CHP. Dashed lines are fits to equation 4.14.

dispersed material is still stable. $MoTe_2$ appears considerably less stable then the other three materials tested. This is likely a symptom of the higher surface energy measured by IGC in section 4.4.4.

Theoretical analysis shows the concentration of a sedimenting phase can be fit by an exponential as a function of time.[207] The data in figure 4.6 can be fit by the sum of a constant, representing stably dispersed material and a number of exponential decays, each representing a specific type of sedimenting object.

$$A = A_0 + A_1 \exp\left(\frac{-t}{\tau_1}\right) + A_2 \exp\left(\frac{-t}{\tau_2}\right) \tag{4.14}$$

where A_0 represents the absorbance of the stable phase and A_1 & A_2 represent the initial absorbance of two sedimenting phases. For two of the samples there is only one sedimenting phase. Assuming the different phases have similar absorption coefficients A_0, A_1 & A_2 represent the relative populations of each phase. The quantities τ_1 and τ_2 represent sedimentation time constants of each sedimenting phase. Fits to the data are represented by the dashed line in figure 4.6. Fit constants are given in table 4.1.

In each case the first sedimenting phase had extremely small values of population (<5%) with very short time constants (<32 hours). This suggests sedimentation of relatively large objects or unexfoliated crystallites which were not removed on centrifugation.[179] The second sedimenting phase had values for A_2 between 16-36%

	A_0	A_1	τ_1 (h)	A_2	τ_2 (h)
MoS_2	0.84	0	NA	0.16	161
WS_2	0.81	0	NA	0.19	323
$MoSe_2$	0.62	0.02	32	0.36	977
$MoTe_2$	0.63	0.04	11	0.33	447

Table 4.1: Sedimentation fit parameters found from fitting the data in figure 4.6 using equation 4.14.

of the initially dispersed material with long time constants (>160 hours) implying much smaller objects. These results are consistent with analysis of the sediment for other liquid phase exfoliated layered materials,[55] which were also characterised by a combination of large particles similar in size to the starting material and small nanosheets similar to the stable exfoliated stock, consistent with two sedimenting phases. A small but positive $\triangle H_{Mix}$ implies these dispersions are metastable at best, although some metastable colloids can be stable for very long times.[3] Most importantly for applications, the stable dispersed phase (A_0) has values between 62-84%, meaning the majority of exfoliated material is stable for long time frames.

4.4.3 *Surface Energy*

Once confirmed that the dispersed material consists of exfoliated few layer nanosheets, we can consider the exfoliation mechanism and relate it to solution thermodynamics. The exfoliated material is typically hundreds of nm in width. As such we can assume the solvent-nanosheet interaction takes place primarily at the basal plane surface. This is understood via the enthalpy of mixing in terms of the surface energy based solubility parameters as in equation 4.13.[4] The maximum dispersed concentration (The dispersed nanosheet volume fraction is proportional to the concentration via the sheet density, $C = \rho\phi$) is obtained when solvent and nanosheet surface energies are well matched, minimizing $\triangle H_{Mix}$. So the maximum dispersed volume fraction can be expressed as[208]

$$\phi \propto \exp\left[-\frac{\bar{v}}{RT}\frac{\partial\left(\triangle H_{Mix}/V\right)}{\partial\phi}\right] \tag{4.15}$$

where $\bar{v}$ is the volume per mole of dispersed material and T the absolute temperature. Modelling the nanosheet as a high aspect ratio cylinder or disk of diameter D_{NS}, and subbing into equation 4.15 with equation 4.13 gives

$$\phi \propto \exp\left[-\frac{\pi D_{NS}^2}{2kT}\left(\sqrt{\gamma_S}-\sqrt{\gamma_{NS}}\right)^2\right] \tag{4.16}$$

This can be simplified using the expression $(x-a)^2 = 4a\left(\sqrt{x}-\sqrt{a}\right)^2$ when $x \approx a$ or when the fwhm is less than half the centre value of the Gaussian, as it is here. In terms of dispersed concentration then, one expects a Gaussian shaped peak as a function of solvent surface energy (via the surface tension).

$$C \propto \exp\left[-\frac{\pi D_{NS}^2}{8\gamma_{NS}kT}\left(\gamma_S-\gamma_{NS}\right)^2\right] \tag{4.17}$$

Such plots are shown in figure 4.7. Appreciable amounts of material are only dispersed for surface tensions ~40 mJ/m^2 which is very similar to the case for other van der Waals bound solids CNTs, h-BN & graphene.[2, 3]

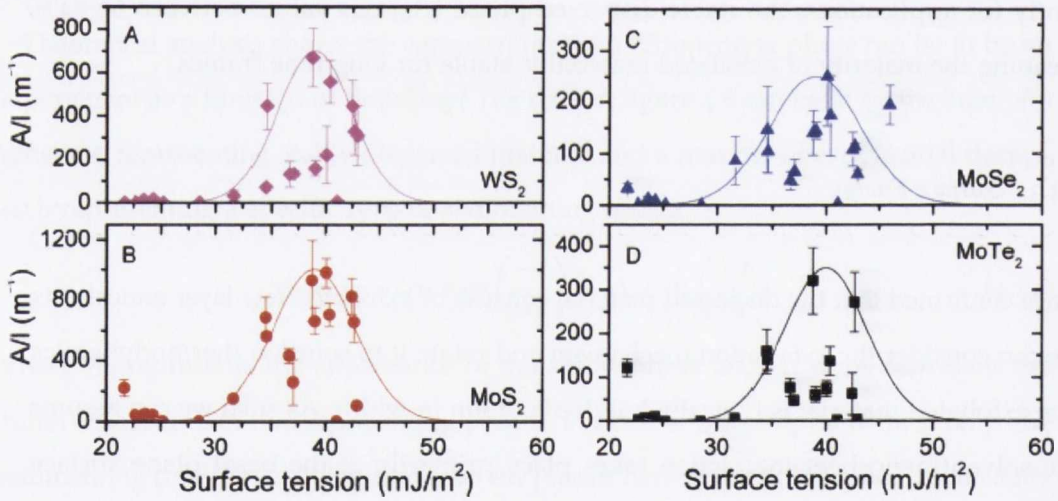

Figure 4.7: A/l (proportional to dispersed conc) for each TMD dispersed in a range of solvents plotted as a function of solvent surface tension, bound by Gaussian envelope functions.

For each material a Gaussian envelope function has been fitted using a trial and error approach, varying the peak position and width in steps of 0.25 until the corresponding best fit (highest R^2) is obtained on the log C versus χ curve as in figure 4.9. In each case,

a portion of solvents give dispersed concentrations significantly below the envelope. From the relation of the FWHM to nanosheet diameter, a value of ~5 nm can be calculated.

$$FWHM = \frac{1.6}{D_{NS}}\sqrt{\frac{8\gamma_{NS}kT}{\pi}} \tag{4.18}$$

Such an estimate is roughly 2 orders of magnitude smaller than the entities viewed with electron microscopy. For the sizes of the flakes viewed a fwhm of < 1 mJ/m^2 would seem more appropriate. The broadening noted here is not currently understood though it does suggest this analysis does not fully describe the solvent-nanosheet interactions present. In the case of nanotubes it has been suggested that entropic effects associated with the ordering of solvent molecules at the material-solvent interface can partly explain the discrepancy.[208] The entropy associated with the solvent molecules at the nanomaterial surface would have quite a different (lower) configurational entropy than those in the bulk of the solvent.

One further point to note is the lack of solvents with surface tension > 45 mJ/m^2. As such we cannot populate the right side of the graphs to a level which would reasonably demonstrate the fall off of concentration at high surface tension. Specifically $MoTe_2$ data has a large degree of scatter meaning it is not possible to confidently assign the position or width of the Gaussian envelope function for this material. It may well be the case that this dataset represents the low energy tail of a peak centred at higher surface energy.

The apparent peaks at ~70 mJ/m^2 suggest the model used here at least serves as a useful guide for choosing solvents for these TMDs. The fact that the peak positions are at similar values for each material suggests the surface energy and strength of interactions between the nanosheets varies only weakly with chalcogenide or transition metal atom species. For dispersion interactions the interaction strength is proportional to the square of the product of the polarizability and the atomic number density, $\alpha^2 (NV)^2$.[204] As α scales roughly with the atomic volume, this quantity is roughly constant and so relatively independent of the material being dispersed. For compound materials such as TMDs this is a gross oversimplification but constitutes an argument

that chemically dissimilar materials such as graphene, BN & TMDs all have similar surface energies and thus similar solvent choices for efficient exfoliation.

4.4.4 *Inverse Gas Chromatography & Computational Modelling*

In collaboration with this work (with Prof. Shane Bergin) inverse gas chromatography (IGC) has been performed to experimentally measure the surface energy of MoS_2, $MoSe_2$ & $MoTe_2$independently from solubility data. This technique is based on retention of organic vapours by a compacted powder of the solid. WS_2 was excluded from this part of the study as liquid N_2 adsorption measurements indicated a significant fraction of micro pores for this material, rendering IGC data analysis unreliable.

Whilst IGC is most suited to the dispersive component of the surface energy it can also be used to infer a value for the contributing non-dispersive interactions via the free energy of adsorption. Results from these experiments estimate total surface energy of MoS_2 & $MoSe_2$ to be very similar, ~75 mJ/m^2, whilst $MoTe_2$ is higher at ~120 mJ/m^2.

The values for MoS_2 & $MoSe_2$ are close to that inferred from solubility data, suggesting surface energy can be used as a valid solubility parameter to a first order approximation. The value for $MoTe_2$ is significantly higher however. As alluded to already, the peak in figure 4.7 may be an artefact of the fact that most common organic solvents have surface tensions < 45 mJ/m^2. In line with recent computer modelling,[209] the surface energy of $MoTe_2$ may well be higher than that of MoS_2 & $MoSe_2$. Te has a larger polarizability volume (0.96 nm^3) compared with S (0.73 nm^3) and Se (0.75 nm^3). Also, the interacting chalcogen sheets are packed more tightly in the tellurides, resulting in an increased attractive force across the van der Waals gap.[1] Finally, the Mo-Te bond is the longest of the three materials investigated here[23] and has the smallest difference in electronegativity (0.06), compared with the Mo-S (0.42) and Mo-Se (0.39) bonds.[210] One must also consider the possibility that a higher density of defects and or impurities may be present in the $MoTe_2$ powder, which would contribute high energy sites, increasing the measured surface energy. Indeed, Te rich surfaces are well known to be susceptible to oxidation.[211] A higher surface

energy would mean re-aggregation of nanosheets is more likely. This is reflected in the sedimentation data in figure 4.6 where the $MoTe_2$-CHP dispersion is confirmed to be considerably less stable than the other three materials investigated.

The apparent values for the surface energies of these layered materials of 70 mJ/m^2 is in conflict with values of 260 mJ/m^2 and 284 mJ/m^2 calculated computationally for the MoS_2 basal plane some years ago.[212, 213] More recent computer simulations using density functional theory (DFT) have been carried out in collaboration with this work (with Prof. Stefano Sanvito). The value obtained for the surface energy of MoS_2 ~180 mJ/m^2 is still a factor of 2 higher than the value suggested by the solubility data for surface energy. This may be in part due to these computations not taking into account screening by the surrounding solvent medium as they are carried out in a vacuum, rather than solvent medium.

4.4.5 *Traditional Solubility Parameters*

As we have seen, when concentration is plotted versus surface energy many samples have concentrations lower than expected from the envelope function. This is due to the surface energy being a crude solubility parameter. Hildebrand and Hansen solubility parameters of organic solvents are widely known and so it may be more useful to interpret the dispersed concentration in terms of traditional solubility parameters based on the cohesive energy density.

As van der Waals solids don't easily vaporize their solubility parameters must be inferred. By dispersing a material in a range of solvents and measuring the absorbance or concentration we can then use this as a weighting factor. This ensures successful solvents only contribute in proportion to their ability to exfoliate. The weighted average of the solvent solubility parameters then gives an approximate value for the nanomaterial's solubility parameters.

$$\{\delta_i\} = \frac{\sum_{solvent} C\delta_{i,sol}}{\sum_{solvent} C} \tag{4.19}$$

From similar arguments as for the case of surface energy, the dispersed nanosheet

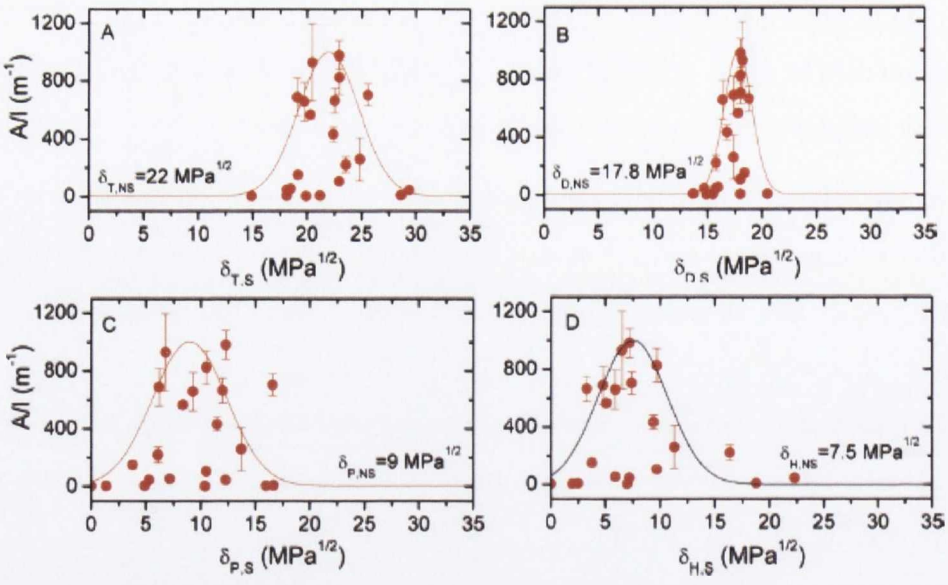

Figure 4.8: A/l for MoS_2 dispersed in a range of solvents as a function of Hildebrand (A) and Hansen (B-D) parameters. The fit is a Gaussian envelope function.

concentration should scale as a Gaussian with solvent Hildebrand parameter. For MoS_2 this is shown to be the case in figure 4.8 with a clear peak close to 22 $MPa^{1/2}$ bound by an envelope function. Again there are many points lying below this function. As the cohesive energy density consists of contributions from polar and H-bonding interactions as well as the dispersive component, Hansen parameters should also be tested. A/l is plotted against Hansen parameters for MoS_2 in figure 4.8 B-D. In each case peaks are manifest centred at 17.8, 9 and 7.5 $MPa^{1/2}$ for δ_D, δ_P, and δ_H respectively and the data are bound by Gaussian envelope functions. Similar results were obtained for the other materials and are included in table 4.2. For all plots there are still data points with concentrations below the envelope function. This is expected as equation 4.11 shows a given data point will only match the envelope function if the other two solubility parameters of solvent and nanosheet match also.

Interestingly the peak widths are smaller for the dispersive parameter graphs compared with the polar and H-bonding data. This bears a link with Hansen's inclusion of the factors of 1/4 in equation 4.11, which predicts polar and H-bonding peaks should be twice as wide as the dispersive peak. This is roughly what we see, justifying the introduction of the empirical factor of 1/4.

	$\delta_{T,NS}$ (MPa$^{1/2}$)	fwhm$_T$ (MPa$^{1/2}$)	$\delta_{D,NS}$ (MPa$^{1/2}$)	fwhm$_D$ (MPa$^{1/2}$)	$\delta_{P,NS}$ (MPa$^{1/2}$)	fwhm$_P$ (MPa$^{1/2}$)	$\delta_{H,NS}$ (MPa$^{1/2}$)	fwhm$_H$ (MPa$^{1/2}$)
WS_2	21.5	4.5	18	3.3	8	6.5	7.5	5
MoS_2	22	6.5	17.8	3	9	8	7.5	7.5
$MoSe_2$	22.5	6.5	17.8	2.5	8.5	8	6.5	6
$MoTe_2$	21	5	17.8	3.5	8	6	6.5	4.5

Table 4.2: Centers (δ) and widths (fhwm) for all Hildebrand and Hansen Parameter envelope functions (Found manually and subject to considerable error).

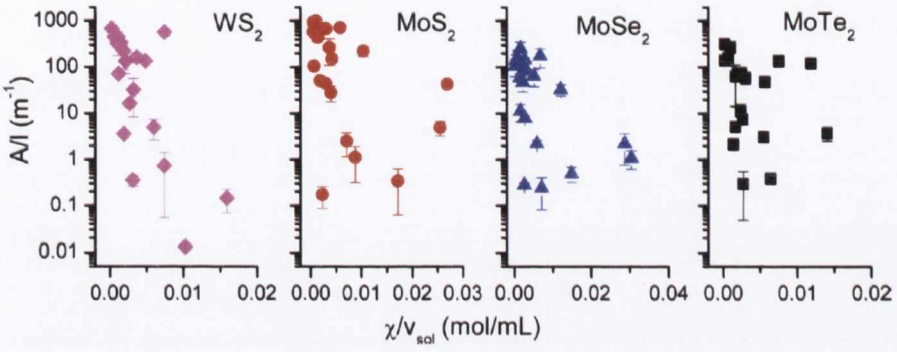

Figure 4.9: A/l for all four TMDs dispersed in a range of solvents plotted as a function of Flory-Huggins parameter divided by solvent molar volume. Solubility theory predicts linear bahaviour.

Now that we have values for δ_D, δ_P, and δ_H for the nanosheets we can calculate $\frac{\chi}{v_s}$ for each nanosheet-solvent combination. If solubility theory is a viable model to describe the interactions equation 4.11 predicts that $\frac{A}{l}$ should decay exponentially with $\frac{\chi}{v_s}$. Whilst there is considerable scatter, this general trend is shown in figure 4.9. Whilst solubility parameters based on surface energy and cohesive energy density describe the dispersion of nanosheets in solvents to first order or at least qualitatively, they do not fully describe the solvation mechanism. Nevertheless, the predictive power of such a method facilitates the discovery of many new working solvents for liquid phase exfoliation of low dimensional nanostructures.

4.5 CONCLUSIONS

A comprehensive study of the dispersability of MoS_2, $MoSe_2$, $MoTe_2$ & WS_2 in a range of solvents has been carried out. Relatively high concentrations (table 4.3) are only

obtained in solvents with surface energies close to 70 mJ/m^2 (surface tension close to 40 mJ/m^2), agreeing with solubility theory which predicts nanomaterials to be well dispersed in solvents with matching surface energy. We have also described the data in terms of Hildebrand and Hansen's traditional cohesive energy density based solubility parameters. In all cases the dispersed concentration falls off exponentially with the Flory-Huggins parameter, suggesting solubility theory can be used to understand the interactions between the solvent medium and nanosheets.

The solubility parameters of each material investigated are very similar (table 4.2), meaning the same set of solvents can be used to exfoliate each material. This is important from the perspective of applications requiring mixing such as conductive composites[53, 55] (with graphene or nanotubes) or bulk nano-heterojunction solar cells.[157–159]

A significant degree of scatter in the experimental data means the solubility theory used here is a good first order description and can give qualitative information on the dispersion of layered compounds. However, computational and IGC experimental data suggest specific solvent-solute interactions for nanostructures, that could aid or discourage solubility, are not accounted for in the theory.

4.6 APPENDIX

	WS_2		MoS_2		$MoSe_2$		$MoTe_2$	
	Solvent	A/l (m^{-1})	Solvent	A/l (m^{-1})	Solvent	A/l (m^{-1})	Solvent	A/l (m^{-1})
1	CHP	669	NMP	978	NMP	250	CHP	320
2	GBL	557	CHP	927	GBL	174	NVP	272
3	Cyclo-hexanone	444	DMEU	823	N8P	146	N8P	159
4	DMEU	444	GBL	701	Benzonitrile	144	Cyclo-hexanone	140
5	NVP	329	N8P	685	CHP	140	GBL	137
6	DMSO	309	Benzonitrile	661	NVP	114	IPA	121
7	NMP	221	NVP	655	DMEU	108	DMA	76.8
8	Benzonitrile	159	Cyclo-hexanone	561	Cyclo-hexanone	105	NMP	74.1
9	DMF	133	DMA	429	Benzyl Ether	86.1	DMEU	62.6
10	DMA	131	DMF	256	DMF	63.6	Benzonitrile	60.7
11	N8P	70.1	IPA	218	DMSO	59.6	DMF	47.9
12	Benzyl Ether	31.6	Benzyl Ether	149	DMA	46.6	H2O	14.3
13	Ethyl Acetate	15.9	DMSO	103	IPA	32.6	Ethyl Acetate	11.1
14	Chloro-naphthalene	4.88	Vinyl Acetate	50.0	Vinyl Acetate	11.1	Benzyl Ether	7.38
15	Vinyl Acetate	3.54	Ethyl Acetate	43.6	Ethyl Acetate	7.84	DMSO	5.11
16	H2O	1.91	Methanol	42.3	H2O	7.48	Methanol	3.87
17	Methanol	1.16	Chloro-naphthalene	2.44	Chloro-naphthalene	2.20	Hexane	3.78
18	Toluene	0.72	H2O	2.11	Methanol	1.08	Chloro-naphthalene	3.13
19	Acetone	0.35	Toluene	1.10	Hexane	0.50	Vinyl Acetate	2.16
20	Hexane	0.14	Hexane	0.34	Acetone	0.28	Toluene	0.39
21	IPA	0.01	Acetone	0.17	Toluene	0.24	Acetone	0.30

Table 4.3: A/l values measured for all TMDs in 21 solvents

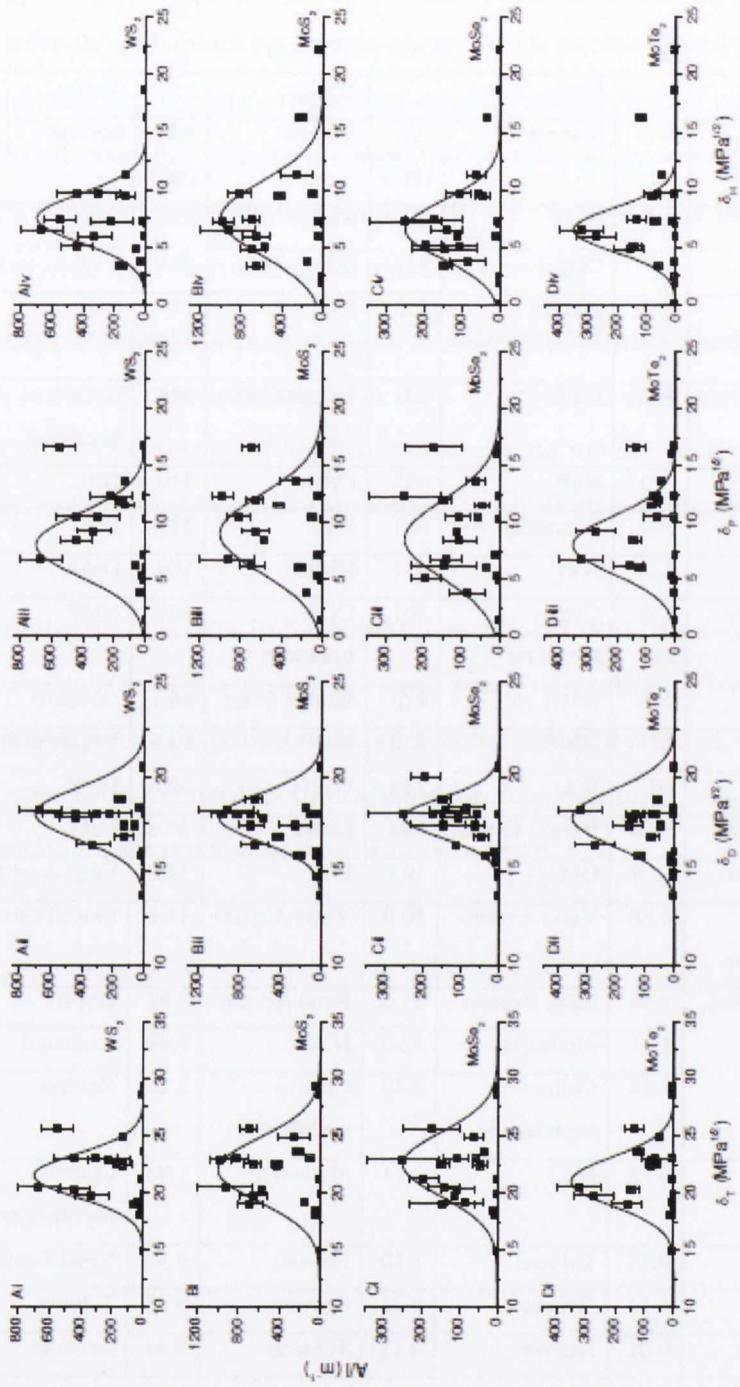

Figure 4.10: A/l for all four TMDs dispersed in a range of 21 solvents as a function of Hildebrand (T) and Hansen (D, P & H) parameters. The fits are Gaussian envelope functions.

5

PERCOLATION SCALING IN LIQUID PHASE EXFOLIATED HYBRID FILMS

5.1 INTRODUCTION

Once the nanosheets have been exfoliated in a liquid, normal solution processing techniques can be applied, making the formation of films straightforward.[2, 51] Such processes are quick, easy and insensitive to environmental conditions. However, films of these as-produced layered materials are unfortunately endowed with low electrical conductivity due to the large number of interflake junctions. This could potentially limit any intrinsically useful properties they possess. For example, transition metal oxides such as layered MnO_2[54] and MoO_3[55] show much promise as supercapacitor electrodes due to their high theoretical pseudo-capacitances and excellent cycle-life. Exfoliated MoS_2 has shown promise as a candidate for the anode material in lithium ion batteries due to its large reversible capacity, flexibility and stability.[124, 214–217] Bi_2Te_3 is known as an exceptional thermoelectric material at room temperature.[127] In practise, the low conductivity associated with these materials thus far has severely limited their development in these areas.

Fortunately, as layered compounds and carbon nanotubes[3, 218] may be exfoliated in the same set of solvents it is possible to produce composite dispersions (and so composite films) by simple mixing.[2, 51] This is a very straightforward yet powerful technique because it will allow the fabrication of a wide range of composite types through various combinations of components and compositions. Importantly, if nano-conductors such as nanotubes[219] or graphene[220] are added to insulators or semiconductors such as MoS_2, the resulting composite conductivity is potentially tuneable over a wide range. This has the potential to solve the conductivity problem

by preparing composites of a range of layered materials loaded with graphene or nanotubes.

When preparing such composites, it is critical to keep the nano-conductor content to a minimum. Most importantly, conducting fillers take up space and reduce the amount of active material present which can perturb the original properties of the matrix. This poses a significant problem for battery or supercapacitor electrodes.[54, 221] Secondly, some nanoconductors such as carbon nanotubes or metallic nanowires can be expensive (~$1000/g), making composites with high loading levels economically unattractive.

In this chapter, MoS_2 is used as a model compound to investigate how the conductivity of composites of layered materials embedded with both nanotubes and graphene scales with nano-conductor content. It is shown that these systems follow percolation theory and that conductivity as high as 40 S/m can be achieved for nanotube content as low as 4 vol%.

5.2 PERCOLATION

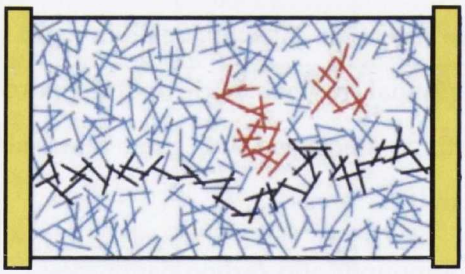

Figure 5.1: Network showing conducting backbone formed at φ_C (navy). Also shown are isolated clusters which do not span the network and result in dead ends (red). Adapted from [222]

Percolation theory is a mathematical model for connectivity and transport in complex systems. Its usefulness lies in the fact that a number of properties can be obtained from a couple of simple algebraic relationships when close to the critical threshold due to the principle of universality. Site and bond percolation models treat the space as

an infinitely sized grid with sites having occupation probability, p. Small occupation probability results in many isolated sites with occasional pairs of neighbouring sites both occupied, forming a cluster. Cluster size grows as p is increased, giving rise to a correlation length (radius of the largest cluster).[223] As the occupancy increases, more isolated clusters continue to grow and begin to coalesce. Once one cluster dominates and forms a connected path spanning the grid from one side to the other, the critical occupancy p_c has been reached. This is illustrated for the case of (navy) rods in figure 5.1. Above this connectivity increases, tending to a maximum at $p = 1$.[223]

Above this critical threshold the occupancy can be described by a simple power law; $P(p) \propto (p - p_c)^t$. This scaling and its critical exponent, t, exhibit universality (the threshold does not). Universality refers to being a function only of the dimensionality of the space. Herein lies the simplifying power of percolation theory, the details of the microstructure matter little as far as the connectivity is concerned. Therefore, there is no need to use a grid. A continuum, housing randomly arranged independent geometrical objects, where connectivity results from object overlap will suffice. Now instead of occupancy probability we work with volume fraction, i.e. the probability that a point chosen at random lies within one of conducting objects, to define the connectivity. In reality the system has finite size. Important length scales pertaining to this are the system size and correlation length. Once the system size is much larger than cluster size or correlation length the clusters are not affected by the finite boundaries and behave much like an infinite system.[224]

Our system consists of conductive fillers; 2D graphene flakes or 1D single wall carbon nanotubes (SWNTs), embedded in an insulating matrix of porous MoS_2 flakes. The flow of charge in a heterogeneous porous medium is predominantly controlled by connectivity i.e. conductivity and flow barriers. The conductivity of the network may then be described by electrical percolation, whereby at some critical volume fraction of conductive filler, there exists a conductive path spanning the network. This is characterised graphically as a sharp increase in conductivity over a small range of volume fraction once the percolation threshold has been reached.

5.3 SAMPLE PREPARATION

With both the conductive filler and insulating matrix being exfoliable in the same set of solvents, composite or hybrid films can be prepared through simple mixing once the dispersion concentrations are known. The sample preparation stages of composites are very important as they directly affect the network formation. Processing influences the materials' aspect ratios, which explicitly impact the percolation threshold. This is because of the associated increase in surface area with aspect ratio whereby more contacts can be made between conductive particles, increasing the connectivity. Thus it is necessary to form films in a timely manner, to minimize any re-aggregation of nanoconductor due to van der Waals forces at this crucial stage. Also, the degree of dispersion polydispersity can decrease or increase the percolation threshold depending on geometry and whether the dimensions making up the aspect ratio are coupled or not.[225]

5.3.1 *Dispersions*

We purchased powdered MoS_2, graphite and P3 single walled carbon nanotubes (SWNTs) from Fluka Analytics, Sigma Aldrich and Carbon Solutions Inc. respectively and used all as supplied.

5.3.1.1 *MoS_2 and Graphene Dispersions*

Typical MoS_2 and graphene dispersions were made as described previously.[2, 174] In both cases 100 mg of powder was added to 10 ml of N-Methyl Pyrrolidone (NMP) in a glass vial. These were sonicated in a Branson 1510E-MT sonic bath (20 kHz) for three hours followed by probe sonication (Vibracell, GEX750, 35%×750 W) for a further three hours. After standing overnight, the dispersions were centrifuged in a Hettich Mikro 22R at 1500 RPM (226 g) for 90 minutes. The top 6ml of each dispersion were then removed for further use.

5.3.1.2 *P3 Single Wall Carbon Nanotubes Dispersion*

The SWNT dispersion was prepared by adding 20 mg of starting powder to 10 ml of NMP in a glass vial. This sample was then bath sonicated for one hour, followed by 30 minutes probe sonication at 20% amplitude, followed by bath sonicated for one more hour. This sample was centrifuged at 5500 RPM for 90 minutes and the top 6 ml retained.

5.3.2 *Hybrid Dispersion Mixing and Composite Film Formation*

In each case the dispersed concentration was measured by filtration and weighing. Because all dispersions were made in the same solvent it was possible to blend these dispersions to make composite dispersions of any desired mass ratio. A series of MoS_2-graphene and MoS_2-SWNT blended dispersions were made with MoS_2 content spanning the entire range from 0% to 100%. These composite dispersions were diluted in isopropanol (IPA) and filtered through nitrocellulose membranes (25 nm pore size, Millipore) to give films of diameter 36 mm. The film thickness was close to 150 nm in all cases as verified by atomic force microscopy. This thickness is large enough to ensure the electrical conductivity is bulk-like and not controlled by thickness effects.[222, 226] TiAu electrodes (5&45 nm thick, spacing 60-70 μm, channel width 1 cm) were lithographically deposited onto SiO_2 (MoS_2-graphene) or glass (MoS_2-SWNT) substrates. Films were transferred onto electrodes by adhering the film to the substrate with IPA and exposing it to acetone vapour followed by washing in acetone baths to dissolve the remaining membrane.[185]

In order to convert mass fraction to volume fraction, bulk densities of graphene and SWNT were used (2200 and 1800 kg/m^3 respectively). The density of an MoS_2 only film was measured to be 1925 kg/m^3 (as opposed to 5000 kg/m^3 in bulk, film porosity ~40%) by preparing a number of thick films by filtration and carefully measuring their mass and dimensions. This value is considerably lower than that appropriate for an MoS_2 crystal, due to the free volume found in disordered networks of nanostructures. We consider the composites to consist of the nanocarbons embedded in a porous MoS_2

matrix (density 1925 kg/m^3). In this scenario, the matrix volume is the sum of free volume and the MoS_2 volume.

5.4 RESULTS

5.4.1 *Film Morphologies*

The composite films were characterised using scanning electron microscopy (SEM, Zeiss Ultra Plus). In general, the films appeared uniform when viewed over a large area. Typical images for both types of composites are shown in figure 5.2. Graphene-

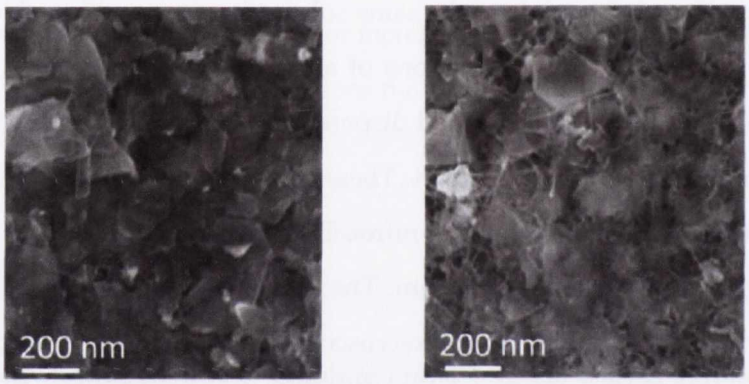

Figure 5.2: SEM images of the surface of 150 nm thin films of (left) an MoS_2-graphene (85:15 by weight) and (right) MoS_2-SWNT (90:10 by weight).

MoS_2 composite films consist of a disordered array of flakes with graphene and MoS_2 indistinguishable from each other. For the SWNT-MoS_2 films, the flakes of MoS_2 appear embedded within a SWNT network.

5.4.2 *Raman Spectroscopy and Elemental Mapping*

Scanning Raman spectroscopy has been used to assess the uniformity of the composite films. Graphene and nanotubes are strongly Raman active materials due to delocalised pi bonds which are easily polarized. Moreover, the linear dispersion relation for these

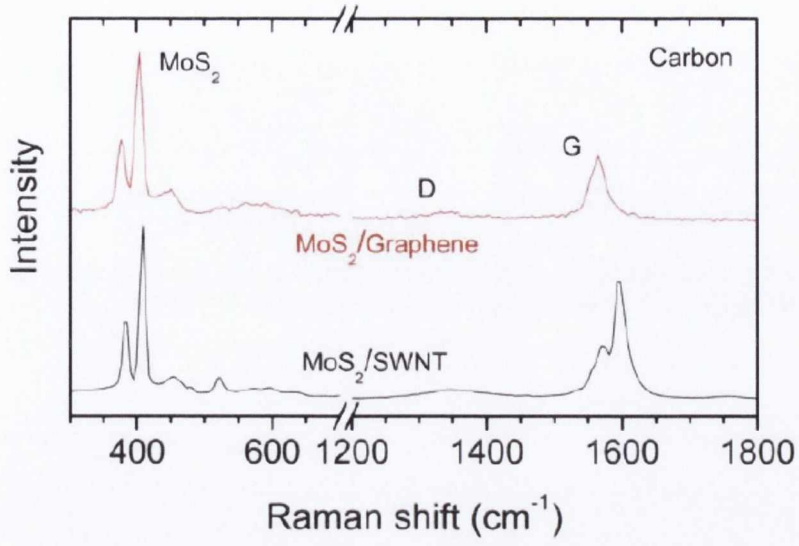

Figure 5.3: Raman spectra for MoS_2-graphene (80:20 by weight) and MoS_2-SWNT (95:5 by weight) films. In each case the spectra are averages over 50 spectra taken along a line scan of 180 μm in length.

materials ensures the Raman process is resonant at all wavelengths in the case of graphene.[34] Thus its signal is much enhanced compared to that of MoS_2 meaning only spectra for low volume % graphene and SWNT composite films were used for this purpose.

Characteristic Raman spectra are shown in figure 5.3 for both types of composite films produced. Clearly present are the E^1_{2g} (~383 cm^{-1}) and A_{1g} (~409 cm^{-1}) modes of MoS_2 [39] and the characteristic G band (1580 cm^{-1}) of carbon based materials.[227, 228] The D bands are hardly observable due to the quality of both SWNTs and exfoliated graphene. Elemental Raman maps of local areas of the films were obtained by measuring the ratio of the MoS_2 A_{1g} peak intensity to that of the carbon G band. These are shown in figure 5.4 for graphene and SWNT based films respectively. Both composite types show relatively good uniformity down to length scales of a few μm i.e. close to the size scale expected for exfoliated nanosheets.[2, 4, 174, 181]

The hybrid film uniformity can be assessed quantitatively by assuming that the Raman intensity for a mode associated with a given material is proportional to the

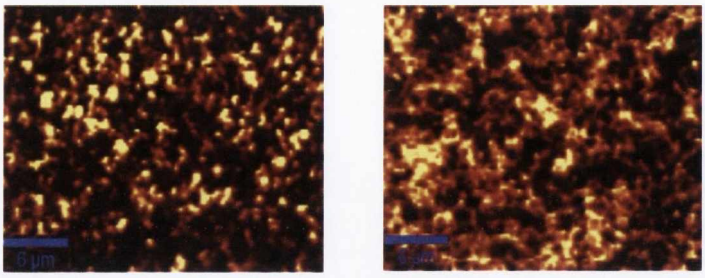

Figure 5.4: Raman maps measured on a grid of 120 x 120 points over an area of 30 μm x 30 μm for MoS_2-graphene (90:10 by weight) and MoS_2-SWNT (90:10 by weight) films. Represented by plotting the intensity ratio of the $A_{1g}MoS_2$ to carbon G-band.

mass that material under the beam. Combining this with the definition of the mass fraction of carbon (i.e. SWNT or graphene),

$$M_f = \frac{M_C}{M_C + M_{MoS2}} \tag{5.1}$$

it can be shown the ratio of MoS_2 to carbon Raman intensity is given by

$$\frac{I_{MoS2}}{I_C} \propto \frac{1}{M_f} - 1 \tag{5.2}$$

assuming spatial uniformity. The ratio of MoS_2 to carbon Raman intensity, (averaged over 15,000 measurements taken over a local area of ~0.5 × 0.5 mm) versus $M_f^{-1} - 1$ is plotted in figure 5.5 for both composite types. Very good linearity is found for the MoS_2-SWNT composite films showing them to be spatially well uniform. However, while still linear, the data for the MoS_2-graphene composite films was relatively scattered suggesting them to be slightly less spatially uniform.

5.4.3 *Current-Voltage Characteristics*

The electrical properties of these composites have been measured using a Karl Suss probe station and a Keithley 2400 source meter controlled by a LabView program. I-V curves are plotted for a range of MoS_2-graphene and MoS_2-SWNT composites from 0%-100% carbon content in figures 5.6 and 5.7 respectively. In both cases, the

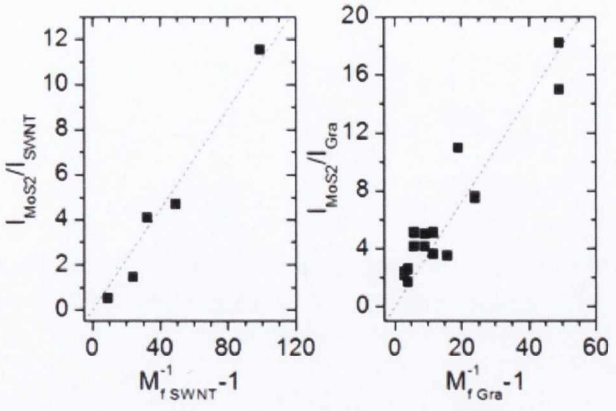

Figure 5.5: Plot of the ratio of intensity of MoS_2 to carbon peaks versus $M_{f\text{-}carbon}^{-1}$-1. This plot is expected to be linear for a uniformly deposited film.

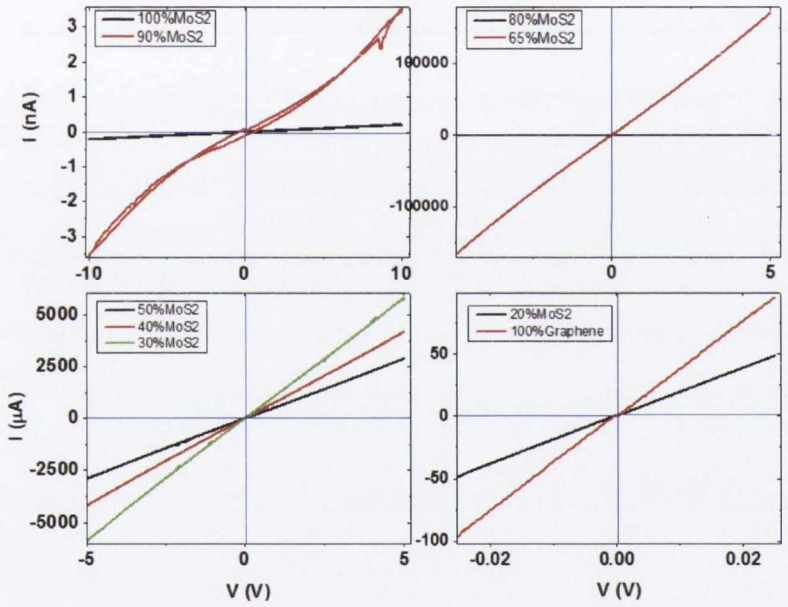

Figure 5.6: I-V curves showing the evolution of the films electrical characteristics as the conductive content is increased from 0%-100% graphene. Once the system has percolated the conduction is dominated by the conductor and so linear I-V's with no hysteresis are obtained.

I-V's become progressively linear and demonstrate reduced hysteresis between up and down sweeps, up to the percolation threshold. Once the threshold has been reached and the first conducting backbone spans the network, conduction is governed by the

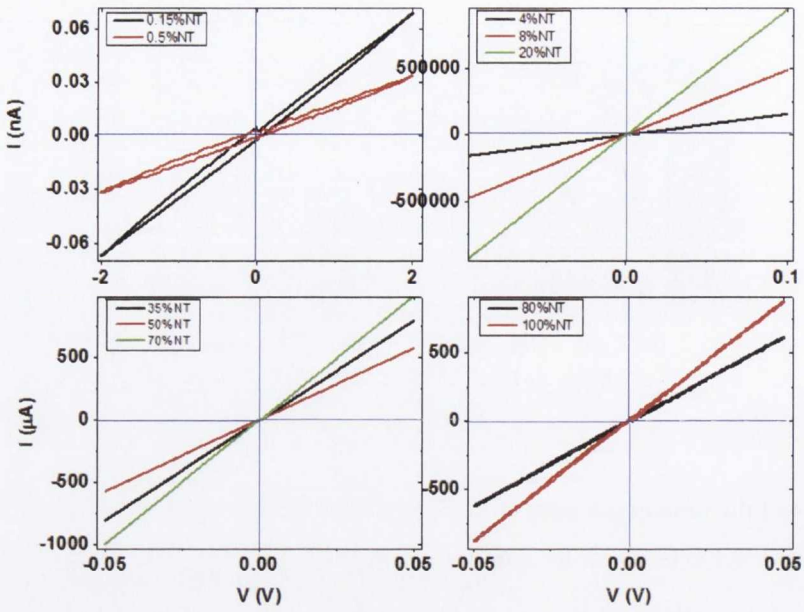

Figure 5.7: I-V curves similar to figure 5.6 but for SWNT-MoS_2 composites with the conductive content again varied from 0%-100% SWNTs. The percolation threshold for this system is much lower (~2.5%) due to the higher aspect ratio of the SWNTs compared with graphene.

conductor rather than the MoS_2 network and perfectly linear I-V curves are obtained. The hysteresis noted between the down and up sweeps of the I-V's when below the percolation threshold is most likely due to trap filling effects.[229] Traps that are filled on the up sweep take time to be freed and remain full on the downward sweep, allowing increased current at an equivalent voltage.

5.4.4 *DC Conductivity and Electrical Percolation*

The DC conductivity was measured for all films from the I-V curves and plotted as a function of volume fraction of the conductive carbon component, φ, in figure 5.8. For each composite type, the conductivity increased from 6×10^{-7} S/m for the MoS_2 only film to 103 S/m and 670 S/m for the graphene-only and SWNT-only films respectively. For each composite type, the conductivity increased dramatically over a narrow range

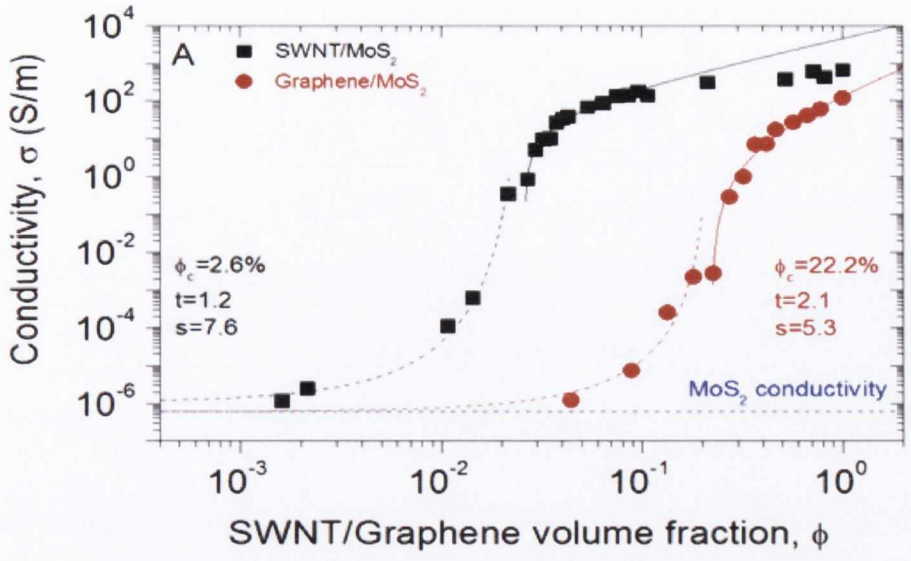

Figure 5.8: Graph of conductivity versus carbon volume fraction for the composites studied.

of volume fraction; ~1-3 vol% and 15-30 vol% for MoS_2-SWNT and MoS_2-graphene composites respectively.

Composite	ϕ_c	t	s	σ_C (S m^{-1})	σ_{MoS_2} (S m^{-1})
MoS_2–SWNT	2.6%	1.2	7.6	4530	8.8×10^{-7}
MoS_2–graphene	22.2%	2.1	5.3	129	6.0×10^{-7}

Table 5.1: Percolation fit parameters: ϕ_c is the critical volume fraction or percolation threshold, t is the universal exponenet above the threshold whereas s is the exponent below the threshold, σ_C and σ_{MoS_2} denote the conductivities of the oure conductive and insulating phases respectively.

5.4.4.1 *Above Percolation Threshold ($\phi > \phi_c$)*

Such a steep increase in conductivity over a narrow range of volume fraction is behaviour consistent with percolation effects. When an electrically conducting filler is added to an insulating matrix, significant increases in conductivity can only occur once the first conducting path through the sample is formed. The volume fraction of filler

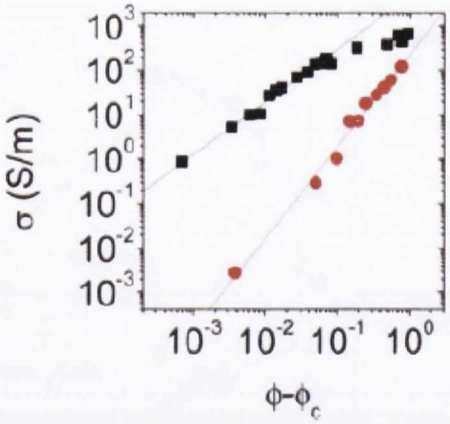

Figure 5.9: Conductivity plotted as a function of (φ-φ_c) for both types of composite films above percolation. These datasets have been fit to equation 5.3.[53]

where this occurs is known as the percolation threshold, ϕ_c. Above the percolation threshold the conductivity scales as[223, 230]

$$\sigma_{DC} = \sigma_C \left(\frac{\phi - \phi_c}{1 - \phi_c} \right)^t \tag{5.3}$$

where σ_C is nominally the conductivity of a film of the conducting filler alone and t is the percolation exponent. Percolation theory has been applied to mixtures of graphite in a hexagonal boron nitride matrix.[230, 231] However, these composites were prepared by pressing mixtures of unexfoliated graphite and boron nitride powders into discs. The work described in this chapter represents the first example of percolation studies of an exfoliated nanosheet filler in a matrix of exfoliated nanosheets.

The data has been analysed for both composite types in terms of equation 5.3 as shown in figure 5.9. While the data for the MoS_2-graphene composites follows equation 5.3 extremely well over the entire range, the MoS_2-SWNT composites only follow the percolation scaling law for volume fractions close to the percolation threshold. From the fits, we find the percolation thresholds to be $\phi_c = 2.6$ vol% and $\phi_c = 22.2$ vol% for the MoS_2-SWNT and MoS_2-graphene composites respectively (all fit constants are given in table 5.1).

For both 1- and 2-dimensional fillers in three dimensional composites, the percolation threshold is generally thought to be close to the ratio of smallest to largest

dimension.[232] Thus, the value of ϕ_c found for the MoS_2-SWNT system is typical of what is generally found[233] and is consistent with nanotube bundle diameters of ~10 nm coupled with lengths of ~μm.

5.4.4.2 *The Percolation Threshold ϕ_c*

The value of ϕ_c observed for the MoS_2-graphene system is much larger than values previously reported for 3-dimensional composites with graphene as a filler (~1 vol%).[234] In addition, it is much smaller than the fixed percolation threshold of ~67% expected for 2-dimensional composites with mutually penetrable planar fillers.[235] However, the result here is consistent with recent theoretical predictions that, for composites of randomly oriented, monodisperse conducting discs in an insulating matrix, the percolation threshold is actually independent of disk diameter.[225] This work suggests ϕ_c to scale only with disk thickness, a, as $\phi_c = \frac{2a}{\lambda(5\pi+6)}$, where λ is the hopping distance. This equation should apply in the limit where λ and a are both very much smaller than the width of the disks, as is the case here. Taking $a = 1$ nm and $\phi_c = 22.2$ vol%, gives a value of $\lambda \approx 0.4$ nm, which seems reasonable. Applying the same theory to perfectly parallel disks (in the limit of very large aspect), which arguably is more realistic for our type of system, gives a similar result: $\phi_c = a/8\lambda$, in which case $\lambda \approx 0.6$ nm.

Hard extended objects have an excluded volume, which cannot be penetrated by the centre of mass of a similar object without contacting each other.[236] Excluded volume models assume an infinite aspect ratio for filler particles.[225] The percolation threshold is now instead a function of this excluded volume, rather than the aspect ratio. Thus it is expected to increase. Using a core-shell approximation, particles may only overlap within a penetrable shell volume, defined by λ. Despite assuming monodispersity, volume exclusion models match experimental values for the percolation threshold well when large aspect ratio filler particles are used.[237]

In addition, the percolation exponents were observed to be $t = 1.2$ and $t = 2.1$ for the MoS_2-SWNT and MoS_2-graphene composite networks respectively. The former value is close to the universal exponent of $t = 1.33$[223] expected for 2-dimensional composite networks and consistent with a number of nanotube containing composites.[233]

However, the graphene exponent is considerably higher and close to the universal exponent of $t = 2.0$,[223] expected for 3-dimensional composite networks. Values of $t > 2$ have been observed previously in graphene-polystyrene composites.[234, 238] Here they are accounted for by a distribution in the junction resistances, whereby the problem is no longer a pure site one but also partially a bond one.[230] In this case the exponent consists of the universal exponent and a non-universal part which depends specifically on the details of the system. However, the matrix here is not a polymer, which would coat the graphene flakes and strongly affect the tunnel barriers between them. The SWNT data deviates from the percolation scaling law for $\phi > 0.1$. Above this volume fraction the data fits an empirical scaling law of the type $\sigma \propto \phi^m$ where $m = 0.6$. Indeed it is known that the scaling relation (equation 5.3) often does not hold far away from ϕ_c.[225]

5.4.4.3 *Below Percolation Threshold ($\phi < \phi_c$)*

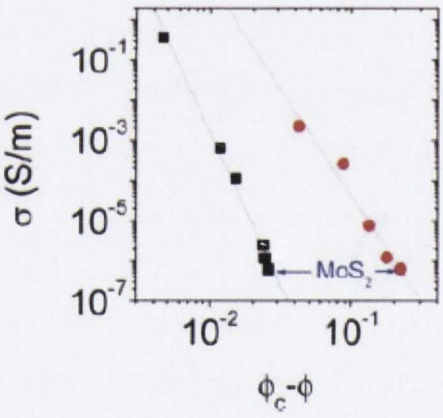

Figure 5.10: Conductivity plotted as a function of (φ_c-φ) for both types of composite films below percolation. These datasets have been fit to equation 5.4.[53]

The DC conductivity below the percolation threshold is also described by a scaling law:[223, 239]

$$\sigma_{DC} = \sigma_{MoS2} \left(\frac{\phi_c - \phi}{\phi_c} \right)^{-s} \tag{5.4}$$

where σ_{MoS_2} is the conductivity of the matrix and s is a second percolation exponent. This equation has been fit to the data for both composites as shown in figure 5.10

obtaining values of $s = 7.6$ and $s = 5.3$ for the MoS_2-SWNT and MoS_2-graphene composites respectively. These are extremely high values. While there is little experimental data available, previous reports have clustered close to the predicted value of $s = 1$.[230, 240–242] It is unclear why the values found here are so high.

It is worth noting that although the degree of exfoliation currently achievable by the methods used here is very good, it is not perfect. Both MoS_2 and graphene are expected to be present as thin multilayer flakes rather than monolayers while the nanotubes are present as bundles rather than individual SWNTs. Future work will no doubt lead to improvements in the exfoliation state of all components. For the graphene and SWNTs (i.e. the conducting filler), improvements in degree of exfoliation should result in reduction in percolation threshold and so significant increases in conductivity at lower filler content. However, it is less clear as to the effect of MoS_2 (i.e. the matrix) exfoliation state on the film properties. It has been suggested that the exponent s seems sensitive to details of the network microstructure even more so than the percolation threshold. This has been studied for the pressed disks of graphite and boron nitride. Powders poured by different methods resulted in similar values for the percolation threshold. However, a large spread in s values was found. Whilst s is sensitive, t remains universal and does not depend on microstructure, only on dimension.[230] In addition we must consider that our insulating matrix material, MoS_2, is not fully insulating and some conduction can occur via hopping below the percolation threshold.

5.5 DISCUSSION

Conductivity percolation has been widely studied experimentally for nanotube-polymer composites.[233] Theoretically such systems have also been studied though usually with the limitation of modelling the flexible nanotubes as rigid rods. This means there is a lot of data which one can compare to. Due to it being relatively new, much less experimental[234] and theoretical[238] published work exists for graphene. Given that there is a large body of literature on the conductivity percolation problem it may prove

helpful in gaining a deeper understanding of certain issues in our novel, exfoliated composite system.

5.5.0.4 *Decreased conductivity of NTs far away from ϕ_c*

The SWNT-MoS_2data deviates from equation 5.3 for volume fractions far above ϕ_c as in figure 5.8. Though the scaling relation is only strictly expected to hold close to the threshold, it holds over the whole range for the graphene-MoS_2composites. A number of factors could be at play and deserve further consideration.

1. The conductivity of nanotube networks is known to be a strong function of the tube dimensions, increasing with average tube length as $L_{av}{}^{1.46}$.[243] Sonication has been used here so the SWNTs in the dispersion used may be skewed toward shorter lengths due to scission.[176]

2. The SWNTs used in this work (P3) are functionalised to aid their dispersion in common solvents. Whilst this may assist in lowering the percolation threshold, functionalisation of NTs can disrupt the pi-conjugation, leading to reduced conductivity.[244]

3. Though a function of bundle diameter (SWNTs) or flake thickness (graphene), inter-conductor junctions in SWNT networks are usually at least an order of magnitude more resistive than in graphene networks. Acid treatment could be used to decrease the junction resistances.[245, 246]

4. It is well known that only ~1/3 of SWNTs in any given batch are metallic. Semiconducting SWNTs will increase the percolation threshold in proportion to their abundance, as non-conducting species may act as dead ends in the network. The effect is not as pronounced as one may expect as semiconducting tubes in dead ends do not contribute.[225]

5. The alignment of SWNTs has a strong effect on ϕ_c. However it also impacts the network conductivity.[232] Partial alignment should help whereas lower than expected conductivities are expected for highly aligned networks due to the reduced number of tube-tube contacts.[244]

5.5.0.5 *High percolation threshold for graphene composites*

Whilst the core-shell excluded volume model used may justify the high percolation threshold observed for the graphene-MoS_2 composites, a number of other potential reasons may also exist.

1. As assessed by Raman spectroscopy in figure 5.5, the graphene-MoS_2 composites are much less uniform. This points toward some re-aggregation of graphene flakes either in the dispersion on blending and/or on film formation. Whilst they can be dispersed in the same set of solvents, the surface energy of graphene may be slightly different to that for MoS_2,[213] meaning they will prefer to bind to each other. Re-aggregation on film formation will also decrease the number of graphene-graphene contacts resulting in a lower than expected conductivity,[247] which we also observe.

2. Partial alignment of graphene sheets could increase the percolation threshold. However with exfoliated sheets typically ~1 μm wide and only a couple of nm thick they are expected them to align themselves parallel with the substrate as observed previously.[248] This is because in the limit of very large aspect, the angular freedom of the disks is much reduced due to the excluded volume.[225]

3. In the core-shell model, the percolation threshold of rod-like particles is found to depend only on the higher order moments of the size distribution, with a similar result for spherical particles. This likely means it also holds for disk shaped particles.[225, 249] Sonication induced scission of low dimensional nanostructures has been well established to occur.[55, 174–176] The scission energy scales with the number of bonds that must be broken, i.e. the cross-sectional area. This effect is undesirable as it not only positively skews the length distribution towards shorter lengths but is also responsible for a degree of coupling between normally independent dimensions (length and thickness for flakes, length and diameter for tubes). This introduces a conflict of interests when trying to minimise the percolation threshold and leads to it actually increasing for a polydisperse mixture. This is because for a given energy input, long tubes are easier to break

than wide ones[225] and large crystallites result in fewer, thicker nanosheets compared with small crystallites which give more, thinner nanosheets.[55] It is not the polydispersity itself which leads to the increase in ϕ_c, only if there is this dimensional coupling. As one can see looking at figure 5.11, if one had long,

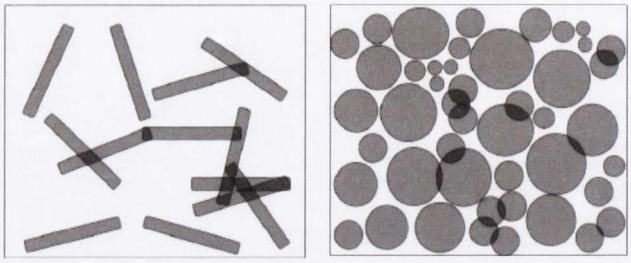

Figure 5.11: Effects of local heterogeneity on percolation in random microstructures. Percolating cluster of rods (left), longer rods would contribute disproportionately, lowering ϕ_c. Percolating system of polydisperse spheres, presence of small spheres bridge free volume between two larger spheres, increasing packing density and so lowering ϕ_c.[250]

thin tubes, the effect of polydispersity would then decrease φ_c as longer rods contribute more to a growing network than short ones. Similarly for spheres, small spheres can bridge gaps of free volume between larger spheres.[250]

5.5.0.6 *Variance in ϕ_c for SWNT-polymer composites in the literature*

The large body of work that exists for SWNT-polymer composites allows comparison of universal exponents as well as non-universal percolation thresholds. On contemplation, the large spread in values observed for ϕ_c is almost obvious.

In reality the system always has a finite size. Once the system size is much larger than the cluster size or correlation length then clusters don't notice the finite system boundaries, and behave much like an infinite system. The correlation length in the SWNT-based composites is likely larger than that for the graphene-based composites. This will lead to a degree of scatter in the conductivity datasets as one is only able to sample from distribution of possible configurations. This can be visualised with the aid of the illustration in figure 5.12.

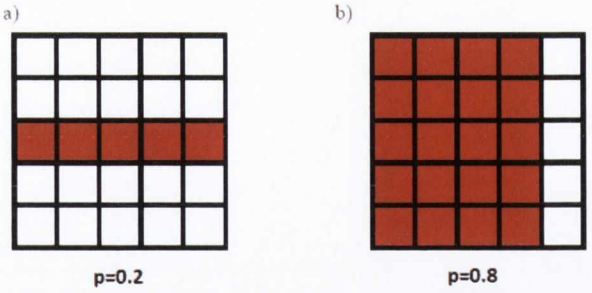

Figure 5.12: Percolation only exists once the first conducting pathway through the medium is formed and is based on probability. This may describe the large degree of scatter seen in the case of the percolation curve for SWNT-MoS_2 composites in figure 5.13. Different configurations of connectivity may exist at a given loading level due to the finite system size. An extreme case of this is shown here, where a) has percolated whereas b) has not even though it has a much higher loading. Adapted from [224]

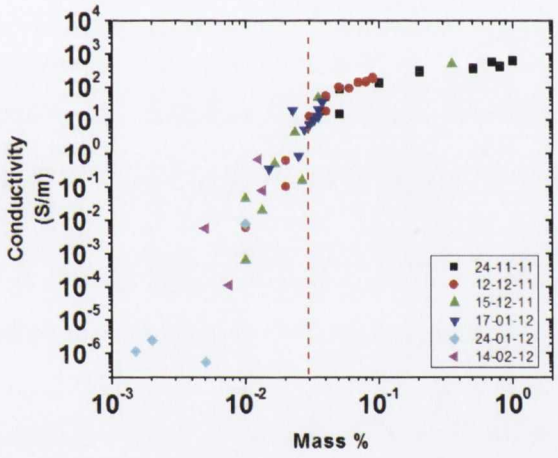

Figure 5.13: Percolation graph showing scatter found around threshold in SWNT-MoS_2system. The dates in the legend refer to the dates the composites were electrically tested. All films are from the same dispersion and film set but sampled from different regions across the vacuum filtered master-film on porous membrane. Such a degree of scatter is put down to the larger correlation length of nanotubes versus graphene sheets, meaning they feel the finite size of the system more and only a distribution of connectivity is being sampled each time a film is made. Electrical measurements were carried out using a Karl Suss probe station and a Keithley 2400 source meter controlled by a LabView program.

As is shown in figure 5.13 for the SWNT based composites, a large degree of scatter was found in the data close to the percolation threshold. At exactly the same occupancy, slightly differently connected clusters may manifest as in the illustration in figure 5.12. This is why simulations use many more runs for calculating the conductivity close to the critical volume fraction, to offset the higher sample-sample variation in conductivity in this region.[238] If the system size increased towards infinity, such scatter would reduce, regressing to a smooth plot for an infinite system.[224]

So the combined effects of size and connectivity variations between differently processed nanotube composites explains in part the large variance in percolation thresholds seen, even for systems with similar mean aspect ratio.

5.6 CONCLUSIONS

Thin film composites of both SWNTs and exfoliated graphene nanosheets (the conducting nanofiller) in a matrix of exfoliated MoS_2 nanosheets have been prepared. A combination of scanning electron microscopy and Raman spectroscopy showed the mixtures to be uniform to a length-scale of ~microns. Electrical measurements showed an increase in conductivity of up to ~9 orders of magnitude on addition of nanoconductors. In both cases, the conductivity obeyed percolation scaling laws both above and below the percolation threshold. The percolation thresholds were $\phi_c = 2.6$ vol% and $\phi_c = 22.2$ vol% for the MoS_2-SWNT and MoS_2-graphene composites respectively.

For the SWNT filled composites, this low percolation threshold means that conductivities as high as ~40 S/m for volume fractions as low as ~4 vol% are realisable. Similar results are expected to be found for other exfoliated layered compounds filled with nanoconductors. Such materials will be important in a range of applications from thermoelectric devices to electrodes in batteries and supercapacitors.

This work represents the first detailed study of such 2D–2D and 1D–2D composites. Further work is required to understand the role of the matrix nanostructure in determining the performance of such composites. From a thermoelectric standpoint it would be interesting to investigate how the thermal conductivity scales with filler

volume fraction in these systems as well as systems using Bi_2Te_3 nanosheets as the matrix.

6

PHOTOCONDUCTIVITY OF SOLUTION PROCESSED SEMICONDUCTING FILMS

6.1 INTRODUCTION

Photoconductivity may serve as a probe to study fundamental loss mechanisms associated with trapping and recombination present within a material. An understanding of these processes and their origin is useful in improving solar cell efficiencies. Recombination processes can be studied by measuring the photocurrent as a function of both time and light intensity. When the sample is not pure and highly crystalline localised states stemming from defects and disorder can trap free carriers. These behave as recombination centres for minority carriers, decreasing their lifetime.[251] Such non-radiative recombination retards both open circuit voltage and short circuit current, substantially decreasing the deliverable power output of the cell.

6.1.1 *Photoconductivity*

Light incident on a semiconducting material with energy sufficient to promote carriers into the conduction band (CB) will result in photon absorption. In the absence of reflection losses, the process of optical absorption can be described through the wavelength dependent absorption co-efficient, α, using Beer's Law

$$I = I_0 \exp(-\alpha x) \tag{6.1}$$

I_0 is the incident light intensity on a sample of thickness x. Absorption is intrinsic (i.e. band to band) in the case of a pure crystalline material and can be either direct or indirect depending on the nature of the bandgap. This will result in excitation of an electron into the CB, leaving a hole in the valence band (VB) and so an electron-hole

pair is formed. Direct gap materials absorb a large portion of light at the surface whereas light penetrates much deeper into indirect gap materials. When there is a degree of disorder/defects present extrinsic absorption into and out of the ensuing localised states can also occur depending on the optical cross-section.[252]

Under the influence of an applied field the excited charge carriers take part in transport and boost the conductivity. This light induced change in conductivity is known as photoconductivity.[252, 253]

$$\sigma_0 = q\left(n_0\mu_{n0} + p_0\mu_{p0}\right) = \sigma_{Dark} \tag{6.2}$$

$$\triangle\sigma = q\left(\triangle n\mu_n + \triangle p\mu_p\right) = \sigma_{PC} \tag{6.3}$$

$$\sigma_{Light} = \sigma_{Dark} + \sigma_{PC} \tag{6.4}$$

Usually it is dominated by one type of carrier, simplifying the analysis. In polycrystalline media, photo-excitation can also change the carrier mobility,[253] in which case

$$\sigma_{Light} = (n_0 + \triangle n)\, q\,(\mu_0 + \triangle\mu) \tag{6.5}$$

and

$$\sigma_{PC} = q\mu_0\triangle n + (n_0 + \triangle n)\, q\triangle\mu \tag{6.6}$$

The continuity equation for electrons (and similarly for holes) reads

$$\frac{\partial n}{\partial t} = G - \sum_i \left[n\beta_i\left(N_i - n_i\right)\right] + \sum_i \left\{n_i N_C \beta_i \exp\left[-\left(\frac{E_C - E_i}{kT}\right)\right]\right\} + \frac{\nabla \cdot J_n}{q} \tag{6.7}$$

where G equals the generation rate (units of $m^{-3}s^{-1}$), the second term on the right represents trapping of free electrons due to localised states and the third term represents de-trapping. N_i is the total density of the i^{th} localised state, n_i is the density of the electron occupied i^{th} localised state, β_i is the capture co-efficient of the i^{th} localised state for free electrons and $(E_C - E_i)$ is the ionisation energy of the i^{th} localised state. Additionally the current density for electrons is defined as

$$J_n = nq\mu_n E + qD_n\nabla n \tag{6.8}$$

where the first term on the right is due to drift, E is the electric field and the second term due is to diffusion with D_n the diffusion co-efficient. Finally Poisson's Equation is used to determine the net space charge in the material

$$\nabla \cdot E = \frac{Q}{\epsilon_r \epsilon_0} \tag{6.9}$$

Combining equations 6.8 and 6.9 and subbing into equation 6.7 can be simplified by the following three assumptions:

1. Assume charge neutrality, $Q = 0$
2. Neglect diffusion in bulk, $\nabla n = \nabla p$
3. Replace the trapping and de-trapping terms with $\frac{-n}{\tau_n}$ where τ_n is an appropriately defined lifetime.

At steady state ($\frac{\partial n}{\partial t} = 0$ and generation rate = recombination rate) equation 6.7 then reads

$$\triangle n = G\tau_n \tag{6.10}$$

where the change in carrier density is equal to the product of the generation rate and the free carrier lifetime (only includes time spent in CB, not time spent in traps). Additional complexity arises when τ_n is a function of G, which may give rise to slope greater or less than unity on a logarithmic plot of σ_{PC} against G.

Steady state photoconductivity as a function of light intensity can be used to obtain information about the recombination mechanism of the excess carriers as

$$\sigma_{PC} = KF^{\gamma} \tag{6.11}$$

where K and γ (the exponent) are material constants. Large values of both constants lead to large photocurrents. In crystalline systems there is a low density of traps at discrete energies and γ normally equals either 1 or 0.5 for the cases of mono and bimolecular recombination respectively. However in more disordered systems, intermediate values of γ are most often found.[254] These are accounted for in a model including a distribution of localised states which decays exponentially as one moves away from the band-edge. On illumination the electron quasi-Fermi level and

electron demarcation level (seen next section, 6.1.2) split and separate further with the quasi-Fermi level moving closer towards the CB as the light intesnity increases. The occupation of trapping centres is now increased, converting such states into recombination centres. This results in a decrease in lifetime as the light intensity increases whihc is responsible for γ values <1.[255]

6.1.2 *Localised States - Trapping, De-trapping and Recombination*

As mentioned, in the simplest case of a pure crystalline semiconductor absorption excites band to band transitions. Such a system constitutes a trap free material and all excited carriers will contribute to the photoconductivity. However, in the presence of defects, impurities and/or disorder localised states manifest within the forbidden energy gap as explained in section 2.5.3. Extrinsic absorption to and from these localised states may also then take place. All these processes are illustrated in figure 6.1.

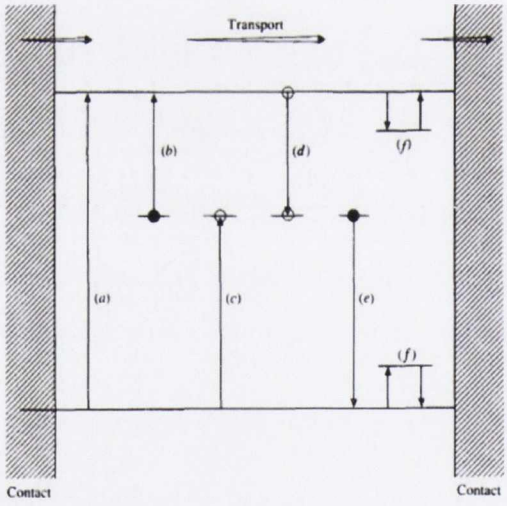

Figure 6.1: Processes involving localised states within the bandgap of a semiconductor on absoprtion of light. (a) intrinsic band-band absorption, (b) & (c) extrinsic absorption out of & into traps, (d) deep trapping, (e) recombination and (f) shallow trapping/ de-trapping.Bube [252]

Localised states complicate the photoconductivity, as depending on their energy with respect to the (steady-state) Fermi energy these states may act as charge traps or recombination centres.[253, 255] Traps act as potential wells for mobile carriers. Once trapped, they are removed from conduction until re-released to the band. This gives rise to a reduced effective mobility. In the event that an oppositely charged carrier is also captured at the same site both electron and hole will recombine. The distinction between trap and recombination centre is ambiguous as it depends on the ambient temperature as well as the light intensity being used. The term demarcation energy is used to conceptually distinguish between the two; a carrier captured at the demarcation level is equally likely to be re-emitted to its respective band as it is to recombine with an oppositely charged carrier. So any level lying between the steady state Fermi level and the demarcation level will act as a recombination centre. Localised levels lying above the steady state Fermi level behave as traps.[255]

When traps are present the excitation pours electrons into the trap states until they are filled. This induces a delay in reaching the steady state photoconductivity and increases the response time as

$$\tau_0 = \left(1 + \frac{n_t}{n}\right) \tau_n \tag{6.12}$$

where n_t is the number of trapped carriers, τ_0 is the measured response time and τ_n again is the lifetime of the free carriers. Similarly on decay trapped carriers take time to be thermally emptied back into their bands before recombining. In the case where the density of trap states is much larger than the density of free carriers ($n_t \gg n$) the observed rate of decay will be dominated by the rate of trap emptying rather than by recombination. Deep lying traps are filled first and the rate of emission from a trap is inversely proportional to its energy depth within the gap as[256, 257]

$$\tau^{-1} \propto \exp\left(\frac{-\triangle E}{kT}\right) \tag{6.13}$$

6.1.3 *Photoconductivity of MoS_2*

Being an indirect gap semiconductor, with an bandgap of 1.3 eV,[24, 32] the photoconductivity of bulk MoS_2 has been investigated at least since the 1960s in the form of single crystal samples.[258, 259] This indirect gap originates at the top of the valence band maximum (VB) at Γ and extends to the conduction band minimum (CB), situated halfway between the high-symmetry Γ and K points, at Λ in the Brillouin zone. In addition to this fundamental gap, MoS_2 is also known for its optical gap at the K-point. This is responsible for the spin-orbit split A & B exciton peaks in the MoS_2 absorption spectra (figure 6.2 b).

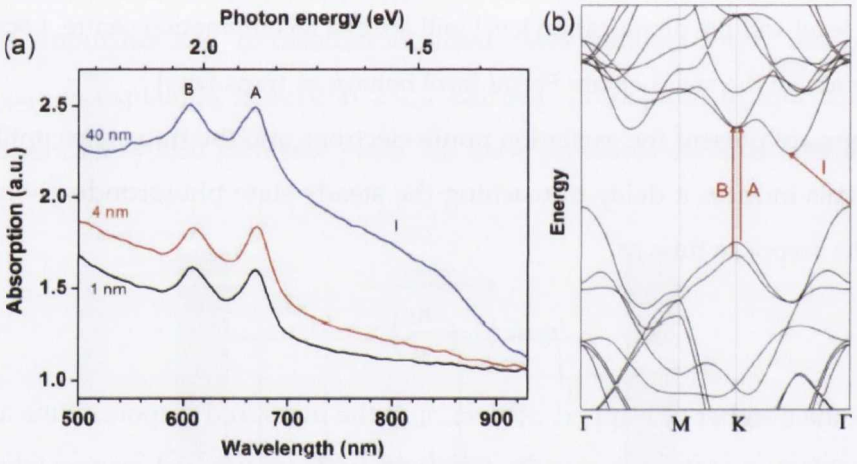

Figure 6.2: (a) Absorption spectra of MoS_2crystals of different thickness. Broad absorption tail 'I' corresponding to indirect transition for 40 nm thick sample which becomes progressively weaker as the crystal is thinned. (b) Bulk MoS_2 band structure. Direct transitions of A and B excitons, corresponding to spin-orbit split VB occur at K-point. Indirect transition I originates at Γ and terminates halfway between Γ and K. [6]

6.1.3.1 *Monolayer MoS_2*

Monolayers of MoS_2 have generated much interest due to their exceptional electronic and optical properties. They have been demonstrated as active components in opto-

electronic devices such as phototransistors,[260–262] and LEDs,[263] and show much promise for use as an absorbing layer in solar cells.[87, 142]

As a transistor, monolayer MoS_2 shows promising photoconductive properties.[262] Due to the magnitude of its bandgap, high responsivity (880 A/W) can be obtained with low noise equivalent power (dark off-current ~2 pA). A direct bandgap allows for efficient carrier extraction whilst the atomically thin channel ensures a high degree of electrostatic control.

As the layer number is reduced there is a progressive quantum confinement induced up-shift in the indirect gap from the bulk value. In the limit of the monolayer thickness it becomes favourable for the bandgap of this material to transform into a 1.9 eV direct gap semiconductor.[22, 27, 31] This results in an increase in photoluminescence (PL) efficiency as large as 10^4 in monolayer samples,[31] whereas in bulk it is a weak phonon-assisted process with negligible quantum efficiency. The direct gap on the other hand shows minimal interlayer coupling effects as the bandstructure at the K-point is mostly composed of metal d_{z^2} orbitals. Such electronic transitions do not require the absorption or emission of a phonon to occur, meaning they absorb light far more efficiently, justifying its reputation as a promising candidate for optoelectronic applications

6.1.3.2 *Bulk MoS_2*

Despite its shortcomings, bulk MoS_2 has a number of potential advantages over its monolayer form. Its lower bandgap extends its spectral response from UV to IR as shown in figure 6.2 by the indirect absorption tail.[6] Coupled with its high thermal stability, this has highlighted another niche area for bulk MoS_2 as a broadband detector in high-temperature environments.[88] Usually photodetectors used in high temperature environments require wide bandgap semiconductors/insulators such as diamond, and so are only capable of deep UV detection. Also, higher drive currents are possible in the ballistic limit for bulk MoS_2 due to the lower bandgap and a threefold increase in the density of states at the conduction band minimum.[73] Lower surface area leads to fewer surface states and less sensitivity to atmosphere & oxidation.[265] Finally, in its bulk form the CB-edge shifts down in energy whilst the VB-edge shifts

Author	Device	Process	γ ($\Delta I = KP^{\gamma}$)	Light	Metal	$R = \Delta I/P_{in}$	τ
Yin[261]	ML transistor	Mech. Exfol.	1	W lamp	TiAu	7.5 mA/W	50 ms
Lopez-Sanchez[262]	ML transistor	Mech. Exfol.	Sublinear	561 nm	Au	880 mA/W	5 s
Tsai[88]	FL MSM photodetector	Thermolysis	0.71	532 nm	Au	0.57 mA/W	100 μs
Zhang[260]	ML transistor	CVD	1	532 nm	TiAu	780 A/W	3 s
Choi[6]	FL transistor	Mech. Exfol.	1	W lamp	TiAu	100mA/W	n/a
*Esmaeli-Rad[148]	FL MSM photodetector	Mech. Exfol.	n/a	532 nm	Au	n/a	n/a

Table 6.1: Comparison of photoconductivites of different MoS_2 based systems. ML stands for monolayer, whereas FL stands for few-layer. *Esmaeli-Rad device is based on a:Si-MoS_2 hybrid hetero-junction MSM.[148] For comparison, photoresponsivities for graphene are ~0.5 mA/W,[264] whereas those for a conventional Si pn junction diode are ~300 A/W.

up,[63] meaning localised states within the bandgap of bulk MoS_2 should be shallower, with subsequently shorter charge-carrier retention times.[?] This also renders ohmic contacts easier to make to bulk than monolayer MoS_2.[102]

6.1.3.3 *Between Bulk and Monolayer*

As the bandgap is modulated by layer number between the bulk and monolayer limits this can be exploited to minimise thermalisation losses on absorption of energetic photons.[266] Despite some loss of low-dimensional properties (few layer MoS_2 shows

an appreciable PL efficiency, not negligible as in bulk but nowhere near as bright as for monolayer)[31], three layer MoS_2 photo-transistors (E_g= 1.35 eV) show good photo-detection capability for red and green light, whereas bi-layer (1.65 eV) and monolayer (1.82 eV) transistors are optimised for absorption at the green-UV end of the spectrum.

All the work outlined above has been performed on samples prepared by CVD growth or mechanical exfoliation. As is shown in this chapter, another way to exfoliate 2D materials is in the liquid phase. This method constitutes a quick and easy, cost-effective way of producing these materials in large quantities as dispersions. These dispersions can be easily formed into films or composites and have been used successfully in electrochemical applications.[16] However, relatively few optoelectronic device applications have been developed for the materials processed in this way thus far. In this chapter, liquid exfoliation techniques are used to give partially exfoliated, but solution processable dispersions. These can be formed into thin films which show promising photoconductive properties.

6.2 SAMPLE PREPARATION AND CHARACTERISATION

6.2.1 *Dispersion*

6.2.1.1 *Sonication*

The MoS_2 starting powder was purchased from Sigma Aldrich (<2 μm particle size) and used as supplied. Nano-platelets of MoS_2 were exfoliated and suspended in liquid using well-established solvent exfoliation techniques.[2, 4, 10, 181] MoS_2 powder (10 g) was added to HPLC-grade isopropanol (IPA, 100 ml) in a glass beaker.

The sample was sonicated with a stand-mounted ultrasonic tip (Heilsher model UP200S, 200 W, 24 kHz) for 24 hours at 60% amplitude in pulsed mode with 2 s on and 1 s off. This results in formation of a dispersion of MoS_2 nano-platelets with a wide range of sizes and thicknesses. When exfoliating layered materials in liquids, a centrifugation step is normally employed post sonication to remove the larger nano-platelets and

any partially exfoliated crystallites.[2, 4, 181] However, we found that films prepared from centrifuged MoS_2 dispersions always displayed pinholes extending from top to bottom as evidenced by electrical shorting when electrodes were applied in a sandwich structure.

6.2.1.2 *No Centrifugation*

Here, centrifugation is avoided as it was found films of un-centrifuged MoS_2 to be generally pinhole free. Shorting can occur in films consisting of discrete nano-scale entities, even when films are relatively uniform and free of well-defined pinholes, due to diffusion of metal through the porous internal structure of the film. That shorting occurs for centrifuged films but not non-centrifuged samples implies the film microstructure depends strongly on the sample processing. Further work is needed to fully understand such effects. Having not been centrifuged, the dispersions here expected to contain larger MoS_2 nano-platelets and small crystallites as well as thin nanosheets due to not being centrifuged. However, most importantly, they are still solution processable.

6.2.2 *Flake Size Characterisation: TEM and AFM*

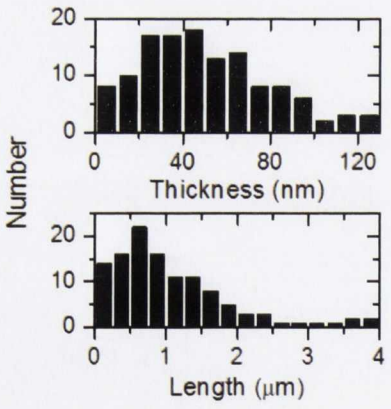

Figure 6.3: Thickness and length distributions of MoS_2 nano-platelets as measured by AFM (on SiO_2) and TEM respectively.

6.2.2.1 *TEM*

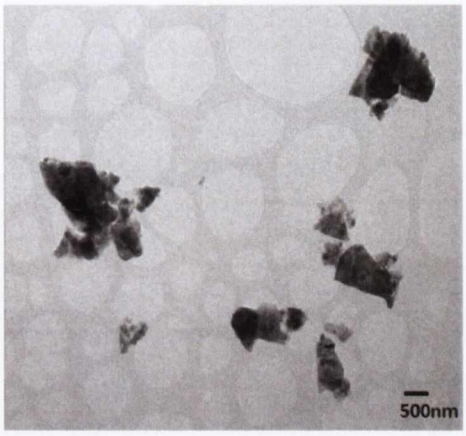

Figure 6.4: TEM of solution processed MoS_2 nano-platelets.

To investigate the nature of the dispersed MoS_2, TEM characterisation was performed (figure 6.4). Typical images show the presence of micron sized nano-platelets which are largely electron opaque, suggesting the nano-platelets to be relatively thick. The lateral nano-platelet dimensions were measured and showed typical nano-platelets to be approximately 1 μm in length (figure 6.3).

6.2.2.2 *AFM*

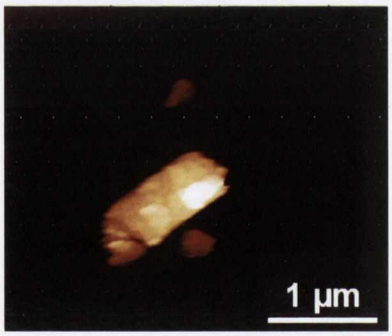

Figure 6.5: AFM image of an MoS_2 nano-platelet deposited on SiO_2 substrate.

To measure the nano-platelet thickness, a few drops of dispersion were deposited onto Si/SiO_2 (200 nm oxide thickness) substrates. These were allowed dry in ambient air before imaging with AFM (figure 6.5). Measurement of the thickness of many nano-platelets allowed statistical analysis (figure 6.3) showing a broad distribution,

peaked around 50 nm. This is consistent with the presence of both well and poorly exfoliated nano-platelets as expected.

6.2.3 *Film Formation and Morphology*

These dispersions were used to form thin films for electrical testing. In order to avoid the formation of pinholes, a number of film formation methods were attempted before settling on a technique based in principle on the Langmuir-Blodgett method. A 250 ml conical flask was filled to the brim with Millipore Water and, using a micro-pipette; a few drops of the MoS_2 dispersion were slowly dropped onto the rim of the flask and allowed to flow down into the water. This technique employs MoS_2's inherent hydrophobicity: the interaction with water drives the MoS_2 to the surface while the IPA enters the water sub-phase where it mixes with the water due to its significant H-bonding component. The conical flask is ideal for keeping the concentration of IPA low in a larger body of water, whilst allowing film formation over a smaller area.

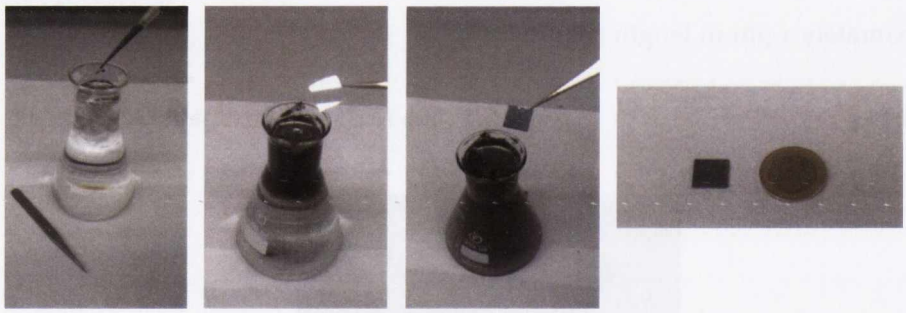

Figure 6.6: MoS_2 film formation process on a water surface in conical flask. Once film is formed across the whole meniscus, the ITO-coated glass substrate is dipped in and pulled out to coat it. Films are then let dry in atmosphere before heating on a hotplate at 250 °C for 3 minutes. Photograph of MoS_2 film after 9 dipping cycles (right) before Au top contact evaporated.

At first the MoS_2 aggregates form at a number of independent nucleation sites. However, as more dispersion is added these sites coalesce resulting in the entire liquid surface becoming covered with a film of MoS_2 nano-platelets. To transfer this film onto a substrate, an indium tin oxide (ITO) covered glass slide (1.2 cm x 1.2 cm) was

inserted below the surface using a set of tweezers and slowly pulled out at an angle of ~75° to the horizontal. This resulted in the ITO-glass being coated with a thin film of MoS_2 nano-platelets. This film was allowed to dry naturally in ambient air until appearing dry. It was then placed onto a hotplate at 250 °C for 3 minutes before being removed and allowed to cool. The MoS_2 film thickness was increased by re-dipping a number of times. However, the water had to be changed every 2-3 coatings to avoid excessive IPA content compromising the film formation.

6.2.3.1 *SEM*

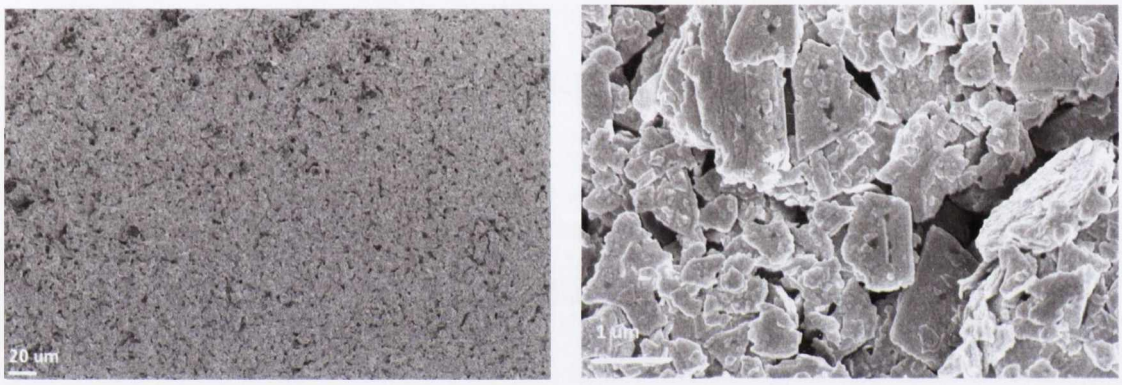

(a) SEM far field image of film of MoS_2 nanoplatelets (b) SEM near field image of film of MoS_2 nanoplatelets

Figure 6.7: SEM of MoS_2 film

The resultant films were dark grey and appeared visually uniform (figure 6.6). SEM examination (Zeiss Ultra Plus SEM) showed them to be continuous over length scales greater than a few microns (figure 6.7a). However, when viewed at higher magnification it becomes clear that they are composed of a disordered array of MoS_2 nano-platelets (figure 6.7b).

The film for which electrical data is presented had a thickness of ~6 μm (achieved after 9 dips). However, this thickness varied by ~20% over a line scan of 800 μm (Dektak 6M Stylus Profiler) showing that this film formation method could certainly be improved. The surface roughness is exacerbated by not centrifuging the dispersion, resulting in thicker than usual nanoplatelets comprising the films. For liquid phase

exfoliated low dimensional nanostructures, the thickness at which a continuous film can be formed (not in the percolative regime) is proportional to the smallest dimension of the entities comprising the film.[226] This is the flake thickness in the case of 2D nanoplatelets and so thicker platelets lead to rougher films.

6.2.4 *Raman and Absorbance Spectra*

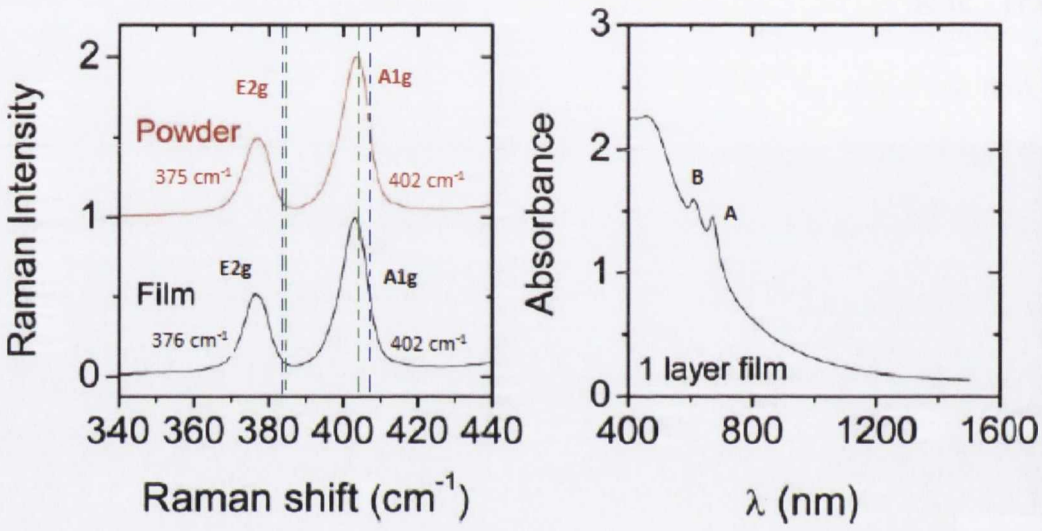

Figure 6.8: Raman spectra of both starting powder and film prepared from uncentrifuged MoS_2 dispersion where the blue dashed lines represent literature values for bulk and green corresponds to the monolayer(left). Extinction spectrum of an MoS_2 film prepared by a single dipping cycle (right).

Raman spectra were recorded for the films (figure 6.8). Raman spectra of exfoliated MoS_2 flakes should approach that of bulk for flakes thicker than 6 layers.[39] Peak positions for these films coincide with literature values for bulk,Lee et al. [39], Li et al. [41] although the value for the E^1_{2g} in-plane mode found here is lower than expected (~384 cm^{-1}). Whilst some slight shifts for powdered samples can be expected,[267] it is unclear here why the E^1_{2g} values here are low in both powdered and film samples. However both types of sample contain a large degree of disorder and high density of flake edges, which is known to affect the spectra of layered materials.[34, 228]

Also measured was the absorbance spectrum of a thin film prepared from a single dipping cycle on an ITO/Glass substrate. Thicker films as prepared for electrical characterisation were dark grey and did not transmit any light. The spectrum displays the expected peaks for MoS_2, though they are likely superimposed on a scattering background.[2]

6.2.5 *Metal Contacts*

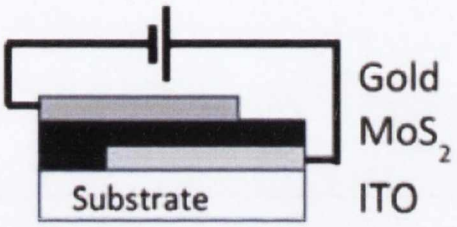

Figure 6.9: Electrode structure fabricated in out of plane geometry. The sample was illuminated from the tranparent ITO side

Devices were fabricated by evaporating a gold electrode (~50 nm thick, 1.98 mm^2 electrode overlap area) on top of the MoS_2 film to give an ITO/MoS_2/Au sandwich structure arrangement in the out-of-plane direction (figure 6.9). After evaporation, films were annealed in air at 200 ° C for 1 hour. This resulted in roughly an order of magnitude increase in conductivity and reduction in the noise current.

Bulk MoS_2 is an n-type 1.3 eV indirect gap semiconductor.[24, 32] The conduction band edge, Fermi energy and valence band edge are at energies of 4.4, 4.8 and 5.6 eV below the vacuum level respectively.[268]

6.2.5.1 *ITO*

Indium tin oxide (ITO) is a common transparent conducting oxide often used in touch screen displays and solar cells. As a widegap semiconductor with a bandgap of 3.8 eV, it transmits photons throughout the visible spectrum. For conductive applications, it is degenerately doped with its Fermi level lying high up in the conduction band, giving it a relatively low workfunction of ~4.7 eV.[269] Thus it is expected to form a neutral

contact for electron injection into the MoS_2 conduction band.[87] Such a contact should behave ohmically for sufficiently low current demands.[253]

6.2.5.2 *Gold*

The nature of the gold contact to bulk MoS_2 is more contentious and deserves further consideration. In the simplest case, non-covalently bonded metal-semiconductor junctions are expected to form a Schottky Barrier. The height is then modelled as the difference between metal work function (ϕ_M) and semiconductor electron affinity (χ_S): $\phi_B = \phi_M - \chi_S$. Using the work-function for gold (~5.1 eV), a barrier height of ~0.7 eV is expected at the Au-MoS_2 interface. However such a model is rarely followed in practise due to the presence of surface and interface states.

It is well known that gold bonds covalently with sulfur via thio-bonds.[270] Whilst saturated sulfur atoms on the MoS_2 <0001> basal plane do not bond strongly to Au,[82] our films consist of a disordered array of nanoplatelets, with numerous exposed edges, containing unsaturated sulfur bonds.[271] Thus there is some scope for alloying at the metal-semiconductor interface when evaporating the metal directly onto the semiconductor film, as has been done here. This may lead to a reduced barrier height and improved ohmicity of the contact as in the case of Ni contacts on Si, which alloy to form nickel silicide.[94]

The effect of the grain boundaries themselves on contact formation should also be considered. Spatially resolved current-voltage measurements on MoS_2 and WS_2 films explicitly show rectifying I-V's are only possible when the contact does not touch grain boundaries.[272, 273] At the grain boundaries the semiconductor is effectively heavily doped, leading to ohmic conduction when metal is deposited onto these regions.

In any case, the samples tested here are highly resistive, ensuring the dominant voltage drop is incurred across the bulk of the semiconductor film as demonstrated by the symmetric I-V curves around the origin.[274] Thus we propose ohmic-like (non-rectifying) contacts for both ITO and Au.

6.3 RESULTS

The experiments outlined here were performed for films of three different thicknesses (4, 5 & 6 μm measured using a Dektak 6M Stylus profilometer). Results for all films tested were similar and all subsequent data analysis has been performed for the 6 μm thick film.

In order to study the photoconductivity of MoS_2 the sample is illuminated through the ITO with a full spectrum solar simulator (Newport 96000), fitted with a Xe-arc discharge lamp (150 W) and air mass (AM) 1.5 filter. The lamp was calibrated against a standard Si based reference cell. Light intensity at the sample was controlled using a set of neutral density filters (NDFs) purchased from Newport.

6.3.1 *Current-Voltage Characteristics*

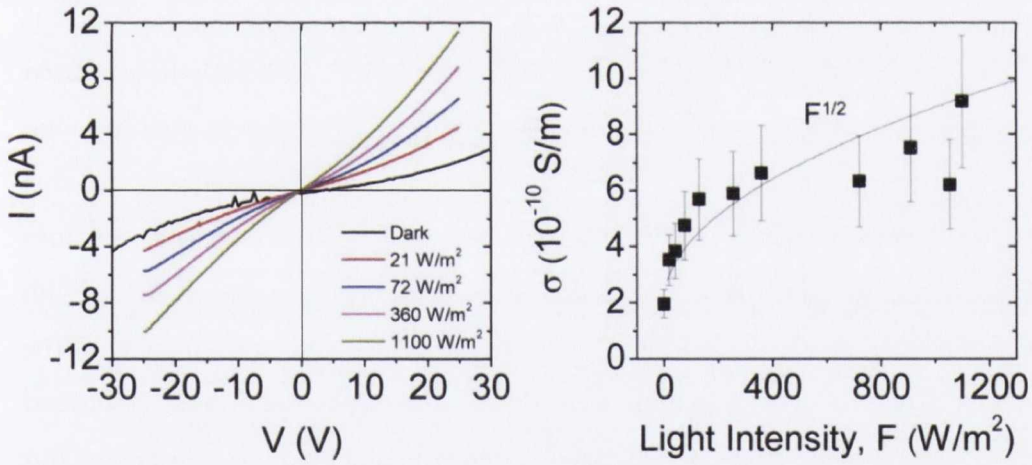

Figure 6.10: I-V curves for an MoS_2 film in the dark and under various light intensities (left). Measured conductivity as a function of light intensity (right). The fit illustrates square root behaviour as $\sigma_{Light} = \sigma_{Dark} + KF^{\gamma}$.

I-V curves were first measured in dark (figure 6.10 (left)). Such curves are symmetric about the origin. Also, when plotted logarithmically their slope is linear up until ~25 V, implying ohmic conduction to be dominant within this voltage range. Conductivity has

been calculated between -5 V to +5 V to be roughly 2 x 10^{-10} S m^{-1}. This is consistent with a three order of magnitude reduction when compared with in-plane conductivity (10^{-7} S m^{-1}) for similarly processed films.[53] This conductivity anisotropy is similar for graphite and suggests current to be limited by interflake transport, whereby layer to layer transport is more resistive than in-plane.[275]

Shown in figure 6.10 (left) are I-V curves measured for the same MoS_2 film, illuminated at different light intensities (F) compared to the dark curve. Again, all curves are symmetric and linear at low voltage, with some slight non-linearity observed at higher voltages. Conductivity increases with light intensity showing a four-fold increase, reaching 8 x 10^{-10} S m^{-1} for F = 1100W/m^2. As shown in figure 6.10 (right), this increase scales with roughly the square root of the light intensity ($F^{1/2}$), consistent with bimolecular recombination.[276] However, bimolecular recombination is usually observed in insulators where the density of optical carriers greatly exceeds thermal carriers in the dark, i.e. when $\triangle n \gg n_0$.

The sub-linear dependence of photoconductivity on light intensity observed is consistent with materials containing broad trap distributions.Halpern [254], Pal et al. [277, 278], Maan and Goyal [279] Such materials show power-law behaviour expressed as in equation 6.11. Recent photoconductive studies of TMDs are limited to mono or few layer MS_2 based varieties. Most of these report linear dependence[6, 260, 261] of photocurrent on light intensity, though some do report sub-linear[262] values with γ values between 0.5[280] and 0.71.[88] These materials are semiconductors with reasonably high dark carrier densities, making bimolecular recombination unlikely. The sub-linear dependence in these cases is attributed to the presence of traps associated with the surface of the flakes or substrates. Whilst the bulkier flakes comprising our films have the advantage of a smaller ratio of surface to bulk atoms, such films contain numerous flake junctions & edges which will contribute localised states within the bandgap. These can trap photo-generated carriers, leading to sub-linear intensity dependence of the photo-current.[253]

6.3.2 *Transient Photocurrent Response*

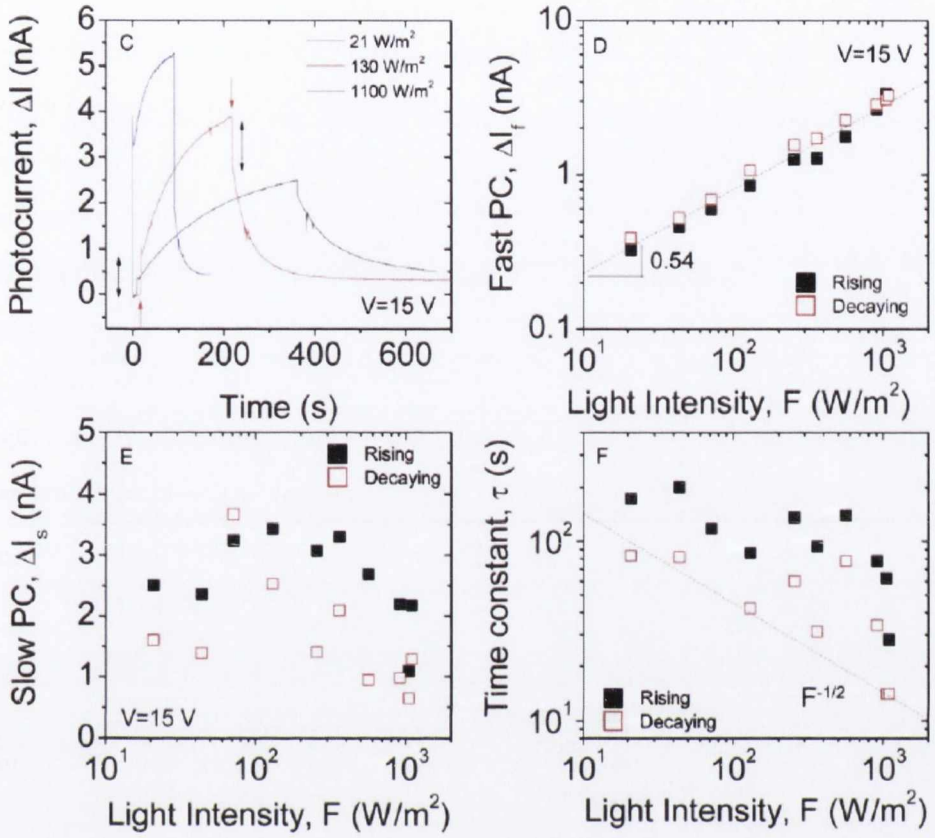

Figure 6.11: (top-left) Photocurrent (PC) plotted versus time for three different light intensities at 15 V. For the red curve the arrows indicate the times the light was switched on and off whilt the black double-headed arrows illustrate the fast portions of the rise and decay. (top-right) Fast components of PC rise and decay plotted versus light intensity (F). The dashed line is a power law fit. (bottom-left) Slow components of both rise and decay of PC versus F. (bottom-right) Time constants for both rising and decating photocurrents plotted versus F. The dashed line represents $F^{-1/2}$ behaviour.

The intensity dependence of the photocurrent was investigated by repeating electrical characterisation under different light intensities in the range from 0-1100 W m^{-2}. Current was measured as a function of time at constant bias (15 V, within the linear region of the I-V curves). During the measurement, the light's beamline was obstructed

by a shutter to switch it on & off. Examples of the resultant curves are shown in figure 6.11 (top-left). Lowest intensities were tested first to minimize heating of the sample on an insulating substrate.

For all light intensities the photocurrent exhibits a fast increase followed by a slow increase to steady state on illumination. To test whether true steady state had been reached, some curves were left to run for several hours with no deviation in the steady state value of photocurrent. For the purpose of illustration the as-shown curves in figure 6.11(top-left) have been truncated at the steady-state value. The fast component is associated with the initial equilibration of the carrier generation and recombination rates and occurs on the timescale of the carrier lifetime.[253, 281] This is of the order of ns in MoS_2.[6] The slow component is due to trap filling. Similarly on the decay once the light is switched off, the fast component is due to the recombination of free carriers. Thermal freeing of trapped charges is responsible for the observed slow decay . Such a slow photoresponse is expected in films with a large density of trap states.[253]

6.3.2.1 *Mono-exponential*

The slow photocurrent increase can be fit to a mono-exponential function of the form

$$\triangle I_R = \triangle I_{f,R} + \triangle I_{s,R}\left(1 - \exp\left(\frac{-t}{\tau_R}\right)\right) \tag{6.14}$$

where the fast component of the photocurrent rise is $\triangle I_{f,R}$ and $\triangle I_{s,R}$ is the slow component of the photocurrent rise. The time constant is τ_R. Similarly, the slow photocurrent decay can be fit to

$$\triangle I_D = \triangle I_{s,D} \exp\left(\frac{-t}{\tau_D}\right) + \triangle I_{PPC,D} \tag{6.15}$$

where $\triangle I_{s,D}$ is the fast component of the photocurrent decay, $\triangle I_{PPC,D}$ is the persistent photocurrent and τ_D the time constant.

A mono-exponential function fit is characteristic of a single type of trapping centre where re-trapping of freed carriers is negligible.Bube [252], Rose [255], Maan and Goyal [279], Haynes and Hornbeck [281] In the presence of different type trapping centres the photocurrent decays as the sum of a number of exponential terms with different time constants. The dark current on decay can be slightly higher than before

illumination. This persistent photoconductivity (PPC) is a common effect in disordered systems and is associated with deep traps.[255, 282, 283]

6.3.3 *Intensity Dependence of Photocurrent & Time Constants*

The fast components of photocurrent rise and decay have been plotted logarithmically against F in figure 6.11 (top-right). In both cases they sit on the same line, consistent with γ from equation 6.11 equal to 0.54. This is very close to the 0.5 expected for bimolecular recombination. However care must be taken here as the relationship between this fast component and the trap distribution is not yet clear. Indeed power law behaviour whose exponent is controlled solely by the details of the trap distribution is well known.[252]

The slow component of the rise and decay of the photocurrent was also plotted as a function of F in figure 6.11 (bottom-left). There is no apparent correlation on light intensity. This behaviour is not surprising as the slow component depends on the trap density.[253] The persistent photoconductivity (PPC, section 6.4.2) was close to 0.5 nA for all samples.

In figure 6.11 (bottom-right) time constants for the rise and decay of photocurrent are plotted against F and tend to fall off as roughly $F^{-1/2}$. It has been shown that when the τ_D scales with intensity as $\tau_D \propto F^{-\gamma}$, this means the observed time constant equals the carrier lifetime (including time spent in traps).[284] That this lifetime is so long indicates that trapping is a problem in these films. Increasing the level of the light intensity used to excite the sample corresponds to a higher free charge carrier density. Under excitation, once thermal equilibrium is reached, a quasi-Fermi level for electrons, greater than that in the dark is established (instead of one Fermi level for the whole system now have one each for electrons and holes, electrons and holes are now in thermal equilibrium with their respective bands but not with each other).[253, 255] This quasi-E_F (E_{Fn} for electrons) can be related to the original E_F in the dark by[284]

$$E_{Fn,quasi} = E_{Fn} - kT \ln\left(\frac{\sigma_{photo}}{\sigma_{dark}}\right) \tag{6.16}$$

As the quasi-Fermi level for electrons increases, moving towards the conduction band in the light, it incorporates more localised states which are now subsequently converted into recombination centres.[253, 255] At high light intensity, more traps are filled and so bear less influence on prolonging carrier lifetime. Also, the now larger amount of recombination centres increase recombination, resulting in faster decays and thus lower time constants. This behaviour of response time with light intensity is characteristic of a continuous distribution of traps within the gap.[255]

6.3.4 *Wavelength Dependent Photocurrent*

After long illumination times, the photocurrent saturates at $\triangle I_R = \triangle I_{f,R} + \triangle I_{s,R}$. Here this saturation photocurrent increases weakly with intensity. As a result, the saturation photoresponsivity (usually defined as $R = \frac{\triangle I_{R,sat}}{F}$) falls with increasing intensity. However, at low intensity R = 10^{-4} A W^{-1} (measured at 15 V), similar to both the lower end of the range reported for CVD grown TMDs[285] and early graphene photodetectors.[264] However, this does not consider the wavelength dependence of the photoconductivity. To test this, the wavelength dependence of the photoconductive response was measured using a set of band-pass filters and the solar simulator.

Initially a monochromator was used to try and measure the action spectrum. However a number of factors along with the poor responsivity prevented this. Slow speed of response prevented lock in detection. In addition, it is difficult to collimate and collect white light from an extended source such as an arc-discharge lamp. Add in the effects of mirror losses, narrow bandwidth and the grating efficiencies from the monochromator and there is not enough power incident on the sample to produce a measurable response from the background.

This resulted in performing the measurement with broadband colour filters to allow more power incident on the sample, at the expense of a loss in spectral resolution. Filters with 10 nm fwhm and centre wavelengths varying from 350 nm to 800 nm in 50 nm steps were used. The transmission of each filter is shown in figure 6.12a. The Xe lamp background spectrum is shown in black in figure 6.12b. The relative transmission

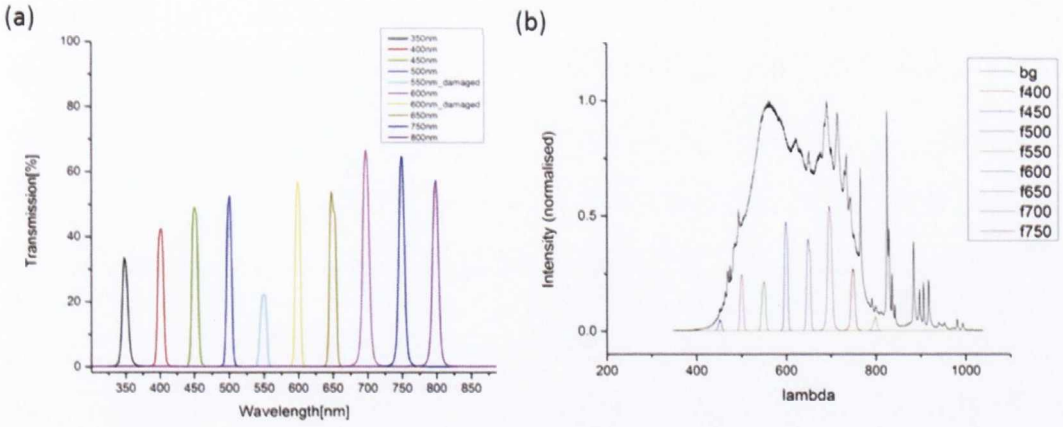

Figure 6.12: (a) Transmittance of 10 nm fwhm colour filters (b) Colour filter transmittance modulated by output from Xe lamp.

through each filter was then calculated by multiplying the normalised background by the filter function. These functions represent the spectral region over which the sample was excited for each measurement.

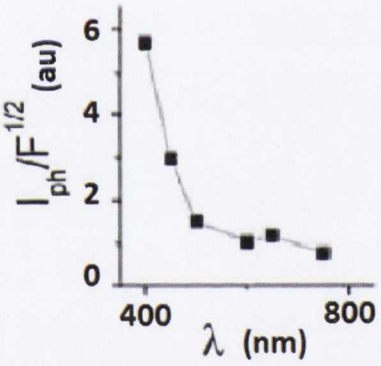

Figure 6.13: Wavelength dependent saturated photocurrent for a film prepared from 9 dipping cycles.[112]

Because the photocurrent scales roughly as $F^{1/2}$, the measured photocurrent divided by the square root of the integrated incident intensity is used.[285] This is plotted versus wavelength in figure 6.13. The spectral response is found to increase with decreasing wavelength as expected from the absorbance spectrum. We see an apparent peak around 650 nm consistent with the A exciton position in MoS_2.[1] In addition, the spectral response increases sharply below 500 nm as observed previously for

MoS_2 monolayers.[262] This suggests that the photoresponsivity calculated using the absorbed power would be considerably higher than the value quoted above.

6.4 DISCUSSION

6.4.1 *Metal Contacts*

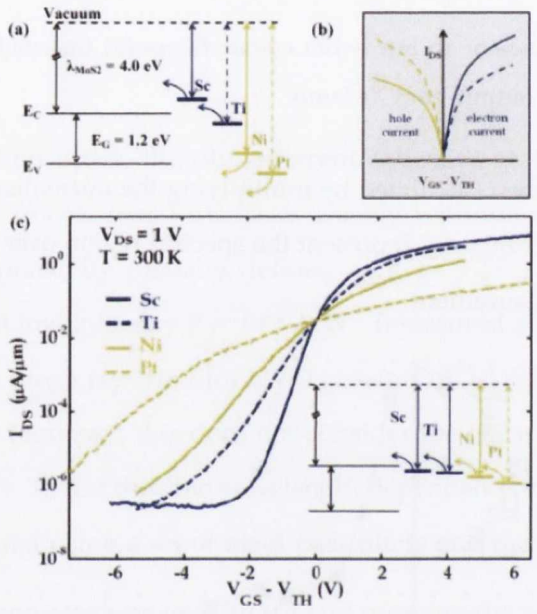

Figure 6.14: (a) Expected band lineups of metals and resulting (b) Simulated I-V curves on few layer MoS_2, from standard band alignment theory. (c) In reality the metal work-function is pinned close to the CB of MoS_2 in all cases resulting in electron injection with some finite barrier.[7]

During the time the experiments in this chapter were conducted and written up, gold was widely believed by the community to form an Ohmic contact to monolayer MoS_2.[72] Following on from this, temperature-dependent studies of different metals deposited on few-layer MoS_2 showed that most metals, except those endowed with extremely low work-functions (e.g. scandium ~3.5 eV), formed contacts with some finite barrier.[7] The height of this barrier depends only weakly on metal work-function, consistent with Fermi-level pinning. The previous claims of ohmicity of the gold contact

were made due to the linearity of I-V curves at room temperature and low voltage. However, standard emission theory does not consider the thermally assisted tunnelling current component which is responsible for such a perceived ohmic contact at room temperature.[7]

In retrospect, the symmetry of the I-V's manifest from the asymmetric electrodes (ITO & Au) chosen here may well be due to pinning of the Fermi level. The rhetoric for proposing ohmic contacts at the metal-semiconductor interface at the time of writing was as presented in section 6.2.5

6.4.2 *Persistent Photoconductivity*

In order to minimize heating of the sample on an insulating substrate lowest light intensities were tested first. However, some small increase in dark current was noted throughout the duration of the experiment. This is characteristic of persistent photoconductivity (PPC). PPC is a common effect associated with deep traps in disordered films and occurs when a portion of the photo-generated carriers cannot flow out of the material via the contacts..[255**?**] It has been observed previously in TMD films.[260, 283] In films of other chalcogen containing compounds (chalcopyrite and II-VI semiconductors), anion vacancies have been identified as the source of the PPC.[286] However, these materials have different bonding and crystal structures to MoS_2 and it is unlikely such defects are the source in this case. Indeed, it is well known that S-vacancies are common and have a low formation energy in MoS_2, contributing a prominent defect level close to the conduction band.[93, 95]

6.5 CONCLUSIONS

In this chapter a method has been developed to prepare solution processed thin films of MoS_2 which can be fabricated into photodetectors. These show a four-fold increase in conductivity on exposure to 1 sun broadband illumination. Due to the presence of

traps the photo-response scales sub-linearly with intensity and slowly with time. The photoresponsivity is similar to that of early reports for graphene.[264]

The ability to prepare photodetectors from inorganic nanomaterials by solution processing based techniques is an important step and should allow facile fabrication of large area devices at low cost. This work is considered a first step toward solution exfoliated 2D optoelectronic devices.

7

VARIATIONS OF DARK AND PHOTOCONDUCTIVITY IN NANOSHEET NETWORKS BY VARYING TMD

7.1 INTRODUCTION

The most heavily studied TMDs are MoS_2 and WS_2, although many more of these materials exist.[16, 32] Depending on the combination of metal and chalcogen atoms these materials can exist as insulators, semiconductors or metals. Group VI (Mo or W) TMDs are nominally semiconducting. As the mass of the chalcogen atom increases (i.e. from S to Se to Te), the bandgap decreases,[5, 23, 24, 26, 33, 45, 287–289] with optical bandgaps of ~1.8, 1.5 & 1.1 eV for the sulfides, selenides and tellurides respectively. Such a reduction in energy gap as anion weight increases is due to increased covalency of the bonding.[25] In addition, they have indirect bandgaps ranging from ~1.4 to 1.0 eV. For a given TMD, the band structure depends sensitively on the layer number, allowing still further opportunity to tune the bandgap for specific applications.[266] As such, these materials have generated a large amount of interest due to the possibility of using them in electronic or optoelectronic applications.

MoS_2 and WS_2 are well known to exhibit photoconductivity in their mono and few layer forms.[6, 85, 88, 260–262, 280, 285] Photoconductivity is an excellent starting point for the demonstration of the optoelectronic capability of networks of liquid exfoliated nanosheets. However thus far, the photoconductivity of other group VI MSe_2 and MTe_2 based TMDs has not been studied in mechanically cleaved, CVD-grown or solution cast forms. This is unfortunate as these materials would extend the spectral range of any device whose operation requires optical absorption.

In this chapter the first comparative study of the photoconductivity of solution processed films of MoS_2, $MoSe_2$, $MoTe_2$, WS_2 and WSe_2 nanosheets is reported. Being

hydrophobic due to their low surface tension,[181] these materials self assemble into thin-films on a water surface and can be easily transferred onto substrates. Such films have been deposited onto lithographically pre-patterned Au electrodes on SiO_2 to make photoresistors. The photocurrent response of these to a range of light intensities from a broadband source has been investigated as a function of time and intensity. Significant differences in performance are found, ultimately stemming from the broad range of dark conductivities in these materials.

7.2 SAMPLE PREPARATION

7.2.1 *Dispersions*

All materials were > 99% pure and purchased in powder form. For each material supplier and particle sizes were as follows: MoS_2 (Sigma Aldrich, <2 μm), $MoSe_2$ (Materion, <45 μm), $MoTe_2$ (Materion, <10 μm), WS_2 (Sigma Aldrich, <2 μm) and WSe_2 (Materion, <5 μm). In all cases suspensions were prepared by adding 2.5 g of TMD powder to 50 ml of N-Methyl-2-pyrrolidone (NMP) from Sigma Aldrich in a glass beaker. Samples were sonicated using a stand mounted ultrasonic tip (Heilsher model UP200S, 200 W, 24 kHz) for 1.5 hours at 60% amplitude in pulsed mode (1 s on, 1 s off).

Following sonication, samples were transferred into glass vials and centrifuged at 5500 RPM for 2 hours in a Hettich Mikro 22R. A high RPM was chosen in order to remove the smallest flakes from these suspensions. This resulted in slightly coloured but light transparent supernatants with the majority of the material compacted at the bottom of the vial. At this point a solvent exchange was performed to facilitate working in a poorer, but easier to remove, low boiling point solvent. The supernatant was decanted and replaced with the same volume of HPLC grade isopropanol (IPA) before re-sonicating in a Branson 1510E-MT sonic bath (20 kHz) for 30 minutes. Following this, the samples were again centrifuged at 5500 RPM for a further two hours and the supernatant decanted once more. This step should remove a further

portion of the smallest flakes as well as residual NMP likely left behind after the supernatant was first decanted. Samples were then topped up again with HPLC IPA and bath sonicated for a further 10 minutes to help homogenise the mixture.

The centrifugation regime chosen here ensures the suspensions are mostly composed of larger flakes and partially exfoliated crystallites. Smaller flakes have a larger ratio of edge atoms to basal plane atoms. Films made with smaller, better exfoliated flakes can exhibit negative photoconductivity effects on illumination, whereby the film becomes more resistive than in the dark.[187] These effects are known to occur in MoS_2 films[290] and will be studied in more detail in future work. Here the aim is to simply compare the effect on the photoresponse of the films by varying the transition metal atom (M=Mo or W) and the chalcogen atom (X=S, Se or Te). As such larger, less well exfoliated platelets are used to make the films.

7.2.2 *Film and Electrode Fabrication*

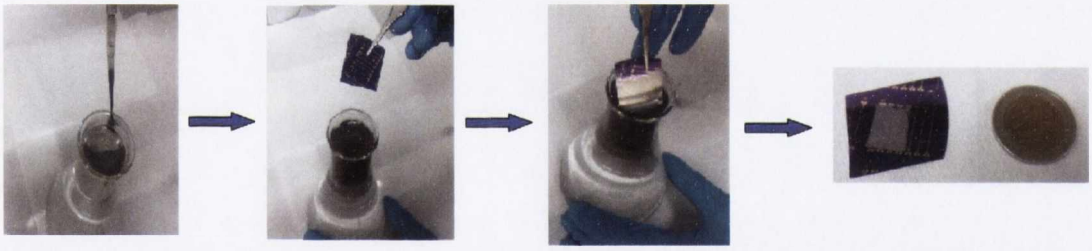

Figure 7.1: Film formation process on water surface, based in principle on the Langmuir-Blodgett method. Dispersion dripped onto rim of conical flask filled with DI water. The IPA enters the water sub-phase whereas the hydrophobic TMD nanosheets are repelled to the surface. At first nucleation sites form on the meniscus, as more dispersion is added these sites coalesce and form a film. The substrate is then dipped below the surface and pulled out at a slight angle to transfer the film before allowing to air dry and placing on a hotplate at 200 °C for three minutes.

These suspensions were used to form simple thin film two terminal devices for electrical testing for all five TMDs. Films were deposited onto SiO_2/Si substrates (300 nm SiO_2) using a method based in principle on the Langmuir-Blodgett method, as

described in the previous chapter (as in figure 7.1). Once transferred, the films were let dry in ambient conditions until all solvent had evaporated after a couple of minutes. At this point they were placed onto a hotplate at 200 °C for 3 minutes to promote adherence to the substrate and contacts.

The films here are deposited using a low grade, proof of principle technique, meaning they are not optimally adhered to the substrate. A post anneal step could be used to promote film adhesion but has not been employed here. These films are composed of relatively thick, bulky flakes. The inherent inhomogeneity in their surface morphology can make contact deposition on top of the films tricky. Films comprised of thinner flakes adhere better and are less rough, but are not studied here for reasons mentioned before. Lithographically pre-fabricated Au electrodes on SiO_2/Si substrates are used due to its high work function (5.1 eV). Though expected to be more suitably matched to the CB of MoS_2,[7, 82] low workfunction metals allows the formation of an undesirable oxide layer at the surface when transferring a film on top of the contact in ambient conditions.

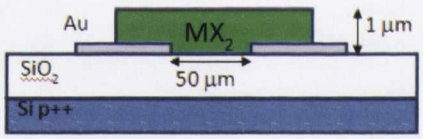

Figure 7.2: Schematic of the device arrangement used in this work.

The devices formed had channel length and width of 50 µm and 1 cm respectively. This channel length is much larger than even the maximum nanosheet size meaning that inter-flake charge transfer will play an important role in the electrical properties.

Silver paint and wire were used to connect the devices to a source meter. All electrical measurements were performed using a Keithley 2400 controlled by a LabView program.

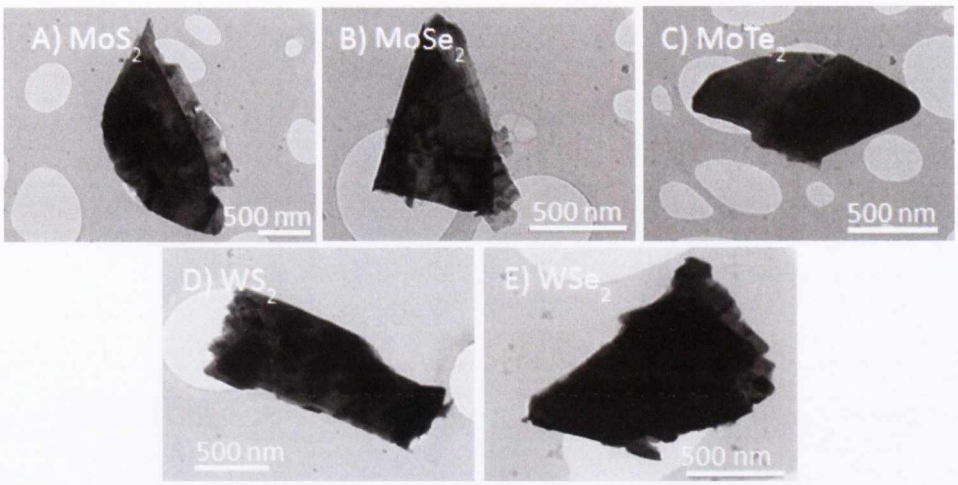

Figure 7.3: (A-E) TEM images of nanoplatelets. All are electron opaque suggesting them to be thicker than usually seen for Liquid Phase Exfoliation. This is due to the size selection method used here, to isolate thicker, bulk entities.

7.3 CHARACTERISATION

7.3.1 *TEM*

TEM analysis showed the resulting material to consist of electron-opaque, micron sized nano-platelets (figure 7.3 A-E). The opacity of these objects confirms them to be much thicker than are found using normal liquid exfoliation. The mean nanosheet length varied from 1.4 to 0.6 μm depending on the TMD type . However also noted is the presence of some smaller entities (hundreds of nm in length). This is consistent with the work in chapter 6 on non-centrifuged suspensions of MoS_2, prepared to investigate photoconductivity in the out of plane direction.[112] Even though the mean size of the nano-platelets composing the dispersions here are relatively large, importantly, they are still solution processable.

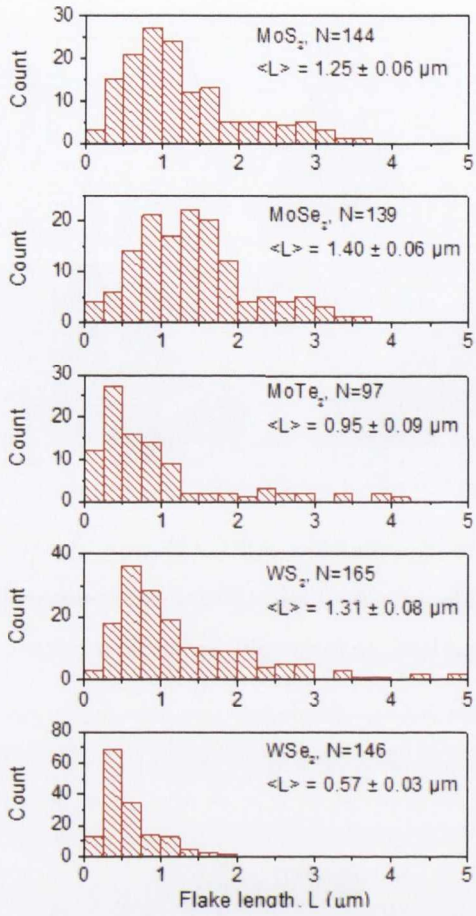

Figure 7.4: Flake length statistics measured using TEM. The length is defined as the longest dimension of the flake. The quoted errors are standard errors of the distribution. The mean length scales approximately inversely with density suggesting the variation in size occurs during centrifugation.

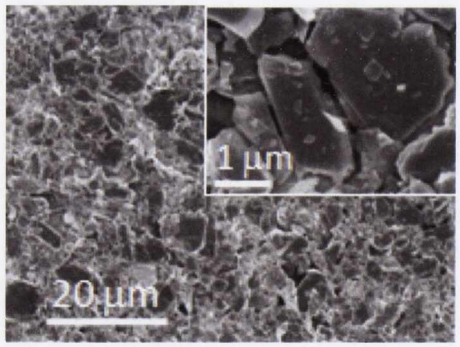

Figure 7.5: SEM image of typical MoS_2 film with magnified view in inset.

7.3.2 *SEM*

These size-selected nanosheet dispersions have been used to prepare thin films from each of the five nanosheet types. The as-formed films were estimated to be roughly 1 μm thick from the mass of each material deposited onto the water surface. In all cases, they were very dark grey to almost black in colour and appeared uniform to the naked eye. SEM examination (Zeiss Ultra Plus) shows continuous films when viewed at large length scales (>10 μm) (figure 7.5). However, when viewed at higher magnification, films are confirmed to be composed of a disordered array of TMD flakes (inset).

7.3.3 *Raman Spectroscopy*

Raman spectra for films and powders of all materials were recorded (figure 7.6). Peak positions coincide well with literature values for bulk,[5, 40, 44] with slight shifts as is sometimes the case for powdered samples.[112, 267] This is not surprising as in the case of the films, the substrate interaction is stronger. Also, as the grating used here has a resolution of 1800 lines/mm it is not sufficient to resolve the two characteristic TMD phonon modes which are almost degenerate in WSe_2 (E^1_{2g} at 248 cm^{-1} & A_{1g} at 250.8 cm^{-1}). Instead a single peak appears centred at ~250 cm^{-1}. Gratings with 2400 lines/mm are capable of resolving the peaks sufficiently.[43]

7.4 RESULTS

Solution-processing based techniques have been used here to exfoliate layered crystals of TMDs into suspensions of nanosheets which can then be formed into thin films. The aim of this work is to compare the photoconductive properties of such films for a range of TMDs. When prepared in this way, the films consist of disordered networks of exfoliated nanosheets.[2] In general, solution processing tends to give nanosheets with a range of sizes and thicknesses.[52] The bandgap of all TMDs tends to vary strongly with nanosheet thickness – for example, while monolayer MoS_2 has a direct bandgap

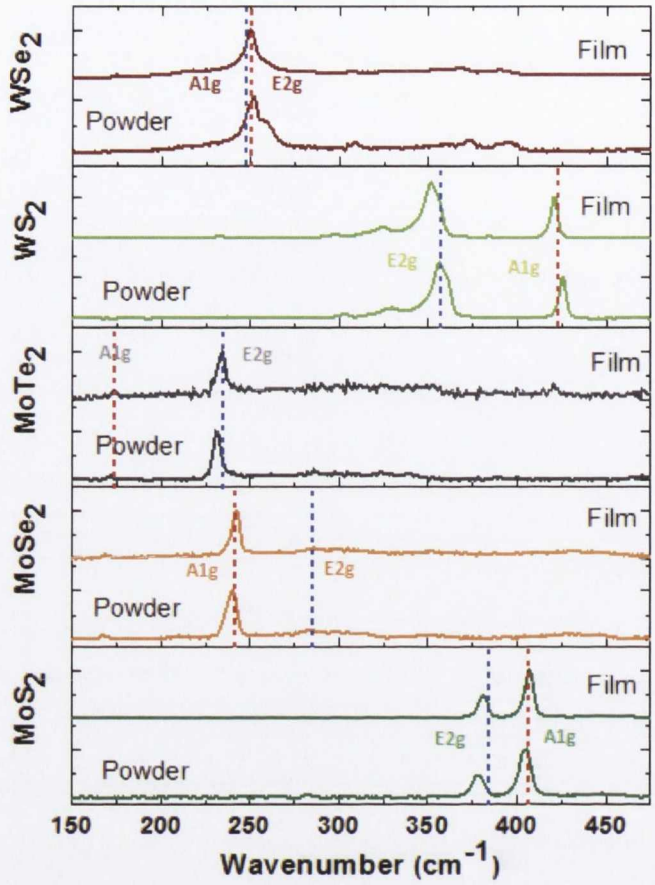

Figure 7.6: Raman spectra of both powder and films for all materials studied. The literature values of the in plane E^1_{2g} mode positions are marked blue whereas the out of plane A_{1g} mode positions are marked in red..

of 1.8 eV, thicker nanosheets (e.g. bilayers, trilayers etc) have lower indirect bandgaps. Above ~6 layers, the indirect band gap approaches that of a bulk crystal (~1.25 eV for MoS_2). This is a problem for a study such as this one because a film of as-prepared nanosheets will contain platelets of all thicknesses from 1 to >10 monolayers. This will render the electronic properties of the network both spatially inhomogeneous and ill-defined, making comparisons between materials difficult. This issue is addressed by removing all thin nanosheets from the dispersion before film formation. This will result in thin films consisting predominately of nanosheets with >10 layers, all of which have bandgaps identical to the bulk value.

7.4.1 *I-V Curves*

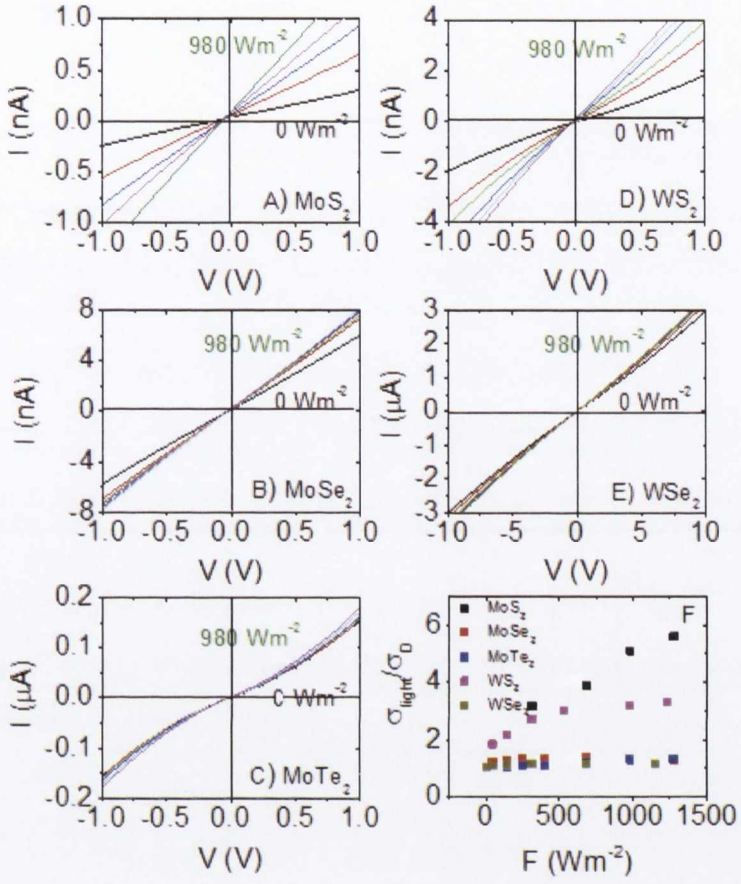

Figure 7.7: Dark and illuminated current-voltage curves measured for thin films of A) MoS_2, B) $MoSe_2$ C) $MoTe_2$, D) WS_2 and E) WSe_2. In all cases, the incident intensity varied from ~50 to 980 W/m². N.B. The current scales in A, B and D are nA while in C and E they are μA. F) Ratio of conductivity under illumination to dark conductivity, plotted versus incident intensity, for all five materials.

7.4.1.1 *Dark*

Shown in figure 7.7 are I-V curves taken for each material in the dark. As expected for a resistor, all such curves are symmetric about zero, suggesting Ohmic-like contacts in all cases.[291] The dark conductivities (as determined from the slope of the curve around the origin) varied strongly over the material set from ~10^{-6} S/m for MoS_2 to ~10^{-3} S/m for WSe_2. The data for MoS_2 is similar to previous data for in-plane conductivity in

solution processed films.[53] However, it is ~3 orders of magnitude higher than that found for out of plane measurements on similarly prepared films,[112] consistent with conductivity anisotropies in layered materials such as graphite.

7.4.1.2 *Light*

All curves remain symmetric about the origin with linear, followed by supralinear regions as observed for the dark current. In addition, clear increases in conductivity with light intensity are observable. The ratio of conductivity under illumination to dark conductivity ($\frac{\sigma_{light}}{\sigma_{dark}}$) is plotted versus light intensity in figure 7.7 F. It is clear from this data that the photoconductive effect is strongest in MoS_2, followed by WS_2 with the other materials showing relatively weak effects.

It is also worth noting that, for each material, the voltage range over which the I-V curves display linearity broadens slightly as a function of light intensity. This is a common effect in polycrystalline semiconductor films and is associated with a slight lowering of potential barriers present at the interflake junctions due to the presence of photo-generated carriers.[117, 118, 120, 252, 292] This will manifest itself as a small increase in carrier mobility with light intensity.

7.4.2 *Photocurrent-Time Response*

To compare the time dependence of the photoresponse of different MX_2 films current was measured as a function of time at a constant low bias (1 V) by opening and closing a shutter between lamp and sample while increasing the intensity each time the shutter was closed. Typical examples of current-time traces are shown in figure 7.8 A-E. For all light intensities, on illumination the photocurrent exhibits a fast increase followed by a slow increase to steady state (SS) as observed previously for out of plane measurements on MoS_2 films.[112] The same pattern for the decay is followed in the opposite order once illumination is ceased. The fast components are associated with the initial equilibration of the carrier generation and recombination rates. The slow components are due to trap filling and emptying on rise and decay respectively. A slow

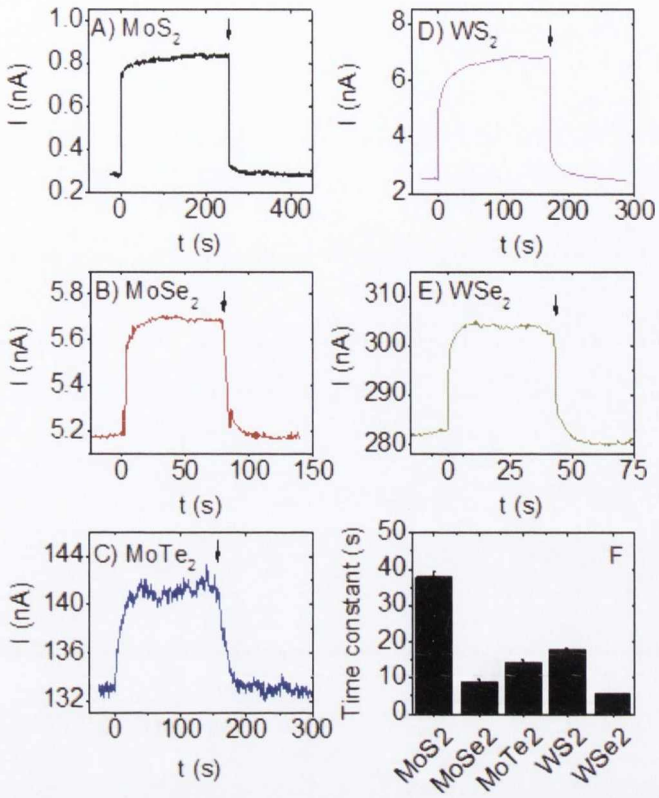

Figure 7.8: Current versus time graphs for A) MoS_2, B) $MoSe_2$ C) $MoTe_2$, D) WS_2 and E) WSe_2. In all cases the light was turned on at t=0 s (F=250 W/m^2) and turned off at the time indicated by the arrow. Note that in all cases, exponential rises and decays of photocurrent were observed. F) Average time constants associated with the photocurrent rise, measured at F=250 W/m^2, for each material.

photoresponse such as that observed here is expected in films with a large density of trap states.[253]

7.4.3 *Light Intensity Dependence of Photocurrent*

The steady state photocurrent, $\triangle I_{SS}$, has been measured as a function of light intensity for all five materials. This has been converted into photoconductivity, defined as $\sigma_{PC} = \sigma_{Light} - \sigma_{Dark}$, using $\sigma_{PC} = \frac{\triangle I_{SS} L}{wtV}$ where L is the electrode spacing (50 μm), w is

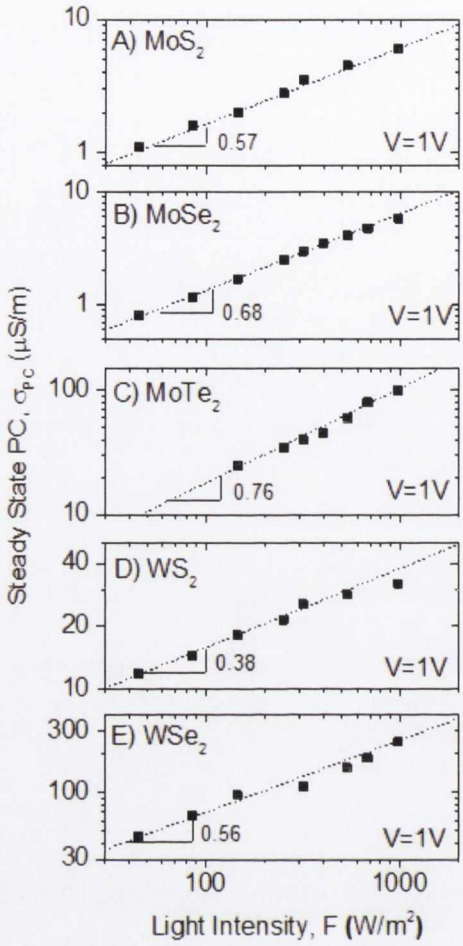

Figure 7.9: Steady state photoconductivity plotted versus light intensity for A) MoS_2, B) $MoSe_2$ C) $MoTe_2$, D) WS_2 and E) WSe_2.

the electrode length (1 cm), t is the film thickness (1 μm) and V is the applied voltage (1 V). This data is plotted in figure 7.9 A-E.

The first thing to note is the significant variation of the maximum observed photoconductivity (i.e. that at 1000 W/m^2). This varies from <10 μS/m for MoS_2 to >200 μS/m for WSe_2. In each case, a sublinear dependence of photoconductivity on light intensity is observed, in agreement with previous measurements on films of liquid exfoliated MoS_2 nanosheets.[112] This behaviour is consistent with a number of reports[254, 277**?** , 278] on materials containing broad trap distributions, which all show power-law behaviour, usually expressed as

$$\sigma_{PC} = KF^{\gamma} \tag{7.1}$$

where K and γ are material constants. Large values of both constants lead to large photocurrents. Such behaviour is consistent with a simple model by Rose[253, 255] for materials with exponential trap distributions which will be further discussed below. Fitting the data showed K to vary over ~2 orders of magnitude (see figure 7.10 B), with values of γ ranging from 0.38 (WS_2) to 0.76 ($MoTe_2$). This is reasonably consistent with Rose's model which predicts that $0.5 \leq \gamma \leq 1$ for systems with broad trap distributions within the bandgap.

7.4.4 *Variation of Dark Conductivity with E_g*

The data above clearly demonstrates trap-limited photoconductivity for all five TMDs studied. Figures 7.7 and 7.9 show photoconductive behaviour which varies significantly from material to material. It would be of great interest to begin to develop an understanding as to the nature of these differences. The most basic physical parameter which varies across this material set is the bandgap. Because this study is based on dispersions containing relatively thick nanosheets, the appropriate bandgap is the bulk indirect bandgap. This varies from ~1.0 eV for $MoTe_2$ to ~1.4 eV for WS_2. Whilst the narrower bandgap for $MoSe_2$ and $MoTe_2$ ensures absorption of a greater percentage of the broadband light, this will not be the only mechanism affecting the photoconductive response.

Shown in figure 7.10 A is the dark conductivity plotted as a function of bulk (indirect) bandgap for all five materials studied. The open symbols represent the mean values averaged over a number of different samples while the closed symbols represent the data collected from the samples for which the photoconductivity data was presented above. This graph shows a clear trend, with dark conductivity falling with increasing bandgap for both Mo- and W-based TMDs. This is reminiscent of the behaviour expected for intrinsic semiconductors (i.e. with Fermi energy close to the centre of the gap), where the conductivity is given by

$$\sigma_{Dark} = \mu e N_C \exp\left(\frac{-E_g}{2kT}\right) \tag{7.2}$$

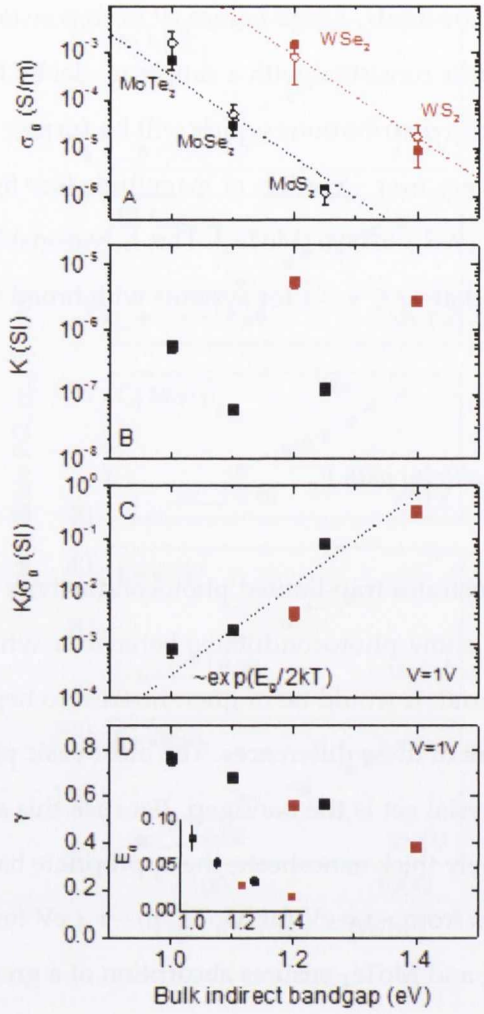

Figure 7.10: Bandgap dependence of photo-conductive parameters. A) Dark conductivity, B) K-parameter (equation 7.1), C) ratio of K parameter to dark conductivity and D) intensity exponent plotted versus bulk, indirect bandgap. In A), the dashed lines represent $\sigma_{Dark} \propto \exp\left(\frac{-E_g}{2kT}\right)$, the open symbols represent the mean over ~5 independent samples, while the closed circles represent the samples used for the presented photoconductivity measurements.

Here μ is the electron (hole) mobility, N_C is the effective number of states per volume in the conduction (valence) band and E_g is the energy gap. In principle, the effective

number of conduction band states per volume depends only on fundamental constants. For a 3D semiconductor:[253]

$$N_C = 2\left(\frac{2\pi kTm^*}{h^2}\right)^{\frac{3}{2}} \tag{7.3}$$

where m^* is the effective carrier mass. Equation 7.2 has been fit separately to the data for both the Mo- and W-based TMDs, finding good fits in each case. Assuming equation 7.2 can be applied to these systems, these fits imply a number of things.

7.4.4.1 *Intrinsic Semiconductors*

The fact that the experimental data displays slopes very close to -1/2kT would suggest the Fermi energies to be very close to the centres of the bandgaps for each material.[253] This will be discussed in more detail below. That all three Mo-based materials sit on the same line implies that they have very similar mobilities. In addition, the data implies the W-based compounds to have similar mobilities to each other but different to the MoX_2 compounds. However, taking the fits at face value allows one to extract values of μN_C for both Mo- and W-based materials of 6×10^{23} and 7×10^{25} $V^{-1}s^{-1}m^{-1}$ respectively. Taking the 3D equation for N_C (and taking $m^* = 0.5m_e$)[293] gives mobility values of 635 and 77600 $cm^2/V\,s$. Mobilities of no more than ~1 $cm^2/V\,s$ may be expected in networks such as these.[294] Thus, these values are much too high, suggesting that if equation 7.2 is applicable, the effective density of states in such 2D materials to be considerably higher than given by equation 7.3.

7.4.4.2 *Doping and Compensation*

As mentioned above, equation 7.2 is valid only for intrinsic semiconductors where the Fermi energy is close to the bandgap. However, many papers have demonstrated that TMDs tend to be doped, resulting in Fermi energies close to the conduction band edge. Much of what is known about TMD doping generally comes from computational studies on MoS_2.[107, 108] Many papers have shown that few and monolayer MoS_2 samples tend to be unintentionally n-doped.[7, 70–75] Intrinsic defects such as stoichiometric deficiencies in compound semiconductors contribute localised states within the gap which can act as dopants depending on their energy.[272, 273] Sulfur vacancies have a

low formation energy in MoS_2[93, 97] and are thought to contribute a level close to the CB of its monolayer. This type of defect is known to be easier to produce and reside in higher concentration at flake edges than in the basal plane[97] and has been suggested as the source of the Fermi level pinning close to the CB.[93, 95] However some reports also exist throughout the literature which show p-type operation of MoS_2.[295, 296] This has been expanded on recently by studying locally resolved electrical characteristics of an MoS_2 sample.[94] Explicitly shown are areas of high n and p-type inducing defect densities on a common sample. Thus the conductivity of MoS_2 seems to depend on the experimental details in a non-trivial way. This aligns with older studies on bulk MoS_2 which commonly showed both n[109, 297] and p-type[297, 298] operation. Much less is known about doping in other TMDs.

However, liquid exfoliated nanosheets are not particularly clean, tending to have non-trivial quantities of adsorbed residual solvent that is very hard to remove.[200] It is entirely possible that such adsorbed impurities tend to dope the nanosheets, bringing the Fermi energy toward the centre of the gap. Our method's use of organic solvents may induce effects not seen elsewhere in the literature. Indeed NMP has a high boiling point and is notoriously difficult to remove completely. In addition, the disordered films here contain a large density of flake edges. This influences the film doping via the localised states they produce. A scenario may well exist whereby the semiconductors here contain both donor (N_d) and acceptor (N_a) dopant species, resulting in a compensated semiconductor. The polarity of the conductivity is then governed by ($N_d - N_a$) with intrinsic behaviour expected if $N_d \approx N_a$.[36, 80]

7.4.4.3 *Effect of Mobility*

It cannot be ruled out the possibility that the bandgap dependence observed in figure 7.10 A is at least partially due to a systematic variation of mobility with bandgap in addition to the variation of carrier density implied by equation 7.2. This can be addressed by removing the effect of mobility from the data.

From the fits in figure 7.9, the parameter K is plotted versus bulk indirect bandgap in figure 7.10 B. This clearly shows the WX_2 compounds to display K-values which are

10-100 times larger than those of the MoX_2 systems. Sub-linear power-law dependence of photoconductivity on intensity such as observed here has been treated in a simple model by Rose.[253, 255] He considered materials with a broad trap distribution which decays exponentially from the band edge as $\exp\left(\frac{-\triangle E}{E_0}\right)$ where $\triangle E$ is the energy relative to the band edge and E_0 is the characteristic trap energy. In this case, Rose derived an equation for the photo-induced carrier density, n_{PC}, which can be expressed as

$$n_{PC} = N_C \left[\frac{f}{N_T v S N_C}\right]^{\frac{E_0}{(kT+E_0)}} \tag{7.4}$$

where N_C is the effective density of states in the conduction band, f is the electron-hole pair generation rate ($s^{-1}m^{-3}$), N_T is the total trap density (m^{-3}), v is the thermal velocity of the carriers, S is the recombination cross-section and E_0 is the representative trap energy (from the band edge). Assuming the films are thick enough to absorb all incident light in the resonant regime (approximated here as photon energies larger than the direct bandgap of the material), then f is related to the total incident intensity F by $f = aF$ where a is related to the fraction of incident light absorbed:

$$a = \frac{\int_{\nu=\frac{E_{g,direct}}{h}}^{\nu=\infty} \frac{I(\nu)}{h\nu} d\nu}{\int_{\nu=0}^{\nu=\infty} I(\nu)\, d\nu} \tag{7.5}$$

where $I(\nu)$ is the incident intensity in the range between ν and ν+dν. Note that a is not expected to vary dramatically between materials. Assuming a solar spectrum, a falls from 0.4 to 0.15 as the direct bangdgap is increased from 1.1 to 1.9 eV. With this in mind, equation 7.1 can be re-written in the form

$$\sigma_{PC} = KF^{\gamma} = \mu e N_C \left[\frac{F}{F_0}\right]^{\gamma} \tag{7.6}$$

where $F_0 = \frac{N_T v S N_C}{a}$ and $\gamma = \frac{E_0}{(kT+E_0)}$. Therefore, the material properties are now contained in F_0 and γ. Then $K = \frac{\mu e N_C}{F_0^{\gamma}}$, suggesting the difference in K-values between WX_2 and MoX_2 compounds is due to differences in either μ or the trap related properties described by F_0^{γ}.

In order to separate the effects of mobility from trapping we consider the ratio of K and σ_{Dark}:

$$\frac{K}{\sigma_{Dark}} = \frac{\exp\left(\frac{E_g}{2kT}\right)}{F_0^{\gamma}} \tag{7.7}$$

Values of K/σ_{Dark} are plotted versus (indirect) bandgap in figure 7.10 C and show a clear scaling with $e^{E_g/2kT}$ for all materials. This implies that the differences in σ_{Dark} and K-values observed in figures 7.10 A and B are mainly due to mobility differences between MoX_2 and WX_2 compounds rather than strong variations in F_0^γ. Indeed from this data, we can show that the F_0^γ values are similar for all five materials, varying from 6×10^{11} for $MoTe_2$ to 7×10^{12} for WSe_2 (in SI units).

However, this data also highlights the limitations in Rose's model. Because the values of F_0^γ vary only weakly between materials, the variations in γ described above imply F_0 to vary over ~12 orders of magnitude among the materials studied. This is not realistic, meaning that while Rose captured the over-all behaviour with his model, the details are not correct.

7.4.5 *Photosensitivity*

This data clearly shows that the relatively poor photoresponse (represented here by $\frac{\sigma_{Light}}{\sigma_{Dark}}$) for $MoSe_2$, WSe_2 and $MoTe_2$ (figure 7.7 (bottom-right)) results from the large dark conductivities associated with these materials (figure 7.10 A). Relative to the dark case, at 980 W/m^2 the conductivity rises by a factor of 4 in the case of MoS_2 (best material) and a factor of just 0.15 in the case of WSe_2 (worst). High dark currents are especially undesirable in photo-detection. This facilitates choice of a high bandgap material or insulators, to limit background of thermal carriers for practical applications. In addition to affecting the lowest measurable illumination high dark current also decreases sensitivity at low light levels.[299, 300] This can be seen explicitly in figure 7.7 F, where the lowest light intensities used produced no measureable signal in the case of $MoTe_2$. Thus the dark conductivities of most of the TMDs studied here are too high for photo-detection capabilities, especially when used with in-plane geometry.[148]

Shown in figure 7.10 D is data for γ plotted versus the indirect bandgap for all five materials. This clearly shows a falloff in γ as the bandgap increases from 0.76 for $MoTe_2$ to 0.38 for WS_2. While sublinear intensity dependence has been observed for a number of materials,[254, 277**?** , 278] it is not usually observed for TMDs. This is because

recent photoconductive studies of TMDs have been dominated by measurements on individual nanosheets of mono or few layer MS_2 samples. Most of these report linear dependence[6, 260, 261] of photocurrent on light intensity with only a minority reporting sub-linear[64, 262] behaviour with γ values between 0.5[280] and 0.71.[88] In these cases, the sub-linear dependence is attributed to the presence of traps associated with the surface of the flakes. Liquid exfoliated nanosheets contain many flake edges which contribute localised states within the bandgap. Whether these states act as traps or recombination centres depends on the level of light intensity. As F increases, more trap states for electrons are converted into recombination centres, decreasing the majority carrier lifetime.[253, 255] Therefore it is common for disordered semiconducting films to display diminished responsivity at high light intensities and so values of $\gamma<1$.[254]

Rose's model links the exponent γ, to the characteristic trap energy, E_0, as described above. The data here has been used to calculate E_0 for each material (figure 7.10 D, inset). This data suggests the trap energy to fall off smoothly with bandgap, indicating the wider-gap materials to have shallower traps. The reason for this is not currently understood. More detailed experimental work, or indeed computer modelling, is needed to understand in more detail the trap states in these materials. This will be critical if disordered networks of nanosheets are to be used in future optoelectronic applications.

7.5 DISCUSSION

7.5.1 *Gold Contacts*

Gold electrodes have been chosen to contact films of all five TMDs. Au has commonly been used to make ohmic-like contacts to MoS_2 monolayers[72, 83, 84] at room temperature.[7, 94]This is in contrast to what would be expected from standard band alignment arguments, a contradiction that has been attributed to factors such as Fermi level pinning close to the CB.[7] The low formation energy associated with S-vacancies

for MoS_2 ensures they are a common defect in this material and should contribute a localised level within the bandgap close to the CB.[93–97]

Some finite barrier is often reported when using Au to contact thicker MoS_2 [6, 85–88] and WS_2[147, 301] samples. However, the barrier is often lower than that expected for a typical metal-semiconductor junction.[7, 94, 147] In addition to Fermi level pinning due to intrinsic stoichiometric defects such as S-vacancies, the situation is further complicated in thin films by the effects of grain boundaries. Such boundaries contain a high defect density and thus a large number of defect/disorder induced gap states (DIGS). Only sub-micron area electrodes, not in contact with grain boundaries are capable of manifesting rectifying I-Vs.[272, 273, 302]

Several studies on the electrical properties of WSe_2 have been published recently.[69, 102, 104] This material is less prone to Fermi level pinning than MoS_2 and can operate in both[69] p-type[104] or n-type[102] mode, depending on the contact metal selected. Much less work has so far been published on electrical characterisation of $MoSe_2$[112][303, 304] and $MoTe_2$.[305]

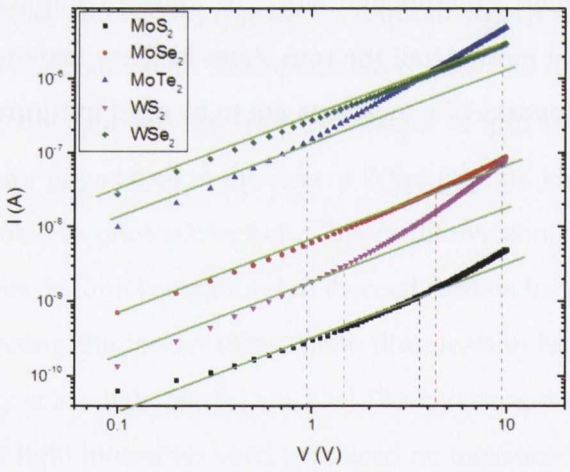

Figure 7.11: log-log plot of I-V curves for each TMD studied in this work. All materials display ohmic conduction (m=1 marked by green straight line as a guide to the eye), at least up to ~1 V with pre-patterned Au electrodes.

The decision to use gold on all five materials was based on a desire for consistency coupled with data from preliminary experiments which showed all materials to give symmetric I-V curves when using gold electrodes. Films of each material studied here

have been processed with the exact same procedure and are all characterised by a similar degree of disorder. Furthermore, differences in the bulk band structures[19, 22, 24, 26, 206, 268, 306] of TMDs are much less pronounced than for monolayers. Also in our favour is the fact that TMD CB offsets are also known to be much smaller than the VB offsets. This is due to the increased repulsion between M d_{z^2} and X p_x+p_y orbitals which make up the CB, as opposed to that between M $d_{x^2-y^2}$+d_{xy} and X p_x+p_y orbitals responsible for the formation of the VB.[23]

With this in mind one can tentatively propose a similar scenario at the metal semiconductor interface for each material here. This could also be related to a somewhat fortuitous pinning of the Fermi level close to the CB, resulting in an ohmic-like contact at room temperature. Such a contact would be consistent with the linear I-V curves at low voltages as in figure 7.7. This can be visualised more conveniently on a log-log plot as in figure 7.11. This implies ohmic conduction within this voltage range, though some non-linearity is noted at higher voltages. Future studies will no doubt find other metals more appropriate.

7.5.2 *Time Constants*

In most cases, the time constants associated with the slow rise and decay of photocurrent fall off with intensity as expected for systems with a distribution of localised states. Such behaviour is consistent with an increased number of such states acting as recombination centres at higher intensities once illumination has ceased.[253, 255] However, the data is much more scattered than that previously observed for out of plane, solution processed MoS_2 photodetectors.[112] The time constants, measured for a rising photocurrent in each material at a fixed intensity of F=250 W m^{-2}, are given in figure 7.8 F and are typically tens of seconds. Interestingly, the MoS_2 time constant is lower than that observed from out of plane photocurrent measurements (~100 s).[112] In any case, this data shows the photoresponse to be trap-limited for all five materials.[253]

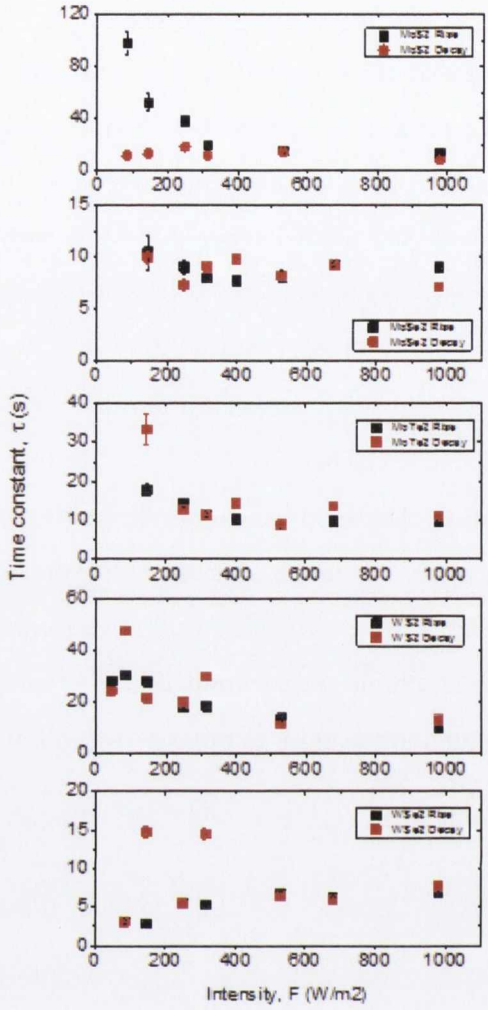

Figure 7.12: Measured time constants associated with both rise and decay of photocurrent with time for all materials, plotted versus incident intensity. Exponential behaviour is only clearly observable due to signal to noise ratio.

The poorer relation of time constants to intensity fall off in this chapter compared with the last may be explained in part by the lower voltage used to bias the films here (1 V versus 15 V in chapter 6). At lower biases the time dependent I(t) curves are not as well defined in shape as at higher biases, making the fitting of the exponential more difficult. Trapped charge also distorts the signal throughout this part of the measurement.

7.6 CONCLUSION

Photoconductivity measurements on thin films, prepared from disordered networks of nanosheets of five transition metal chalcogenides have been performed. Significant differences in performance, with both dark- and photo-conductivity varying widely between materials are found. The dark conductivity falls exponentially with bandgap with clear differences between Mo- and W-based materials. The photoconductivity could also be clearly differentiated between Mo- and W-based materials.

Both the time- and intensity-dependence of the photoconductivity indicate the photoresponse to be limited by the presence of traps. The practical disadvantages of this are a slow photoresponse and a sublinear dependence of photoconductivity on intensity. Because of the dependence of dark conductivity on bandgap, the ratio of photo- to dark conductivity is much larger for the wide bandgap TMDs (MoS_2 and WS_2) even though they tend to display relatively small photoconductivities. Thus, this palette of materials presents different options, dependent on whether high absolute or relative photocurrent is required.

The production of solution-processed films of inorganic nanosheets is still very much in its infancy. One can imagine many ways to improve these systems. For example, in the future much greater control will be developed over the size and thickness of nanosheets, leading to much more uniform networks.[226] In addition, the development of better film formation techniques, whether by spray, inkjet or blade coating will lead to more controllable film morphologies. Moreover, chemistries might be developed to modify or eliminate the effect of traps, perhaps by healing chalcogen vacancies or pacifying edge states.[307]

The work in this chapter plays a part in the early stages of development of opto-electronic applications of solution processed nanosheet networks. It is believed that this field has much promise and will play an important role on the development of nanostructured printed electronics.

8

CONCLUSIONS AND FUTURE WORK

8.1 CONCLUSIONS

In this work a comprehensive study of the dispersability of MoS_2, $MoSe_2$, $MoTe_2$ & WS_2 in a range of solvents has been carried out to investigate the effect of transition metal atom and chalcogen atom on solubility. Relatively high concentrations (table 4.3) are only obtained in solvents with surface energies close to 70 mJ/m^2 (surface tension close to 40 mJ/m^2), agreeing with solubility theory which predicts nanomaterials to be well dispersed in solvents with matching surface energy. The data have also been described in terms of Hildebrand and Hansen's traditional cohesive energy density based solubility parameters. In all cases the dispersed concentration falls off exponentially with the Flory-Huggins parameter, suggesting solubility theory can be used to understand the interactions between the solvent medium and nanosheets.

The solubility parameters of each material investigated are very similar (table 4.2), meaning the same set of solvents can be used to exfoliate each material. This is important from the perspective of applications requiring mixing such as conductive composites[53, 55] (with graphene or nanotubes) or bulk nano-heterojunction solar cells.[157–159]

A significant degree of scatter in the experimental data means the solubility theory used here is a good first order description and can give qualitative information on the dispersion of layered compounds. However, computational and IGC experimental data suggest specific solvent-solute interactions for nanostructures, that could aid or discourage solubility, are not accounted for in the theory.

Liquid phase exfoliation constitutes a solution processing method which makes it amenable to industrial scale-up.[200] However films formed from such a method have

an inherently poor conductivity due to the disordered nature of the resulting network and large associated density of inter-flake junctions. This led to the preparation of thin film composites of both SWNTs and exfoliated graphene nanosheets (the conducting nano-filler) in a matrix of exfoliated MoS_2 nanosheets. A combination of scanning electron microscopy and Raman spectroscopy shows these mixtures to be uniform down to a length-scale of ~microns. An increase in conductivity of up to ~9 orders of magnitude is realisable on addition of the nano-conducting phase. In both cases, the conductivity obeys percolation scaling laws both above and below the percolation threshold. The percolation thresholds are $\phi_c = 2.6$ vol% and $\phi_c = 22.2$ vol% for the MoS_2-SWNT and MoS_2-graphene composites respectively.

For the SWNT filled composites, this low percolation threshold means that conductivities as high as ~40 S m^{-1} for volume fractions as low as ~4 vol% are achievable. Similar results are expected to be found for other exfoliated layered compounds filled with nanoconductors. Such materials will be important in a range of applications from thermoelectric devices to electrodes in batteries and supercapacitors. This work represents the first detailed study of such 2D–2D and 1D–2D composites. Further work is required to understand the role of the matrix nanostructure in determining the performance of such composites.

A method has been developed to prepare solution processed thin films of MoS_2 which can be fabricated into photodetectors. These show a four-fold increase in conductivity on exposure to one-sun broadband illumination. Due to the presence of traps the photo-response scales sub-linearly with intensity and slowly with time. The photoresponsivity is similar to that of early reports for graphene.[264]

The ability to prepare photodetectors from inorganic nanomaterials by solution processing based techniques is an important step and should allow facile fabrication of large area, solution exfoliated 2D optoelectronic devices at low cost.

Although it is the most widely studied, MoS_2 is only one of a group of six Mo and W based semiconducting TMDs. Photoconductivity measurements have been performed on thin films, prepared from disordered networks of nanosheets of five transition metal dichalcogenides; MoS_2, $MoSe_2$, $MoTe_2$, WS_2 and WSe_2. Significant

differences in performance, with both dark- and photo-conductivity varying widely between materials are found. The dark conductivity falls exponentially with bandgap with clear differences between Mo- and W-based materials. The photoconductivity could also be clearly differentiated between Mo- and W-based materials.

Again, both the time- and intensity-dependence of the photoconductivity indicate the photoresponse to be limited by the presence of traps. The practical disadvantages of this are a slow photoresponse and a sublinear dependence of photoconductivity on intensity. Because of the dependence of dark conductivity on bandgap, the ratio of photo- to dark conductivity is much larger for the wide bandgap TMDs (MoS_2 and WS_2) even though they tend to display relatively small photoconductivities. Thus, this palette of materials presents different options, dependent on whether high absolute or relative photocurrent is required.

The production of solution-processed films of inorganic nanosheets is still very much in its infancy. One could imagine many ways to improve these systems. For example, in the future much greater control over the size and thickness of nanosheets is expected, leading to much more uniform networks.[226] In addition, the development of better film formation techniques, whether by spray-, inkjet- or blade coating will lead to more controllable film morphologies. Moreover, chemistries might be developed to modify or eliminate the effect of traps, perhaps by healing chalcogen vacancies or pacifying edge states.[307]

It is hoped that the work in this thesis plays a part in the early stages of the development of optoelectronic applications for solution processed nanosheet networks. It is believed that this field has much promise and will play an important role on the development of nanostructured printed electronics.

8.2 FUTURE WORK

8.2.1 *Negative Photoconductivity*

The decision to use un-centrifuged MoS_2 dispersion to test the photoconductivity was initially borne out of practical concerns to stop the electrodes shorting when fabricating the photodetector in an out-of-plane sandwich structure. Fabricating such devices in an in-plane geometry bypasses these constraints, allowing one to use standard centrifuged dispersions comprising smaller, thinner nanosheets. However, once such devices were fabricated an anomaly was noticed in the conductivity on broadband illumination, whereby the film becomes more resistive a short time after illumination following an initial increase as in figure 8.1.

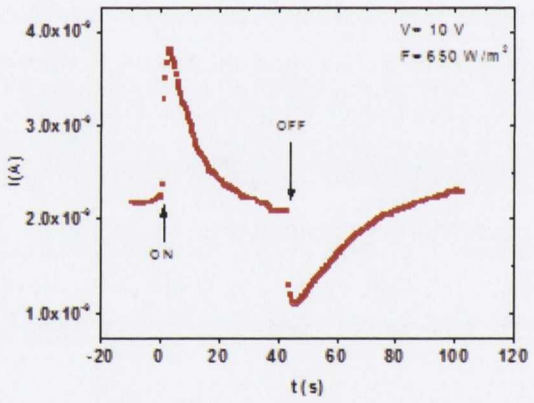

Figure 8.1: Negative photoconductivity, whereby film becomes more resistive under illumination than in the dark

Such effects have been noticed in MoS_2 some time ago.[290] This effect has also been noted sporadically throughout the literature in other semiconducting systems with certain impurities.[308] The effect can be explained by a simple model in which two distinct trapping levels are present within the bandgap, as in figure 8.2.[309–311]

1. The light is turned on and electrons are initially excited from the VB to the upper impurity level in the bandgap

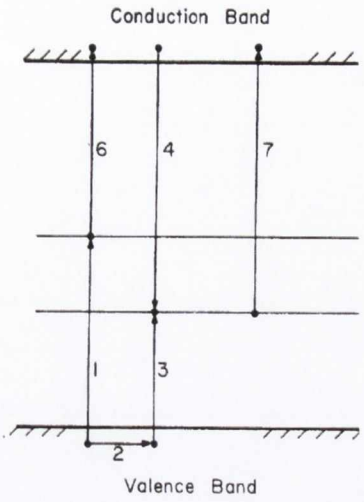

Figure 8.2: Transitions involved in negative photoconductivity model of Johnson & Levinstein. Adapted from Penchina et al. [311].

2. The hole left behind in the VB is now free to conduct
3. After a short time this free hole recombines at the lower impurity level, which is normally occupied by electrons
4. An excited electron is then trapped at this lower impurity level
5. The light is turned off and holes are no longer being generated in the VB
6. Electrons are slowly thermally excited to the CB from the upper impurity level
7. Photons of higher energy excite electrons from the lower impurity level to the CB, giving an additional positive photoconductivity

The effect can occur if minority carriers are optically freed from a localised level within the bandgap due to rapid recombination with majority carriers. It is rarely seen as in order for this effect to manifest a number of conditions must be co-fulfilled: The thermal freeing of electrons from shallow levels must be slower than recombination at the lower impurity level, holes must not recombine at the higher level which must remain above the (quasi) Fermi level, the cross-section of the states for the majority carriers at the higher level must be less than that at the lower level and the density of states at the lower impurity level and its cross-section for minority carriers must not be too small.[253]

Whilst this affect may not be useful for optoelectronic applications it is an interesting phenomenon to study. As things stand it seems as if the effect is induced when smaller nanosheets are present in the dispersion as is the case when using the usual centrifugation regime of 1500 RPM for 90 minutes. Smaller nanosheets have a larger ratio of edge sites to basal plane sites than larger, less well exfoliated platelets. Such edge sites are chemically and electrically very different to bulk MoS_2 which could be responsible for the effects seen.[60, 271] With this in mind a study has been conducted in conjunction with recent size selection methods developed using different centrifuge regimes.[52] The aim is to discern at roughly what size the negative photoconductivity becomes prominent, if it is indeed a size related effect. The data is yet to be fully analysed, but no such negative photoconductivity effects have been seen for MoS_2 or WS_2 so far.

Such size selection protocols have been developed using aqueous surfactant solutions as the solvent medium. Films were washed with DI water post processing to remove any lingering surfactant; it may well be the case that some surfactant still remained which had the effect of passivation of previously electrically active states within the bandgap. Alternately, the presence of NMP, which has not been used in this study (but was used in previous studied on centrifuged dispersions) may be responsible for the negative photoconductivity. One more effect that has not been investigated to this end also is the degree of dispersion polydispersity. With these layered materials having bandgaps which are a strong function of layer number[22, 312] between the bulk and monolayer limits, the effect could be a symptom of the energetic disorder that polydispersity may induce. More work is needed to fully characterise and understand the source of such effects so that they may be minimised in future optoelectronic device fabrication.

8.2.2 *Solution Processed Devices*

The feasibility for liquid phase exfoliation to be implemented with mature technologies like inkjet printing has been demonstrated recently by our group having fabricated

low-end photodetectors on transparent flexible substrates (figure).[187] This can be

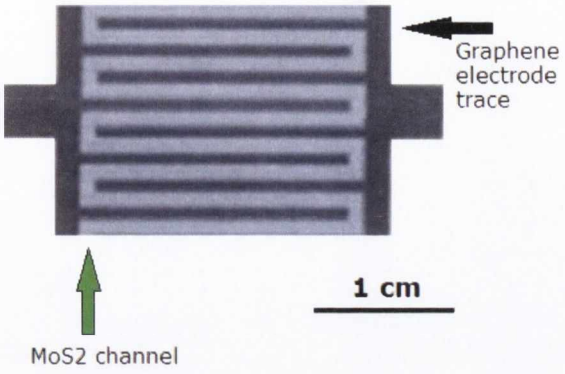

Figure 8.3: All inkjet printed photodetector with liquid phase exfoliated graphene electrodes and MoS_2 active channel printed on flexible PET substrate.[187]

done as solution processing techniques (dip-coating, spraying or inkjet printing) are low temperature, which also makes them inherently much easier to process. As such, they can be fabricated quickly and cheaply. To this end, it would be logical to begin to develop liquid phase processed materials for applications in other areas than just photo-detection such as FETs and solar cells.

Once suspended in liquids, nanosheets can be cheaply and easily deposited to form networks.[187, 313] Here the main limitation will be that the carrier mobility in a network would be expected to be much smaller than that in an individual nanosheet because of the necessity of inter-sheet hopping. However, in networks of carbon nanotubes[314] and graphene nanosheets[315, 316], the ratio of nano-object to network mobilities is often as low as 100. As TMD nanosheets have mobilities of ~100 cm^2/V s,[72] it may be possible to develop networks of nanosheets with mobilities of a few cm^2/V s, competitive with printable organics.[294]

In order to develop printed electronics applications of 2D materials, appropriate methods to controllably disperse high quality nanosheets in liquids are required. Importantly a method has recently been developed which allows the nanosheets to be sorted by size.[52] Such dispersions of exfoliated nanosheets are extremely processable and combining different types of nanomaterials will allow the production of a wide range of devices from these dispersions.

9

APPENDIX

BIBLIOGRAPHY

[1] Wilson, J. A., and Yoffe, A. D. (1969) The transition metal dichalcogenides discussion and interpretation of the observed optical, electrical and structural properties. *Advances in Physics 18*, 193–335.

[2] Coleman, J. N. et al. (2011) Two-Dimensional Nanosheets Produced by Liquid Exfoliation of Layered Materials. *Science 331*, 568–571.

[3] Bergin, S. D., Sun, Z., Rickard, D., Streich, P. V., Hamilton, J. P., and Coleman, J. N. (2009) Multicomponent Solubility Parameters for Single-Walled Carbon Nanotube-Solvent Mixtures. *ACS Nano 3*, 2340–2350.

[4] Hernandez, Y. et al. (2008) High-yield production of graphene by liquid-phase exfoliation of graphite. *Nature Nanotechnology 3*, 563–568.

[5] Tonndorf, P., Schmidt, R., Bottger, P., Zhang, X., Borner, J., Liebig, A., Albrecht, M., Kloc, C., Gordan, O., and Zahn, D. R. (2013) Photoluminescence emission and Raman response of monolayer MoS2, MoSe2 and WSe2. *Optics express 21*, 4908–4916.

[6] Choi, W., Cho, M. Y., Konar, A., Lee, J. H., Cha, G.-B., Hong, S. C., Kim, S., Kim, J., Jena, D., Joo, J., and Kim, S. (2012) High-Detectivity Multilayer MoS2 Phototransistors with Spectral Response from Ultraviolet to Infrared. *Advanced Materials 24*, 5832–5836.

[7] Das, S., Chen, H.-Y., Penumatcha, A. V., and Appenzeller, J. (2013) High Performance Multilayer MoS2 Transistors with Scandium Contacts. *Nano Letters 13*, 100–105.

[8] Lewis, N. S., and Crabtree, G. (2005) Basic Research Needs for Solar Energy Utilization: report of the Basic Energy Sciences Workshop on Solar Energy Utilization, April 18-21, 2005.

[9] Novoselov, K. S. (2004) Electric Field Effect in Atomically Thin Carbon Films. *Science 306*, 666–669.

[10] Nicolosi, V., Chhowalla, M., Kanatzidis, M. G., Strano, M. S., and Coleman, J. N. (2013) Liquid Exfoliation of Layered Materials. *Science 340*, 1226419–1226419.

[11] Novoselov, K. S., Jiang, D., Schedin, F., Booth, T. J., Khotkevich, V. V., Morozov, S. V., and Geim, A. K. (2005) Two-dimensional atomic crystals. *Proceedings of the National Academy of Sciences of the United States of America 102*, 10451–10453.

[12] Castro Neto, A. H., Peres, N. M. R., Novoselov, K. S., and Geim, A. K. (2009) The electronic properties of graphene. *Reviews of Modern Physics 81*, 109–162.

[13] Bonaccorso, F., Sun, Z., Hasan, T., and Ferrari, A. C. (2010) Graphene photonics and optoelectronics. *Nature Photonics 4*, 611–622.

[14] Balandin, A. A., Ghosh, S., Bao, W., Calizo, I., Teweldebrhan, D., Miao, F., and Lau, C. N. (2008) Superior Thermal Conductivity of Single-Layer Graphene. *Nano Letters 8*, 902–907.

[15] Scarpa, F., Adhikari, S., and Srikantha Phani, A. (2009) Effective elastic mechanical properties of single layer graphene sheets. *Nanotechnology 20*, 065709.

[16] Chhowalla, M., Shin, H. S., Eda, G., Li, L.-J., Loh, K. P., and Zhang, H. (2013) The chemistry of two-dimensional layered transition metal dichalcogenide nanosheets. *Nature Chemistry 5*, 263–275.

[17] Wilson, A., and Wilson, *Semi-Conductors and Metals: An Introduction to the Electron Theory of Metals*; Cambridge physical tracts; Cambridge University Press, 2011.

[18] McGovern, I. T., Williams, R. H., and Parke, A. W. (1979) The electronic structure of MoS2 and alphaMoTe2 by photoelectron spectroscopy using line and synchrotron sources. *Journal of Physics C: Solid State Physics 12*, 2689.

[19] Boker, T., Severin, R., Muller, A., Janowitz, C., Manzke, R., Voss, D., Kroger, P., Mazur, A., and Pollmann, J. (2001) Band structure of MoS 2, MoSe 2, and alpha-

MoTe 2: angle-resolved photoelectron spectroscopy and ab initio calculations. *Physical Review B 64*, 235305.

[20] Mattheiss, L. (1973) Band structures of transition-metal-dichalcogenide layer compounds. *Physical Review B 8*, 3719.

[21] Mattheiss, L. (1973) Energy Bands for 2H-NbSe_ ${$2$}$ and 2H-MoS_ ${$2$}$. *Physical Review Letters 30*, 784–787.

[22] Kuc, A., Zibouche, N., and Heine, T. (2011) Influence of quantum confinement on the electronic structure of the transition metal sulfide TS2. *Physical Review B 83*.

[23] Kang, J., Tongay, S., Zhou, J., Li, J., and Wu, J. (2013) Band offsets and heterostructures of two-dimensional semiconductors. *Applied Physics Letters 102*, 012111–012111.

[24] Jiang, H. (2012) Electronic Band Structures of Molybdenum and Tungsten Dichalcogenides by the GW Approach. *The Journal of Physical Chemistry C 116*, 7664–7671.

[25] Beal, A. R., and Hughes, H. P. (1979) Kramers-Kronig analysis of the reflectivity spectra of 2H-MoS2, 2H-MoSe2 and 2H-MoTe2. *Journal of Physics C: Solid State Physics 12*, 881.

[26] Coehoorn, R., Haas, C., Dijkstra, J., Flipse, C. J. F., de Groot, R. A., and Wold, A. (1987) Electronic structure of MoSe_{2}, MoS_{2}, and WSe_{2}. I. Band-structure calculations and photoelectron spectroscopy. *Physical Review B 35*, 6195–6202.

[27] Splendiani, A., Sun, L., Zhang, Y., Li, T., Kim, J., Chim, C.-Y., Galli, G., and Wang, F. (2010) Emerging Photoluminescence in Monolayer MoS2. *Nano Lett. 10*, 1271–1275.

[28] others,, et al. (1997) Occupied and unoccupied electronic band structure of WSe_ ${$2$}$. *Physical Review B 55*, 10400.

[29] Mak, K. F., He, K., Lee, C., Lee, G. H., Hone, J., Heinz, T. F., and Shan, J. (2012) Tightly bound trions in monolayer MoS2. *Nature Materials*

[30] Tributsch, H. (1979) Electrochemical Solar Cells based on Layer Type Transition Metal Compounds, Performance of Electrode Material. *Solar Energy Materials 1*, 257–269.

[31] Mak, K. F., Lee, C., Hone, J., Shan, J., and Heinz, T. F. (2010) Atomically Thin MoS_{2}: A New Direct-Gap Semiconductor. *Physical Review Letters 105*.

[32] Wang, Q. H., Kalantar-Zadeh, K., Kis, A., Coleman, J. N., and Strano, M. S. (2012) Electronics and optoelectronics of two-dimensional transition metal dichalcogenides. *Nature Nanotechnology 7*, 699–712.

[33] Tongay, S., Zhou, J., Ataca, C., Lo, K., Matthews, T. S., Li, J., Grossman, J. C., and Wu, J. (2012) Thermally Driven Crossover from Indirect toward Direct Bandgap in 2D Semiconductors: MoSe2 versus MoS2. *Nano Letters*

[34] Ferrari, A. C., and Basko, D. M. (2013) Raman spectroscopy as a versatile tool for studying the properties of graphene. *Nature Nanotechnology 8*, 235–246.

[35] others,, et al. (2003) Double resonance Raman spectroscopy of single-wall carbon nanotubes. *New Journal of Physics 5*, 157.

[36] Kittel, C. *Introduction to solid state physics*; Wiley: Hoboken, NJ, 2005.

[37] Verble, J., and Wieting, T. (1970) Lattice Mode Degeneracy in MoS2 and Other Layer Compounds. *Physical Review Letters 25*, 362–365.

[38] Sekine, T., Izumi, M., Nakashizu, T., Uchinokura, K., and Matsuura, E. (1980) Raman Scattering and Infrared Reflectance in 2H-MoSe2. *Journal of the Physics Society Japan 49*, 1069–1077.

[39] Lee, C., Yan, H., Brus, L. E., Heinz, T. F., Hone, J., and Ryu, S. (2010) Anomalous Lattice Vibrations of Single- and Few-Layer MoS2. *ACS Nano 4*, 2695–2700.

[40] Berkdemir, A., Gutierrez, H. R., Botello-Mendez, A. R., Perea-Lopez, N., Elias, A. L., Chia, C.-I., Wang, B., Crespi, V. H., Lopez-Urias, F., Charlier, J.-C., Terrones, H., and Terrones, M. (2013) Identification of individual and few layers of WS2 using Raman Spectroscopy. *Scientific Reports* 3.

[41] Li, H., Zhang, Q., Yap, C. C. R., Tay, B. K., Edwin, T. H. T., Olivier, A., and Baillargeat, D. From Bulk to Monolayer MoS2: Evolution of Raman Scattering. *Advanced Functional Materials*

[42] Molina-Sanchez, A., and Wirtz, L. (2011) Phonons in single-layer and few-layer MoS_{2} and WS_{2}. *Physical Review B* 84.

[43] Zhao, W., Ghorannevis, Z., Amara, K. K., Pang, J. R., Toh, M., Zhang, X., Kloc, C., Tan, P. H., and Eda, G. (2013) Lattice dynamics in mono- and few-layer sheets of WS2 and WSe2. *Nanoscale* 5, 9677.

[44] Yamamoto, M., Wang, S. T., Ni, M., Lin, Y.-F., Li, S.-L., Aikawa, S., Jian, W.-B., Ueno, K., Wakabayashi, K., and Tsukagoshi, K. (2014) Strong Enhancement of Raman Scattering from a Bulk-Inactive Vibrational Mode in Few-Layer $MoTe_2$. *ACS Nano* 140331124934002.

[45] Zhao, W., Ghorannevis, Z., Chu, L., Toh, M., Kloc, C., Tan, P.-H., and Eda, G. (2012) Evolution of Electronic Structure in Atomically Thin Sheets of WS2 and WSe2. *ACS Nano*

[46] Sahin, H., Tongay, S., Horzum, S., Fan, W., Zhou, J., Li, J., Wu, J., and Peeters, F. M. (2013) Anomalous Raman Spectra and Thickness Dependent Electronic properties of WSe2. *arXiv:1303.5861*

[47] Eda, G., Yamaguchi, H., Voiry, D., Fujita, T., Chen, M., and Chhowalla, M. (2011) Photoluminescence from chemically exfoliated MoS2. *Nano Letters*

[48] Joensen, P., Frindt, R., and Morrison, S. (1986) Single-layer MoS2. *Materials Research Bulletin* 21, 457–461.

[49] Morales, J., Santos, J., and Tirado, J. (1996) Electrochemical studies of lithium and sodium intercalation in MoSe2. *Solid state ionics* 83, 57–64.

[50] Fang, H., Tosun, M., Seol, G., Chang, T. C., Takei, K., Guo, J., and Javey, A. (2013) Degenerate n-Doping of Few-Layer Transition Metal Dichalcogenides by Potassium. *Nano Letters 13*, 1991–1995.

[51] Smith, R. J., King, P. J., Lotya, M., Wirtz, C., Khan, U., De, S., O Neill, A., Duesberg, G. S., Grunlan, J. C., Moriarty, G., Chen, J., Wang, J., Minett, A. I., Nicolosi, V., and Coleman, J. N. (2011) Large-Scale Exfoliation of Inorganic Layered Compounds in Aqueous Surfactant Solutions. *Advanced Materials 23*, 3944–3948.

[52] Backes, C. et al. (2014) Edge and confinement effects allow in situ measurement of size and thickness of liquid-exfoliated nanosheets. *Nature Communications 5*.

[53] Cunningham, G., Lotya, M., McEvoy, N., Duesberg, G. S., van der Schoot, P., and Coleman, J. N. (2012) Percolation scaling in composites of exfoliated MoS2 filled with nanotubes and graphene. *Nanoscale*

[54] Higgins, T. M., McAteer, D., Coelho, J. C. M., Sanchez, B. M., Gholamvand, Z., Moriarty, G., McEvoy, N., Berner, N. C., Duesberg, G. S., Nicolosi, V., and Coleman, J. N. (2014) The Effect of Percolation on the Capacitance of Supercapacitor Electrodes Prepared from Composites of Manganese Dioxide Nano-Platelets and Carbon Nanotubes. *ACS Nano* 140908114115005.

[55] Hanlon, D., Backes, C., Higgins, T. M., Hughes, M., O Neill, A., King, P., McEvoy, N., Duesberg, G. S., Mendoza Sanchez, B., Pettersson, H., Nicolosi, V., and Coleman, J. N. (2014) Production of Molybdenum Trioxide Nanosheets by Liquid Exfoliation and Their Application in High-Performance Supercapacitors. *Chemistry of Materials* 140213071119008.

[56] Lee, J.-H., Lee, E. K., Joo, W.-J., Jang, Y., Kim, B.-S., Lim, J. Y., Choi, S.-H., Ahn, S. J., Ahn, J. R., Park, M.-H., Yang, C.-W., Choi, B. L., Hwang, S.-W., and Whang, D. (2014) Wafer-Scale Growth of Single-Crystal Monolayer Graphene on Reusable Hydrogen-Terminated Germanium. *Science 344*, 286–289.

[57] Laskar, M. R., Ma, L., K, S., Park, P. S., Krishnamoorthy, S., Nath, D. N., Lu, W., Wu, Y., and Rajan, S. (2013) Large Area Single Crystal (0001) Oriented MoS2 Thin Films. *arXiv:1302.3177*

[58] Cong, C., Shang, J., Wu, X., Cao, B., Peimyoo, N., Qiu, C., Sun, L., and Yu, T. (2014) Synthesis and Optical Properties of Large-Area Single-Crystalline 2D Semiconductor WS_2 Monolayer from Chemical Vapor Deposition. *Advanced Optical Materials 2*, 131–136.

[59] van der Zande, A. M., Huang, P. Y., Chenet, D. A., Berkelbach, T. C., You, Y., Lee, G.-H., Heinz, T. F., Reichman, D. R., Muller, D. A., and Hone, J. C. (2013) Grains and grain boundaries in highly crystalline monolayer molybdenum disulphide. *Nature Materials 12*, 554–561.

[60] Najmaei, S., Liu, Z., Zhou, W., Zou, X., Shi, G., Lei, S., Yakobson, B. I., Idrobo, J.-C., Ajayan, P. M., and Lou, J. (2013) Vapour phase growth and grain boundary structure of molybdenum disulphide atomic layers. *Nature Materials*

[61] Roy, K., Mukhopadhyay, S., and Mahmoodi-Meimand, H. (2003) Leakage current mechanisms and leakage reduction techniques in deep-submicrometer CMOS circuits. *Proceedings of the IEEE 91*, 305–327.

[62] Tosun, M., Chuang, S., Fang, H., Sachid, A. B., Hettick, M., Lin, Y., Zeng, Y., and Javey, A. (2014) High-Gain Inverters Based on WSe_2 Complementary Field-Effect Transistors. *ACS Nano 8*, 4948–4953.

[63] Liu, H., Neal, A. T., and Ye, P. D. (2012) Channel Length Scaling of MoS_2 MOSFETs. *ACS Nano 6*, 8563–8569.

[64] Yim, C., O'Brien, M., McEvoy, N., Riazimehr, S., Schafer-Eberwein, H., Bablich, A., Pawar, R., Iannaccone, G., Downing, C., Fiori, G., Lemme, M. C., and Duesberg, G. S. (2014) Heterojunction Hybrid Devices from Vapor Phase Grown MoS2. *Scientific Reports 4*.

[65] Jariwala, D., Sangwan, V. K., Wu, C.-C., Prabhumirashi, P. L., Geier, M. L., Marks, T. J., Lauhon, L. J., and Hersam, M. C. (2013) Gate-tunable carbon

nanotube-MoS2 heterojunction pn diode. *Proceedings of the National Academy of Sciences 110*, 18076–18080.

[66] Cheng, R., Li, D., Zhou, H., Wang, C., Yin, A., Jiang, S., Liu, Y., Chen, Y., Huang, Y., and Duan, X. (2014) Electroluminescence and Photocurrent Generation from Atomically Sharp WSe_2 /MoS_2 Heterojunction *pn* Diodes. *Nano Letters* 140908130432001.

[67] Pospischil, A., Furchi, M. M., and Mueller, T. (2014) Solar-energy conversion and light emission in an atomic monolayer pn diode. *Nature Nanotechnology 9*, 257–261.

[68] Ross, J. S., Klement, P., Jones, A. M., Ghimire, N. J., Yan, J., Mandrus, D. G., Taniguchi, T., Watanabe, K., Kitamura, K., Yao, W., Cobden, D. H., and Xu, X. (2014) Electrically tunable excitonic light-emitting diodes based on monolayer WSe2 pn junctions. *Nature Nanotechnology 9*, 268–272.

[69] Das, S., and Appenzeller, J. (2013) WSe2 field effect transistors with enhanced ambipolar characteristics. *Applied Physics Letters 103*, 103501.

[70] Gu, W., Shen, J., and Ma, X. (2014) Fabrication and electrical properties of MoS2 nanodisc-based back-gated field effect transistors. *Nanoscale research letters 9*, 1–5.

[71] Pradhan, N. R., Rhodes, D., Zhang, Q., Talapatra, S., Terrones, M., Ajayan, P. M., and Balicas, L. (2013) Intrinsic carrier mobility of multi-layered MoS2 field-effect transistors on SiO2. *Applied Physics Letters 102*, 123105.

[72] Radisavljevic, B., Radenovic, A., Brivio, J., Giacometti, V., and Kis, A. (2011) Single-layer MoS2 transistors. *Nature Nanotechnology 6*, 147–150.

[73] Kim, S., Konar, A., Hwang, W.-S., Lee, J. H., Lee, J., Yang, J., Jung, C., Kim, H., Yoo, J.-B., Choi, J.-Y., Jin, Y. W., Lee, S. Y., Jena, D., Choi, W., and Kim, K. (2012) High-mobility and low-power thin-film transistors based on multilayer MoS2 crystals. *Nature Communications 3*, 1011.

[74] Ayari, A., Cobas, E., Ogundadegbe, O., and Fuhrer, M. S. (2007) Realization and electrical characterization of ultrathin crystals of layered transition-metal dichalcogenides. *Journal of Applied Physics 101*, 014507.

[75] Ghatak, S., Pal, A. N., and Ghosh, A. (2011) Nature of Electronic States in Atomically Thin MoS $_2$ Field-Effect Transistors. *ACS Nano 5*, 7707–7712.

[76] Bolotin, K., Sikes, K., Jiang, Z., Klima, M., Fudenberg, G., Hone, J., Kim, P., and Stormer, H. (2008) Ultrahigh electron mobility in suspended graphene. *Solid State Communications 146*, 351–355.

[77] Fivaz, R., and Mooser, E. (1967) Mobility of charge carriers in semiconducting layer structures. *Physical Review 163*, 743.

[78] Kaasbjerg, K., Thygesen, K. S., and Jacobsen, K. W. (2012) Phonon-limited mobility in n-type single-layer MoS_{2} from first principles. *Physical Review B 85*.

[79] Huang, A. P., Yang, Z. C., and Chu, P. K. (2010) Hafnium-based high-k gate dielectrics. *Advances in Solid State Circuits Technologies* 333–350.

[80] Sze, S., and Ng, K. *Physics of Semiconductor Devices*; Wiley, 2006.

[81] Pearman, D. Electrical Characterisation and Modelling of Schottky barrier metal source/drain MOSFETs. Ph.D. thesis, 2007.

[82] Popov, I., Seifert, G., and Tomanek, D. (2012) Designing Electrical Contacts to MoS_{2} Monolayers: A Computational Study. *Physical Review Letters 108*.

[83] Radisavljevic, B., Whitwick, M., and Kis, A. (2011) Integrated Circuits and Logic Operations Based on Single-Layer MoS2. *ACS nano*

[84] Lembke, D., and Kis, A. (2012) Breakdown of High-Performance Monolayer MoS $_2$ Transistors. *ACS Nano 6*, 10070–10075.

[85] Tsai, D.-S., Lien, D.-H., Tsai, M.-L., Su, S.-H., Chen, K.-M., Ke, J.-J., Yu, Y.-C., Li, L.-J., and He, J.-H. (2014) Trilayered MoS2-MSMl Photodetectors: Photogain and Radiation Resistance. *IEEE Journal of Selected Topics in Quantum Electronics 20*, 30–35.

[86] Lee, K., Kim, H.-Y., Lotya, M., Coleman, J. N., Kim, G.-T., and Duesberg, G. S. (2011) Electrical Characteristics of Molybdenum Disulfide Flakes Produced by Liquid Exfoliation. *Advanced Materials* n/a–n/a.

[87] Shanmugam, M., Durcan, C. A., and Yu, B. (2012) Layered Semiconductor Molybdenum Disulfide Nanomembrane Based Schottky-Barrier Solar Cells. *Nanoscale*

[88] Tsai, D.-S., Liu, K.-K., Lien, D.-H., Tsai, M.-L., Kang, C.-F., Lin, C.-A., Li, L.-J., and He, J.-H. (2013) Few-Layer MoS2 with High Broadband Photogain and Fast Optical Switching for Use in Harsh Environments. *ACS Nano*

[89] Rhoderick, E., and Williams, R. *Metal-semiconductor contacts*; Monographs in electrical and electronic engineering; Clarendon Press, 1988.

[90] Padovani, F., and Stratton, R. (1966) Field and Thermionic Emission in Schottky Barriers. *Solid-State Electronics 9*, 695–707.

[91] Crowell, C. (1965) The Richardson Constant for Thermionic Emission in SB Diodes. *Solid-State Electronics 8*, 395–399.

[92] Bhat, K., and Madras, I. I. o. T. Lecture 15: Ohmic Contacts on Semiconductors.

[93] Zhou, W., Zou, X., Najmaei, S., Liu, Z., Shi, Y., Kong, J., Lou, J., Ajayan, P. M., Yakobson, B. I., and Idrobo, J.-C. (2013) Intrinsic Structural Defects in Monolayer Molybdenum Disulfide. *Nano Letters 13*, 2615–2622.

[94] McDonnell, S., Addou, R., Buie, C., Wallace, R. M., and Hinkle, C. L. (2014) Defect-Dominated Doping and Contact Resistance in MoS $_2$. *ACS Nano 8*, 2880–2888.

[95] Liu, D., Guo, Y., Fang, L., and Robertson, J. (2013) Sulfur vacancies in monolayer MoS2 and its electrical contacts. *Applied Physics Letters 103*, 183113.

[96] Komsa, H.-P., Kurasch, S., Lehtinen, O., Kaiser, U., and Krasheninnikov, A. V. (2013) From point to extended defects in two-dimensional MoS_{2}: Evolution of atomic structure under electron irradiation. *Physical Review B 88*.

[97] Komsa, H.-P., Kotakoski, J., Kurasch, S., Lehtinen, O., Kaiser, U., and Krasheninnikov, A. V. (2012) Two-Dimensional Transition Metal Dichalcogenides under Electron Irradiation: Defect Production and Doping. *Physical Review Letters 109*.

[98] Das, S., and Appenzeller, J. (2013) Where Does the Current Flow in Two-Dimensional Layered Systems? *Nano Letters 13*, 3396–3402.

[99] Das, S., and Appenzeller, J. (2013) Screening and interlayer coupling in multilayer MoS2. *physica status solidi (RRL) Rapid Research Letters 7*, 268–273.

[100] Sui, Y., and Appenzeller, J. (2009) Screening and Interlayer Coupling in Multilayer Graphene Field-Effect Transistors. *Nano Letters 9*, 2973–2977.

[101] Podzorov, V., Gershenson, M. E., Kloc, C., Zeis, R., and Bucher, E. (2004) Novel High-Mobility Field-Effect Transistors Based on Transition Metal Dichalcogenides. *arXiv preprint cond-mat/0401243*

[102] Liu, W., Kang, J., Sarkar, D., Khatami, Y., Jena, D., and Banerjee, K. (2013) Role of Metal Contacts in Designing High-Performance Monolayer n-Type WSe_2 Field Effect Transistors. *Nano Letters 13*, 1983–1990.

[103] Chuang, H.-J., Tan, X., Ghimire, N. J., Perera, M. M., Chamlagain, B., Cheng, M. M.-C., Yan, J., Mandrus, D., TomÃ¡nek, D., and Zhou, Z. (2014) High Mobility WSe_2 p - and n - Type Field-Effect Transistors Contacted by Highly Doped Graphene for Low-Resistance Contacts. *Nano Letters 14*, 3594–3601.

[104] Fang, H., Chuang, S., Chang, T. C., Takei, K., Takahashi, T., and Javey, A. (2012) High-Performance Single Layered WSe2 p-FETs with Chemically Doped Contacts. *Nano letters 12*, 3788–3792.

[105] Baugher, B. W. H., Churchill, H. O. H., Yang, Y., and Jarillo-Herrero, P. (2014) Optoelectronic devices based on electrically tunable pn diodes in a monolayer dichalcogenide. *Nature Nanotechnology 9*, 262–267.

[106] Keyes, R. W. (2005) Physical limits of silicon transistors and circuits. *Reports on Progress in Physics 68*, 2701–2746.

[107] Dolui, K., Rungger, I., and Sanvito, S. (2013) Origin of the n-type and p-type conductivity of MoS_{2} monolayers on a SiO_{2} substrate. *Physical Review B 87*.

[108] Dolui, K., Rungger, I., Das Pemmaraju, C., and Sanvito, S. (2013) Possible doping strategies for MoS_{2} monolayers: An ab initio study. *Physical Review B 88*.

[109] El-Mahalawy, S. H., and Evans, B. L. (1977) Temperature dependence of the electrical conductivity and hall coefficient in 2H-MoS2, MoSe2, WSe2, and MoTe2. *physica status solidi (b) 79*, 713–722.

[110] Singh, J., and Shimakawa, K. *Advances in Amorphous Semiconductors*; Taylor & Francis, 2003.

[111] Gatensby, R., McEvoy, N., Lee, K., Hallam, T., Berner, N. C., Rezvani, E., Winters, S., O Brien, M., and Duesberg, G. S. (2014) Controlled synthesis of transition metal dichalcogenide thin films for electronic applications. *Applied Surface Science 297*, 139–146.

[112] Cunningham, G., Khan, U., Backes, C., Hanlon, D., McCloskey, D., Donegan, J. F., and Coleman, J. N. (2013) Photoconductivity of solution-processed MoS2 films. *Journal of Materials Chemistry C*

[113] Madan, A., and Shaw, M. *The physics and applications of amorphous semiconductors*; Academic Press, 1988.

[114] Morigaki, K. *Physics of Amorphous Semiconductors*; Imperial College Press, 1999.

[115] Adler, D. *Amorphous Semiconductors*; CRC Press, 1971.

[116] what-when how,, and Information, I. D. T. a. Electrical Properties of Polymers, Ceramics, Dielectrics, and Amorphous Materials Part 2 http://what-when-how.com/electronic-properties-of-materials/electrical-properties-of-polymers-ceramics-dielectrics-and-amorphous-materials-part-2/.

[117] Card, H. C., and Yang, E. S. (1977) Electronic processes at grain boundaries in polycrystalline semiconductors under optical illumination. *Electron Devices, IEEE Transactions on 24*, 397–402.

[118] Kazmerski, L. L. *Polycrystalline and amorphous thin films and devices*; Academic Press, 1980.

[119] Hartnagel, H. *Semiconducting transparent thin films*; Institute of Physics Pub., 1995.

[120] Sukach, A. V., Tetyorkin, V. V., and Krolevec, N. M. (2010) Mechanisms of carrier transport in CdTe polycrystalline films. *Semiconductor Physics, Quantum Electronics & Optoelectronics 13*, 221–225.

[121] Voiry, D., Salehi, M., Silva, R., Fujita, T., Chen, M., Asefa, T., Shenoy, V. B., Eda, G., and Chhowalla, M. (2013) Conducting MoS_2 Nanosheets as Catalysts for Hydrogen Evolution Reaction. *Nano Letters 13*, 6222–6227.

[122] Voiry, D., Yamaguchi, H., Li, J., Silva, R., Alves, D. C. B., Fujita, T., Chen, M., Asefa, T., Shenoy, V. B., Eda, G., and Chhowalla, M. (2013) Enhanced catalytic activity in strained chemically exfoliated WS2 nanosheets for hydrogen evolution. *Nature Materials 12*, 850–855.

[123] Wang, J.-Z., Lu, L., Lotya, M., Coleman, J. N., Chou, S.-L., Liu, H.-K., Minett, A. I., and Chen, J. (2013) Development of MoS_2 -CNT Composite Thin Film from Layered MoS_2 for Lithium Batteries. *Advanced Energy Materials 3*, 798–805.

[124] Feng, C., Ma, J., Li, H., Zeng, R., Guo, Z., and Liu, H. (2009) Synthesis of molybdenum disulfide MoS2 for lithium ion battery applications. *Materials Research Bulletin 44*, 1811–1815.

[125] Tai, S.-Y., Liu, C.-J., Chou, S.-W., Chien, F. S.-S., Lin, J.-Y., and Lin, T.-W. (2012) Few-layer MoS2 nanosheets coated onto multi-walled carbon nanotubes as a low-cost and highly electrocatalytic counter electrode for dye-sensitized solar cells. *Journal of Materials Chemistry 22*, 24753.

[126] Son, J. S., Choi, M. K., Han, M.-K., Park, K., Kim, J.-Y., Lim, S. J., Oh, M., Kuk, Y., Park, C., Kim, S.-J., and Hyeon, T. (2012) n-Type Nanostructured Thermoelectric Materials Prepared from Chemically Synthesized Ultrathin Bi_2Te_3 Nanoplates. *Nano Letters 12*, 640–647.

[127] Tang, X., Xie, W., Li, H., Zhao, W., Zhang, Q., and Niino, M. (2007) Preparation and thermoelectric transport properties of high-performance p-type Bi[sub 2]Te[sub 3] with layered nanostructure. *Applied Physics Letters 90*, 012102.

[128] Ramesh, R. (2012) SunShot Vision Study. *Technical Document US DoE Sunshot Initiative*

[129] Tao, M. (2008) Inorganic Photovoltaic Solar Cells: Silicon and Beyond. *The Electrochemical Society* 30–35.

[130] (2013) BP Statistical Review of World Energy 2013. *BP Statistical Review of World Energy 62*.

[131] Feldman, D., Barbose, G., Margolis, R., Wiser, R., Darghouth, N., and Goodrich, A. *Photovoltaic (PV) pricing trends: historical, recent, and near-term projections*; 2012.

[132] PV-Education, Detailed Balance http://pveducation.org/pvcdrom/solar-cell-operation/detailed-balance.

[133] Perlin, J. *Silicon solar cell turns 50*; 2004.

[134] Nagle, T. Quantum Efficiency as a Device-Physics Interpretation Tool for Thin-Film Solar Cells. Ph.D. thesis, 2007.

[135] Lindholm, F. A., Fossum, J. G., and Burgess, E. L. (1979) Application of the superposition principle to solar-cell analysis. *Electron Devices, IEEE Transactions on 26*, 165–171.

[136] Gorlich, P. R. *Photoconductivity in solids*; Routledge & K. Paul, 1967.

[137] Kayes, B. M., Nie, H., Twist, R., Spruytte, S. G., Reinhardt, F., Kizilyalli, I. C., and Higashi, G. S. 27.6record for single-junction solar cells under 1 sun illumination. Photovoltaic Specialists Conference (PVSC), 2011 37th IEEE. 2011; pp 000004–000008.

[138] Wurfel, P. (2002) Thermodynamic limitations to solar energy conversion. *Physica E: Low-dimensional Systems and Nanostructures 14*, 18–26.

[139] Kirchartz, T., Taretto, K., and Rau, U. (2009) Efficiency Limits of Organic Bulk Heterojunction Solar Cells. *The Journal of Physical Chemistry C 113*, 17958–17966.

[140] Shockley, W., and Queisser, H. J. (1961) Detailed Balance Limit of Efficiency of pn Junction Solar Cells. *Journal of Applied Physics 32*, 510–519.

[141] Nelson, C. A., Monahan, N. R., and Zhu, X.-Y. (2013) Exceeding the Shockley-Queisser limit in solar energy conversion. *Energy & Environmental Science 6*, 3508.

[142] Bernardi, M., Palummo, M., and Grossman, J. C. (2013) Extraordinary Sunlight Absorption and One Nanometer Thick Photovoltaics Using Two-Dimensional Monolayer Materials. *Nano Letters* 130710144533003.

[143] Chang, H.-Y., Yang, S., Lee, J., Tao, L., Hwang, W.-S., Jena, D., Lu, N., and Akinwande, D. (2013) High-Performance, Highly Bendable MoS_2 Transistors with High-K Dielectrics for Flexible Low-Power Systems. *ACS Nano 7*, 5446–5452.

[144] Pu, J., Yomogida, Y., Liu, K.-K., Li, L.-J., Iwasa, Y., and Takenobu, T. (2012) Highly Flexible MoS_2 Thin-Film Transistors with Ion Gel Dielectrics. *Nano Letters 12*, 4013–4017.

[145] Bertolazzi, S., Brivio, J., and Kis, A. (2011) Stretching and Breaking of Ultrathin MoS2. *ACS Nano 5*, 9703–9709.

[146] Loher, T., Tomm, Y., Pettenkofer, C., Klein, A., and Jaegermann, W. (2000) Structural dipoles at interfaces between polar II-VI semiconductors CdS and CdTe and non-polar layered transition metal dichalcogenide semiconductors MoTe2 and WSe2. *Semiconductor science and technology 15*, 514.

[147] Shanmugam, M., Bansal, T., Durcan, C. A., and Yu, B. (2012) Schottky-barrier solar cell based on layered semiconductor tungsten disulfide nanofilm. *Applied Physics Letters 101*, 263902.

[148] Esmaeili-Rad, M. R., and Salahuddin, S. (2013) High Performance Molybdenum Disulfide Amorphous Silicon Heterojunction Photodetector. *Scientific Reports 3*.

[149] Chuang, S., Kapadia, R., Fang, H., Chia Chang, T., Yen, W.-C., Chueh, Y.-L., and Javey, A. (2013) Near-ideal electrical properties of InAs/WSe2 van der Waals heterojunction diodes. *Applied Physics Letters 102*, 242101.

[150] Kosmider, K., and Fernandez-Rossier, J. (2012) Electronic properties of the MoS2-WS2 heterojunction. *arXiv:1212.0111*

[151] Lin, Y., Li, X., Xie, D., Feng, T., Chen, Y., Song, R., Tian, H., Ren, T., Zhong, M., Wang, K., and Zhu, H. (2013) Graphene/semiconductor heterojunction solar cells with modulated antireflection and graphene work function. *Energy & Environmental Science 6*, 108.

[152] Ma, Y., Dai, Y., Guo, M., Niu, C., and Huang, B. (2011) Graphene adhesion on MoS2 monolayer: An ab initio study. *Nanoscale 3*, 3883.

[153] Sachs, B., Britnell, L., Wehling, T. O., Eckmann, A., Jalil, R., Belle, B. D., Lichtenstein, A. I., Katsnelson, M. I., and Novoselov, K. S. (2013) Doping Mechanisms in Graphene-MoS2 Hybrids. *arXiv:1304.2236*

[154] Britnell, L., Ribeiro, R. M., Eckmann, A., Jalil, R., Belle, B. D., Mishchenko, A., Kim, Y.-J., Gorbachev, R. V., Georgiou, T., Morozov, S. V., Grigorenko, A. N., Geim, A. K., Casiraghi, C., Neto, A. H. C., and Novoselov, K. S. (2013) Strong Light-Matter Interactions in Heterostructures of Atomically Thin Films. *Science 340*, 1311–1314.

[155] Bertolazzi, S., Krasnozhon, D., and Kis, A. (2013) Nonvolatile Memory Cells Based on MoS_2/Graphene Heterostructures. *ACS Nano 7*, 3246–3252.

[156] Kroemer, H., and Schubert, E. Lecture 17:Band Diagrams of Heterostructures http://faculty.ksu.edu.sa/Kayed/Pages/QMAppliedtoSemiconductorDevicesByEFSchube 2004.

[157] Rath, A. K., Bernechea, M., Martinez, L., de Arquer, F. P. G., Osmond, J., and Konstantatos, G. (2012) Solution-processed inorganic bulk nano-heterojunctions and their application to solar cells. *Nature Photonics*

[158] Gur, I., Fromer, N. A., Geier, M. L., and Alivisatos, A. P. (2005) Air-Stable All-Inorganic Nanocrystal Solar Cells Processed from Solution. *Science 310*, 462–465.

[159] Shanmugam, M., Bansal, T., Durcan, C. A., and Yu, B. (2012) Molybdenum disulphide/titanium dioxide nanocomposite-poly 3-hexylthiophene bulk heterojunction solar cell. *Applied Physics Letters 100*, 153901.

[160] Snyder, J., and Toberer, E. (2008) Complex thermoelectric materials. *Nature Materials 7*, 105–115.

[161] Group, C. T. The Science of Thermoelectric Materials http://thermoelectrics.caltech.edu/thermoelectrics/index.html.

[162] Rowe, D. *CRC Handbook of Thermoelectrics*; Taylor & Francis, 1995.

[163] UK Governement, E. E. f. (2013) Element Energy Report for UK Government on Potential for Recovering and Using Surplus Heat from Industry.

[164] Dresselhaus, M. S., Chen, G., Tang, M. Y., Yang, R. G., Lee, H., Wang, D. Z., Ren, Z. F., Fleurial, J.-P., and Gogna, P. (2007) New Directions for LowDimensional Thermoelectric Materials. *Advanced Materials 19*, 1043–1053.

[165] Poudel, B., Hao, Q., Ma, Y., Lan, Y., Minnich, A., Yu, B., Yan, X., Wang, D., Muto, A., Vashaee, D., Chen, X., Liu, J., Dresselhaus, M. S., Chen, G., and Ren, Z. (2008) High-Thermoelectric Performance of Nanostructured Bismuth Antimony Telluride Bulk Alloys. *Science 320*, 634–638.

[166] Xu, L., Garrett, M. P., and Hu, B. (2012) Doping Effects on Internally Coupled Seebeck Coefficient, Electrical, and Thermal Conductivities in Aluminum-Doped TiO2. *The Journal of Physical Chemistry C 116*, 13020–13025.

[167] Costescu, R. M. (2004) Ultra-Low Thermal Conductivity in WAl2O3 Nanolaminates. *Science 303*, 989–990.

[168] Goodson, K. E. (2007) MATERIALS SCIENCE: Ordering Up the Minimum Thermal Conductivity of Solids. *Science 315*, 342–343.

[169] Chiritescu, C., Cahill, D. G., Nguyen, N., Johnson, D., Bodapati, A., Keblinski, P., and Zschack, P. (2007) Ultralow Thermal Conductivity in Disordered, Layered WSe2 Crystals. *Science 315*, 351–353.

[170] Teweldebrhan, D., Goyal, V., and Balandin, A. A. (2010) Exfoliation and Characterization of Bismuth Telluride Atomic Quintuples and Quasi-Two-Dimensional Crystals. *Nano Letters 10*, 1209–1218.

[171] Minnich, A. J., Dresselhaus, M. S., Ren, Z. F., and Chen, G. (2009) Bulk nanostructured thermoelectric materials: current research and future prospects. *Energy & Environmental Science 2*, 466.

[172] Mason, T. J. (2003) Sonochemistry and sonoprocessing: the link, the trends and (probably) the future. *Ultrasonics Sonochemistry 10*, 175–179.

[173] Suslick, K. S., and Price, G. J. (1999) Applications of ultrasound to materials chemistry. *Annual Review of Materials Science 29*, 295–326.

[174] Khan, U., O Neill, A., Lotya, M., De, S., and Coleman, J. N. (2010) High-Concentration Solvent Exfoliation of Graphene. *Small 6*, 864–871.

[175] O Neill, A., Khan, U., and Coleman, J. N. (2012) Preparation of High Concentration Dispersions of Exfoliated MoS2 with Increased Flake Size. *Chem. Mater.*

[176] Hennrich, F., Krupke, R., Arnold, K., Rojas Stutz, J. A., Lebedkin, S., Koch, T., Schimmel, T., and Kappes, M. M. (2007) The Mechanism of Cavitation-Induced Scission of Single-Walled Carbon Nanotubes. *The Journal of Physical Chemistry B 111*, 1932–1937.

[177] Mason, T., and Lorimer, J. *Sonochemistry: Theory, Applications and Uses of Ultrasound in Chemistry*; Ellis Horwood series in physical chemistral; Ellis Horwood, 1988.

[178] Inc, S. M. VCX-750 User Manual.

[179] O Neill, A., Khan, U., Nirmalraj, P. N., Boland, J., and Coleman, J. N. (2011) Graphene Dispersion and Exfoliation in Low Boiling Point Solvents. *J. Phys. Chem. C 115*, 5422–5428.

[180] Hernandez, Y., Lotya, M., Rickard, D., Bergin, S. D., and Coleman, J. N. (2009) Measurement of Multicomponent Solubility Parameters for Graphene Facilitates Solvent Discovery. *Langmuir 26*, 3208–3213.

[181] Cunningham, G., Lotya, M., Cucinotta, C. S., Sanvito, S., Bergin, S. D., Menzel, R., Shaffer, M. S. P., and Coleman, J. N. (2012) Solvent Exfoliation of Transition Metal Dichalcogenides: Dispersibility of Exfoliated Nanosheets Varies Only Weakly between Compounds. *ACS Nano 6*, 3468–3480.

[182] Agency, S. o. C. E. P. Office of Environmental Health Hazard Assessment Safe Drinking Water and Toxic Re-enforcement Act. 1986.

[183] Hettich, Hettich Mikro 22R User manual.

[184] Kim, H., Mattevi, C., Kim, H. J., Mittal, A., Mkhoyan, K. A., Riman, R. E., and Chhowalla, M. (2013) Optoelectronic properties of graphene thin films deposited by a Langmuir-Blodgett assembly. *Nanoscale 5*, 12365.

[185] Doherty, E. M., De, S., Lyons, P. E., Shmeliov, A., Nirmalraj, P. N., Scardaci, V., Joimel, J., Blau, W. J., Boland, J. J., and Coleman, J. N. (2009) The spatial uniformity and electromechanical stability of transparent, conductive films of single walled nanotubes. *Carbon 47*, 2466–2473.

[186] Sorel, S., Khan, U., and Coleman, J. N. (2012) Flexible, transparent dielectric capacitors with nanostructured electrodes. *Applied Physics Letters 101*, 103106.

[187] Finn, D., Lotya, M., Cunningham, G., Smith, R., McCloskey, D., Donegan, J., and Coleman, J. N. (2013) Inkjet deposition of liquid-exfoliated graphene and MoS2 nanosheets for printed device applications. *Journal of Materials Chemistry C*

[188] Li, X., Zhang, G., Bai, X., Sun, X., Wang, X., Wang, E., and Dai, H. (2008) Highly conducting graphene sheets and Langmuir-Blodgett films. *Nature Nanotechnology 3*, 538–542.

[189] Harris, D. *Quantitative Chemical Analysis, Sixth Edition*; W. H. Freeman, 2003.

[190] Varian/Agilent, Cary 6000i User Manual. 2012.

[191] Clark, B., Frost, T., Russell, A., and Group, U. S. *UV Spectroscopy: Techniques, Instrumentation and Data Handling*; Springer, 1993; (Great Britain).

[192] Coleman, J. N. PY4P04 NanoScience Course Notes.

[193] Jeol, Jeol-2100 TEM Manual.

[194] Spence, J. *Experimental high-resolution electron microscopy*; Oxford University Press, 1988.

[195] Temescal, FC 2000 User Manual.

[196] Keithley, Keithley 2400 Sourcemeter Manual.

[197] Bao, Z., and Locklin, J. *Organic Field-Effect Transistors*; Taylor & Francis, 2007.

[198] Newport, Oriel Instruments 150 W Solar Simulator Manual.

[199] (Oriel), N. Solar Simulation Manual.

[200] Paton, K. R. et al. (2014) Scalable production of large quantities of defect-free few-layer graphene by shear exfoliation in liquids. *Nature Materials*

[201] Hughes, J. M., Aherne, D., and Coleman, J. N. (2013) Generalizing solubility parameter theory to apply to one- and two-dimensional solutes and to incorporate dipolar interactions. *Journal of Applied Polymer Science 127*, 4483–4491.

[202] Atkins, P. W., and Paula, J. D. *Physical Chemistry*; W.H. Freeman, 2006.

[203] Barton, A. (1975) Solubility parameters. *Chemical Reviews 75*, 731–753.

[204] Israelachvili, J. *Intermolecular and Surface Forces*; Elsevier Science, 2010.

[205] Hansen, C. M. *Hansen solubility parameters: a user's handbook*; CRC Press, 2007.

[206] Bromley, R., Murray, R., and Yoffe, A. (1972) The band structures of some transition metal dichalcogenides. III. Group VIA: trigonal prism materials. *Journal of Physics C: Solid State Physics 5*, 759.

[207] Nicolosi, V., Vrbanic, D., Mrzel, A., McCauley, J., O Flaherty, S., Mihailovic, D., Blau, W. J., and Coleman, J. N. (2005) Solubility of Mo6S4.5I4.5 nanowires. *Chemical Physics Letters 401*, 13–18.

[208] Marguerite Hughes, J., Aherne, D., Bergin, S. D., O Neill, A., Streich, P. V., Hamilton, J. P., and Coleman, J. N. (2012) Using solution thermodynamics to describe the dispersion of rod-like solutes: application to dispersions of carbon nanotubes in organic solvents. *Nanotechnology 23*, 265604.

[209] Bjorkman, T., Gulans, A., Krasheninnikov, A. V., and Nieminen, R. M. (2012) van der Waals Bonding in Layered Compounds from Advanced Density-Functional First-Principles Calculations. *Physical Review Letters 108*.

[210] James, A., and Lord, M. *MacMillan's Chemical and Physical Data*; MacMillan, 1992.

[211] Durose, K., Edwards, P., and Halliday, D. (1999) Materials aspects of CdTe/CdS solar cells. *Journal of Crystal Growth 197*, 733–742.

[212] Fuhr, J. D., Sofo, J. O., and Saul, A. (1999) Adsorption of Pd on MoS2 (1000): Ab initio electronic-structure calculations. *Physical Review B 60*, 8343.

[213] Weiss, K., and Phillips, J. M. (1976) Calculated specific surface energy of molybdenite (MoS 2). *Physical Review B 14*, 5392.

[214] Bindumadhavan, K., Srivastava, S. K., and Mahanty, S. (2013) MoS2-MWCNT hybrids as a superior anode in lithium-ion batteries. *Chemical Communications 49*, 1823–1825.

[215] Chang, K., and Chen, W. (2011) In situ synthesis of MoS2/graphene nanosheet composites with extraordinarily high electrochemical performance for lithium ion batteries. *Chemical Communications 47*, 4252.

[216] Xiao, J., Choi, D., Cosimbescu, L., Koech, P., Liu, J., and Lemmon, J. P. (2010) Exfoliated MoS2 Nanocomposite as an Anode Material for Lithium Ion Batteries. *Chemistry of Materials 22*, 4522–4524.

[217] Hwang, H., Kim, H., and Cho, J. (2011) MoS2 Nanoplates Consisting of Disordered Graphene-like Layers for High Rate Lithium Battery Anode Materials. *Nano Lett. 11*, 4826–4830.

[218] Bergin, S. D., Sun, Z., Streich, P., Hamilton, J., and Coleman, J. N. (2010) New Solvents for Nanotubes: Approaching the Dispersibility of Surfactants. *The Journal of Physical Chemistry C 114*, 231–237.

[219] Baughman, R. H. (2002) Carbon Nanotubes–the Route Toward Applications. *Science 297*, 787–792.

[220] Geim, A. K. (2009) Graphene: Status and Prospects. *Science 324*, 1530–1534.

[221] Whittingham, M. S. (2004) Lithium Batteries and Cathode Materials. *Chemical Reviews 104*, 4271–4302.

[222] King, P., Higgins, T., De, S., Nicoloso, N., and Coleman, J. (2012) Percolation Effects in Supercapacitors with Thin, Transparent Carbon Nanotube Electrodes. *ACS Nano*

[223] Stauffer, D., and Aharony, A. *Introduction To Percolation Theory*; Taylor & Francis, 1994.

[224] King, P. R., Buldyrev, S. V., Dokholyan, N. V., Havlin, S., Lopez, E., Paul, G., and Stanley, H. E. (2002) Percolation theory. *: London Petrophysical Society Newsletter 10*.

[225] Otten, R. H. J., and van der Schoot, P. (2011) Connectivity percolation of polydisperse anisotropic nanofillers. *The Journal of Chemical Physics 134*, 094902.

[226] De, S., King, P., Lyons, P., Khan, U., and Coleman, J. (2010) Size effects and the problem with percolation in nanostructured transparent conductors. *ACS nano*

[227] Duesberg, G. S., Loa, I., Burghard, M., Syassen, K., and Roth, S. (2000) Polarized Raman spectroscopy on isolated single-wall carbon nanotubes. *Physical review letters 85*, 5436.

[228] Ferrari, A. C., Meyer, J. C., Scardaci, V., Casiraghi, C., Lazzeri, M., Mauri, F., Piscanec, S., Jiang, D., Novoselov, K. S., Roth, S., and Geim, A. K. (2006) Raman Spectrum of Graphene and Graphene Layers. *Physical Review Letters 97*.

[229] Lu, M., Nicolai, H. T., Wetzelaer, G.-J. A. H., and Blom, P. W. M. (2011) Effect of n-type doping on the hole transport in poly(p-phenylene vinylene). *Journal of Polymer Science Part B: Polymer Physics 49*, 1745–1749.

[230] Wu, J., and McLachlan, D. S. (1997) Percolation exponents and thresholds obtained from the nearly ideal continuum percolation system graphite-boron nitride. *Physical Review B 56*, 1236.

[231] Wu, J., and McLachlan, D. S. (1998) Scaling behavior of the complex conductivity of graphite-boron nitride percolation systems. *Physical Review B 58*, 14880.

[232] Celzard, A., McRae, E., Deleuze, C., Dufort, M., Furdin, G., and Mareche, J. F. (1996) Critical concentration in percolating systems containing a high-aspect-ratio filler. *Physical Review B 53*, 6209.

[233] Bauhofer, W., and Kovacs, J. Z. (2009) A review and analysis of electrical percolation in carbon nanotube polymer composites. *Composites Science and Technology 69*, 1486–1498.

[234] Stankovich, S., Dikin, D. A., Dommett, G. H. B., Kohlhaas, K. M., Zimney, E. J., Stach, E. A., Piner, R. D., Nguyen, S. T., and Ruoff, R. S. (2006) Graphene-based composite materials. *Nature 442*, 282–286.

[235] Quintanilla, J. A., and Ziff, R. M. (2007) Asymmetry in the percolation thresholds of fully penetrable disks with two different radii. *Physical Review E 76*, 051115.

[236] Balberg, I., Anderson, C. H., Alexander, S., and Wagner, N. (1984) Excluded volume and its relation to the onset of percolation. *Physical Review B 30*, 3933–3943.

[237] White, S. I., Mutiso, R. M., Vora, P. M., Jahnke, D., Hsu, S., Kikkawa, J. M., Li, J., Fischer, J. E., and Winey, K. I. (2010) Electrical Percolation Behavior in

Silver Nanowire-Polystyrene Composites: Simulation and Experiment. *Advanced Functional Materials 20*, 2709–2716.

[238] Hicks, J., Behnam, A., and Ural, A. (2009) A computational study of tunneling-percolation electrical transport in graphene-based nanocomposites. *Applied Physics Letters 95*, 213103.

[239] Pang, H., Chen, T., Zhang, G., Zeng, B., and Li, Z.-M. (2010) An electrically conducting polymer graphene composite with a very low percolation threshold. *Materials Letters 64*, 2226–2229.

[240] McLachlan, D., Chiteme, C., Heiss, W., and Wu, J. (2003) The correct modelling of the second order terms of the complex AC conductivity results for continuum percolation media, using a single phenomenological equation. *Physica B: Condensed Matter 338*, 256–260.

[241] McLachlan, D. S., Chiteme, C., Park, C., Wise, K. E., Lowther, S. E., Lillehei, P. T., Siochi, E. J., and Harrison, J. S. (2005) AC and DC percolative conductivity of single wall carbon nanotube polymer composites. *Journal of Polymer Science Part B: Polymer Physics 43*, 3273–3287.

[242] Efros, A. L., and Shklovskii, B. I. (1976) Critical Behaviour of Conductivity and Dielectric Constant near the Metal, Non-Metal Transition Threshold. *physica status solidi (b) 76*, 475–485.

[243] Hecht, D., Hu, L., and Gruner, G. (2006) Conductivity scaling with bundle length and diameter in single walled carbon nanotube networks. *Applied Physics Letters 89*, 133112–133112–3.

[244] Moniruzzaman, M., and Winey, K. I. (2006) Polymer Nanocomposites Containing Carbon Nanotubes. *Macromolecules 39*, 5194–5205.

[245] Nirmalraj, P. N., Lyons, P. E., De, S., Coleman, J. N., and Boland, J. J. (2009) Electrical Connectivity in Single-Walled Carbon Nanotube Networks. *Nano Letters 9*, 3890–3895.

[246] Nirmalraj, P., Lutz, T., Kumar, S., Duesberg, G., and Boland, J. (2011) Nanoscale Mapping of Electrical Resistivity and Connectivity in Graphene Strips and Networks. *Nano letters*

[247] De, S., and Coleman, J. N. (2011) The effects of percolation in nanostructured transparent conductors. *MRS Bulletin 36*, 774–781.

[248] Eda, G., and Chhowalla, M. (2009) Graphene-based Composite Thin Films for Electronics. *Nano Lett. 9*, 814–818.

[249] Otten, R. H. J., and van der Schoot, P. (2009) Continuum Percolation of Polydisperse Nanofillers. *Physical Review Letters 103*.

[250] Systems, M. O. C. E. E. VII. Porous Media Lecture 32: Percolation. 2011.

[251] Romeo, N. (1979) Thin film heterojunction solar cells. *Materials Chemistry 4*, 571–590.

[252] Bube, R. H. *Photoelectronic Properties of Semiconductors*; Cambridge University Press, 1992.

[253] Bube, R. H. *Photoconductivity of solids*; Wiley, 1960.

[254] Halpern, V. (1988) The intensity dependence of the steady-state photoconductivity in amorphous semiconductors. *Journal of Physics C: Solid State Physics 21*, 2555.

[255] Rose, A. *Concepts in photoconductivity and allied problems*; Interscience Publishers, 1963.

[256] Konstantatos, G., and Sargent, E. H. (2007) PbS colloidal quantum dot photoconductive photodetectors: Transport, traps, and gain. *Applied Physics Letters 91*, 173505.

[257] Moazzami, K., Murphy, T. E., Phillips, J. D., Cheung, M. C.-K., and Cartwright, A. N. (2006) Sub-bandgap photoconductivity in ZnO epilayers and extraction of trap density spectra. *Semiconductor Science and Technology 21*, 717–723.

[258] Evans, B., and Thompson, K. (1968) The photovoltage in thin crystals of MoS2. *Journal of Physics D: Applied Physics 1*, 1619.

[259] Fortin, E., and Sears, W. (1982) Photovoltaic effect and optical absorption in MoS2. *Journal of Physics and Chemistry of Solids 43*, 881–884.

[260] Zhang, W., Huang, J.-K., Chen, C.-H., Chang, Y.-H., Cheng, Y.-J., and Li, L.-J. (2013) High-Gain Phototransistors Based on a CVD MoS $_2$ Monolayer. *Advanced Materials* n/a–n/a.

[261] Yin, Z., Li, H., Li, H., Jiang, L., Shi, Y., Sun, Y., Lu, G., Zhang, Q., Chen, X., and Zhang, H. (2012) Single-Layer MoS2 Phototransistors. *ACS Nano 6*, 74–80.

[262] Lopez-Sanchez, O., Lembke, D., Kayci, M., Radenovic, A., and Kis, A. (2013) Ultrasensitive photodetectors based on monolayer MoS2. *Nature Nanotechnology*

[263] Sundaram, R. S., Engel, M., Lombardo, A., Krupke, R., Ferrari, A. C., Avouris, P., and Steiner, M. (2013) Electroluminescence in Single Layer MoS $_2$. *Nano Letters* 130329131217003.

[264] Xia, F., Mueller, T., Lin, Y.-m., Valdes-Garcia, A., and Avouris, P. (2009) Ultrafast graphene photodetector. *Nature Nanotechnology 4*, 839–843.

[265] Qiu, H., Pan, L., Yao, Z., Li, J., Shi, Y., and Wang, X. (2012) Electrical characterization of back-gated bi-layer MoS2 field-effect transistors and the effect of ambient on their performances. *Applied Physics Letters 100*, 123104.

[266] Lee, H. S., Min, S.-W., Chang, Y.-G., Park, M. K., Nam, T., Kim, H., Kim, J. H., Ryu, S., and Im, S. (2012) MoS2 Nanosheet Phototransistors with Thickness-Modulated Optical Energy Gap. *Nano Letters 12*, 3695–3700.

[267] Windom, B. C., Sawyer, W. G., and Hahn, D. W. (2011) A Raman Spectroscopic Study of MoS2 and MoO3: Applications to Tribological Systems. *Tribology Letters 42*, 301–310.

[268] Shimada, T., Ohuchi, F., and Parkinson, B. (1994) Work Function and Photothreshold of Layered Metal Dichalcogenides. *Jpn. J. Appl. Phys., Part 1, 33*, 2696–2698.

[269] Schlaf, R., Murata, H., and Kafafi, Z. H. (2001) Work function measurements on indium tin oxide films. *Journal of Electron Spectroscopy and Related Phenomena 120*, 149–154.

[270] Biddle, V., and Publications, B. B. *Laboratory Manual for Chemistry: Precision and Design*; A Beka Book Publications, 1986; (Firm).

[271] Bollinger, M., Lauritsen, J., Jacobsen, K., Norskov, J., Helveg, S., and Besenbacher, F. (2001) One-Dimensional Metallic Edge States in MoS2. *Physical Review Letters 87*.

[272] Maurel, C., Ajustron, F., Pechou, R., Seine, G., and Coratger, R. (2006) Electrical behavior of the Au/MoS2 interface studied by light emission induced by scanning tunneling microscopy. *Surface Science 600*, 442–447.

[273] Ballif, C., Regula, M., Levy, F., Burmeister, F., Schafle, C., Matthes, T., Leiderer, P., Niedermann, P., Gutmannsbauer, W., and Bucher, R. (1998) Submicron contacts for electrical characterization of semiconducting WS2 thin films. *Journal of Vacuum Science & Technology A: Vacuum, Surfaces, and Films 16*, 1239–1243.

[274] Schroder, D. *Semiconductor Material and Device Characterization*; Wiley, 2006.

[275] Tian, X., Itkis, M. E., Bekyarova, E. B., and Haddon, R. C. (2013) Anisotropic Thermal and Electrical Properties of Thin Thermal Interface Layers of Graphite Nanoplatelet-Based Composites. *Scientific Reports 3*.

[276] Danielson, E., Ooi, Z.-E., Lombardo, C. J., and Dodabalapur, A. (2013) Bimolecular recombination coefficient calculation by in situ potentiometry in a bulk heterojunction organic photovoltaic material. *Applied Physics Letters 102*, 173304.

[277] Pal, R., Yadav, S., Aghinotri, A., Kumar, D., and Kumar, A. (2009) Composition Dependence of Photoconductivity in Amorphous Se70Te30xZnx Thin Films. *Journal of Non-Oxide Glasses Vol 1*, 285–291.

[278] Pal, R., JI, K., Agnihotri, A., Singh, C., Yadav, S., and Kumar, A. (2009) Temperature and Intesnity Dependence of Photoconductivity in amorphous Se70Te26Zn4 and Determination of Defect Centres. *Chalcogenide Letters 6*, 29–34.

[279] Maan, A., and Goyal, D. (2007) Photoconductivity in thin films of SbxSe100-x glasses. *Optoelectronics and Advanced Materials - Rapid Communications*

[280] Perea-Lopez, N., Lin, Z., Pradhan, N. R., Iniguez-Rabago, A., Laura Elias, A., McCreary, A., Lou, J., Ajayan, P. M., Terrones, H., Balicas, L., and Terrones, M. (2014) CVD-grown monolayered MoS $_2$ as an effective photosensor operating at low-voltage. *2D Materials 1*, 011004.

[281] Haynes, J. R., and Hornbeck, J. A. (1955) Trapping of minority carriers in Silicon. II. n-type Silicon. *Physical Review 100*, 606.

[282] Salis, M., Anedda, A., Quarati, F., Blue, A. J., and Cunningham, W. (2005) Photocurrent in epitaxial GaN. *Journal of Applied Physics 97*, 033709.

[283] Lee, Y., Hu, S., Tiong, K., Shen, J., Chen, K., and Huang, Y. (2008) Temperature dependence anisotropic photoconductivity in 2H-MoSe2 single crystals. *Journal of Alloys and Compounds 448*, 44–48.

[284] Adriaenssens, G. J., Baranovskii, S. D., Fuhs, W., Jansen, J., and Oktu, O. (1995) Photoconductivity response time in amorphous semiconductors. *Physical Review B 51*, 9661.

[285] Perea-Lopez, N., Elias, A. L., Berkdemir, A., Castro-Beltran, A., Gutierrez, H. R., Feng, S., Lv, R., Hayashi, T., Lopez-Uias, F., Ghosh, S., Muchharla, B., Talapatra, S., Terrones, H., and Terrones, M. (2013) Photosensor Device Based on Few-Layered WS $_2$ Films. *Advanced Functional Materials* n/a–n/a.

[286] Lany, S., and Zunger, A. (2005) Anion vacancies as a source of persistent photoconductivity in II-VI and chalcopyrite semiconductors. *Physical Review B 72*.

[287] Yun, W. S., Han, S. W., Hong, S. C., Kim, I. G., and Lee, J. D. (2012) Thickness and strain effects on electronic structures of transition metal dichalcogenides: 2H-MX_{2} semiconductors (M = Mo, W; X = S, Se, Te). *Physical Review B 85*.

[288] Ma, Y., Dai, Y., Guo, M., Niu, C., Lu, J., and Huang, B. (2011) Electronic and magnetic properties of perfect, vacancy-doped, and nonmetal adsorbed MoSe2, MoTe2 and WS2 monolayers. *Physical Chemistry Chemical Physics 13*, 15546.

[289] Kumar, A., and Ahluwalia, P. K. (2012) Electronic structure of transition metal dichalcogenides monolayers 1H-MX2 (M = Mo, W; X = S, Se, Te) from ab-initio theory: new direct band gap semiconductors. *The European Physical Journal B 85*.

[290] Serpi, A. (1992) Negative Photoconductivity in MoS2. *physica status solidi (a) 133*, K73–K77.

[291] Stallinga, P. *Electrical Characterization of Organic Electronic Materials and Devices*; Wiley, 2009.

[292] Mazumdar, N., Sarma, R., Sarma, B. K., and Das, H. L. (2006) Photoconductivity of ZnTe thin films at elevated temperatures. *Bulletin of Materials Science 29*, 11–14.

[293] Wickramaratne, D., Zahid, F., and Lake, R. K. (2014) The Thermoelectric Performance of Few-Layer Transition Metal Dichalcogenides. *arXiv preprint arXiv:1401.0502*

[294] Baeg, K.-J., Caironi, M., and Noh, Y.-Y. (2013) Toward Printed Integrated Circuits based on Unipolar or Ambipolar Polymer Semiconductors. *Advanced Materials 25*, 4210–4244.

[295] Zeng, Z., Yin, Z., Huang, X., Li, H., He, Q., Lu, G., Boey, F., and Zhang, H. (2011) Single-Layer Semiconducting Nanosheets: High-Yield Preparation and Device Fabrication. *Angewandte Chemie International Edition 50*, 11093–11097.

[296] Fontana, M., Deppe, T., Boyd, A. K., Rinzan, M., Liu, A. Y., Paranjape, M., and Barbara, P. (2013) Electron-hole transport and photovoltaic effect in gated MoS2 Schottky junctions. *Scientific Reports 3*.

[297] Grant, A. J., Griffiths, T. M., Pitt, G. D., and Yoffe, A. D. (1975) The electrical properties and the magnitude of the indirect gap in the semiconducting transition metal dichalcogenide layer crystals. *Journal of Physics C: Solid State Physics 8*, L17.

[298] Thakurta, S. R., and Dutta, A. K. (1983) Electrical conductivity, thermoelectric power and hall effect in p-type molybdenite (MoS2) crystal. *Journal of Physics and Chemistry of Solids 44*, 407–416.

[299] Choubey, B., Joseph, D., Aoyama, S., and Collins, S. Dark current reduction techniques for wide dynamic range logarithmic CMOS pixels. 30th International Congress of Imaging Science. 2006.

[300] Ghanbarzadeh, S., Abbaszadeh, S., and Karim, K. S. (2014) Low Dark Current Amorphous Silicon Metal-Semiconductor-Metal Photodetector for Digital Imaging Applications. *IEEE Electron Device Letters 35*, 235–237.

[301] Sik Hwang, W., Remskar, M., Yan, R., Protasenko, V., Tahy, K., Doo Chae, S., Zhao, P., Konar, A., (Grace) Xing, H., Seabaugh, A., and Jena, D. (2012) Transistors with chemically synthesized layered semiconductor WS2 exhibiting 105 room temperature modulation and ambipolar behavior. *Applied Physics Letters 101*, 013107.

[302] Kodama, N., Hasegawa, T., Okawa, Y., Tsuruoka, T., Joachim, C., and Aono, M. (2010) Electronic States of Sulfur Vacancies Formed on a MoS_2 Surface. *Japanese Journal of Applied Physics 49*, 08LB01.

[303] Chamlagain, B., Li, Q., Ghimire, N. J., Chuang, H.-J., Perera, M. M., Tu, H., Xu, Y., Pan, M., Xaio, D., Yan, J., Mandrus, D., and Zhou, Z. (2014) Mobility Improvement and Temperature Dependence in $MoSe_2$ Field-Effect Transistors on Parylene-C Substrate. *ACS Nano* 140416143016002.

[304] Larentis, S., Fallahazad, B., and Tutuc, E. (2012) Field-effect transistors and intrinsic mobility in ultra-thin MoSe2 layers. *Applied Physics Letters 101*, 223104.

[305] Fathipour, S. (2013) Exfoliated MoTe2 Field-Effect Transistor. *IEEE* 115–116.

[306] Gong, C., Zhang, H., Wang, W., Colombo, L., Wallace, R. M., and Cho, K. (2013) Band alignment of two-dimensional transition metal dichalcogenides: Application in tunnel field effect transistors. *Applied Physics Letters 103*, 053513.

[307] Makarova, M., Okawa, Y., and Aono, M. (2012) Selective Adsorption of Thiol Molecules at Sulfur Vacancies on MoS_2 (0001), Followed by Vacancy Repair via S-Dissociation. *The Journal of Physical Chemistry C 116*, 22411–22416.

[308] Akimov, B. A., Bogoyavlenskiy, V. A., Ryabova, L. I., and Vasilkov, V. N. (2000) Experimental study of negative photoconductivity in n-PbTe(Ga) epitaxial films. *arXiv:cond-mat/0009209* Phys. Rev. B 61, 16045 (2000).

[309] Johnson, L., and Levinstein, H. (1960) Infrared properties of gold in germanium. *Physical Review 117*, 1191.

[310] Wei, P.-C., Chattopadhyay, S., Yang, M.-D., Tong, S.-C., Shen, J.-L., Lu, C.-Y., Shih, H.-C., Chen, L.-C., and Chen, K.-H. (2010) Room-temperature negative photoconductivity in degenerate InN thin films with a supergap excitation. *Physical Review B 81*, 045306.

[311] Penchina, C. M., Moore, J. S., and Holonyak Jr, N. (1966) Energy levels and negative photoconductivity in cobalt-doped silicon. *Physical Review 143*, 634.

[312] Kang, J., Liu, W., Sarkar, D., Jena, D., and Banerjee, K. (2014) Computational Study of Metal Contacts to Monolayer Transition-Metal Dichalcogenide Semiconductors. *Physical Review X 4*.

[313] Withers, F. et al. (2014) Heterostructures Produced from Nanosheet-Based Inks. *Nano Letters 14*, 3987–3992.

[314] Rouhi, N., Jain, D., and Burke, P. J. (2011) High-Performance Semiconducting Nanotube Inks: Progress and Prospects. *ACS Nano 5*, 8471–8487.

[315] Eda, G., Fanchini, G., and Chhowalla, M. (2008) Large-area ultrathin films of reduced graphene oxide as a transparent and flexible electronic material. *Nature Nanotechnology 3*, 270–274.

[316] Torrisi, F., Hasan, T., Wu, W., Sun, Z., Lombardo, A., Kulmala, T. S., Hsieh, G.-W., Jung, S., Bonaccorso, F., Paul, P. J., Chu, D., and Ferrari, A. C. (2012) Inkjet-Printed Graphene Electronics. *ACS Nano 6*, 2992–3006.